UNIVERSIDAD DE GRANADA

Ph.D Thesis

Study and development of flexible electronic nanodevices for biosensing applications

---

Author
Mr. Alejandro Toral López

Tutors
Dr. Andrés Godoy Medina
Dr. Enrique González Marín

A thesis submitted in fulfilment of the requirement to obtain the International Doctor degree as a part of the
Programa de Doctorado en Tecnologías de la Información y la Comunicación
in the
Pervasive Electronics Advanced Research Laboratory
Departamento de Electrónica y Tecnología de Computadores

Granada, December 28, 2021

UNIVERSIDAD DE GRANADA

PhD Thesis

Estudio y desarrollo de nanodispositivos electrónicos flexibles para aplicaciones biosensoras

Author
Mr. Alejandro Toral López

Tutors
Dr. Andrés Godoy Medina
Dr. Enrique González Marín

A thesis submitted in fulfilment of the requirement to obtain the International Doctor degree as a part of the *Programa de Doctorado en Tecnologías de la Información y la Comunicación*
in the
Pervasive Electronics Advanced Research Laboratory
Departamento de Electrónica y Tecnología de Computadores

Granada, December 28, 2021

Editor: Universidad de Granada. Tesis Doctorales
Autor: Alejandro Toral López
ISBN: 978-84-1117-265-3
URI: http://hdl.handle.net/10481/73964

CONTENTS

Study and development of flexible electronic nanodevices for biosensing applications

by Mr. Alejandro Toral López

University of Granada, Departamento de Electrónica y Tecnología de Computadores

Pervaisve Electronics Advanced Research Laboratory

Abstract

This Thesis aims to develop a comprehensive set of numerical tools specifically designed to analyse 2D materials (2DMs) based Field-Effect Transistor-based Biosensor (BioFET)s. These tools are intended to provide a deeper understanding of their operation principles and to shed light in the fundamental physical and electrical magnitudes involved in their optimization. To that end, a self-consistent numerical platform has been implemented able to solve the set of coupled equations that describes the structure, comprising the FET device and the electrolyte solution containing the biological sample.

On the one hand, for the simulation of the FET device, a semi-classical approach combining Poisson, Schrödinger and continuity equations under a Drift-Diffusion (DD) paradigm is considered. In more detail Poisson equation is solved in a 2D cross-section of the structure including Fermi-Dirac statistics, while the Schrödinger equation is included in order to treat highly confined structures, being simplified in some particular scenarios. In addition, two different approaches for the implementation of the diffusive transport have been considered: i) the conventional current equation with both, drift and diffusion components and ii) a description based on the gradient of the Fermi level. Both implementations are equivalent under the assump-

tion of a non-degenerate semiconductor, although the latter enables a more sophisticated treatment as it enables the integration of the material properties at the device level. Based on it, the work explores the capability to integrate arbitrary Density of States (DoS) profiles achieved from *ab-ibitio* calculations to describe the semiconductor material. This is by itself a significant step forward in the state-of-the-art computational electronics by enabling the integration of atomic level features into semi-classical device level simulations following the multi-scale paradigm. A model for charge traps situated at the interfaces of the FET channel is also implemented with a flexible definition of their energetic profile and spatial location enabling a fine description of these non-idealities in electronic devices. Moreover, both charge transport and charge traps models are extended to include time dependence, and additional tool that provides us with the capability of simulating FETs in the transient regime.

On the other hand, the modelling of the biological sample encompasses the liquid electrolyte and the sensing interface. The description of the electrolyte addresses the distribution of simple ions by the electrostatic potential. It is extended to include the contribution of non-Coulombic interactions near the solid-liquid interface using the Potentials of Mean Force (PMF), and the contribution of chemical reactions that take place in buffer solutions related with the pH regulation. Concerning the sensing interface, it involves the adsorption of simple ions at the solid-liquid interface, which is integrated in the simulations making use of a generic Site-Binding (SB) model that makes possible to handle complex chained reactions taking place at the solid surface. For the specific case of biomolecular sensors, the specific receptors introduced by the surface functionalization are also integrated in the simulations. This requires a more thoughtful development due to the complexity of the elements to be modelled, i.e., the receptor-target molecule complexes formed at the sensor surface during the sensing process. In this regard, two aspects are treated in detail: the charge distribution of receptor and target molecules and the location of receptors on the sensing interface. The former is related with the physical properties of the molecules, while the latter is dependent on the structure of the sensor. With regards to the charge distribution of molecules, three models are proposed with different levels of detail. The simplest one considers a box-shaped charge distribution with different regions where the ion permeability can be controlled. Along with it, a specific model for DNA molecules is developed aiming for a detailed description of this remarkable biomolecule. Finally, a third one is implemented focused on a detailed depiction of the charge distribution of molecules. This last approach enables the integration of external charge distribution profiles providing the connection with *ab-initio* calculations, assess as those provided by Molecular Dynamics (MD).

The numerical simulator resulting from the combination of the aforementioned models has been exploited to study different device concepts and physical aspects connected to the design of FET and BioFET devices. All these results come along with the validation process of each module of the simulator.

First, the models related with the FET device are compared against experimental results extracted from the literature reproducing to an excellent degree the behaviour of these devices. In addition, the two aforementioned implementations of the DD transport model, i.e. based on drift and diffusion currents or the gradient of the Fermi level, are compared providing similar results when the material band-structure is approximated by a parabolic dispersion relationship.

Next, the FET simulator is employed to perform some relevant studies. For example, it is used to evaluate graphene based devices and specifically the impact of access regions on the response of Graphene Field-Effect Transistor (GFET)s, showing a significant contribution to the asymmetric transfer response commonly observed in these devices regardless the intrinsic electron and hole properties. The numerical simulator is then utilized to evaluate the impact of mechanical strain in GaSe MOSFET devices. To that end, the Fermi-level-gradient definition of the DD current is used to evaluate locally strained channels by using a DoS profile from atomistic calculations. The results obtained not only reveal the great potential of this implementation but also provide some insights on the capabilities of strain engineering as a method to dope 2D materials, that is still one of the major obstacles in the technological adoption of these crystals in nanoelectronics. Finally, the time dependent implementations of the transport model and of the interface traps are used to study the impact of the latter in the commonly observed hysteresis in MoS_2 MOSFET. In that case, the high flexibility to define the energetic profile of these traps enables a fine study and characterization of an experimental study carried out by.

The numerical models for the complex electrolyte and sensing interface were, as well, validated against experimental results available in the bibliography obtaining an excellent agreement. These modules, together with the developed FET simulation tool, compose the complete BioFET simulation platform. This platform is next applied to study several proposals of 2D materials based BioFET sensors. First, the impact of different box-shaped models for the receptor-target complex commonly used in the simulation of BioFETs, is analysed. These models provide a rapid and efficient modelling for generic molecules, and are an approximation (although still a coarse one) similar to those used by TCAD simulators. The results obtained illustrate how the different box models lead to distinct simulated sensor responses, highlighting the importance of the appropriate selection

of the model. Next, the numerical simulator is used to evaluate the capabilities of graphene based BioFETs for the detection of SARS-CoV-2. This study uses a sophisticated fine model for the receptor and receptor-target complex with a detailed charge distribution of these molecules. The results of the fine-level molecule modelling illustrate that this simulation scheme is able to capture the impact of the specific shape of molecule in the response of the device, and thus, its inherent capability to integrate data from a lower abstraction level for the receptor-target complex in a multi-scale fashion, what constitutes a pioneering work in the field. Next, the impact of device-to-device variability in MoS_2 based DNA-BioFETs is addressed. This analysis takes advantage of some randomization features integrated in the sensing interface model specifically designed to evaluate the impact of random variations in the placement of the molecule receptors in the response of the sensor. This type of analysis is not covered in the literature of BioFET devices, so it entails a noticeable contribution to the state-of-the-art. The results obtained reveal a non-negligible impact of the variability in the sensing interface, specially in those variations related with the activation of receptors. Finally, the effects related with the solid-liquid interface are studied, and more specifically the integration of information from the PMF profiles into the SB model, giving rise to an *avant-garde* model for surface ion adsorption.

In summary, the work collected in this Thesis encompasses a flexible and powerful numerical simulator able to describe with great detail the particular features of BioFET devices. The platform is validated against experimental FET and BioFET devices, reproducing them excellently, and it is latter exploited in several studies that yield relevant for the modelling of 2DM-based FET and BioFET devices and their optimization.

Estudio y desarrollo de nanodispositivos electrónicos flexibles para aplicaciones biosensoras

by Mr. Alejandro Toral López

University of Granada, Departamento de Electrónica y Tecnología de Computadores

Pervaisve Electronics Advanced Research Laboratory

Resumen

El objetivo de esta Tesis es desarrollar una herramienta de simulación orientada al análisis de biosensores basados en estructuras de efecto campo (BioFET) utilizando materiales 2D (2DMs). Dicho simulador busca proporcionar un mejor entendimiento del funcionamiento de estos sensores y de las magnitudes clave para su optimización. Con tal fin, se ha implementado un código basado en un esquema iterativo capaz de resolver el conjunto de ecuaciones que definen el comportamiento de la estructura, que comprende el dispositivo FET, la interfaz sensora y el electrolito.

Por un lado, para la simulación del dispositivo FET se ha considerado un esquema semi-clásico que integra las ecuaciones de Poisson, Schrödinger y la ecuación de continuidad mediante el modelo Deriva-Difusión. De forma más detallada, la ecuación de Poisson se resuelve en una sección transversal de la estructura, asumiendo que esta es invariante en la dirección omitida y considerando estadística de Fermi-Dirac para las distribuciones de carga. Con respecto a la ecuación de Schrödinger, se tiene en cuenta en estructuras con fuerte confinamiento (siendo esta aproximada en algunos casos particulares). En lo que respecta al modelo de transporte, se han llevado

a cabo dos implementaciones diferentes: i) la implementación convencional basada en las componentes separadas de deriva y difusión de la corriente y ii) la implementación basada en el gradiente del nivel de Fermi. Ambas son equivalentes para el caso de semiconductores no degenerados, aunque la segunda permite una descripción más detallada del material semiconductor. Concretamente, se ha trabajado en la integración de una DoS arbitraria obtenida a partir de cálculos *ab-initio*, que caracteriza al material semiconductor, y se puede utilizar en las simulaciones del dispositivo. Esto supone un salto importante en el estado del arte actual, permitiendo la integración de particularidades de nivel atómico en simulaciones a nivel de dispositivo. También se ha implementado un modelo para trampas de carga enfocado en la flexibilidad a la hora de definir el perfil energético de estas y su localización en la estructura. Estos modelos también han sido extendidos para incluir la dependencia temporal y poder evaluar dispositivos tipo FET en el régimen transitorio.

Por otro lado, el modelado de la interfaz biológica agrupa al electrolito y los elementos de la interfaz sensora. El modelo para el electrolito aborda la distribución de los iones simples debido al potencial electrostático. Dicho modelo ha sido extendido para incluir interacciones no culombianas cerca de la interfaz solido-disolución mediante los perfiles PMF, y la contribución de las reacciones químicas de regulación del pH que se dan en disoluciones tipo *buffer*, comúnmente utilizadas como sustrato de muestras biológicas. En relación con la interfaz sensora, esta integra la adsorpción de iones en la superficie del dispositivo utilizando una implementación generalista del modelo SB, que permite incluir reacciones complejas en la superficie del dispositivo. Para el caso concreto de sensores biomoleculares, las simulaciones también incluyen los elementos añadidos por la funcionalización del sensor. Este apartado requiere un tratamiento especial por la complejidad de los elementos modelados: los compuestos receptor-objetivo formados en la superficie del sensor en el proceso de medida. Al respecto de esto, el modelo trata dos aspectos principales: distribución de carga asociada a las moléculas y la localización de receptores en la superficie del dispositivo. El primero de ellos está relacionado con las propiedades físicas de las moléculas mientras que el segundo se relaciona con la estructura del sensor. Con respecto a la distribución de carga de las moléculas, se han propuesto tres modelos que la abordan con diferentes niveles de detalle. El más básico de estos considera una distribución en forma de caja con diferentes regiones en las que es posible controlar su permeabilidad con respecto a la distribución de iones. El segundo de ellos se centra en el caso específico de las moléculas de ADN. El último modelo permite la integración de distribuciones de carga arbitrarias extraídas de métodos *ab-initio*, tales como cálculos MD.

El simulador numérico resultado de la integración de estos modelos se

ha utilizado para estudiar diferentes aspectos relacionados con el diseño de dispositivos FET y BioFET. La extracción de estos resultados se ha llevado a cabo junto con la validación de los modelos.

Inicialmente, se han validado los modelos relacionados con el dispositivo FET usando resultados experimentales extraídos de la bibliografía, proporcionando un excelente ajuste con los mismos. Además, se han comparado las dos implementaciones para la ecuación DD mostrando resultados muy similares cuando la estructura de bandas del material se aproxima con una dispersión parabólica.

A continuación, se ha utilizado el esquema de simulación para dispositivos FET para llevar a cabo varios estudios. Primeramente, se ha analizado el impacto de las regiones de acceso en la respuesta de dispositivos MOSFET de Grafeno, observándose su importante contribución a la asimetría frecuentemente observada en estos dispositivos, con independencia de las propiedades intrínsecas de electrones y huecos. Posteriormente, se ha puesto el foco en el efecto de la deformación mecánica en dispositivos MOSFET basados en GaSe. Para tal fin, la implementación basada en el gradiente del nivel de Fermi ha sido utilizada en combinación con perfiles de DoS extraídos de cálculos atomísticos. Los resultados obtenidos no solo muestran el gran potencial de este esquema, sino que también proporcionan detalles sobre las opciones de la tecnología de deformación mecánica como un método para conseguir el dopado de los 2DMs, lo cuál es todavía un desafío para la utilización de estos materiales en las tecnología nanoeletrónica actual. Finalmente, se han utilizado los modelos en los que se incluye la dependencia temporal para evaluar el impacto de las trampas de carga en la histéresis comúnmente observada en dispositivos MOSFET basados en MoS_2. La flexibilidad que proporciona el modelo en la definición del perfil energético de las trampas ha permitido el estudio y caracterización detallada de un dispositivo experimental.

El esquema de simulación para el electrolito y la interfaz sensora también ha sido validado utilizando resultados experimentales extraídos de la bibliografía, obteniendo un excelente ajuste de los datos. Estos modelos, junto con los correspondientes para los dispositivos FET, definen el esquema completo para los BioFETs. Una vez validado dicho esquema, ha sido utilizado para realizar algunos estudios relacionados con este tipo de dispositivos. Inicialmente, se ha analizado el impacto del modelo más básico para las moléculas (distribución de carga en regiones en forma de caja), que constituye una solución rápida y eficiente para el modelado de moléculas de forma genérica, además de ser la mejor aproximación (aunque todavía tosca) utilizada en simuladores TCAD. Los resultados obtenidos muestran como las diferentes opciones de este modelo resultan en diferentes respuestas del sensor, lo cual revela la importancia de la correcta elección del modelo a la hora

de simular estos dispositivos. A continuación, el simulador se ha utilizado para evaluar las características de BioFETs basados en grafeno para la detección de SARS-CoV-2. Este estudio utiliza el modelo detallado para la distribución de la carga de las moléculas, integrando datos a nivel atómico. Los resultados obtenidos muestran que el simulador es capaz de capturar el impacto de la distribución de la carga de la molécula receptora y sus cambios cuando es activada por la molécula objetivo. Con esto se presenta un modelo capaz de integrar datos de un nivel de abstracción menor dando lugar a un modelo multiescala que constituye un importante paso adelante en el campo. Posteriormente, se ha estudiado la variabilidad en sensores BioFET basados en MoS_2 para la detección de ADN. Para este análisis se ha utilizado la posibilidad de aleatorizar la distribución y la activación de las moléculas receptoras. Este tipo de análisis no es común en la literatura, por lo que se trata de una contribución importante en el estado del arte. Los datos muestran un impacto no despreciable de esta aleatorización, en especial la asociada a la activación de los receptores. Finalmente, se han estudiado los efectos relacionados con la interfaz solido-líquido. Concretamente, se ha puesto el foco sobre la integración de la información de los perfiles PMF en el modelo SB mediante una constante de reacción equivalente. Diferentes esquemas de reacciones han sido utilizados y comparados con los resultados utilizando los perfiles PMF para evaluar las posibilidades de emular el comportamiento de estos últimos.

En conclusión, esta Tesis ha dado como resultado un simulador numérico que ha mostrado gran potencial para la descripción de las particularidades de los dispositivos BioFET. Dicho simulador ha sido validado con éxito utilizando datos experimentales disponibles en la bibliografía y posteriormente ha sido utilizado para llevar a cabo varios estudios que han permitido conocer mejor los dispositivos FET y BioFET basados en 2DMs.

Part I

Introduction

CHAPTER 1

Introduction to 2D materials BioFETs

1.1 State-of-the-art

Electronic technology has experienced an astonishing development in the last half century. The kick off of this adventure dates back to the transition from vacuum tubes towards solid-state devices enabled by the invention of the Bipolar Junction Transistor (BJT) in 1948 by the hand of John Bardeen, Walter Brattain and William Shockley [1]. This breakthrough brought about a significant reduction in the power requirements and size of the devices, promoting their quick deployment. The next significant event was the emergence of the Metal-Oxide-Semiconductor Field-Effect Transistor (MOSFET), patented in 1960 by Kahng Dawon and M. M. Atalla [2]. Since then, MOSFET have become the cornerstone of electronic circuits for computational and telecommunication applications. The continuous shrinking of size and reduction of power consumption of these devices have been the main drivers of the relentless advance of this technology, following the so-called Moore's Law [3], a prediction that turned into a major guideline for the semiconductor industry[1], stating that the transistor size will be reduced by a half in just 18 months. The advances focused on the reduction of the FETs are thus labelled as "More-Moore", whose best example can be found in devices for logic and memory applications. Along with the improvements in digital electronics and the corresponding computation capabilities, other developments have been focused on providing a wide diversification of functionalities for the MOSFET (RF applications, sensors, actuators, etc.) and are usually gathered under the "More-Than-Moore" umbrella [4] (Figure 1.1).

Among these devices, sensors and actuators become of great interest due to their ability to capture information from the environment and interact with it. Electronic sensors base their operation on physical principles that

[1] It could also be considered as a paradigmatic example of a self-fulfilling prophecy.

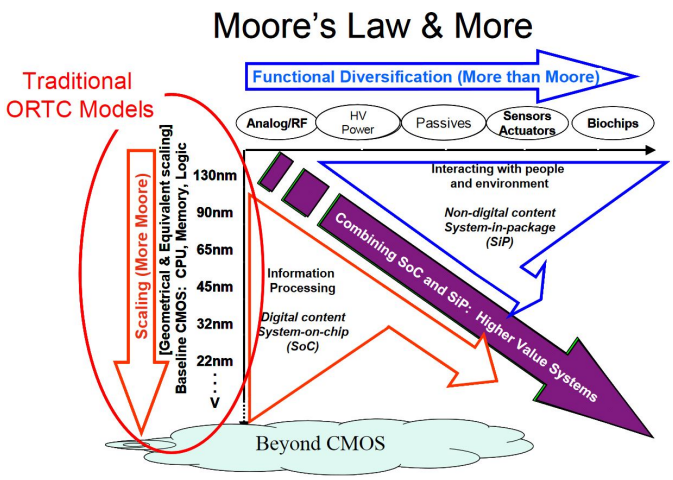

Figure 1.1: Classification of the trends in the evolution of the electronic technologies extracted from [4].

associate changes of the magnitude of interest with variations on the electrical properties of a semiconducting material. The goal is to translate as much information as possible into electrical signals that can be easily processed and stored. Among the myriad of available sensors, those based on MOSFET provide inherent benefits as the mature fabrication process for digital electronics can be used with minor modifications, and straightforwardly integrated with the elements to process the information, giving rise to the so-called System on Chip (SoC), allowing a two-fold improvement: noticeable cost and power reduction, and increased functionality. These features are of great importance for Internet of Things (IoT) technologies, that are currently expanding due to their application for environment monitoring in many different fields.

A particular niche in the sensors field regards chemical and biomolecular FET sensors, which extract information arising from chemical reactions or biomolecular interactions in both static and dynamic regimes, and are therefore able to complement or replace other invasive, expensive and time-consuming techniques [5]. State-of-the-art commercial solutions in chemical detections are primarily based on label-based methods, in which the sample is processed before any measurement can be carried out, to allow the detection of the target molecules via measurable parameters like fluorescence or colorimetry. However, the sample labelling entails high operation cost, lack of portability and limitations for real-time applications. For these reasons, label-free detection methods are of great interest for rapid detection and continuous monitoring applications. These features are specially appealing to medical and security areas (point-of-care solutions, drug detection,

genomics, homeland security), which also benefit from aforementioned IoT technologies.

FETs sensors constitute the label-free electronic alternative for chemical and biomolecular sensing. Their operation principle mimics the one of MOSFETs where an electric field is used to modulate the conductivity of a semiconductor channel located between two conductive regions placed at its edges. The electric field is originated from a metallic contact separated from the semiconductor by an insulating layer. The first FETs specifically designed for chemical and biological sensing applications were the Ion-Sensitive Field-Effect Transistor (ISFET)s [6]. In these sensors the gate is removed and the channel conductivity is modified by the presence of ions or molecules over the insulating layer, giving rise to the corresponding change of the current flowing through the structure. A further development came after with the introduction of a reference electrode. This was an important advance with several works demonstrating its relevance for the proper operation of the device [7, 8] as it sets the electrolyte potential with respect to the device substrate, resulting in a more stable operation of the device [7].

Since the emergence of ISFETs back in the 70's and 80's, they have experienced a continuous progress expanding the range of sensing applications. They have already been employed as chemical sensors to measure pH [9, 10], potassium (K^+) [11, 12] or calcium ions (Ca^{2+}) [13]. In the more general case of Field-Effect Transistor-based Biosensor (BioFET), they have been demonstrated to detect the presence of viruses [14], proteins [15, 16] or cancer markers [17], as shown in Figure 1.2. In addition to biomolecule detection, BioFETs are also used to monitor more complex scenarios such as cell activity [18, 19**?** , 20]. In the last two decades they have strongly come back in the spotlight thanks to the auspicious progresses made with new structures and materials. In particular, nanowire-based BioFETs have demonstrated a notable boost of the sensitivity compared to previous devices [19, 21, 22]. Nevertheless, their integration with current planar technology is still challenging and the shift from laboratory to commercialization is quite limited. In this context, the employment of two-dimensional materials (2DMs) is expected to overcome some of these limitations, allowing high sensitivity, integration with CMOS technology and direct surface functionalization [16, 23, 24, 25].

The recently developed 2DMs technology has demonstrated an extraordinary potential not only for BioFET but also for regular FET devices. The main characteristic of these materials is their minimal thickness (i.e., monoatomic or monomolecular), making the assembly of very thin crystals with perfectly uniform surfaces possible. This unique feature solves the problem arising from abrupt surface interruption and dangling bonds in extremely thin devices based on bulk materials, which results in a significant

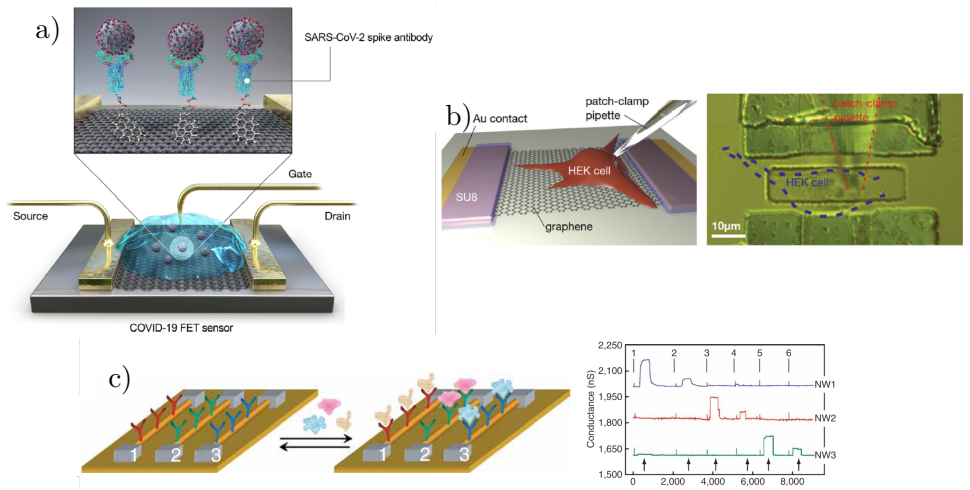

Figure 1.2: Examples of application of BioFET devices: a) virus detection (extracted from [14]), b) cell activity monitoring (extracted from [23]) and multiplexed detection of cancer markers (extracted from [17]).

performance degradation. The electronic properties of 2DMs have been on the scope in the past 18 years since the isolation of Graphene in 2004 [26]. Graphene is characterized by a honeycomb-shaped lattice of carbon atoms, depicting extraordinary physical properties: good thermal and electrical conductivity, mechanical flexibility, etc. One remarkable characteristic of this material is its electronic band structure, which is characterized by the absence of band gap, a fundamental feature that enhances the carrier mobility but, on the other hand, reduces its applicability for logic devices.

The continuous seek for alternative 2DMs was boosted with the discovery of the so-called Transition Metal Dichalcogenides (TMD), whose composition follows the formula MX_2, where M is a transition metal (like Molybdenum (Mo), Tungsten (W) or Tantalum (Ta) among others) and X a chalcogen (like Sulphur (S), Selenium (Se) or Tellurium (Te) among others). The combination of these species results in different properties, e.g. Ta generates highly conductive materials while Mo typically produces semiconductor ones [27]. The family of 2DMs has been steadily enlarged including other groups such as the so-called X-enes [28] (silicene [29], germanene [30], antimonene [31]) or Metal Monochalcogenides (MM) (GaSe [32], GaTe). In addition to the remarkable electronic properties of the monolayer version of 2DMs, several layers can be stacked as depicted in Figure 1.3 to modulate their characteristics.

In these multilayer 3D structures, atoms are still strongly linked in each plane through covalent bonds, while layers are linked through weak van der

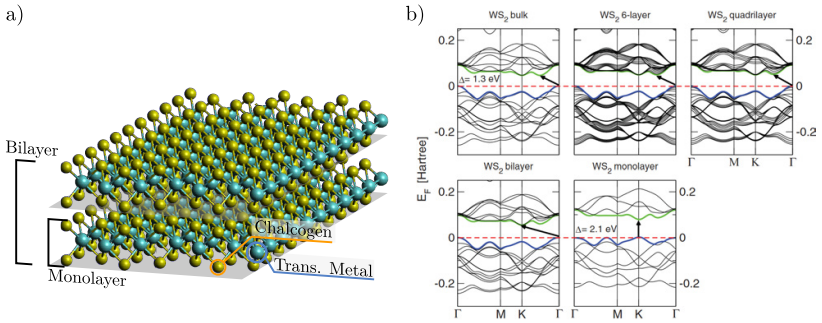

Figure 1.3: a) Example of bilayer structure of a TMD semiconductor and b) band diagrams of WS_2 extracted from [33] showing their change with the number of stacked layers.

Waals forces. Despite of the weakness of these out-of-plane bounds, they can still alter the electrical properties of the resulting multilayer material. An example of this is depicted in Figure 1.3b where the band structure of WS_2 is plotted for different number of stacked layers. As the number of layers is increased, the size of the band gap is modified, shifting from a direct gap in the monolayer scenario to an indirect bandgap for any other case. Black Phosphorous (BP) is another example, as its bandgap and optical absorption spectra vary with the number of layers, showing a redshift as this value increases [34].

Moreover, monolayers and multilayers of different materials can be stacked to form van der Waals heterostructures, behaving as metamaterials with new properties, such as superconductivity [35], and widening the possibilities for new physical effects. Regarding the implementation of MOSFET devices with 2DMs, their minimal thickness provides great promise to overcome short channel effects [36], and their mechanical flexibility allows the implementation of fully flexible devices [37, 38].

Several proofs of concept of BioFETs based on 2DMs have already been successfully developed and tested [14, 16, 19, 23, 24, 39, 40], even including mechanical deformation in the device [41, 42]. However, their operation principles, optimization keys and other related issues such as reliability, scalability, contact resistances, hysteresis, etc., are currently under intensive research targeting for market-ready-solutions. 2DMs-based BioFETs are thus under the spotlight both experimentally [16, 24, 25, 41, 43, 44] as well as theoretically, via numerical simulation, [45, 46, 47, 48, 49, 50, 51]. The experimental works can be classified according to the device-target interface into two groups: Electrolyte-Insulator-Semiconductor (EIS) and Electrolyte-Semiconductor (ES).

In the devices with an EIS structure, an insulator layer is placed between the electrolyte and the semiconductor channel. Its surface is functionalized

(usually via silanization) so to attach receptor agents (e.g. antibody-(TNF-alpha), PSA-mAb, etc) able to capture the target molecules [16, 24, 43]. This insulator layer prevents reactions between the ions contained in the solution and the semiconductor. However, it reduces the electrostatic coupling between the target molecules and the semiconductor material [52]. In addition, most of the gate insulators have a hydrophilic nature that hinders the surface functionalization and reduces the binding efficiency [18]. These problems are intended to be solved with ES BioFETs, where the insulator layer is removed leaving the semiconductor directly in contact with the electrolyte. It is important to note that in these devices the semiconductor is the only region exposed to the solution, all other elements of the device, e.g. source and drain contacts, are isolated from the solution to avoid unintended reactions.

Some 2D materials, like MoS_2 , reduced-graphene Oxide (r-GO) and graphene (commonly used in biological sensors) show an hydrophobic behaviour, and this property can been exploited to suppress the insulator layer [24, 25] and deposit the functionalization layer employed to attach the receptor molecules directly on the semiconductor surface. The operation of biosensors without the functionalization layer has been also tested [25, 53] showing changes in the device response, which indicates that the bare surface of these materials can be responsive to detect the proximity of molecules, but without the required selectivity.

Most of the works focus on sensors immersed in a wet environment, i.e. an electrolyte. However, some of them evaluate the device performance when the sensing step is carried out in a dry environment [25, 40]. In general, the procedure followed in those cases consists on: i) exposing the sensor to the sample, ii) flushing the unbound target molecules, iii) drying the device surface, and iv) performing the electrical characterization of the device. This makes possible the removal of the reference electrode from the structure, as there is no electrolyte during electrical characterization, and prevents side reactions at the device surface that could mask the impact of the target molecules. However, these devices cannot be used for *in vivo* measurements, where controlling the environment is not as straightforward as in a laboratory, making the drying step close to impossible. This issue can be extended to wearable devices or similar cases where the environment is not a factor under control.

The experimental works previously mentioned require the development of simulation and modelling tools able to predict and to explain the results observed in the laboratory. They should make possible to understand and rationalize the non-idealities observed, unveiling optimization keys to speed the device development. The simulation of BioFETs has been commonly addressed using either commercial Technology Computer Aided De-

sign (TCAD) tools [45, 46, 47, 54], specifically designed to simulate semiconductor devices, or *ad-hoc* software developed to analyze more specific scenarios [49, 55, 56, 57]. Using either of these solutions, there are two main elements to be described: i) the semiconductor device and ii) the sample, composed by the electrolyte that contains the target ions and/or molecules. Both components are joined through the solid-liquid interface, where the key processes take place.

TCAD simulations provide a detailed modelling of the semiconductor device, as they have been originally designed for that purpose, but coarse approximations are required to include the effect of electrolyte and biomolecules. Regarding the electrolyte, a common procedure is to model it as a semiconductor with modified properties to emulate those of the solution [47, 49]. This approach is limited to simple electrolytes, precluding its use to analytes where multiple types of ions are present [47]. In the case of biomolecules, there are two main approaches to integrate them in TCAD simulations: i) as a uniform charged layer [45, 47], or ii) as discrete blocks [45, 46]. A uniformly charged layer provides a simple model, as charge and thickness can be modulated to describe different target molecules and concentrations. This can be a reasonable solution for large devices and small target molecules, but it is a coarse approximation for short channel devices, where the spacing between molecules can not be neglected compared with the size of the device. In that regard, discrete block based models constitute a more precise description. They consider each molecule captured by the sensing layer as a charged block, allowing a comprehensive analysis of the device, such as for example the effect of the random activation of receptors in the sensing layer [45]. In that case, however, inactive receptors are modelled as neutral blocks where ions are not allowed to enter, which might generate peculiar potential distributions near the device surface as they are still included in the simulation.

As for *ad-hoc* simulators, they provide a more realistic description of the sensor thanks to a more sophisticated model of the electrolyte and the interface. The price to be paid is i) a reduction of the flexibility compared with TCADs as they are focused on specific geometries, and ii) the time required for their development and testing. Specific non-linear effects such as surface ion adsorption [58] or physical limitations to the interface ion concentration [59] can be included in the electrolyte modelling. In addition to this, electrolytes with multiple ions can be straightforwardly considered, overcoming the TCADs limitations [47]. The modelling of biomolecules can be carried out similarly to TCAD based simulations, where both a uniform charged layer [56, 57] and discrete charged blocks models can be used [60]. Additional descriptions, e.g. based on the dipole moment of the molecules [49, 51], can also be included as boundary conditions for the potential at

the device interface, enabling the inclusion of the molecule orientation and other particularities in their charge distribution.

In all the previous analysis we left aside the type of devices evaluated. In both cases, TCAD and *ad-hoc* solutions, state-of-the-art simulations have primarily dealt with bulk MOSFETs or nanowire based sensors. The option to assess devices based on 2DMs is currently very limited, specially when using TCAD tools, and those using *ad-hoc* software are restricted to a one-dimensional (1D) description of the structure [56, 57], limiting the analysis of relevant factors such as the impact of molecule distribution, short channel effects, etc. This Thesis is intended to contribute to fill this gap by developing a 2D numerical simulator able to study these 2DMs-based chemical and biomolecular sensors.

1.2 Objectives and outline

As mentioned above, despite of the great perspective and advances in 2DMs BioFET, there are numerous challenges to overcome concerning their modelling and rationalization. In this sense, the main goal of this Thesis is to develop a comprehensive set of numerical tools specifically designed to analyze 2DMs-based FET biosensors, able to provide a deeper understanding of their operation principles and to shed light in the fundamental parameters required for their optimization (Figure 1.4).

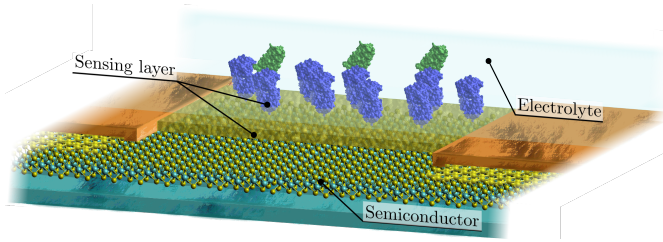

Figure 1.4: Generic structure of 2DMs BioFET device. There are three main elements to be addressed for the modelling of these devices: i) the semiconductor, ii) the sensing layer and iii) the electrolyte.

The objective of the device modelling is to calculate its $I - V$ characteristics under specific conditions, defined by elements such as the external bias, device geometry, presence of different analytes, etc. The device output current is evaluated using the carrier transport description considered, but it also requires the solution of the device electrostatic to evaluate the electrostatic potential distribution (V) that defines the transport conditions. This, however, is not a straight forward step as V is also linked to the carrier distribution provided by the transport model, so a self-consistent solution of

these equations is required. In the case of BioFETs this calculation entails an additional complexity as V is also impacted by the elements related with the sensing interface and the liquid electrolyte. Hence, the main goal can be split into three specific objectives related with the elements to be addressed for the modelling of these devices:

- **Semiconductor modelling: carrier transport**. This aim encompasses the evaluation of the charge distribution and its transport through the semiconductor channel to estimate the output current under different biases and sensing layer conditions.
- **Electrostatic simulation of electrolytes**. The self-consistent electrostatic solution of the electrolyte is an important aspect in the simulation of BioFET and ISFET devices and constitutes the second aim of this Thesis. It involves the analysis of the free charge in the solution of the Poisson equation, which impacts the operating conditions of the device.
- **Modelling of the sensing interface**. This third aim is the key element of the sensor operation, as it deals with the region where the target ions or molecules are captured. The ion adsorption capability of the interface has to be included, as well as a proper modelling of the charge distribution of the receptor and the target molecules attached to the sensing layer.

Each of these contributions is defined by different models according to their particular nature, typically by non-linear functions of V. Then, the simulation of the BioFET entails a set of coupled equations that are solved in a self-consistent manner using the iterative scheme shown in Figure 1.5.

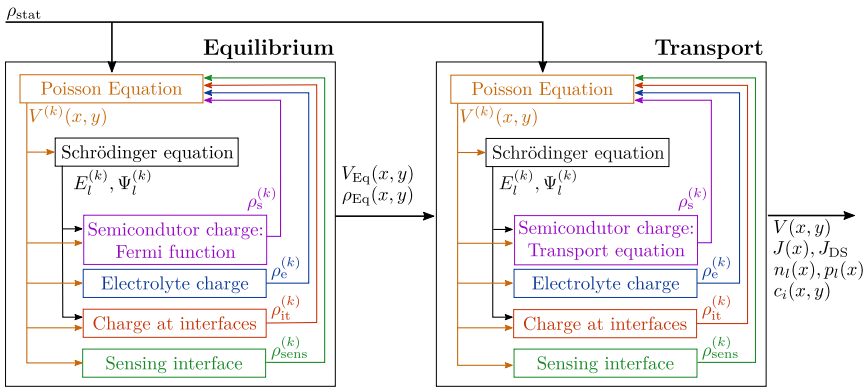

Figure 1.5: Scheme summarising the steps followed to solve the set of equations for the simulation of the device. The calculation of each one requires an specific model that will be combined with the Poisson equation to analyse the device operation.

The text in this Thesis summarises the process developed in this iterative scheme and the main results obtained. To that end, it is organised as follows:

- Part 1: It introduces the context of this Thesis and presents its objective and outline the rest of the manuscript.
- Part 2: The chapters contained in this section are intended to provide the basic background for the next chapters. Chapter 2 introduces some concepts related with solid-state physics that are commonly used to study electronic devices. Next, Chapter 3 focuses on MOSFET devices as the basis for ISFET and BioFET sensors, that are also introduced in this chapter.
- Part 3: This is the core of this Thesis where the developed numerical simulator is described. The method used to address the numerical simulation of BioFET and ISFET devices is explained in detail, with Chapter 4 taking charge of the electrostatics solution, while Chapter 5 describes the models used to simulate the semiconductor FET device, and Chapter 6 introduces those related with the simulation of the liquid electrolyte and sensing interface.
- Part 4: Here, the results obtained during the completion of this work are presented and classified into two groups: i) results related with regular FETs (Chapter 7) and ii) results related with BioFETs (Chapter 8). Each chapter includes the validation of the models along with the main outcomes of the different works performed.
- Part 5: Finally, this part collects the main conclusions and future developments of this work.

Part II

Semiconductor devices physics

CHAPTER 2

Solid state physics

2.1 Introduction

This chapter is devoted to briefly introduce the basic concepts and the required background in solid state physics to be employed in later chapters. A thorough explanation of this topic can be found elsewhere [61, 62]. In particular, we introduce the concept of energy band structure and the theoretical calculations related with it. Several approximations commonly used with electronic devices are also introduced as they will be useful in for the next chapters.

2.2 Energy bandstructure

A comprehensive description of the electrical and optical properties of semiconductor materials starts with the knowledge of their energy bandstructure, as it stems from the intimate interaction among the atoms encompassing the crystal lattice of the material and as it is ruled by quantum mechanics.

The structure of an atom is defined by its core, made up of protons and neutrons, and the cloud of electrons arranged around it forming orbitals and defining several shells as shown in Figure 2.1. The inner electron shells contain the least energetic electrons, deeply bonded to the nucleus and therefore unavailable to participate in any transport process. When several atoms get closer to each other, the interactions among the outer orbitals of each atom modify the energy level distribution giving rise to a quasicontinuum of energy levels, the so-called energy bands.

As a result, the discrete energies of the isolated atom become energy bands dependent on the momentum of the electron in the crystal lattice. In a semiconductor, these bands cover a certain range of energies, and the values outside of this range correspond to forbidden energies (striped region

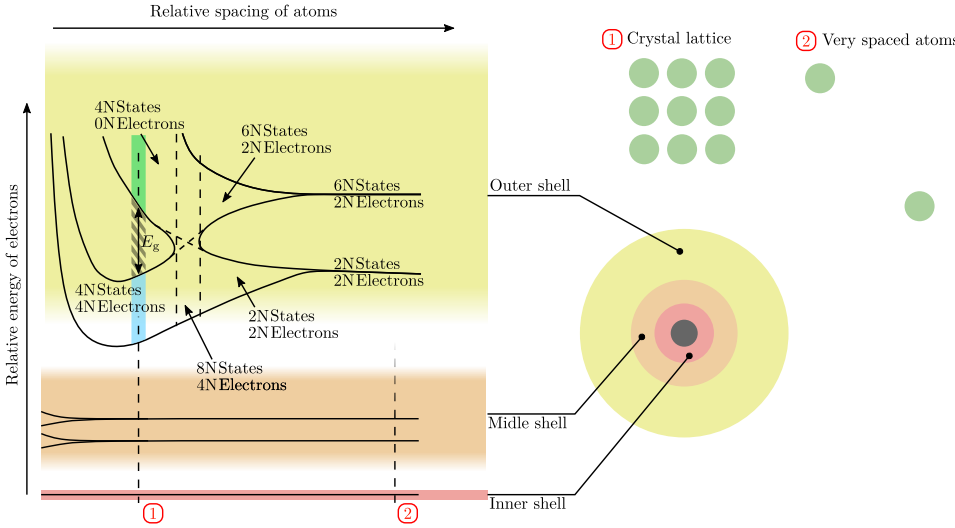

Figure 2.1: Example of the evolution of energy levels of Silicon atoms as a function of the interatomic distance [62]. As the atoms become closer they interact with each other and the energetic distribution of the electrons in the outer shell evolves from discrete levels to bands.

in Figure 2.1). Below and above this forbidden band there are two bands with available states. At $T = 0$ K one of them is full of electrons (blue coloured region in Figure 2.2) and a second one completely empty (green coloured region). These bands are named as valence and conduction band, respectively. Any electron with enough energy to overcome the forbidden band, i.e. the energy gap E_g, would be able to jump from the valence band to the conduction band and move along the crystal. Depending on the value of E_g, the electrical characteristics of the materials are different, and consequently they can be classified into three main groups: Metals, Semiconductors and Insulators (Figure 2.2). Metals are characterized by the lack of band gap, so that there is a continuous range of available states that can be occupied by electrons, making them good electrical conductors. On the contrary, insulators have a very large E_g, requiring a large amount of energy to promote electrons to empty states, turning them into bad electrical conductors. Semiconductors lie in between these two cases, with energy gaps in the range of a few hundreds of meV, enabling the generation of free electrons with a small amount of extra energy. Indeed, at room temperature, thermal energy is enough to kick up free electrons in the semiconductor, although not to the amount of good electrical conductors such as metals.

The interactions that take place in this atomic scale are governed by the laws of quantum mechanics. The duality of wave and particle associated to the electron behaviour can be described (in non-relativistic scenarios) by

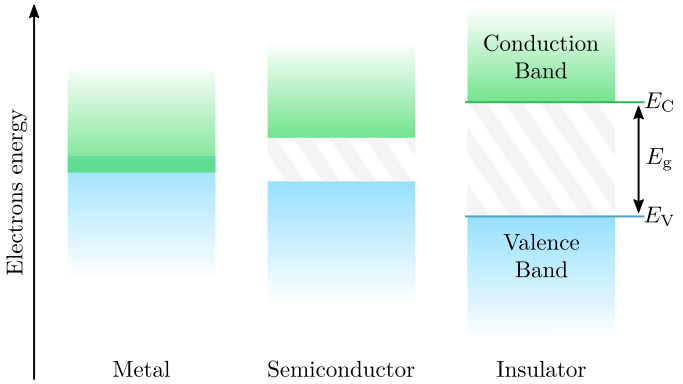

Figure 2.2: Classification of materials according to their band gap E_g.

the Schrödinger equation [63], which for a single electron reads as:

$$i\hbar\frac{\partial}{\partial t}\Psi(\mathbf{r},t) = -\frac{\hbar^2}{2m_0}\nabla^2\Psi(\mathbf{r},t) + \Phi(\mathbf{r},t)\Psi(\mathbf{r},t) \tag{2.1}$$

where i is the imaginary unit, $\hbar$ the reduced Plank constant ($\hbar = h/2\pi$), m_0 the vacuum electron mass, t the time, Ψ the electron wavefunction and Φ the electron potential energy (due to e.g. the presence of other electrons, atoms nuclei and external forces). The analytical solution of this equation can be addressed only for very simple and idealized scenarios, as for example the hydrogen atom. However, its solution becomes almost non affordable when considering a real lattice with several tens or hundreds of atoms. Therefore, the application of different simplifications that lead to a more treatable problem, jointly with the use of computational tools, become mandatory to analyse these challenging situations.

2.3 Density Functional Theory

As already introduced, the energetic distribution of the electrons in the outer shell of the atoms in the crystal lattice provides the necessary information to understand the electrical behaviour of the material. However, as just mentioned, the solution of the Schrödinger equation in these cases is far from trivial. Density Functional Theory (DFT) encompasses the theoretical foundations to address this problem to a very good level of accuracy. It is the result of several efforts to solve the many-particle stationary Schrödinger equation that initiated back in the 30's by D. Hartree and V.A. Fock [64, 65]. Initially, the Hartree method addressed this problem using two main assumptions: i) the mean field approach, namely, an average field can be defined to approximate the instantaneous electrostatic interactions

among electrons, and ii) a many-body wavefunction can be written as the product of the wavefunctions of single particle orbitals. When the variational principle is applied to the many-body Schrödinger equation under the previous assumptions, the Hartree equations are obtained, which need to be self-consistently solved. This method provided a good initial approximation, but still lacked of i) correlation in the interaction between electrons and ii) anti-symmetry of the wavefunction of fermions. This was subsequently addressed in the Hartree-Fock (HF) method that corrects the wavefunction anti-symmetry using the Slater [66] determinant and includes some correlations among electrons. This method along with an additional flexibility in the definition of the wavefunction *ansatz* enabled the development of several post-HF methods.

The Honenberg-Kohn paradigm

Despite the complexity of the HF method, it showed a very poor working with solids so it was soon substituted by the first version of the DFT developed in the 60's and 70's by by W. Kohn and cooworkers [67]. Both, HF and DFT, intend to solve the many-particle stationary Schrödinger equation, but the large complexity of the many-body wavefunction hamper this objective. The great advance of W. Kohn and P. Hohenberg (inspired in the work of L. Thomas and E. Fermi) was to demonstrate that the ground state charge density, that is, the modulus of the ground state wavefunction, is a fundamental quantity in quantum mechanics. In other words, the external potential and the number of electrons considered define an unique solution of the ground state charge density, which is also verified in the reverse way. However, as stated by the first Hohenberg-Kohn theorem [67], the information of the external potential and many-body particle ground state wavefunction is contained in the ground state charge density in a non-trivial way. The second theorem makes use of the variational principle to write the energy of the system as a functional of the charge density, which is minimized by the ground state charge density. This functional is a well-defined mathematical object, but the procedure to calculate it was unknown.

Kohn-Sham equations

W. Kohn and L.J.Sham addressed the translation of this functional into a more practical form. Their proposal was based on approximating the many-electron interacting problem by a many-electron non-interacting problem but using the same ground state charge density [68]. In this new scenario, a non-interacting system, the kinetic energy and the non-interacting electrostatic energy are well known, and the differences with the interacting solutions can be absorbed in the so-called exchange-correlation functional.

As a final result, the functional $E[\phi_i]$ is written in a more suitable way:

$$E[\phi_i] = \sum_{i=1}^{N} \frac{-1}{2} \int \phi_i^*(\mathbf{r}) \nabla^2 \phi_i(\mathbf{r}) + E_{\mathrm{H}}[n(\mathbf{r})] + E_{\mathrm{xc}}[n(\mathbf{r})] + E_{\mathrm{ext}}[n(\mathbf{r})] \quad (2.2)$$

where ϕ_i are the non-interacting orbitals, E_{H} the Hartree functional, E_{xc} the exchange correlation functional, E_{ext} the contribution of external perturbations and $n(\mathbf{r}) = \sum_i |\phi_i|^2$. This approach provides an exact solution for the many-body interacting stationary Schrödinger equation if E_{xc} includes all the differences between the interacting and non-interacting systems, but this is so far not possible. Thus, the problem becomes a non-linear minimization issue for ϕ_i. Nevertheless, the Euler-Lagrange and variational principle can be used to formulate an equivalent set of differential equations resembling the one-particle Schrödinger equation, the so-called Kohn-Sham equations:

$$\left(\frac{-1}{2} \nabla^2 + V_{\mathrm{H}}(\mathbf{r}) + V_{\mathrm{xc}}(\mathbf{r}) + V_{\mathrm{ext}}(\mathbf{r}) \right) \psi_i = \varepsilon_i \psi_i \quad (2.3)$$

where ψ_i are the single particle orbitals, $\frac{-1}{2}\nabla^2$ the kinetic energy, V_{ext} the external potential, V_{H} is the Hartree potential describing the electron-electron Coulomb interactions, and V_{xc} is the exchange correlation potential. The latter need to be approximated, like E_{xc}. Therefore, the problem is to determine E_{xc}. The first proposed was the Local Density Approximation (LDA).

The LDA is based on the decomposition of an inhomogeneous charge density volume into infinitesimal volumes with constant charge density. The exact exchange-correlation energy of an homogeneous system is calculated for each of these volumes. Then, the exchange-correlation energy for the inhomogeneous system is defined as the integral of all these exchange-correlation energies for the infinitesimal volumes. This was firstly solved by D.M. Ceperley and B.J. Alder through quantum Monte-Carlo simulations [69] later parametrised by J. Perdew and A. Zunger in the 80's [70]. This enables practical DFT calculations that have been enhanced in the subsequent years until the current state-of-the-art.

2.4 Density of States

As aforementioned, DFT calculations provides a quite detailed description of the electrical behaviour of a given material trough the energy bands diagram. For those cases where we are interested on the free charge evaluation, e.g. when studying electronic devices, a more handy description is provided by the Density of States (DoS). This parameter describes the amount of

states to be occupied at each energy, and can be extracted from the energy dispersion relationship all along the Brillouin zone:

$$g(E) = \frac{1}{\Omega} \sum_{\mathbf{k}} \delta \left(E - E(\mathbf{k}) \right) \tag{2.4}$$

where Ω is the volume of the Brillouin region associated to the unit cell evaluated where the $E(\mathbf{k})$ profile is defined. The procedure summarised by this expression consists on sum all the contributions of the points in the $\mathbf{k}$ space that are defined for the energy E evaluated. As a result, we obtain the amount of available states in the crystal lattice per unit of energy and volume as a function of the energy. This will be used in the next chapters for both, describe the operation of electronic devices and as a part of the simulator developed.

2.5 Effective Mass Approximation

The DoS profiles simplify the information provided by DFT. Nevertheless, when analysing electronic devices it is still sometimes complex to be handled. Therefore, some approximations are commonly taken when moving to the device level.

Concerning the analysis of electronic devices, we are usually only interested on the energy range near the conduction and valence band edges. The reason why is that the top of the valence one contains the most energetic electrons able to jump into the conduction band, and more specifically, into the bottom valley of this energy band. Therefore, the conduction band minimum will be the most populated region, as it is the closest point to the valence band. Near this point (k_c), the $E(\mathbf{k})$ relationship can be expanded in a Taylor series up to the second order term as:

$$E(\mathbf{k}) = E_\mathrm{c} + \sum_j \left(k_j - k_{\mathrm{c}\,j} \right) \left. \frac{\partial E(\mathbf{k})}{\partial k_j} \right|_{k_\mathrm{c}} + \sum_{i,j} \frac{\left(k_j - k_{\mathrm{c}\,j} \right)}{2} \left. \frac{\partial^2 E(\mathbf{k})}{\partial k_j \partial k_i} \right|_{k_\mathrm{c}} \tag{2.5}$$

where $E_\mathrm{c} = E(\mathbf{k}_\mathrm{c})$ and indexes i and j indicate the $\mathbf{k}$ component in the cartesian coordinates system, that is $i, j \equiv x, y, z$. As k_c corresponds to a minimum, the first order derivative at this point is cancelled. Neglecting components above the second order we have:

$$E(\mathbf{k}) = E_\mathrm{c} + \sum_{i,j} \frac{\left(k_i - k_{\mathrm{c}\,i} \right) \left(k_j - k_{\mathrm{c}\,j} \right)}{2} \left. \frac{\partial^2 E(\mathbf{k})}{\partial k_i \partial k_j} \right|_{k_\mathrm{c}} \tag{2.6}$$

At this point it is possible to define an effective mass from the second

derivative in equation (Eq 2.6),

$$\frac{1}{m^*_{i,j}} = \frac{1}{\hbar^2}\frac{\partial^2 E(\mathbf{k})}{\partial k_i \partial k_j} \tag{2.7}$$

so that, equation (Eq 2.6) can be rewritten as:

$$E(\mathbf{k}) = E_\mathrm{c} + \frac{\hbar^2}{2}\left[\mathbf{k} - k_\mathrm{c}\right]\mathbf{W}\left[\mathbf{k} - k_\mathrm{c}\right]^T \tag{2.8}$$

where the vector $[\mathbf{k} - k_\mathrm{c}]$ and matrix $\mathbf{W}$ are defined as:

$$\left[\mathbf{k} - k_\mathrm{c}\right] = \begin{bmatrix} (k_x - k_{\mathrm{c}\,x}) & (k_y - k_{\mathrm{c}\,y}) & (k_z - k_{\mathrm{c}\,z}) \end{bmatrix} \tag{2.9}$$

$$\mathbf{W} = \begin{bmatrix} 1/m^*_{xx} & 1/m^*_{xy} & 1/m^*_{xz} \\ 1/m^*_{yx} & 1/m^*_{yy} & 1/m^*_{yz} \\ 1/m^*_{zx} & 1/m^*_{zy} & 1/m^*_{zz} \end{bmatrix} \tag{2.10}$$

Using this approximated $E-\mathbf{k}$ relation around k_C, the original Effective Mass Approximation (EMA) Schrödinger equation can be expressed as:

$$-\frac{\hbar^2}{2}\nabla\mathbf{W}\nabla^T\Psi(\mathbf{r}) + \mathbf{U}(\mathbf{r})\Psi(\mathbf{r}) = \left(E(\mathbf{k}) - E_\mathrm{c}\right)\Psi(\mathbf{r}) = E'\Psi(\mathbf{r}) \tag{2.11}$$

The original equation now becomes a simpler problem of a particle of mass $m^*_{i,j}$ where all the information corresponding to the bandstructure is distilled into the effective mass. As will be explained later, this expression is used to evaluate the distribution of carriers in an arbitrary semiconductor, including the specific features corresponding to the electrical and geometrical confinement described by the potential.

2.6 Free charge evaluation

As previously introduced, electrons with energy in excess to the forbidden bandgap are able to jump into empty higher energetic levels of the conduction band and then freely move along the crystal lattice. The occupation of these energy levels, when subjected to quantum mechanics, leads to the distribution functions. In particular, electrons obey the Pauli exclusion principle and consequently follow the Fermi-Dirac distribution, where for a given energy level E is occupation probability is defined as:

$$f(E) = \frac{1}{1 + e^{\frac{E - E_\mathrm{F}}{k_\mathrm{B}T}}} \tag{2.12}$$

where f is the occupation probability, k_B the Boltzmann constant, T the temperature and E_F the Fermi level. The latter is defined as the energy

at which the occupation probability is 50% ($f(E_\mathrm{F}) = 0.5$) or the chemical potential at $T = 0$K, that is the highest occupied energy state. E_F is a key parameter to evaluate the charge distribution in many situations, e.g. when an external electric field is applied or different materials are combined in a heterojunction. $f(E)$ depends on the temperature and it can be employed as a knob to provide electrons the energy required to move from the valence to the conduction band. Figure 2.3 shows how this occupation probability is modified with the temperature: the higher is T, the less steep is the profile of $f(E)$.

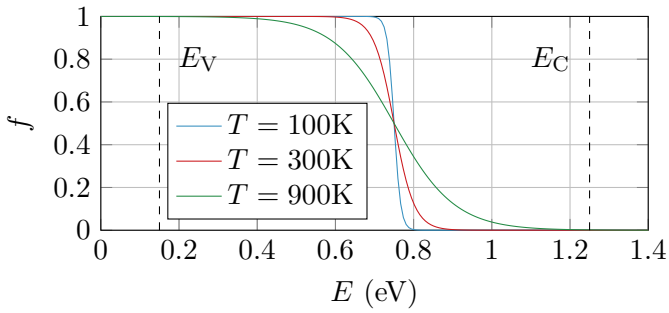

Figure 2.3: Fermi-Dirac occupation probability at different temperatures with $E_\mathrm{F} = 0.75$ eV. This value and the position of the valence (E_V) and conduction (E_C) bands does not match with any specific material, they are set only for exemplary purposes.

So far we have been concerned only about electrons moving into the conduction band. However, once any of them surmounts the bandgap, an empty state is left in the valence band. This can be understood as a "hole" in the conduction band that jumps into the valence band. Holes are addressed also as particles (despite they are "absence of electrons") with positive charge, so there is also an occupation probability associated with them:

$$f_\mathrm{p}(E) = 1 - f_\mathrm{n}(E) = \frac{1}{1 + e^{\frac{E_\mathrm{F} - E}{k_\mathrm{B} T}}} \tag{2.13}$$

where f_n is the occupation probability associated with electrons and f_p the one associated with holes. This expression is valid under equilibrium conditions where electrons and holes share the same Fermi level. In a non-equilibrium scenario this level might be split in two pseudo-Fermi levels, one for holes ($E_\mathrm{F,p}$) and one for electrons ($E_\mathrm{F,p}$).

The occupation probabilities themselves are not able to provide the electron and hole concentrations, n and p, in the semiconductor. They must be combined with the DoS $g(E)$, previously introduced in Section 2.4, the magnitude that describes the amount of available states per unit area and unit of energy. Thus, the electron (n) and hole (p) density are obtained

by integrating the profile of available states along the conduction band and valence band respectively multiplied by their occupation probability:

$$\begin{aligned} n &= \int_{E_\mathrm{C}}^{\infty} g(E) f_\mathrm{n} dE \\ p &= \int_{-\infty}^{E_\mathrm{V}} g(E) f_\mathrm{p} dE \end{aligned} \tag{2.14}$$

where E_C and E_V are the conduction and valence band edges, respectively. The DoS can be obtained from *ab-initio* calculations, although there are some analytical expressions for specific carrier confinement scenarios (see Appendix A). For electrons, these closed expressions follow the formula:

$$n = N_\mathrm{C} \mathcal{F}_n \left(\frac{E_\mathrm{C} - E_\mathrm{F}}{k_\mathrm{B} T} \right) \tag{2.15}$$

where N_C is the effective DoS in the conduction band and $\mathcal{F}_n(x)$ is the n-order Fermi-Dirac integral. The same can be applied to holes where N_V (effective DoS in the valence band) is used instead of N_C. Fermi-Dirac integrals cannot be generally expressed in terms of simpler mathematical functions. However, if the condition $(E_\mathrm{C} - E_\mathrm{F}) > 3k_\mathrm{B}T$ ($(E_\mathrm{F} - E_\mathrm{V}) > 3k_\mathrm{B}T$ in the case of holes) is verified, that is, the semiconductor is non-degenerated, the Fermi-Dirac distribution can be simplified to a very good agreement by the classical Maxwell-Boltzmann distribution and the carrier concentration follows an easy-to-use expression:

$$\begin{cases} n = N_\mathrm{C} e^{-\frac{E_\mathrm{C} - E_\mathrm{F}}{k_\mathrm{B} T}} \\ p = N_\mathrm{V} e^{\frac{E_\mathrm{V} - E_\mathrm{F}}{k_\mathrm{B} T}} \end{cases} \tag{2.16}$$

Charge neutrality

An intrinsic and isolated semiconductor must be electrically neutral, meaning that $n = p = n_\mathrm{i}$ where n_i is the intrinsic carrier concentration, that can be calculated from the previous expressions (in the non-degenerated approximation):

$$\begin{aligned} np = n_\mathrm{i}^2 &= N_\mathrm{C} N_\mathrm{V} e^{-\frac{E_\mathrm{C} - E_\mathrm{F}}{k_\mathrm{B} T}} e^{\frac{E_\mathrm{V} - E_\mathrm{F}}{k_\mathrm{B} T}} \\ &= N_\mathrm{C} N_\mathrm{V} e^{-\frac{E_\mathrm{g}}{k_\mathrm{B} T}} \Rightarrow n_\mathrm{i} = \sqrt{N_\mathrm{C} N_\mathrm{V}} e^{-\frac{E_\mathrm{g}}{2 k_\mathrm{B} T}} \end{aligned} \tag{2.17}$$

A similar procedure can be followed to obtain the intrinsic Fermi level E_i:

$$\begin{aligned} n = p \Rightarrow N_\mathrm{C} e^{-\frac{E_\mathrm{C}-E_\mathrm{F}}{k_\mathrm{B}T}} = N_\mathrm{V} e^{\frac{E_\mathrm{V}-E_\mathrm{F}}{k_\mathrm{B}T}} \Rightarrow \\ \Rightarrow E_\mathrm{i} = \frac{E_\mathrm{C}+E_\mathrm{V}}{2} + \frac{k_\mathrm{B}T}{2}\ln\left(\frac{N_\mathrm{C}}{N_\mathrm{V}}\right) \end{aligned} \tag{2.18}$$

Then, an isolated semiconductor under equilibrium conditions would have a carrier concentration $n = p = n_\mathrm{i}$ and Fermi levels $E_\mathrm{F,n} = E_\mathrm{F,p} = E_\mathrm{i}$

2.7 Doped semiconductors

One of the most powerful features of semiconductors is the possibility to modify their composition in a controlled way. The doping process consists on the substitution of atoms from the original material in the crystal lattice for other chemical elements (impurities). This makes possible to tune the electrical properties of the material by increasing the amount of available electrons (n-type semiconductors) or holes (p-type semiconductors).

N-type semiconductors

N-doped semiconductors show a larger amount of electrons compared with the intrinsic material. In the case of silicon (group IV in the periodic table), atoms from the elements in the group V of the periodic table are added to the lattice. These atoms are able to complete all the covalent bondings with the surrounding atoms, while one electron from its outer shell is unassociated to any of these bounds. As it remains weakly bound to the nucleus, a small amount of energy is enough to release it. As depicted in Figure 2.4, this is equivalent to generate an additional energy level inside the forbidden gap near the conduction band, that is filled with these weakly-bound electrons, so that they can easily move into the conduction band. This process also entails a shift of the Fermi level towards this band.

If the amount of impurities is higher that the intrinsic carrier concentration (n_0, p_0) and most of them are ionized (the unbound electrons occupy states in the conduction band), then the free carrier concentration can be considered equal to the concentration of impurities in the crystal.

P-type semiconductors

In this case the impurities added to the semiconductor provide a large amount of holes. Following with the case of silicon, when the atoms inserted in the lattice belong to elements from the group III, some of the bonds that

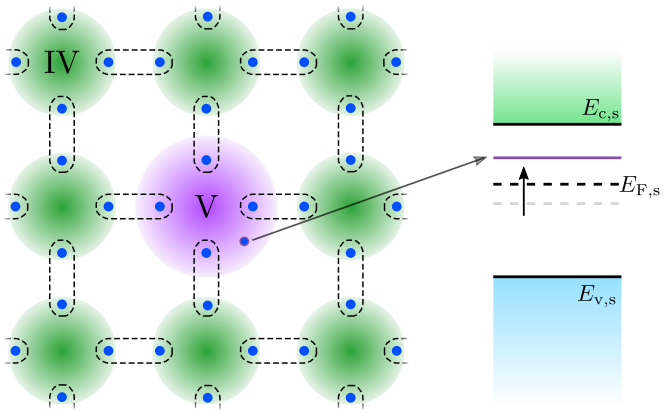

Figure 2.4: Illustration of the impact of group V semiconductors in a silicon crystal to implement a n-type semiconductor. On the right, shift of E_F produced by the presence of additional electrons.

define the lattice are not satisfied. This situation can be analysed in a similar way as in n-type semiconductors: a energy level is generated near the valence band, and electrons from the top of this band can easily jump into that energy level, generating empty states. As a consequence, a shift of the Fermi level towards the valence band occurs.

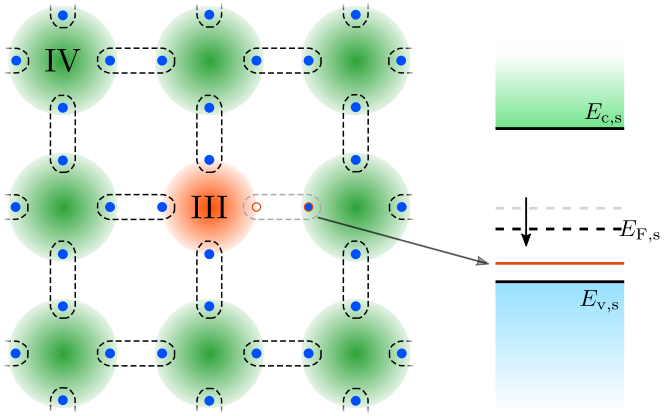

Figure 2.5: Illustration of the impact of III column atoms in a lattice with IV column atoms to implement a p-type semiconductor.

2.7.1 Charge neutrality in doped semiconductors

For high enough doping and the assumption of total dopant ionization, the carrier concentration of doped semiconductors can be estimated from the

density of impurities N_D and N_A. However, a more precise procedure to evaluate the net charge in doped semiconductors is the charge neutrality condition:

$$n_0 + N_D^+ = p_0 + N_A^- \tag{2.19}$$

Here, N_D^+ and N_A^- are the concentration of ionized donor and acceptor impurities, which can be evaluated as [71]:

$$N_D^+ = \frac{N_D}{1 + g_D e^{\frac{E_F - E_D}{k_B T}}} \qquad N_A^- = \frac{N_A}{1 + g_A e^{\frac{E_A - E_F}{k_B T}}} \tag{2.20}$$

where g_D and g_A are the degeneration grade of donor and acceptor impurities, respectively, and they depend on the semiconductor material to be doped. The relation $n_i^2 = n_0 p_0$ is still valid and can be used to define n_0 and p_0 as a function of the impurities concentration:

$$\begin{aligned} n_0 &= \frac{N_D^+ - N_A^- + \sqrt{\left(N_D^+ - N_A^-\right)^2 + 4n_i^2}}{2} \\ p_0 &= \frac{N_A^- - N_D^+ + \sqrt{\left(N_D^+ - N_A^-\right)^2 + 4n_i^2}}{2} \end{aligned} \tag{2.21}$$

If semiconductors are not heavily doped, and the temperature is not too low, it can be assumed that $N_D^+ \approx N_D$ and $N_A^- \approx N_A$. In that case the Boltzmann approximation can be used and the energetic position of the Fermi level can be estimated from the amount of impurities as:

$$E_F = E_i + k_B T \ln\left(\frac{n_0}{n_i}\right) = E_i - k_B T \ln\left(\frac{p_0}{n_i}\right) \tag{2.22}$$

2.8 Work function and electron affinity

The structures of electronic devices commonly involves the connection of different materials. These scenarios can be handled by *ab-initio* methods, but only on the atomic level. Then, in the device level the parameters used to analyse these cases are the work function and electron affinity. These are related with the energy bands and are useful to understand how they are modified in the surroundings of these junctions.

As it is shown in Figure 2.6, the work function ϕ defines the distance between the vacuum level (E_o), i.e. the energy of a free electron in vacuum,

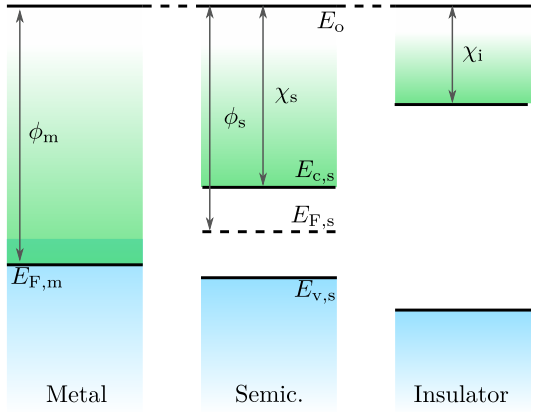

Figure 2.6: Work function ϕ_s and electron affinity χ indicated in the band structure of the three types of materials.

and the Fermi level of the material. In the case of a metal/semiconductor this value is defined as:

$$\phi_s = E_o - E_{F,s} \tag{2.23}$$

The electron affinity χ in semiconductors is a more appropriate concept since, generally, i.e. in undoped semiconductors, there are no states at the position of the Fermi level (that lies within the gap). χ follows a similar definition to ϕ_s but measured from the conduction band edge:

$$\chi_s = E_o - E_{C,s} = \phi_s - (E_{C,s} - E_{F,s}) \tag{2.24}$$

When two materials, of the same nature or not, are joined and there are no external perturbations (e.g. external electric fields), their Fermi levels become aligned. This generates a charge exchange between the materials that originates a reconfiguration of the energy bands. The displacement of the energy bands can be related with differences in ϕ and χ as will be indicated in the next chapter.

CHAPTER 3

Semiconductor devices: MOSFET

3.1 Introduction

Once some basic concepts on solid-state physics for semiconductors have been introduced, it is worthy to shortly described the physics of the structure of the MOSFET device. In that regard, the work function and electron affinity concepts previously introduced in Section 2.8 are relevant. As aforementioned in that section, the Fermi level across the junction of different materials is constant, if there are no external perturbations, and energy bands are reconfigured due to the charge exchange between materials to fulfil that condition. In the case that an external field is applied to the junction, the Fermi levels will be shifted accordingly and the charge will move between the materials due to the gradient in E_{F}. This is essentially the origin of the electrical current through electrical devices, aside from other non-ideal effects. Here, two types of structures are revised as they conform the structure of the MOSFET (Figure 3.1): Metal-Semiconductor (MS) and Metal-Oxide-Semiconductor (MOS). This structure is later extended to include an electrolyte and analyse the basis of ISFET and BioFETs.

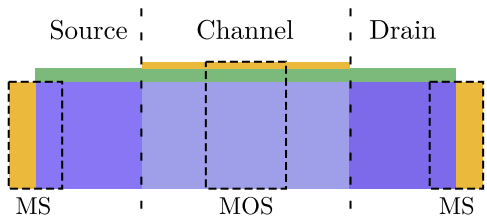

Figure 3.1: Basic structure of a MOSFET: A semiconductor layer with two metals in its sides acting as input/output contacts covered by an insulator, on top of which another metal is placed to act as control input. This gives rise to two MS junctions at the edges and a MOS structure in the centre.

3.2 Metal-Semiconductor junction

The MS structure is commonly encountered at the source and drain contacts, that is, the sides of the MOSFET. There are two scenarios depending on the final configuration of the energy bands: Schottky or rectifier contacts, and Ohmic contacts. To analyse both of them we restrict to conduction by electrons, being the conduction by holes opposite and equivalent. A Schottky contact stems from ϕ_m larger than ϕ_s, which generates the band configuration depicted in Figure 3.2.

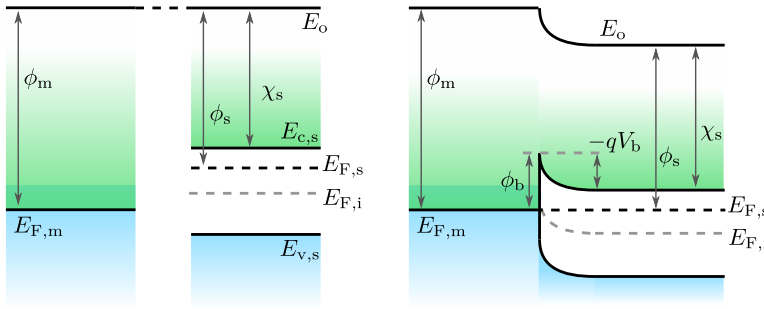

Figure 3.2: Configuration of the energy bands in a n-type Schottky junction.

In this scenario, electrons move from the semiconductor to the metal depleting the region close to the contact and generating a potential barrier that prevents more electrons to reach the junction. As showed in Figure 3.2, for those electrons flowing from the metal into the semiconductor this barrier is defined by the difference between the metal work function and the semiconductor affinity:

$$\phi_b = (\phi_m - \phi_s) + (\phi_s - \chi_s) = \phi_m - \chi_s \tag{3.1}$$

For those electrons flowing in the opposite direction, from the semiconductor to the metal, the barrier is defined by the difference between the work functions:

$$-qV_b = \phi_b - (\phi_s - \chi_s) = \phi_m - \phi_s \tag{3.2}$$

The application of an external bias to this contact will result in a modification of the barrier height, rising or lowering it. The result is the rectifying characteristic of the junction, that defines the device operation.

In order to avoid such dependence of the device behaviour on the contact characteristic, ohmic junctions are preferred for MOSFETs. The band configuration in this latter case is the one depicted in Figure 3.3.

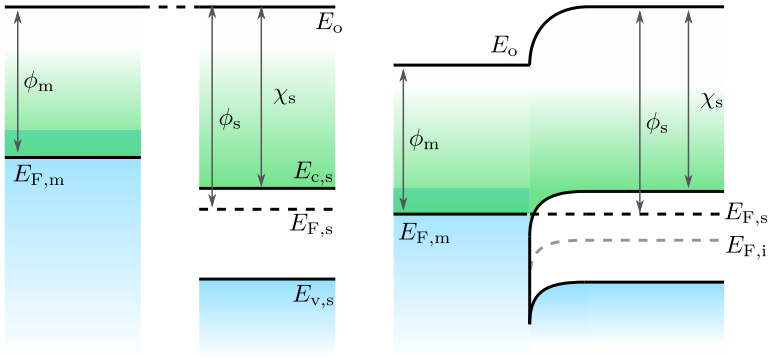

Figure 3.3: Configuration of the energy bands in a Ohmic contact.

As observed in (Eq 3.2) a method to generate this type of contact is to use a metal with a workfunction lower than ϕ_s. Here, electrons can flow due to the lack of barrier-modulation, originating a linear (ohmic) $I - V$ characteristic.

All this analysis can be repeated for the hole conduction (Figure 3.4) where the barrier heights can be evaluated as:

$$\begin{cases} \phi_b = (\phi_s - \phi_m) + (\chi_s + E_g - \phi_s) = \chi_s + E_g - \phi_m \\ -qV_b = \phi_s - \phi_m \end{cases} \tag{3.3}$$

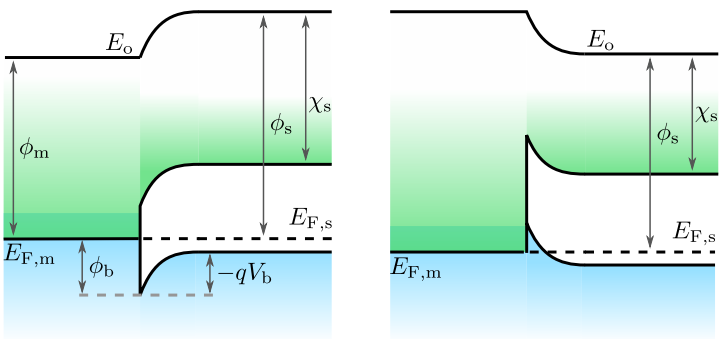

Figure 3.4: Schottky (left) and Ohmic (right) contacts for holes. As can be seen, they correspond to the opposite type of contact for electrons.

3.3 Metal-Insulator-Semiconductor structure

The Metal-Insulator-Semiconductor heterostructure is the core of the MOSFETs operation enabling the transferred control of the resistance of the channel. The application of a voltage at the top metal produces an electric

field in the structure that modulates the amount of mobile charge carriers in the semiconductor. Usually, the main goal is to accumulate or deplete charge in the semiconductor, so that, the conductivity of the channel can be modified by changing the electric field applied to the stack, the so-called field-effect. This region of the semiconductor can be laterally contacted by two highly-conductive regions, the source and drain, in order to quickly inject and extract the mobile carriers. In the following we revise the energy band diagram of this structure as a function of the applied bias. Figure 3.5a shows an example of MOS structure with a p-type semiconductor under no-bias conditions, namely, when Fermi level is constant along the whole structure.

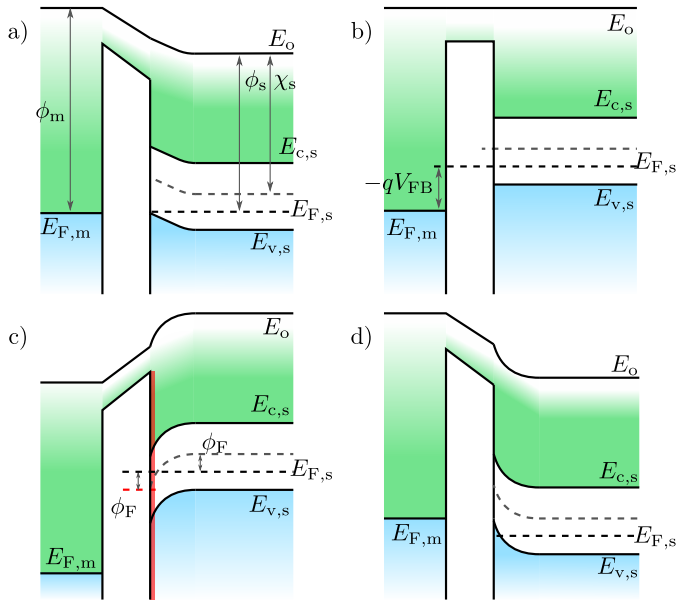

Figure 3.5: a) Band diagram of the MOS structure in an n-type MOSFET in equilibrium. From left to right: Metal, Insulator (Oxide) and Semiconductor (p-type). b) Energy band configuration when a gate voltage equal to the Flat Band potential V_{FB} is applied to the structure and c) when a higher bias is applied. In that case the conduction band becomes close enough to $E_{F,s}$ to generate a thin layer where electrons are the majority carrier (red region). This situation is denominated as inversion. Finally d) represents the accumulation of majority carriers, in this case holes.

The application of a voltage between the metal and the semiconductor shifts $E_{F,m}$ with respect to $E_{F,s}$ by the applied bias V_m:

$$E_{F,m} - E_{F,s} = -qV_m \tag{3.4}$$

In order to keep charge neutrality in the structure, the same amount of positive charge accumulated in the metal due to the application of a positive

potential, is created in the semiconductor with opposite sign. To accommodate these changes in the charge distribution, Fermi level and energy bands in the semiconductor are modified near the insulator interface. The same process occurs in the metal, but in this case the change in the bands is negligible.

Implicitly, we are assuming an ideal insulator that does not contain any charge. From the equilibrium situation depicted in Figure 3.5a, if a positive bias equal to $V_{FB} = \phi_m - \phi_s$ is applied, the initial band bending in the semiconductor is fully compensated as shown in Figure 3.5b. This bias is named the Flat Band potential. If a larger positive bias is applied, more negative charge is accumulated close to the oxide interface in the semiconductor, and the bending of the energy bands is reversed so that E_C becomes closer the the Fermi level, generating a thin region close to the interface where minority carriers (in this case electrons as the substrate is p-type) become majority. Once the distance between $E_{F,s}$ and the intrinsic Fermi level E_i is the same as in the isolated p-type semiconductor but with opposite sign, it can be considered that the semiconductor is switched from p-type to n-type. This region is usually denominated as the inversion region. For the structure depicted in Figure 3.5b, this distance is calculated as:

$$\phi_F = E_i - E_{F,s} = k_B T \ln\left(\frac{N_A}{n_i}\right) \tag{3.5}$$

Any positive bias above this value will increase the concentration of minority carriers near the semiconductor-insulator interface. If, on the contrary, the bias applied is much lower that V_{FB} this charge inversion does not take place and an accumulation of the bulk majority carriers, holes, is produced at the interface (Figure 3.5d). In summary, four different states can be defined for the MOS structure:

$$\begin{cases} \phi_F < & E_i - E_{F,s} & & \text{Accumulation} \\ 0 < & E_i - E_{F,s} & < \phi_F & \text{Depletion} \\ -2\phi_F < & E_i - E_{F,s} & < 0 & \text{Weak inversion} \\ & E_i - E_{F,s} & < -2\phi_F & \text{Strong inversion} \end{cases} \tag{3.6}$$

The previous analysis for n-type channel MOSFET can be extended to p-type channel devices, using potentials with opposite sign. As depicted in Figure 3.6, when $V_M < 0$ holes are collected at the semiconductor-insulator layer generating an inversion channel, while for $V_M > 0$ an accumulation of electrons is produced.

3.4 MOSFET device

The MOSFET is a three terminal electronic device that enables the control of an electric current using a voltage signal by taking advantage of the field-

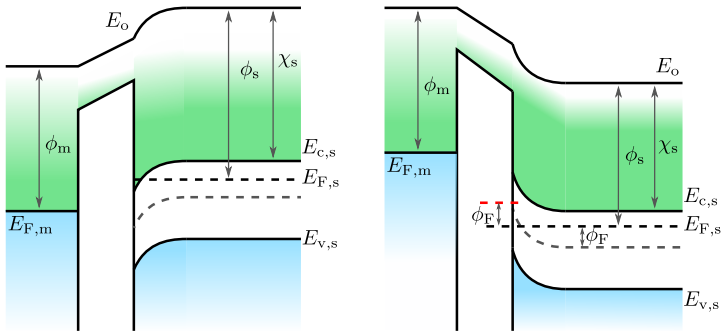

Figure 3.6: Band diagram of a MOS structure for an p-type channel MOSFET under accumulation scenario conditions (left) and charge inversion (right).

effect described in Section 3.3 and two lateral ideally ohmic contacts. The metal contact for the MOS structure at the centre of the structure is named gate while the contacts at the edges are named source and drain. The gate bias V_{GS} controls the conductivity of the channel, while the drain bias V_{DS} is responsible for a longitudinal electric field to move charge carriers along the structure, i.e. generate an electric current through the structure. Therefore, the current through the device is controlled by V_{GS} and V_{DS}, and MOSFET devices are characterized by the dependence of the current through the device I_{DS} as a function of these two biases. This results in two types of curves: output curves $I_{DS} - V_{DS}$ and transfer curves $I_{DS} - V_{GS}$. Examples of these curves are depicted in Figure 3.7.

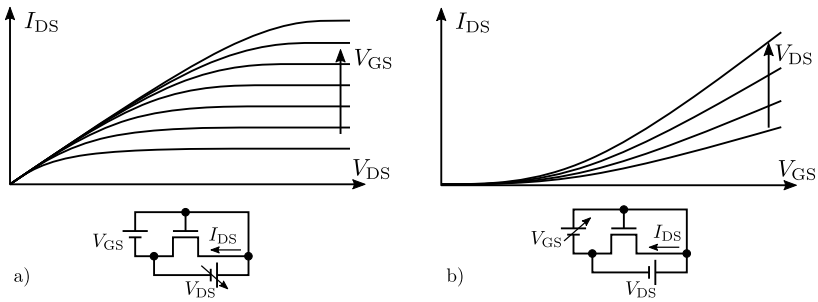

Figure 3.7: Examples of output (a) and transfer (b) curves of a MOSFET device. These two types of curves provides the complete characterization of the devices.

3.5 Chemical FET sensors: EISFET

Once introduced the fundamentals of MOSFET devices, we are ready to describe the operation principle of FET-based chemical and biomolecular sensors. Their structure is similar to the MOSFETs but with the metal gate

replaced by an electrolyte, giving rise to the so-called Electrolyte-Insulator-Semiconductor (EIS) stack (Figure 3.8a). In this Thesis, we will consider liquid electrolytes as solutions where mobile charges correspond to ions instead of electrons and they will distribute according to the electrostatic potential distribution. The equivalent to the electronic Fermi level in the electrolyte is the Redox energy E_{Redox} [72]. Conduction and valence bands have their analogues levels in the oxidation (E_{Ox}) and reduction (E_{Re}) levels. In the regions where E_{Redox} is closer to E_{Ox} negative ions concentration will be higher, while regions where E_{Redox} is closer to E_{Re} positive ions concentration will be predominant. As depicted in Figure 3.8b under equilibrium conditions the Fermi level along the EIS has to be constant, which in this case is translated as $E_{\text{Redox}} = E_{\text{F,s}}$. To reach this equilibrium scenario, ions and electrons/holes move towards or away of the corresponding insulator layer interface generating local changes in the electrostatic potential (which is not flat in the electrolyte as it was in the metal).

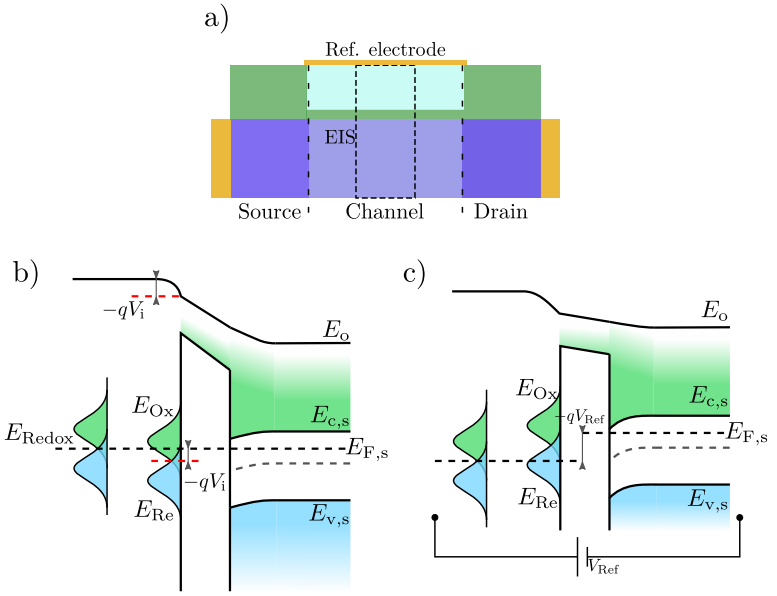

Figure 3.8: Energy band diagram of the EIS structure. At equilibrium a constant Fermi level is translated as $E_{\text{F,s}} = E_{\text{Redox}}$. To reach that situation electrons and ions move towards their respective interfaces with the insulating layer.

In order to determine the potential between the electrolyte and the semiconductor device, a reference electrode is used [9] to drive the E_{Redox} level so it plays the same role as the metal in a MOS structure, as shown in Figure 3.8c. It is worth to note, however, that in the EIS structure is not designed to modulate the current making use of the reference electrode potential, but to detect the presence of ions close to the insulator interface via the change

in the conductivity of the channel. In particular, dangling bonds on the insulator interface are able to capture ions generating a charge located on that interface [73]. Figure 3.9 depicts how this accumulation of charge is able to modify the local electrostatic potential causing a variation of the mobile carrier concentration at the semiconductor-insulator interface.

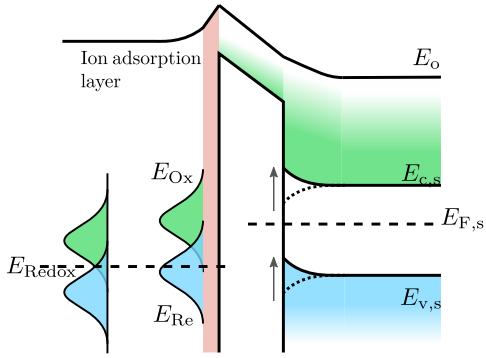

Figure 3.9: Changes in the band structure of the EIS structure when ions are adsorbed at the electrolyte insulator interface. The case depicted in the figure corresponds to the adsorption of negatively charge ions. These ions generate a change in the potental that impacts on both, semiconductor E_{C} and E_{V} and electrolyte E_{Ox} and E_{Re}.

Thus, the conductivity of the semiconductor channel is modified according to the amount of ions adsorbed, giving rise to a connection between the output current of the device and the amount of adsorbed ions. This latter magnitude, as explained in detail in the following chapters, depends on the concentration of ions in the bulk electrolyte, and the potential at the interface. The calculation of that potential follows an intricate process as it is ruled by variables such as ions near the interface, adsorbed ions, charge in the semiconductor, bias conditions, etc. The detailed modelling of those interactions and their numerical integration in the simulator is described later in Chapter 6.

3.6 Biomolecular FET sensors: BioFETs

Following a similar operation principle, BioFETs are able to sense the presence of biomolecules in the electrolyte. The bare structure of the EISFET device is not able to detect biomolecules with enough specificity, so an additional layer is placed on top of the device surface to capture only the target molecules, providing the required specificity to the sensing interface (Figure 3.10).

This sensing layer is defined either by a set of receptor molecules placed after the functionalization of the surface, e.g. with APTES [24, 40, 41], or directly on the device surface [42, 53, 74]. To use one method or another

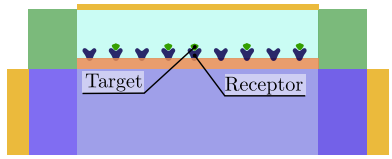

Figure 3.10: Generic structure of a BioFET. This device is similar to the ISFET sensor but an additional sensing layer is deposited on top of the device to host the receptors aiming to capture the target molecules and generate the corresponding change in the output current.

depends on the affinity between the receptor molecules and the insulating layer. As depicted in Figure 3.11, receptors are intended to capture the target molecules at the sensing interface generating a change in the output current of the device. Then, the objective is to evaluate the amount of activated receptors though these changes in I_{DS}.

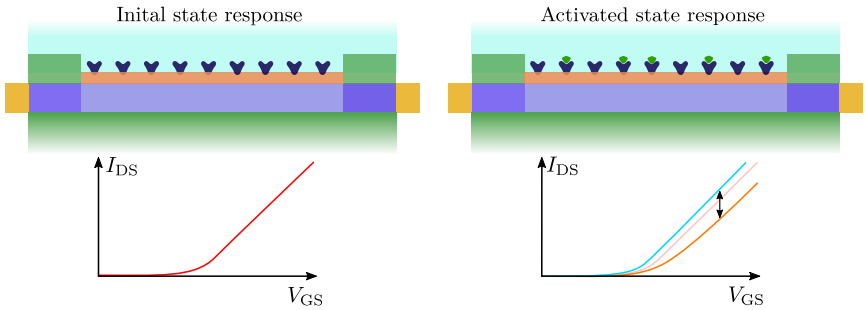

Figure 3.11: Example of the response of the BioFET device. The activation of the receptor molecules generates a change in the output current of the device that can be used to evaluate the amount of receptors activated.

Part III

Simulation methods

CHAPTER 4

Numerical simulation of BioFET devices

4.1 Introduction

As introduced in Chapter 1, the simulation of the BioFET entails a set of coupled equations that are solved in a self-consistent manner using an iterative scheme. These equations encompass the Poisson equation along with the models that described the charge distribution ρ in each region. Hence, the unknowns are the electrostatic potential distribution V and charge distribution in the different regions. As depicted in Figure 4.1, calculations assumes a 2D cross-section of the structure where four main regions are considered to contribute to the overall charge distribution: semiconductor (ρ_s), electrolyte (ρ_e), sensing interface (ρ_{sens}), and interfaces charge (ρ_{it}).

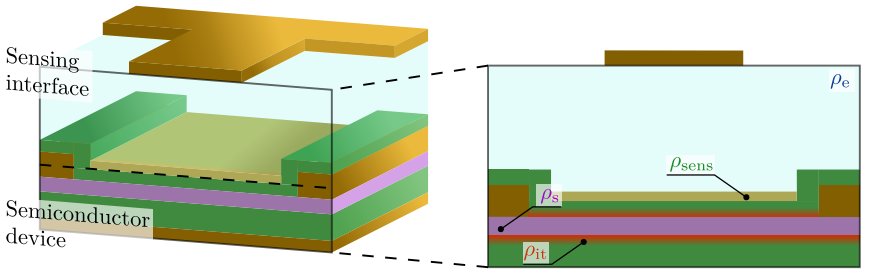

Figure 4.1: Generic structure of the BioFET sensor. Right side of the figure indicates the components of ρ: ρ_s is the semiconductor charge, ρ_e the electrolyte ions charge, ρ_{sens} the charge located at the sensing interface, and ρ_{it} the component associated to charged traps at the interfaces between the materials.

The 2D cross-section corresponds to the XY plane, while the structure is considered invariant along the Z axis. That 2D space is discretized to numerically solve the equations using the FD method (Appendix B). Figure 4.2 shows that the iterative scheme is divided in two consecutive steps: (i) simulation under equilibrium conditions and (ii) simulation for transport

conditions. In the first one, no charge transport through the device is considered. The problem provides an initial guess for the second step where the charge transport is included. This is of main importance as several expressions with non-linear $\rho - V$ relations are involved and the calculations might become unstable if the initial solution introduces large fluctuations in the potential profile. Simulations under equilibrium conditions are less sensitive to such instabilities and, therefore, so they are suitable to generate an optimum initial point for the evaluation of the transport characteristics. The details related with the Poisson equation, that corresponds to the block highlighted in Figure 4.2, are addressed in this chapter, while those of the modelling of the elements in the structure will be addressed in the following chapters, along with their integration in the numerical solution of the complete set of equations.

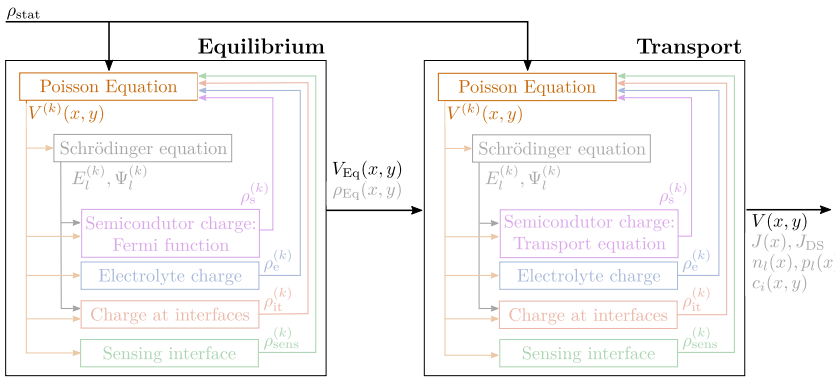

Figure 4.2: Iterative scheme used to solve the coupled equations that describes the BioFET. Blocks highlighted corresponds to those involved in the calculation of the Poisson equation.

4.2 Solving the device electrostatics

First, we need to estimate the electrical potential distribution in the structure that is intertwined with the charged elements, i.e. electrons, holes, dopants, traps, ions or molecules, that might be present in the device. Even at the nanometer scale that characterizes current devices, classical electrodynamics, represented by Poisson equation provide an accurate description of the electrostatic. Thus, the electrostatic potential distribution V produced by the charge ρ present in the structure can be determined from:

$$\nabla\left(\varepsilon\nabla V\right) = -\rho \tag{4.1}$$

where ε is the dielectric constant and the operator ∇ is defined as $\nabla = (\partial/\partial x\ \hat{x}, \partial/\partial y\ \hat{y}, \partial/\partial z\ \hat{z})$. The charge density ρ encompasses all the charges

present in the different elements of the device.

4.2.1 Potential and energy reference definitions

As explained in Chapter 2, the distribution of the energy bands and the Fermi level provides the information required to evaluate the semiconductor and electrolyte charge distribution along the structure, but the charge is connected to the potential through the Poisson equation. It is important, therefore, to establish the relation between energy and V, specifically in the definition of the references for both magnitudes in the simulations.

First, the source metal contact is assumed to be grounded and it is defined as the reference contact, that is, the potential for all the other contacts is defined with respect to the source metal contact. The potential has to be continuous in the whole structure, and the unique energy level that can be continuously defined along the whole structure is the vacuum level E_0. Then the potential can be defined as:

$$E_0 = -q\left(\phi - \phi_{\text{ref}}\right) \tag{4.2}$$

where ϕ is the electrostatic potential and ϕ_{ref} the reference potential, i.e. at the source. Conduction and valence bands can be defined in these terms by using the electron affinity χ_{s} and the band gap E_{g}:

$$\begin{aligned} E_{\text{C}} &= -q\left(\phi - \phi_{\text{ref}}\right) - \chi_{\text{s}} \\ E_{\text{V}} &= -q\left(\phi - \phi_{\text{ref}}\right) - \chi_{\text{s}} - E_{\text{g}} = E_{\text{C}} - E_{\text{g}} \end{aligned} \tag{4.3}$$

In a metal, the electrostatic and electrochemical potential are equal, so the reference potential can be linked with the Fermi level in the source metal contact: $q\phi_{\text{ref}} = E_{\text{F}}|_{\text{S}}$. Despite this metal is not considered inside the simulation region, it can be used to define the potential. Then, the conduction band can be calculated as:

$$E_{\text{C}} = -q\phi + E_{\text{F}}|_{\text{S}} - \chi_{\text{s}} \tag{4.4}$$

The terms in that equation can be re-arranged to evaluate ϕ as:

$$-q\phi = \left(E_{\text{C}} - E_{\text{F}}|_{\text{S}}\right) + \chi_{\text{s}} \tag{4.5}$$

so that the potential V evaluated through the Poisson equation can be linked with ϕ in the following way:

$$\left(E_{\text{C}} - E_{\text{F}}|_{\text{S}}\right) = -q\phi - \chi_{\text{s}} = -qV \tag{4.6}$$

Therefore, the potential across the structure defines the profile of the conduction band with respect to the Fermi level of the semiconductor at the metal source contact which is grounded, as depicted in Figure 4.3.

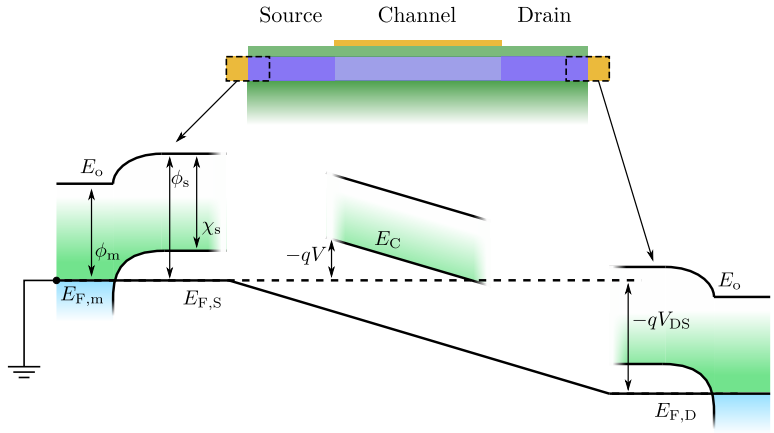

Figure 4.3: Scheme showing the definition of the electrostatic potential in terms of the energy.

4.3 Poisson equation

As already mentioned, the equations are solved in a 2D space, and more specifically in the XY plane and the potential and charge are assumed to be invariant along the Z axis. In that case the Poisson equation can be written as:

$$\nabla\left(\varepsilon\nabla V\right) = \frac{\partial}{\partial x}\left(\varepsilon(x,y)\frac{\partial V(x,y)}{\partial x}\right) + \frac{\partial}{\partial y}\left(\varepsilon(x,y)\frac{\partial V(x,y)}{\partial y}\right) = -\rho(x,y) \tag{4.7}$$

The Poisson equation is discretized making use of the FD method following the criteria depicted in Figure 4.4. V and ρ are defined in the main nodes of the grid, (i,j), while the dielectric constants of the materials are defined in the cells, $(i\pm 1/2, j\pm 1/2)$ and in the longitudinal mid-nodes and vertical mid-nodes, $\varepsilon_{\mathrm{x}i,j\pm 1/2}$ and $\varepsilon_{\mathrm{y}i\pm 1/2,j}$ respectively. Then, the discrete version of (Eq 4.7) reads as follows:

$$\begin{aligned}\nabla\left(\varepsilon(x,y)\nabla V(x,y)\right) \approx \left[\frac{\varepsilon_{\mathrm{y}i+1/2,j}}{\Delta_{\mathrm{y}i+1/2}\delta_{\mathrm{y}i}}\right]V_{i+1,j} + \left[\frac{\varepsilon_{\mathrm{x}i,j+1/2}}{\Delta_{\mathrm{x}j+1/2}\delta_{\mathrm{x}j}}\right]V_{i,j+1} \\ - \left[\frac{1}{\delta_{\mathrm{y}i}}\left(\frac{\varepsilon_{\mathrm{y}i+1/2,j}}{\Delta_{\mathrm{y}i+1/2}} + \frac{\varepsilon_{\mathrm{y}i-1/2,j}}{\Delta_{\mathrm{y}i-1/2}}\right) + \frac{1}{\delta_{\mathrm{x}j}}\left(\frac{\varepsilon_{\mathrm{x}i,j+1/2}}{\Delta_{\mathrm{x}j+1/2}} + \frac{\varepsilon_{\mathrm{x}i,j-1/2}}{\Delta_{\mathrm{x}j-1/2}}\right)\right]V_{i,j} \\ + \left[\frac{\varepsilon_{\mathrm{y}i-1/2,j}}{\Delta_{\mathrm{y}i-1/2}\delta_{\mathrm{y}i}}\right]V_{i-1,j} + \left[\frac{\varepsilon_{\mathrm{y}i,j-1/2}}{\Delta_{\mathrm{x}j-1/2}\delta_{\mathrm{x}j}}\right]V_{i,j-1} \\ = -\rho_{i,j}\end{aligned} \tag{4.8}$$

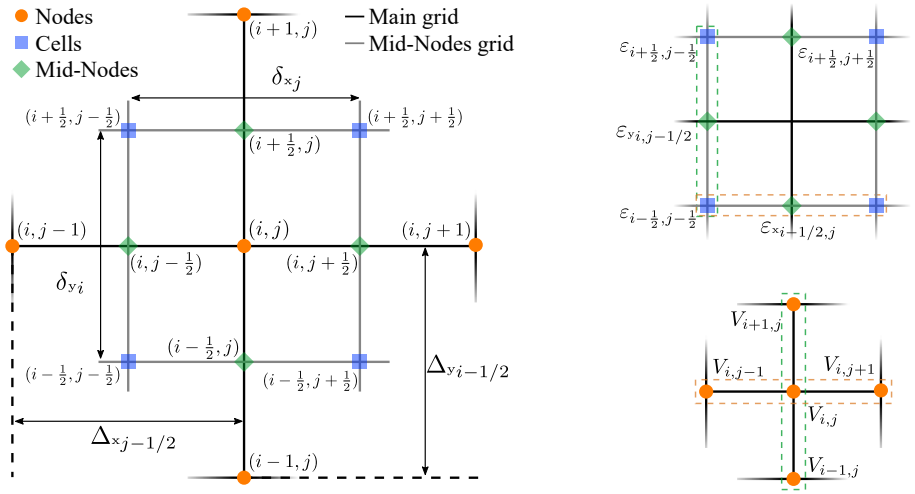

Figure 4.4: Criteria used to map the variables for the discretization of the Poisson equation.

where the approximation comes from the error in the discretization that depends on the grid size. This expression defines a set of equations that can be written in matrix form as:

$$M\mathbf{V} = b \tag{4.9}$$

where M is the matrix that defines the system of equations, b is the independent term defined by $-\rho_{i,j}$, and $\mathbf{V}$ is the variable to be solved and corresponds to the vectorised version of the potential: $V_{i,j} = \mathbf{V}_v$, where $v = i + (j-1)N_{\mathrm{x}}$. The grid size elements (Δ and δ) should be small enough to capture in detail the spacial profiles of the variables analysed. However, this could give rise to large coefficients of M, that are able to generate numerical issues due to a bad conditioning. To avoid this effect, the coefficients of the equations can be re-normalized by the area associated to each node $\delta_{\mathrm{x}j}\delta_{\mathrm{y}i}$. Then, the equations to evaluate $\mathbf{V}$ are finally defined as:

$$\begin{aligned} -\boldsymbol{\rho}_v\mathbf{F}_v &= \mathbf{A}_v\mathbf{V}_{v-1} + \mathbf{B}_v\mathbf{V}_{v+1} + \mathbf{C}_v\mathbf{V}_{v-N_x} + \mathbf{D}_v\mathbf{V}_{v+N_x} + \mathbf{E}_v\mathbf{V}_v \\ v &= 1, \cdots, N_{\mathrm{xy}} \end{aligned} \tag{4.10}$$

$$\begin{aligned} \mathbf{A}_v &= \left(\varepsilon_{\mathrm{x}i,j-1/2}\delta_{\mathrm{y}i}\right)/\Delta_{\mathrm{x}j-1/2} & \mathbf{B}_v &= \left(\varepsilon_{\mathrm{x}i,j+1/2}\delta_{\mathrm{y}i}\right)/\Delta_{\mathrm{x}j+1/2} \\ \mathbf{C}_v &= \left(\varepsilon_{\mathrm{y}i-1/2,j}\delta_{\mathrm{x}j}\right)/\Delta_{\mathrm{y}i-1/2} & \mathbf{D}_v &= \left(\varepsilon_{\mathrm{y}i+1/2,j}\delta_{\mathrm{x}j}\right)/\Delta_{\mathrm{y}i+1/2} \\ \mathbf{E}_v &= -(\mathbf{A}_v + \mathbf{B}_v + \mathbf{C}_v + \mathbf{D}_v) & \mathbf{F}_v &= \delta_{\mathrm{x}j}\delta_{\mathrm{y}i} \end{aligned} \tag{4.11}$$

with $N_{\mathrm{xy}} = N_{\mathrm{x}}N_{\mathrm{y}}$.

4.3.1 Numerical solution of the Poisson equation

The numerical solution of the Poisson equation is based on the Jacobi method, an iterative procedure based on the decomposition of the main matrix describing our system of equations M into two components, D and R, that correspond to the diagonal and off-diagonal elements of M, respectively:

$$M\mathbf{V} = b \Rightarrow M = D + R = \begin{bmatrix} a_{1,1} & \cdots & 0 \\ \vdots & \ddots & \vdots \\ 0 & \cdots & a_{N_{\mathrm{xy}},N_{\mathrm{xy}}} \end{bmatrix} + \begin{bmatrix} 0 & \cdots & a_{1,N_{\mathrm{xy}}} \\ \vdots & \ddots & \vdots \\ a_{N_{\mathrm{xy}},1} & \cdots & 0 \end{bmatrix} \tag{4.12}$$

where N_{xy} is the total number of points in the grid ($N_{\mathrm{xy}} = N_{\mathrm{x}}N_{\mathrm{y}}$). The previous equation can be re-arranged to define an expression based on D and R to obtain $\mathbf{V}$ following an iterative process:

$${}^{\zeta}\mathbf{V} = D^{-1}\left(b - R\,{}^{\zeta-1}\mathbf{V}\right) \Rightarrow {}^{\zeta}\mathbf{V}_v = \frac{1}{a_{v,v}}\left(b_v - \sum_{u,u\neq v}^{N_{\mathrm{xy}}} a_{v,u}\,{}^{\zeta-1}\mathbf{V}_u\right) \tag{4.13}$$

where ${}^{\zeta}$ identifies the iteration. A drawback of this iterative scheme is the requirement of an initial guess for $\mathbf{V}$. For the equilibrium scenario depicted in Figure 4.2, that initial guess is defined by the potential profile from the previous iteration ${}^{\zeta=0}\mathbf{V} = {}^{m-1}\mathbf{V}$. This approach, however, is not applicable for the first iteration of the main scheme, where an initial profile is estimated from the charge neutrality condition (Eq 2.19). In this case, the Fermi level is constant along the structure, so the relation $-qV = E_{\mathrm{C}} - E_{\mathrm{F}}$ can be used to obtain the electron and hole concentrations:

$$N_{\mathrm{C}}\mathcal{F}_n\left(\frac{-qV}{k_{\mathrm{B}}T}\right) + N_{\mathrm{A}}^{-} = N_{\mathrm{V}}\mathcal{F}_n\left(\frac{qV + E_{\mathrm{g}}}{k_{\mathrm{B}}T}\right) + N_{\mathrm{D}}^{+} \tag{4.14}$$

where N_{C}, N_{V} and $\mathcal{F}_n(x)$ are the conduction band effective DoS, the valence band effective DoS, and the n-order Fermi integral, respectively. To define the potential profile for the present iteration ${}^{\zeta}\mathbf{V}$, the Poisson solver performs N_{xy} iterations using the initial guess aforementioned and the charge obtained in the previous iteration ${}^{m-1}\boldsymbol{\rho}$. Once the new potential profile is obtained, the charge profile $\boldsymbol{\rho}$ is updated. This process is repeated until the maximum difference between ${}^{\zeta}\mathbf{V}$ and ${}^{\zeta-1}\mathbf{V}$ is below a given threshold. In that case, we state that a solution for the complete set of equations has been obtained. The iterative nature of the Jacobi method provides a smooth approximation to the final solution, which is of great interest to avoid numerical instabilities. However, in some cases this is not enough to

completely get rid of them (e.g. electrolytes with large ion concentrations). Hence, an intermediate step between the solution of the Poisson equation and the update of the charge density is included aiming to avoid oscillations of the numerical solution. In that step, the changes in the potential profile are weighted by a coefficient β

$$ {}^{m}\mathbf{V} = {}^{m-1}\mathbf{V} + \beta\, {}^{m}\epsilon \tag{4.15} $$

where ${}^{m}\epsilon = \left({}^{\zeta=N_{\mathrm{xy}}}\mathbf{V} - {}^{m-1}\mathbf{V}\right)$ and β is evaluated using the cosine similarity method. That method evaluates the similarity between the error evaluated with the current solution ${}^{m}\epsilon$ and its previous value ${}^{m-1}\epsilon$ to propagate the changes into the final current solution ${}^{m}\mathbf{V}$. This comparison is based on the calculation of the cosine of the angle between vectors ${}^{m}\epsilon$ and ${}^{m-1}\epsilon$:

$$ \beta = \min\left(\beta_0, \frac{1+\alpha}{2}\right) \Rightarrow \alpha = \frac{{}^{m}\epsilon \cdot {}^{m-1}\epsilon}{\|{}^{m}\epsilon\| \|{}^{m-1}\epsilon\|} \tag{4.16} $$

where β_0 is the maximum value of β that is set as an input value for the simulations. This approach is helpful in those cases where the complexity of the structure is able to generate numerical instabilities. As for the coefficient α, it will be close to 1 (β close to β_0) if the changes in the potential points along same direction, that is, ${}^{m}\epsilon$ provides similar ${}^{m}\mathbf{V}$ and ${}^{m-1}\mathbf{V}$ profiles. On the contrary, if different $\mathbf{V}$ profiles are obtained, i.e. ${}^{m}\epsilon$ and ${}^{m-1}\epsilon$ point to different directions, α will be close to -1 (β close to 0). This helps to promote changes that provides a smooth evolution towards the final solution. The whole process described above for the solution of the Poisson equation is depicted in Figure 4.5.

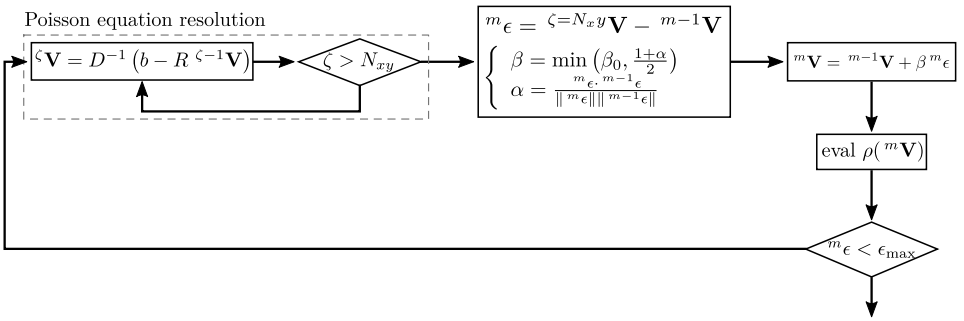

Figure 4.5: Flowchart of the procedure employed to solve the Poisson equation including the potential relaxation step and its integration in the main iterative scheme

4.3.2 Boundary conditions

One of the most important issues to be addressed is the behaviour of the potential along the boundaries of the simulation region, that will be determined by the specific Boundary Conditions (BC) defined at each point. In this case two types of BC are implemented: (i) Dirichlet and (ii) von Neumann.

Dirichlet BC

Dirichlet BC are used along those regions where the potential is fixed, like for example in the metallic contacts. As described in Chapter 3, when no bias is applied to the metal, at the interface of the semiconductor with the metal, the conduction band is defined by the difference between the metal work function and the electron affinity of the semiconductor:

$$E_{\mathrm{C}}|_{\mathrm{cont.}} - E_{\mathrm{F}} = \phi_{\mathrm{m}} - \chi_{\mathrm{semic}} \tag{4.17}$$

If a bias V_{a} is applied to the contact, the Fermi level of the metal is shifted so that $E_{\mathrm{F,m}} - E_{\mathrm{F,semic}} = -qV_{\mathrm{a}}$. This is also translated into the conduction band so that:

$$E_{\mathrm{C}}|_{\mathrm{cont.}} - E_{\mathrm{F}} = \phi_{\mathrm{m}} - \chi_{\mathrm{semic}} - qV_{\mathrm{a}} \tag{4.18}$$

Thus, the value to be considered in those nodes where Dirichlet BC are applied is

$$V_{\mathrm{cont}} = V_{\mathrm{a}} + \frac{\chi_{\mathrm{semic}} - \phi_{\mathrm{m}}}{q} \tag{4.19}$$

von Neumann BC

von Neumann BC are defined by a null electric field normal to the boundary where the condition is applied:

$$(\nabla V) \cdot \hat{n} = 0 \tag{4.20}$$

where $\hat{n}$ is the vector normal to the grid edge. This is the BC condition by default for all the nodes along the edges of the simulation domain. For vertical interfaces, for example, this is implemented as:

$$\frac{\partial V}{\partial x} = 0 \Rightarrow V_{i,j} = V_{i,j-1} \qquad j = 2, N_{\mathrm{x}} \tag{4.21}$$

and the same can be applied to horizontal interfaces:

$$\frac{\partial V}{\partial y} = 0 \Rightarrow V_{i,j} = V_{i-1,j} \qquad i = 2, N_{\mathrm{y}} \tag{4.22}$$

As a result this BC keeps the potential constant in the direction set by $\hat{n}$ near the boundary, and it is assumed to continue in that way far from the simulation domain.

Apart from the von Neumann BC on the potential, it is also possible to apply this null derivative condition on the the electric field normal to the boundary where it is applied:

$$\nabla(\vec{\mathbf{E}} \cdot \hat{n}) = 0 \tag{4.23}$$

This BC is useful for those regions where the potential is expected to change linearly outside the simulation grid, e.g., when the doping level in the edges of the semiconductor is low. It is implemented as:

$$\begin{aligned} \frac{\partial E_{\mathrm{x}}}{\partial x} = 0 \Rightarrow \frac{V_{i,j} - V_{i,j+1}}{\Delta_{\mathrm{x}j+1/2}} = \frac{V_{i,j+1} - V_{i,j+2}}{\Delta_{\mathrm{x}j+2/3}} \\ \frac{\partial E_{\mathrm{y}}}{\partial y} = 0 \Rightarrow \frac{V_{i,j} - V_{i+1,j}}{\Delta_{\mathrm{y}i+1/2}} = \frac{V_{i+1,j} - V_{i+2,j}}{\Delta_{\mathrm{y}i+2/3}} \end{aligned} \tag{4.24}$$

For regions where the charge density is quite high (i.e. highly doped regions where the potential barely changes) this type of BC converges to the von Neumann BC for the potential.

CHAPTER 5

Simulation of the solid state device

5.1 Introduction

This chapter focuses on the models related with the evaluation of the current through the semiconductor device, that corresponds to the blocks of the iterative scheme highlighted in Figure 5.1

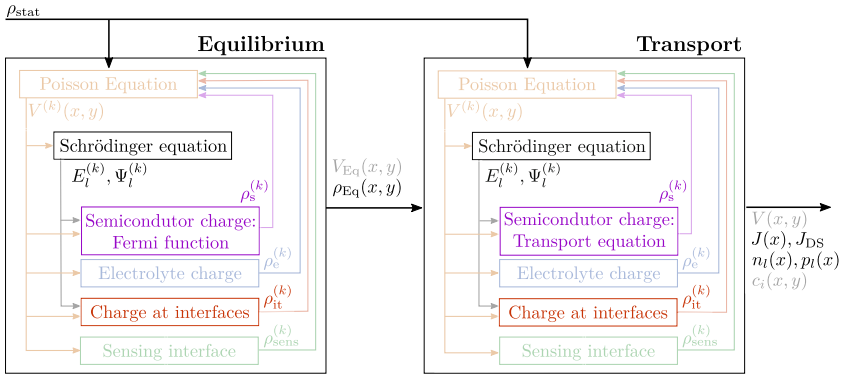

Figure 5.1: Blocks of the iterative scheme involved in the calculation of the current through the semiconductor device.

The modelling of this part entails three equations: i) the Schrödinger equation, ii) the transport model and iii) charge traps. The first one is related with the confinement of charge carriers in the semiconductor. 2DMs are characterised by their minimal thickness, so the quantum effects of such confinement cannot be overlooked. The second one defines the model to describe the movement of carriers through the semiconductor and, therefore, the output current through the device. Finally, the third one involves a common non-ideality in MOSFET devices, interface charge traps. These states are defects in the structure that are able to capture the free charge and impact on the device behaviour.

5.2 Schrödinger equation

This Thesis focuses on planar structures where the carriers are strongly confined, that is, from thin-film semiconductors down to monolayer 2DMs based channels. Consequently, the Schrödinger equation has to be considered in the calculation of the charge distribution to handle with the effect of the carrier confinement in some particular cases. We will discuss here its implementation and connection with the different devices and materials considered.

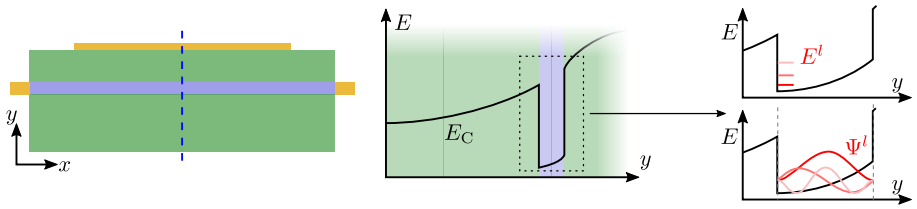

Figure 5.2: Sketch showing the carrier confinement in a vertical stack. The differences in the work functions of the employed materials generate an energetic well where carriers are confined.

Figure 5.2 shows a schematic of a typical device studied in the implemented simulator. The carriers are confined in the thin channel along the vertical direction (Y axis) while the transport takes place along the longitudinal direction (X axis). In the particular case of strongly confined 2D materials, the channel becomes a quantum well and the Schrödinger equation needs to be solved to account for quantization effects. Under the Effective Mass Approximation (EMA) discussed in Section 2.5, the 1D Schrödinger equation in the semiconductor along the Y axis is written as:

$$-\frac{\hbar^2}{2m_o}\frac{\partial}{\partial y}\left(\frac{1}{m_{\mathrm{yy}}(y)}\frac{\partial \Psi^l(y)}{\partial y}\right)+U_{\mathrm{C}}(y)\,\Psi^l(y)=E^l\Psi^l(y) \tag{5.1}$$

where $\hbar$ is the normalized Plank constant, U_{C} the external potential energy profile in the vertical direction that includes the channel potential well where electrons are confined, m_o the electron mass in vacuum, m_{yy} the effective mass (normalized to m_o), and E^l and Ψ^l the eigenenergy and wave-function associated to level l, respectively. The Schrödinger equation defines an eigenvalue problem (where E and Ψ are the unknowns) and can be written in matrix form as:

$$H\Psi = E\Psi \tag{5.2}$$

with H is the Hamiltonian matrix, Ψ the eigenvector and E the associated eigenvalue. H can be obtained from the discretization of the Schrödinger

equation following a procedure similar to the one employed with the Poisson equation:

$$\begin{aligned} H_{i,i-1} &= \frac{\hbar^2}{2m_o}\left(\frac{1}{m_{\mathrm{yy}}}\right)_{i-1/2}\frac{1}{\delta_{\mathrm{y}i}\Delta_{\mathrm{y}i-1/2}} \\ H_{i,i} &= -\frac{\hbar^2}{2m_o}\left(\frac{1}{\delta_{\mathrm{y}_i}}\left[\left(\frac{1}{m_{\mathrm{yy}}}\right)_{i+1/2}\frac{1}{\Delta_{\mathrm{y}i+1/2}}+\left(\frac{1}{m_{\mathrm{yy}}}\right)_{i-1/2}\frac{1}{\Delta_{\mathrm{y}_{i-1/2}}}\right]\right)+V_{\mathrm{E}_c,i} \\ H_{i,i+1} &= \frac{\hbar^2}{2m_o}\left(\frac{1}{m_{\mathrm{yy}}}\right)_{i+1/2}\frac{1}{\delta_{\mathrm{y}i}\delta_{\mathrm{y}i+1/2}} \end{aligned} \tag{5.3}$$

$$\begin{aligned} -\frac{\partial}{\partial y}\left(\frac{1}{m_{\mathrm{yy}}}\frac{\partial}{\partial y}\Psi\right) \approx \left(\frac{1}{m_{\mathrm{yy}}}\right)_{i+1/2}\frac{\Psi_{i+1}}{\delta_{\mathrm{y}i}\Delta_{\mathrm{y}i+1/2}}+\left(\frac{1}{m_{\mathrm{yy}}}\right)_{i-1/2}\frac{\Psi_{i-1}}{\delta_{\mathrm{y}i}\Delta_{\mathrm{y}i-1/2}} \\ -\left(\frac{1}{\delta_{\mathrm{y}i}}\left[\left(\frac{1}{m_{\mathrm{yy}}}\right)_{i+1/2}\frac{1}{\Delta_{\mathrm{y}i+1/2}}+\left(\frac{1}{m_{\mathrm{yy}}}\right)_{i-1/2}\frac{1}{\Delta_{\mathrm{y}i-1/2}}\right]\right)\Psi_i \end{aligned} \tag{5.4}$$

Ψ and E become, thus, discretized wave-functions and energy levels Ψ_i^l and E^l, respectively. The solution of the 1D Schrödinger equation along y is repeated for every position along the longitudinal X axis using the potential energy profile $U_{\mathrm{C}}(y)$ in each vertical slice at a fixed x of the mesh space. The result, after the whole structure is evaluated, is a set of l 2D profiles $\Psi_{i,j}^l$ ($\Psi_{i,j}^l \approx \Psi^l(x,y)$) and 1D profiles E_j^l ($E_j^l \approx E^l(x)$). These values are used later to determine the carrier density and its distribution in the semiconductor channel. Figure 5.3 shows an example of wavefunctions and energy levels for a 10 nm thick energetic well. As known, the lower energy levels are those with larger contribution to the total carrier density, that will be in most cases, thus located close to the centre of the well

5.2.1 Few-layer 2DMs implementation

The method described above is used when evaluating thin film channels, e.g. around 10 nm-thick channels or below, made of traditional bulk semiconductors such as silicon. If the structure evaluated is based on 2D-semiconductors, from monolayer up-to around four/five layers, the notable reduction of the width of the energetic well where carriers are confined provides a very spread distribution of E^l. In this situation, the lower energy level will be the most occupied, while others have a negligible occupation.

Figure 5.4 shows an example of the solution of the Schrödinger equation inside a well with the typical thickness of a 2DMs (0.65 nm) with effective mass equal to $0.622m_o$. In this case the distance between the first and the

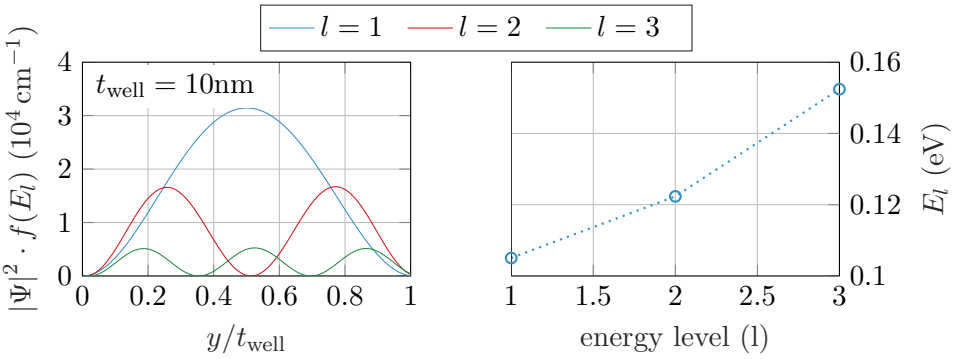

Figure 5.3: Example of wavefunction and energy values in one slice of a MOS structure with a 10 nm-thick semiconductor sandwiched between two 10 nm-thick oxides and gate bias of 0.5 V. Wavefunction profiles are scaled according to the occupation probability of their associated energy level to illustrate the contribution of each band to the distribution of carriers (electrons in this specific case).

second energy level is large: 1.5 eV, which is around $70k_{\text{B}}T$ at room temperature. This evidences that it is unnecessary to evaluate more than one energy level in 2DMs (at least for the same energetic valley) for electronic applications. The wavefunction associated to this first energy can be fitted with a half-sinusoid profile, as shown in Figure 5.4b, with its maximum located at the centre of the structure. Thus, for the monolayer case, it is possible to assume a charge distribution like the one depicted in Figure 5.4b, reducing the computational burden associated to the Schrödinger equation.

When few-layer 2DMs are considered similar quantization scenarios are observed and, typically, one energy level is enough to define to a very good accuracy the conduction band occupied states. The nature of the few-layer material, however, requires of some care when treating the charge distribution in the stack. Since, few-layer 2DMs are composed by several stacked layers weakly bonded through van der Waals forces, independent charge profiles can be considered as a first approximation along with a predominantly in plane charge transport [75].

Thus, these approximations are considered in the implementation of the transport model to reduced to reduce the computational cost of this calculation while including the particularities of these layered materials. We consider that charge is confined in each layer, i.e., there is no charge in the regions between layers and interlayer transport is negligible. Nevertheless, layers are not completely independent, Poisson equation couples them electrostatically. This means that, the charge of outer layers is able to screen the charge of the inner ones. Therefore, the few-layer 2D material is modelled by several narrow energetic wells that correspond to each layer and where only one energy level is considered. As for the charge distribution

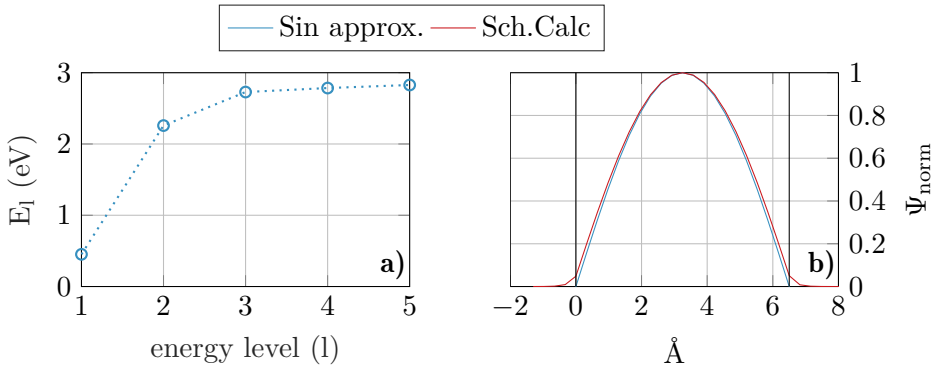

Figure 5.4: (a) Energy levels and (b) wave function profile for the first level calculated with the Schrödinger equation assuming a 0.65 nm-width energetic well (black lines in (b)). The sinusoid approximation depicted in (b) follows the formula: $\Psi = \sin(\pi y / t_{\text{well}})/L$, where L is the normalization constant.

within each individual layer, we assume that the charge is located with a maximum at the centre of the well and vanishes towards its edges, being null outside the well. This way, we consider a wavefunction profile with a sinusoid-shaped profile, as shown in Figure 5.5, defined only by the size of the monolayer ensuring that no charge is placed out of the layer region:

$$\Psi^l(y) = \frac{h(y)}{\int |h(y)|^2 dy}, \quad h(y) = \begin{cases} sin\left((y - y^l)\frac{\pi}{t_{ML}}\right) & y^l \leq y \leq (y^l + t_{ML}) \\ 0 & other \end{cases} \tag{5.5}$$

where y^l is the location of the l-th layer along the Y axis and t_{ML} the monolayer thickness. These Ψ^l profiles are replicated along the longitudinal axis to obtain the 2D profiles $\Psi^l_{i,j}$ for the l-th layer. Concerning the E^l_j profile for each layer, representing the conduction band in each layer, it is linked to the potential, using for each l-th layer the corresponding wavefunction to evaluate the weight of the potential inside that layer, being this procedure particularly beneficial for the convergence stability of the problem:

$$E^l(y) = -\int V|\Psi^l(y)|^2 dy \tag{5.6}$$

5.2.2 Hybrid implementation

An additional implementation meant for channels with more than 5 or 6 layers has been developed, combining the solution of the Schrödinger equation with the simplified model for monolayer and few-layer channels, saving computational time. In this approach, the Schrödinger equation is solved in

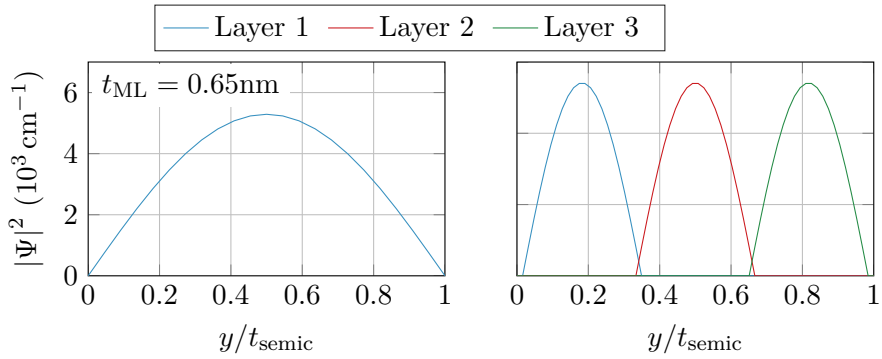

Figure 5.5: Example of wavefunctions for devices with single-layer and 3-layer channels. The charge is concentrated at the centre of the semiconductor and it is null close to the edges of the monolayer.

equilibrium in order to obtain the wave-function and energy profiles, Ψ^l and E^l respectively. Then, the wave-function profiles Ψ^l are used to calculate an overall fixed charge profile $\bar{\Psi}$ for each gate bias. This calculation is defined by the sum of all the Ψ^l profiles weighted by the occupation probability of their respective energy levels, taking into account the change in the potential at the centre of the structure, $V_c = V_c - V(x_c, y_c)$ associated to the gate voltage. This is related with the shift of the energy levels and hence with their occupation.

$$\bar{\Psi} = \sum_l \Psi^l f(E^l) \begin{cases} \phi(y) = \frac{g(y)}{\|g(y)\|} \\ \\ g(y) = \sum_l |\Psi^l(y, x_c)|^2 f\left(E^l - \Delta V_c\right) \end{cases} \tag{5.7}$$

This hybrid implementation makes possible to balance the computational load and the accuracy of many layers material. The evaluation of the transport equation increases the requirement of computational resources severely, so the possibility to use the simplified Schrödinger equation helps to compensate this surge of the computational cost with respect to the equilibrium scenario.

5.3 Free charge evaluation: equilibrium scenario

In equilibrium, where no bias is applied at the source and drain contacts, the Fermi level is constant across the structure, and the charge can be evaluated, in thick structures, directly from the analytical DoS and the energy levels solution of the Schrödinger equation. For the 1D confinement scenario characteristic of the planar devices analysed in this work (Appendix

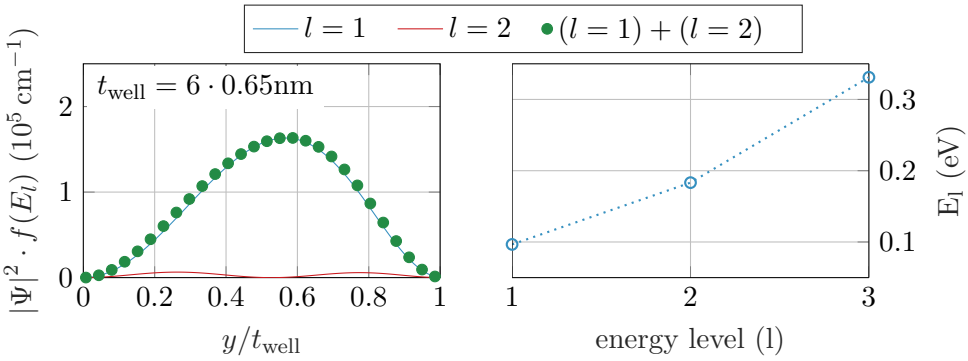

Figure 5.6: Example of wavefunction and energy values in one slice of a MOSFET structure with a 6-layers channel

A), the electron concentration associated to the energy level E^l is defined as:

$$n^l(x) = N_c \mathcal{F}_0 \left(\frac{E_F - E^l(x)}{k_B T} \right) \tag{5.8}$$

where $N_C = (m^* k_B T)/(\pi \hbar^2)$ is the effective conduction band DoS, and $\mathcal{F}_0$ the 0-order Fermi integral. These profiles are combined with their corresponding wave functions to obtain a 2D charge density that will be later used in the Poisson equation:

$$\rho_{semic}(x, y) = q \sum_l n^l(x) |\Psi^l(x, y)|^2 \tag{5.9}$$

When few-layers or monolayer channels are considered, a more elaborated model is implemented in order to deal with arbitrary DoS profile. To that end, the integral of the DoS, required to evaluate the carrier concentration, is pre-calculated as a function of $\widetilde{E}_F = (E_F - E_C)$ and inserted in the calculus as an interpolated function $n(\widetilde{E}_F)$:

$$n(\widetilde{E}_F) = \int_0^\infty g_n(\widetilde{E}) f_n(\widetilde{E}_F) d\widetilde{E} \tag{5.10}$$

This calculation is also extended to the hole concentration, using the appropriate occupation probability function, $1 - f(\widetilde{E}_F - E_g)$. This feature makes possible to consider an arbitrary DoS profile g_n and g_p extracted from *ab-initio* calculations, and, therefore, any material can be considered in the simulations by just providing its corresponding g_n and g_p profiles. We extend this method to include a dependence with the longitudinal x coordinate, so that the DoS profile can change along the channel. This makes possible to include local changes in the structure such as mechanical strain.

5.4 Free charge evaluation: Transport equation

In the MOSFET a current is generated when a difference of potential is applied between the drain and source contacts, giving rise to a flow of charge through it. To evaluate the current magnitude as a function of the voltage applied on different terminals, a transport model is required. The simulator developed in this Thesis is focused on channels around 50 nm-long and above, a range of channel lengths where electrons suffer a significant number of scattering events. In this scenario of diffusive transport, the Drift-Diffusion (DD) description of carrier transport is the most appropriate model to achieve an accurate estimation of the device $I-V$ characteristics. In this case, the current is defined by the product between the carrier density and the effective velocity, which in turn is defined by an effective carrier mobility and the gradient of the Fermi level. That expression can be modified to obtain the more common definition of the current based on the drift and diffusion components, in the case of electron current J_n [76]:

$$J_n = J_{\text{Drift}} + J_{\text{Diff.}} = qn\mu_{\text{n}} \vec{\mathbf{E}} + qD_n \nabla n \tag{5.11}$$

where q is the elementary charge, μ_{n} the electron mobility, D_{n} the diffusion coefficient, and $\vec{\mathbf{E}}$ the electric field. Then, one of these expressions of the current density is employed in the continuity equation:

$$\frac{\partial n}{\partial t} = \frac{1}{q}\nabla J_{\text{n}} + (G-R)_{\text{n}} \tag{5.12}$$

where $(G-R)_{\text{n}}$ is the net electron generation-recombination rate. In a stationary situation $\partial n/\partial t = 0$ and if recombination-generation events are also neglected, $(G-R)_{\text{n}} = 0$, the continuity equation reads as:

$$\nabla J_n = 0 \tag{5.13}$$

The current is assumed to flow longitudinally from source to drain, i.e. there is no current in the vertical direction. Depending on the situation analysed, bulk-semiconductors or 2DMs, the solution of this equation is handled differently.

5.4.1 Thin-film bulk semiconductors

In this case we have implemented the conventional version of the DD equation, i.e. the drift and diffusion components, where the charge concentration associated to each energy level E^l obtained from the Schrödinger equation, is calculated as:

$$J_n^l(x) = n^l \mu_{\text{n}} \frac{\partial E^l}{\partial x} + qD_n \frac{\partial n^l}{\partial x} \tag{5.14}$$

For the sake of brevity we discuss in the following only the electron current density. The hole current density derivation is completely equivalent. The FD method is used to implement this equation in the numerical simulator, following the scheme depicted in Figure 5.7.

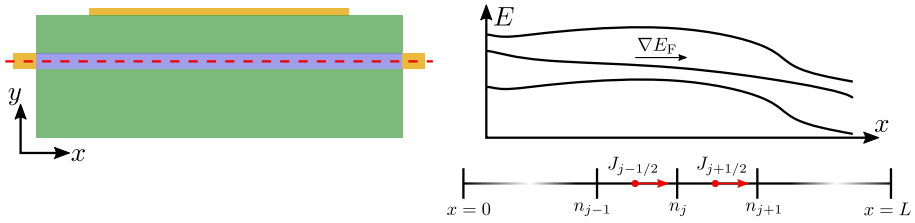

Figure 5.7: Mapping of the variables used in the DD equation. In the 1D grid defined for this axis, the carrier density is defined in the nodes while the current is defined in the mid-nodes, indicating the flow of charge between nodes.

In particular, we follow the discretization procedure reported in [77], which begins with the simplification of (Eq 5.14) using the Einstein relation ($D_\mathrm{n}/\mu_\mathrm{n} = k_\mathrm{B}T/q$):

$$J_n^l(x) = -k_\mathrm{B}Tn^l\mu_\mathrm{n}\frac{\partial(-E^l/k_\mathrm{B}T)}{\partial x} + q\mu_n\frac{k_\mathrm{B}T}{q}\frac{\partial n^l}{\partial x} = k_\mathrm{B}T\mu_n\left(-n^l\frac{\partial \varrho^l}{\partial x} + \frac{\partial n^l}{\partial x}\right) \tag{5.15}$$

In the following, the subscript n and superscript l will be suppressed to simplify notation, since the type of carrier n and the energy level index l will remain constant along the derivation. For the discretization of this expression, the carrier density n and potential ϕ are defined in the nodes of the grid (n_j and ϕ_j), while the mobility μ and the current J are defined in the mid-nodes ($\mu_{j\pm1/2}$ and $J_{j\pm1/2}$), thus representing the flow of charge between nodes. If we consider the continuity equation (Eq 5.13), a relation between the current in two adjacent mid-nodes can be established:

$$J_{j-1/2} = J_{j+1/2} \Rightarrow \begin{cases} J_{j-1/2} = k_\mathrm{B}T\mu_{j-1/2}\left(-n_{j-1/2}\dfrac{\varrho_j - \varrho_{j-1}}{\Delta x_{j-1}} + \dfrac{n_j - n_{j-1}}{\Delta x_{j-1}}\right) \\ J_{j+1/2} = k_\mathrm{B}T\mu_{j+1/2}\left(-n_{j+1/2}\dfrac{\varrho_{j+1} - \varrho_j}{\Delta x_j} + \dfrac{n_{j+1} - n_j}{\Delta x_j}\right) \end{cases} \tag{5.16}$$

where $n_{j-1/2} = (n_j + n_{j-1})/2$. By rearranging terms, an equation system

can be defined to evaluate the carrier density:

$$\begin{aligned} 0 =& n_{j+1}\left(2-\left(\varrho_{j+1}-\varrho_j\right)\right)+n_{j-1}\frac{\mu_{j-1/2}}{\mu_{j+1/2}}\frac{\Delta x_j}{\Delta x_{j-1}}\left(2+\left(\varrho_j-\varrho_{j-1}\right)\right) \\ & -n_j\left[\left(2+\left(\varrho_{j+1}-\varrho_j\right)\right)+\frac{\mu_{j-1/2}}{\mu_{j+1/2}}\frac{\Delta x_j}{\Delta x_{j-1}}\left(2-\left(\varrho_j-\varrho_{j-1}\right)\right)\right] \end{aligned} \tag{5.17}$$

As indicated in [77], this equation system is able to provide nonphysical negative values for the carrier density if $(\varrho_{j+1}-\varrho_j>2)$ and $(\varrho_j-\varrho_{j-1}>2)$. To avoid numerical instabilities in the solution, this system of equations is solved by making use of the Scharffeter-Gummel discretization scheme [77], and more specifically, assuming an exponential relation between ϱ and n:

$$n(x)=a(x)e^{\varrho(x)} \tag{5.18}$$

where $a(x)$ is a positive unknown function defined between nodes j and $j-1$. After that discretization process the current at node $j+1/2$ is rewritten as:

$$J_{j+1/2}=\frac{k_{\mathrm{B}}T}{\Delta_{\mathrm{x}\ j+1/2}}\mu_{j+1/2}\left[n_{j+1}B\left(\Lambda_{j+1}\right)-n_jB\left(-\Lambda_{j+1}\right)\right] \tag{5.19}$$

where $\Lambda_{j+1}=\varrho_{j+1}-\varrho_j$ and $B(x)$ stands for the Bernoulli function:

$$B(x)=\frac{x}{e^x-1} \tag{5.20}$$

With regard to the boundary conditions, the Fermi level at the source and drain edges are known, $E_{\mathrm{F,S}}=0$ eV and $E_{\mathrm{F,D}}=-qV_{\mathrm{DS}}$. This information is used to set the charge density at the edges of the semiconductor as:

$$\begin{aligned} n^l(0)\Big|_S &= g_v\left(\frac{m^*k_{\mathrm{B}}T}{\pi\hbar^2}\right)\mathcal{F}_0\left(\frac{E_F(0)-E^l(0)}{k_BT}\right) \\ n^l(L)\Big|_D &= g_v\left(\frac{m^*k_{\mathrm{B}}T}{\pi\hbar^2}\right)\mathcal{F}_0\left(\frac{E_F(L)-E^l(L)}{k_BT}\right) \end{aligned} \tag{5.21}$$

Finally, once the charge density profiles associated to each sub-band l are obtained, the total charge distribution required for the Poisson equation is calculated as in the previous scenario, by combining n^l with the wavefunctions obtained from the Schrödinger equation:

$$\rho_{\mathrm{semic}}(x,y)=q\sum_l n^l(x)|\Psi^l(x,y)|^2 \tag{5.22}$$

When convergence of the complete iterative scheme is achieved and the final charge profiles n^l are obtained, the total current through the device can be calculated by combining the contribution of all the sub-bands l:

$$J(x)=\sum_l J^l(x) \tag{5.23}$$

5.4.2 Few-Layer 2DMs

In this case, we can use the same approach as before, based on the conventional DD equation, considering transport per-layer instead of sub-band transport. As exposed in Section 5.2, in this case the potential well where electrons are confined is extremely narrow, producing a considerable energetic distance among them, and only the fundamental level will be considered in terms of carrier population. Therefore, under these assumptions, considering a sub-band transport as before is equivalent to deal with a sub-layer transport. In that context, all the previous analysis is extensible to the few-layer 2DMs scenario, combined with the simplified version of the Schrödinger equation previously described in Section 5.2.1.

In parallel to this implementation of the transport model, a second one is developed where the free charge distribution is addressed from a different point of view. The DD transport is still employed, however, the discretization is now performed on a different version of equation (Eq 5.11). Assuming the Boltzmann approximation on the free charge density (Eq 2.16) this expression for the DD transport can be expressed in terms of the Fermi level:

$$J_n = N_{\mathrm{C}} e^{\frac{(E_{\mathrm{F}} - E^l)}{k_{\mathrm{B}} T}} \left(\mu_{\mathrm{n}} \nabla E^l + q \frac{D_{\mathrm{n}}}{k_{\mathrm{B}} T} \nabla \left(E_{\mathrm{F}} - E^l \right) \right) \tag{5.24}$$

assuming the Einstein relation ($D_{\mathrm{n}}/\mu_{\mathrm{n}} = k_{\mathrm{B}} T/q$):

$$J_n = n \left(\mu_{\mathrm{n}} \nabla E^l + \frac{\mu_{\mathrm{n}}}{q} \nabla \left(E_{\mathrm{F}} - E^l \right) \right) = n \mu_{\mathrm{n}} \nabla E_{\mathrm{F}} \tag{5.25}$$

Then, one can use the alternative Fermi-level based equation for each layer:

$$\begin{cases} J^l_{\mathrm{n}} = n^l \mu_{\mathrm{n}} \nabla E^l_{\mathrm{F,n}} \\ J^l_{\mathrm{p}} = p^l \mu_{\mathrm{p}} \nabla E^l_{\mathrm{F,p}} \end{cases} \tag{5.26}$$

By solving the Fermi level profile, expression (Eq 5.10) can be used to evaluate the charge density including explicitly the contribution of a position-dependent DoS that should be previously calculated making use of *ab-initio* or empirical approaches:

$$\begin{cases} n^l(E^l_{\mathrm{F}}) = \displaystyle\int_{E_{\mathrm{C}}}^{\infty} g_{\mathrm{n}}(E) f(E^l_{\mathrm{F}}) d(E) \\ p^l(E^l_{\mathrm{F}}) = \displaystyle\int_{-\infty}^{E_{\mathrm{V}}} g_{\mathrm{p}}(E) \left[1 - f(E^l_{\mathrm{F}}) \right] d(E) \end{cases} \tag{5.27}$$

This scheme provides a detailed description of the semiconductor material properties and their effect on the transport characteristics. For the discretization of the equations, the same criteria as before is considered. Current and mobilities are defined in the mid-nodes, while the carrier density

and the Fermi levels are defined in the grid nodes. In the case of electrons, for the l-th layer the resulting equation system reads as:

$$\begin{aligned} 0 =& \frac{\mu_{j+1/2} n_{j+1/2}}{\Delta x_{j+1/2}} E_{\mathrm{F},j+1} + \frac{\mu_{j-1/2} n_{j-1/2}}{\Delta x_{j-1/2}} E_{\mathrm{F},j-1} + \\ &+ \left(\frac{\mu_{j+1/2} n_{j+1/2}}{\Delta x_{j+1/2}} + \frac{\mu_{j-1/2} n_{j-1/2}}{\Delta x_{j-1/2}} \right) E_{\mathrm{F},j} \end{aligned} \tag{5.28}$$

Once the Fermi level profiles $E^l_{\mathrm{F,n}}$ and $E^l_{\mathrm{F,p}}$ have been calculated, they are combined with the energy levels $E^l(y)$ (Eq 5.6) to evaluate the charge density using the semiconductor DoS. Then, the resulting charge profiles are used in the next iteration of the Poisson equation updating the coefficients of the system of equations (Eq 5.28). This flowchart has shown sporadic stability issues for mid- and high-V_{DS} values, particularly in the first iterations of the main scheme. To solve this challenge the charge profiles are filtered to avoid an excessive variation between iterations before being used to update $E^l_{\mathrm{F,n}}$ and $E^l_{\mathrm{F,p}}$ and evaluate the Poisson equation. The final scheme used to solve Fermi level and charge profiles is depicted in Figure 5.8.

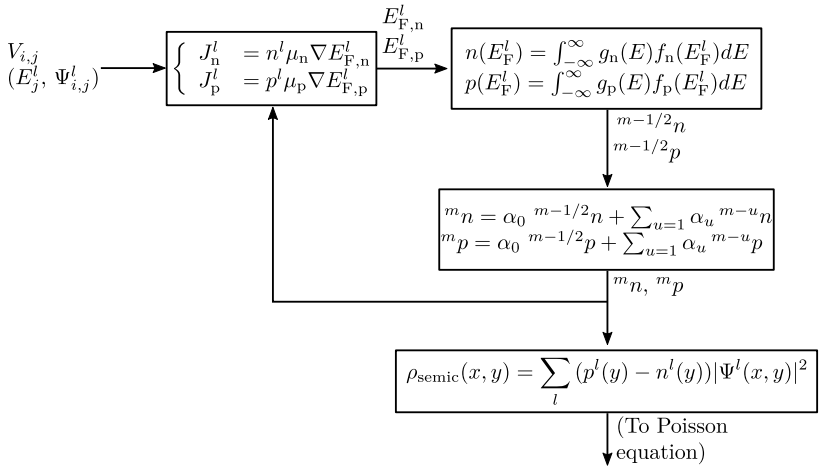

Figure 5.8: Schemes handling the Drift-Diffusion transport equation solution for few-layer devices. Once the Fermi level profiles are obtained and the charge is updated, this is filtered to avoid large changes in the first iterations.

All the method described above is considered for 2DMs semiconductors. Charge transport in Graphene is addressed in a more specific manner. The high recombination ratio in this material makes possible to consider a common Fermi level for both electrons and holes [78]. Under this assumption the Drift-Diffusion transport equation is rewritten as:

$$J = q(\mu_{\mathrm{n}} n + \mu_{\mathrm{p}} p) \nabla E_{\mathrm{F}} \tag{5.29}$$

Equation (Eq 5.28) is valid for this expression of the current just changing $\left(\mu_{j+1/2} n_{j+1/2}\right)$ by $\left(\mu_{\mathrm{n}\,j+1/2} n_{j+1/2} + \mu_{\mathrm{n}\,j+1/2} p_{j+1/2}\right)$. In addition, this scheme depicts an improved numerical stability compared to the previous one, and thus, the charge filtering step is omitted.

5.5 Time dependent numerical simulation

The transport models aforementioned are only valid for stationary biases, that is, there is no change along time of the bias condition of the device. Then, in addition to that stationary bias scheme, a second one is implemented aiming to handle transient simulations of MOSFET devices. A similar iterative procedure is used to solve the equations, the only difference is that the calculus for the different bias evaluations are coupled, that is, the results for a certain bias are used to obtain the solution of the next one. We assume that the propagation of the electromagnetic fields in the structure is much faster than the variation of the terminal biases, so the Poisson equation (Eq 4.1) still provides a good description of the electrostatic potential in the structure. Therefore, the changes in the potential along time originate from the modification of the charge profiles. In this regard, the model for the charge transport needs to be updated to include time dependency using the continuity equation ($(G+R)_{\mathrm{n}} = 0$):

$$-\frac{1}{q}\nabla J = \frac{\partial n}{\partial t} \tag{5.30}$$

This expression is then discretised in both, space and time. If we consider the backward FD approximation (Appendix B) for the time derivative of the charge density n we can write:

$$-\frac{1}{q}\left(J^{(k)}_{j+1/2} - J^{(k)}_{j+1/2}\right)\frac{\Delta_t^{(k)}}{\delta_{x\,j}} - n_j^{(k)} = -n_j^{(k-1)} \tag{5.31}$$

where the index (k) indicates the value for the current time step and $(k-1)$ for the previous one, and $\Delta_t^{(k)}$ stands for the time step of the current time step k. The discretization of the current is not impacted by the time dependence, so the same schemes developed so far can be applied. In this case, the DD equation for the monolayer scenario is discretized following the Scharfetter-Gummel discretization scheme (Eq 5.18). In the particular

case of electrons this discretization results in the following expressions:

$$J^{(k)} = -qn^{(k)}\mu_{\mathrm{n}}\frac{\partial V^{(k)}}{\partial x} + qD_{\mathrm{n}}\frac{\partial n^{(k)}}{\partial x} \Rightarrow$$
$$\Rightarrow \begin{cases} J^{(k)}_{j-1/2} = q\frac{k_{\mathrm{B}}T}{\Delta_{\mathrm{x}\ j-1/2}}\mu_{j-1/2}\left[n^{(k)}_{j}B\left(\Lambda_j\right) - n^{(k)}_{j-1}B\left(-\Lambda_j\right)\right] \\ J^{(k)}_{j+1/2} = q\frac{k_{\mathrm{B}}T}{\Delta_{\mathrm{x}\ j+1/2}}\mu_{j+1/2}\left[n^{(k)}_{j+1}B\left(\Lambda_{j+1}\right) - n^{(k)}_{j}B\left(-\Lambda_{j+1}\right)\right] \end{cases} \tag{5.32}$$

where $\Lambda_{j+1} = \phi_{j+1} - \phi_j$ and B is the Bernoulli function (Eq 5.20). This set of equations is then used to evaluate the carrier profile for the current time step (k) and obtain the corresponding potential profile.

5.6 Surface defects: charge traps

The presence of traps, defects and other non-idealities are unavoidable in most of the semiconductor devices due to the imperfections generated during the fabrication process. For extremely-thin channels, they are mostly located at the interfaces between materials. The charge captured by these traps does not move across the structure, remaining fixed at their specific locations that translates its effect on the device electrostatics, and consequently on the $I-V$ characteristics through the modification of the free carrier densities and their mobility. The presence of these interface traps can be modelled through a DoS distributed in the forbidden energy band as depicted in Figure 5.9.

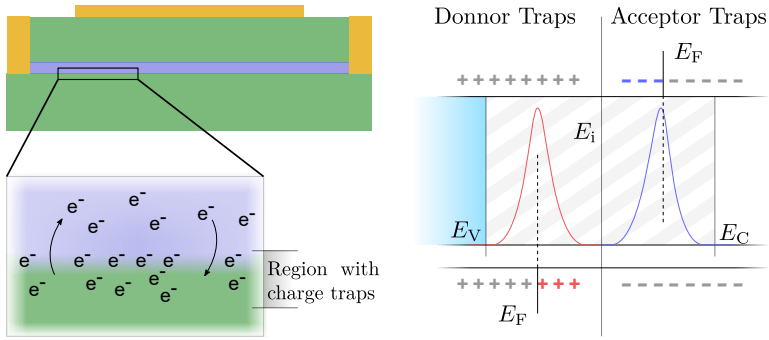

Figure 5.9: Example of interface traps at the semiconductor-insulator interface where electrons are captured or released, depending on the type of traps. As indicated, donor traps release electrons and become positively charged, while acceptor traps capture electrons and become negatively charged. All these processes are controlled by the position of the Fermi level in the semiconductor.

According to their behaviour, interface traps can be classified into two groups: donor and acceptor traps. Donor traps release electrons, becoming

positively charged. On the other hand, acceptor traps are able to capture electrons, so they remain negatively charged when activated. The occupation of these traps is determined by the position of the Fermi level at the semiconductor interface. Taking into account that donor/acceptor traps are charged when they are unoccupied/occupied, and making use of the Fermi-Dirac statistics, the net charge of these traps is defined as:

$$Q_{\mathrm{it}} = q\int_{-\infty}^{\infty} D_{\mathrm{it}}^{\mathrm{d}}\left(E\right)\left[1-f\left(E\right)\right]dE - q\int_{-\infty}^{\infty} D_{\mathrm{it}}^{\mathrm{a}}\left(E\right)f\left(E\right)dE \tag{5.33}$$

where $D_{\mathrm{it}}^{\mathrm{a}}(E)$ and $D_{\mathrm{it}}^{\mathrm{d}}(E)$ refers to the acceptor and donor trap DoS respectively. If we consider that the intrinsic Fermi level E_{i} is the reference energy level, $\hat{E} = E - E_{\mathrm{i}}$, then Q_{it} can be defined as:

$$Q_{\mathrm{it}}(E_{\mathrm{F}}-E_{\mathrm{i}}) = q\int_{-\infty}^{\infty}\frac{D_{\mathrm{it}}^{\mathrm{d}}\left(\hat{E}\right)}{1+e^{-\frac{(E_{\mathrm{F}}-E_{\mathrm{i}})-\hat{E}}{k_{\mathrm{B}}T}}}d\hat{E} - q\int_{-\infty}^{\infty}\frac{D_{\mathrm{it}}^{\mathrm{a}}\left(\hat{E}\right)}{1+e^{-\frac{\hat{E}-(E_{\mathrm{F}}-E_{\mathrm{i}})}{k_{\mathrm{B}}T}}}d\hat{E} \tag{5.34}$$

where $(E_{\mathrm{F}} - E_{\mathrm{i}})$ can be easily related with the electrostatic potential:

$$-qV = E_{\mathrm{C}} - E_{\mathrm{F}} = (E_{\mathrm{i}} - \frac{E_{\mathrm{g}}}{2}) - E_{\mathrm{F}} \Rightarrow qV + \frac{E_{\mathrm{g}}}{2} = E_{\mathrm{F}} - E_{\mathrm{i}} \tag{5.35}$$

This, however, is only valid for the equilibrium scenario where the Fermi level is constant along the structure. When the transport scenario is evaluated, a non-constant Fermi level profile has to be considered. The intrinsic Fermi level can be obtained from the potential profile:

$$-qV = E_{\mathrm{C}} - E_{\mathrm{F,S}} = (E_{\mathrm{i}} - \frac{E_{\mathrm{g}}}{2}) - E_{\mathrm{F,S}} \Rightarrow E_{\mathrm{i}} = -qV + \frac{E_{\mathrm{g}}}{2} + E_{\mathrm{F,S}} \tag{5.36}$$

The Fermi level E_{F} is evaluated from the results obtained with the transport model. As it is also refereed to its value at the source contact ($E_{\mathrm{F,S}} = 0$ eV), the evaluation of Q_{i} is straightforward. The energetic profiles $D_{\mathrm{it}}^{\mathrm{a}}(E)$ and $D_{\mathrm{it}}^{\mathrm{d}}(E)$ are inputs for the simulations, so they do not change during the iterative solution. This make possible to handle arbitrary energetic profiles, either from experimental measurements (like deep-level transient spectroscopy or high-frequency capacitance-voltage measurements) to reproduce the device behaviour or theoretical profiles that can be tuned to fit experimental data.

As indicated in Figure 5.9, the region where charge is captured is not limited to the interface between the materials, as it has a certain depth that can be associated to the roughness of the interface. Therefore, different spatial distribution profiles are defined to distribute the charge obtained following the procedure aforementioned. Table 5.1 summarises the charge distribution profiles along with their respective parameters.

Distribution	
Constant	$t(x) = A_c$ $A_c = N_{it} 2 t_{ins} / t_o^2$
Linear	$t(x) = A_l \left(1 - \frac{x}{t_{ins}}\right)$ $A_l = 4 N_{it} t_{ins} / t_o^2$
Exponential	$t(x, \alpha_e) = A_e \left(e^{-x/\alpha_e}\right)$ $A_e = \frac{N_{it} t_{ins}}{\alpha_e \left(1 - (t_o + \alpha_e) e^{t_o/\alpha_e}\right)}$
Gaussian	$t(x, \alpha_g) = A_g \left(e^{-x^2/2\alpha_g^2}\right)$ $A_g =$ $\frac{N_{it} t_{ins}}{\alpha_g t_o \sqrt{\pi/2}} erf\left(\frac{t_o}{\alpha_g \sqrt{2}}\right) + t_{ins}\left(e^{-t_o^2/(2\alpha_g^2)} - 1\right)$

Table 5.1: Spatial distributions available for interface traps in the simulations of the devices [79].

5.6.1 Time dependent model

In addition to the static model described above, a more advanced one is developed for time dependent simulations. In this regard, there is no specific model for the numerical time dependent simulation of the charging/discharging processes of the interface traps, so a previous analysis is preformed in order to solve this problem.

The charge associated to these traps is considered static in the structure and, consequently, there is no contribution to the transport process, and its effect is sensed through the accumulation of that charge in specific regions. Furthermore, the trapping events associated to them are not instantaneous, they occur at different rates depending on the nature of the trapping event. This behaviour resembles the charging/discharging of a capacitor though a resistance. Then, a time dependent model is build up based on a series RC circuit. The objective is to obtain an expression for the trapped charge as a function of the time constant that characterises the traps, their DoS and the electrostatic potential in the region where they are located.

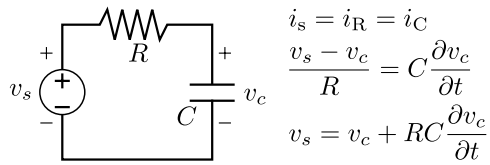

Figure 5.10: Series RC circuit and the differential equation used to build a model for the transient simulation of interface traps.

As indicated in Figure 5.10, the differential equation that defines a series RC circuit can be obtained from the continuity condition of the current that

flows through all the elements of the circuit. This differential equation can be discretised in time using the FD method in order to numerically evaluate v_c for an arbitrary $v_s(t)$. Then, for the time step $k\Delta_t$, the voltage of the capacitor is defined as:

$$v_c^{(k)} = \left[v_s^{(k)} + \frac{RC}{\Delta_t} v_c^{(k-1)}\right] \left(1 + \frac{RC}{\Delta_t}\right)^{-1} \tag{5.37}$$

where Δ_t is the time step. The change in the capacitor charge can be evaluated from the definition of capacitance and v_c:

$$C = \frac{\partial Q_c}{\partial v_c} \Rightarrow Q_c^{(k)} = Q_c^{(k-1)} + C\left(v_c^{(k)} - v_c^{(k-1)}\right) \tag{5.38}$$

Therefore, the aim of this discretization is to get an expression for the charge Q_c able to reproduce the two coupled equations (Eq 5.37) and (Eq 5.38). First, if both equations are solved assuming a step signal for the source voltage, we obtain a capacitor charge profile as the one depicted in Figure 5.11.

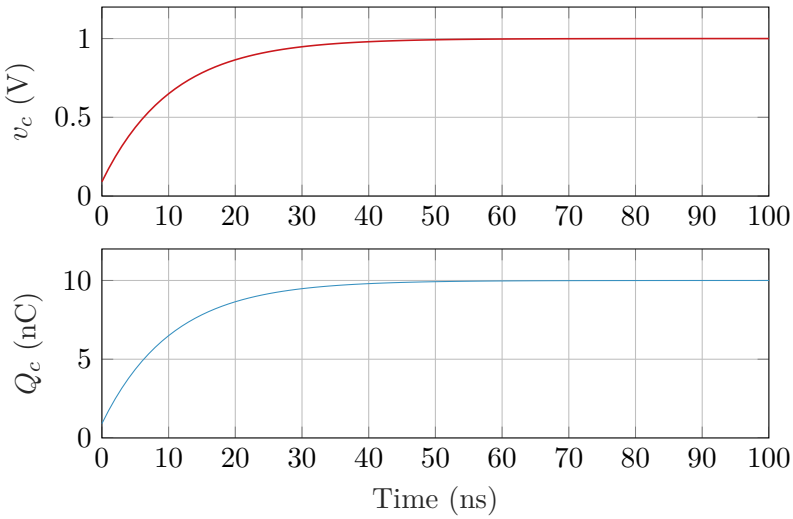

Figure 5.11: Temporal evolution of the capacitor charge in the RC circuit described by equations (Eq 5.37) and (Eq 5.38). The source bias corresponds to a step signal from 0 to 1 V and the elements of the circuit are R=1kΩ and C=10nF.

As depicted in Figure 5.11, the charge starts from an initial value Q_0 and changes progressively up to a maximum $Q_{\max}$. This temporal evolution can be expressed through the expression:

$$Q_c(t) = Q_0 + \Delta Q(t) = Q_0 + (Q_{\max} - Q_0)\,\alpha(t) \tag{5.39}$$

where $\alpha(t)$ is a correction factor used to include the time dependence and speed (time constant) of the traps. Two options were explored for that coefficient: $f(t) = t/(\tau+t)$ and $g(t) = 1-e^{-t/\tau}$. As depicted in Figure 5.12, $f(t)$ is the function that provides a better fits to the expected behaviour.

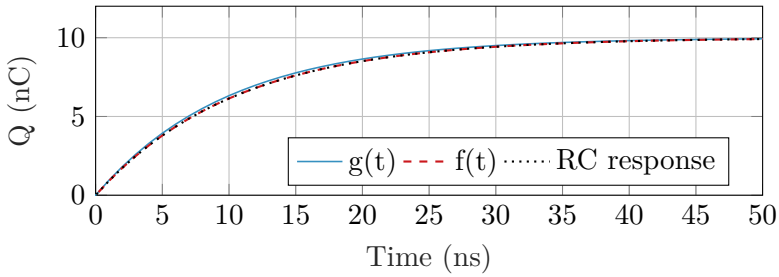

Figure 5.12: Fitting of the results depicted in Figure 5.11 using (Eq 5.39). Two functions were used to define the coefficient α: $f(t) = t/(\tau + t)$ and $g(t) = 1 - e^{-t/\tau}$. The time constant is set to 10 μs, equivalent to an RC circuit with R=1 kΩ and C=10 nF.

All the previous analysis can be used to include time dependency in the model for interface traps exposed in Section 5.6. That section introduced a model to relate the amount of charge captured with the DoS that characterises the traps and the local electrostatic potential. Regarding time dependent simulations, that model would mimic ideal traps with an instantaneous response to changes in the potential, so it has to be combined with expression (Eq 5.39) to introduce the delayed response of charge traps. Looking into the aforementioned discretised version of an arbitrary signal $s(t)$, when the general simulation scheme solves the current time step (k), the results corresponds to the end of the step signal of the interval $[(k-1)\Delta_t, k\Delta_t]$ as showed in Figure 5.13.

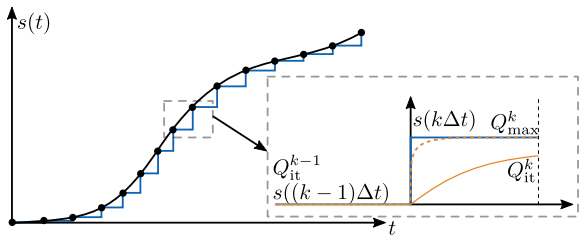

Figure 5.13: Sketch showing the application of the step response behaviour to the simulations using a generic $s(t)$ signal. The value Q^{k-1} defines the initial state of the traps to evaluate their state at the end of the current step Q^k, that will be used later for the calculations for the next time step $k+1$.

Using the example depicted in Figure 5.13, in (Eq 5.39) the initial charge Q_0 corresponds to the charge obtained for the previous time step $Q^{(k-1)}$, and Q_{max} corresponds to the final charge of ideal traps able to react to

the change in the electrostatic potential within the evaluated interval. In summary, the final expression for the model remains as:

$$\begin{cases} Q_{\mathrm{it}}^{(k)} & = Q_{\mathrm{it}}^{(k-1)} + \left(Q_{\mathrm{max}}^{k} - Q_{\mathrm{it}}^{(k-1)}\right) \frac{\Delta_t}{\Delta_t + \tau} \\ Q_{\mathrm{max}}^{k} & = q \int_{E_{\mathrm{V}}}^{E_{\mathrm{i}}} D_{\mathrm{it}}^{\mathrm{d}}(E)\left[1 - f(E)\right] dE - q \int_{E_{\mathrm{i}}}^{E_{\mathrm{C}}} D_{\mathrm{it}}^{\mathrm{a}}(E) f(E)\, dE \end{cases} \tag{5.40}$$

The potential calculated from the Poisson equation in each iteration will impact on Q_{max}^{k} and then on the evaluation of Q_{it}, that will be the final contribution of the charged traps in the Poisson equation, and therefore on a new value of the electrostatic potential.

In all the previous development a common time constant is considered for both charging and discharging processes. This, however, does not necessarily match with a real scenario where the behaviour of charge traps is usually asymmetric regarding these two processes. The update to include this additional feature is straightforward, the conditions $Q_{\mathrm{it}}^{(k-1)} < Q_{\mathrm{max}}^{k}$ and $Q_{\mathrm{it}}^{(k-1)} > Q_{\mathrm{max}}^{k}$ can be checked to use a charging time constant τ_{c} ($Q_{\mathrm{it}}^{(k-1)} < Q_{\mathrm{max}}^{k}$) or a discharging time constant τ_{d} ($Q_{\mathrm{it}}^{(k-1)} > Q_{\mathrm{max}}^{k}$).

CHAPTER 6

Modelling the electrolyte and sensing interface

6.1 Introduction

This final chapter deals with the modelling of the BioFET, specifically the electrolyte and sensing interface, which corresponds to the blocks highlighted in Figure 6.1.

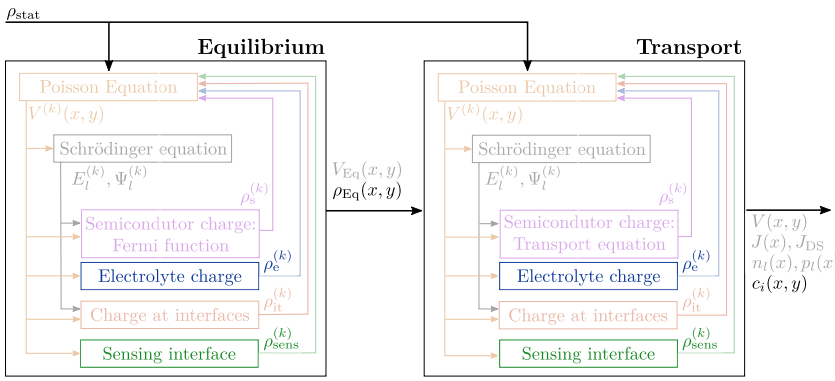

Figure 6.1: Blocks of the iterative scheme involved in the calculation of the charge associated to the liquid electrolyte and the sensing interface.

The charge associated to the liquid electrolyte is essentially defined by the distribution of simple ions. They are impacted by the potential distribution and other side effects, like solid-liquid interface interactions, as will be described in the following. Regarding the sensing interface, its contribution is defined by the elements added to the MOSFET structure to provide it with the biomolecular sensing capability. In this case, there is no dependence with the potential, charge is static, but it is able to impact in a large extent to the response of the sensor. All the details of these models will be addressed in the following.

6.2 Electrolyte description

In ISFET and BioFET devices, the electrolyte becomes an essential element of the system as it plays the role of the sensing target for ISFETs and of the substrate that contains the molecules for BioFETs. The electrical charge in the electrolyte is defined by the ions generated by the dissociation of the salts that define its composition. The dependence of the ion concentration on the electrostatic potential can be modelled by a Boltzmann-like exponential distribution, which for the l-th ion is defined as:

$$c^l = c_0^l e^{-z^l \phi} = c_0^l e^{-z^l \frac{V - V_{\text{ref}}}{k_{\text{B}} T}} \tag{6.1}$$

where c_0^l is the electrolyte bulk ion concentration, z^l its valence, V the electrostatic potential from Poisson equation, and V_{ref} the reference potential of the electrolyte, that is usually set by an electrode immersed in the solution. This expression provides a simple modelling of the electrolyte, which is the most employed approach. However, aiming to achieve a more accurate modelling of the device, the modified Boltzmann relation reported in [59] should be included. This approach considers steric effects, i.e. those related with the limitation of the maximum ion concentration at the interface due to the finite ionic radius: $c_{\text{max}} = r_{ion}^{-3}$. In this case, the modified Boltzmann (mB) distribution reads:

$$c^l = \frac{c_0^l e^{-z^l \phi}}{1 - 2\frac{c_0^l}{c_{\text{max}}^l}\left(1 - \cosh\left(|z^l \phi|\right)\right)} \tag{6.2}$$

Figure 6.2 shows and example of the profiles obtained with this model when it is solved self-consistently with the Poisson equation assuming the structure depicted in the inset. In this case, the radius of the cations (r_+) is larger that the radius of the anions (r_-) to highlight the impact of this parameter on the resulting concentration profile. The data obtained show that this modified version of the classical Boltzmann distribution is a simple approach to account for the physical limitation in the maximum allowed ion concentration in those regions where the electrostatic potential ϕ changes by a large extent. This situation is more likely to take place at solid-liquid interfaces or near charged elements within the electrolyte, e.g. charged molecules.

Despite the fact that steric effects are relevant near the electrolyte-solid interface, they do not account for specific interactions between the interface and the ions in the electrolyte. A via to include these effects is an additional term in the ion distribution expression that modulates the concentration of each ion near the interface. The profile of this new term depends on the ion and the features of the interface [80]:

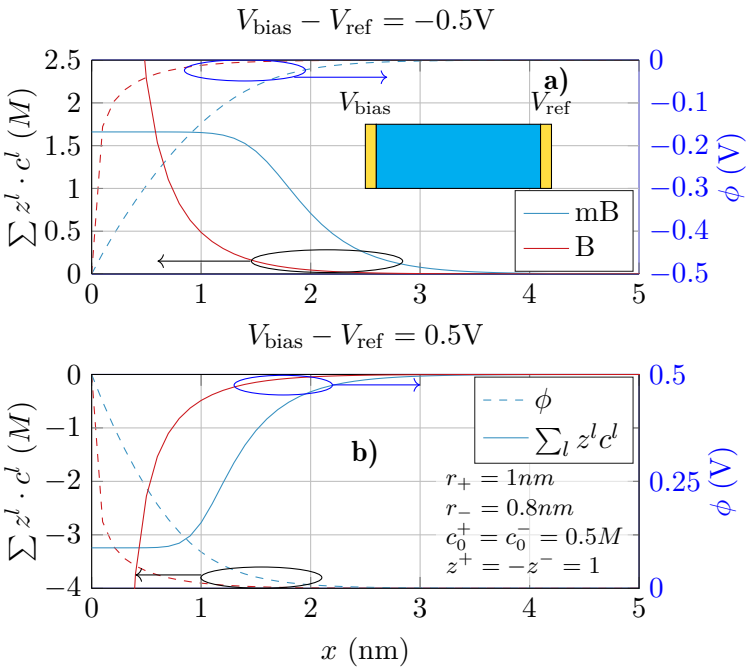

Figure 6.2: Total ion concentration profile (solid lines) and potential profiles (dashed lines) using the Boltzmann (red) and mB (blue) models for the ion distributions. This data is obtained for a negative (a) and positive (b) ϕ value, to illustrate the impact of these two models in the distribution of cations and anions. The inset shows the structure used to obtain the data: an electrolyte (blue) between two parallel contacts (gold).

$$c^l = c_0^l \frac{e^{-z^l\phi}}{1 - 2\frac{c_0^l}{c_{\max}^l}\left(1 - \cosh\left(|z^l\phi|\right)\right)} e^{\phi^l_{\text{PFM}}} \tag{6.3}$$

where ϕ^l_{PFM} contains the information of the Potentials of Mean Force (PMF). These potentials modify the concentration of ions near the solid-liquid interface to include the effect of non-Coulombic interactions in this region. These profiles can be evaluated from empirical models, like Yukawa potentials [81], or extracted from Molecular Dynamics (MD) simulations, that describe the atomic and molecular interactions in the electrolyte with great detail [80, 82]. Figure 6.3 shows an example of the impact that this potential exert on the ion concentration near a solid surface showing either hydrophobic or hydrophilic behaviour. For this representation, the PMF profiles were extracted from [82].

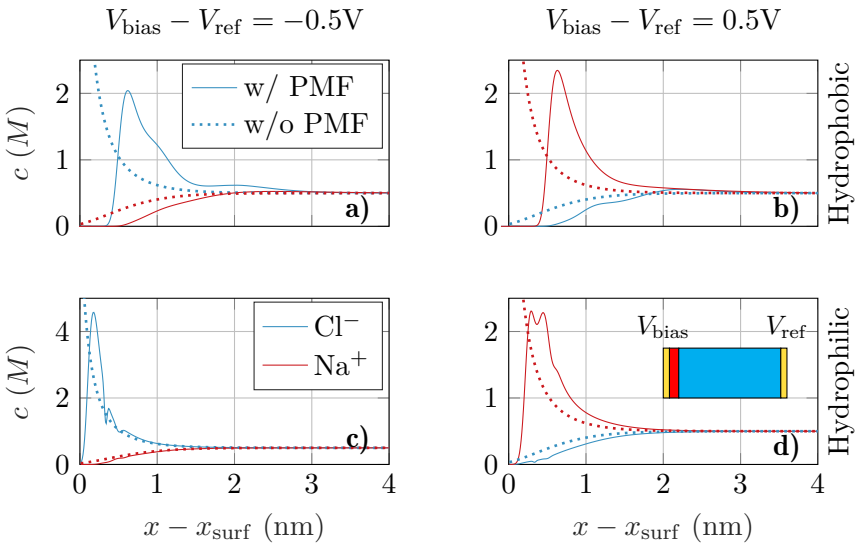

Figure 6.3: Concentration profiles illustrating the impact of PMF potentials on the concentration of Cl^- and Na^+ where the structure depicted in the inset in subplot (d) is evaluated. The surface of the solid region (red) is considered either hydrophobic (a, b) or hydrophilic (c,d). The data without PMF are depicted with dotted lines as a reference. Inset in (d) shows the structure used in the simulations: an electrolyte (blue) in contact with a solid block (red) with a contact beneath (gold).

Figure 6.3 evidences that the nature of the interface has a noticeable impact on the distribution of the ions. First, there is a noticeable influence on the distance between the solid surface and the regions with high ion concentration: hydrophobic surfaces tend to push away ions, while hydrophilic surfaces let them to be closer. Second, the concentrations are modulated by the specific interactions between the ions and the surface.

Once the spacial distribution of each ion inside the electrolyte is determined, the Poisson equation can be self-consistently solved combining all of them to determine the net electrolyte charge as:

$$\rho_{\text{e}} = N_{\text{Avg}} 10^{-3} \sum_{l} z^l c^l \tag{6.4}$$

where N_{Avg} is Avogadro's constant.

Buffer solutions: Phosphate Buffered Saline

In the specific case of BioFET devices, the electrolyte acts as a substrate for the biological analytes to be detected. Usually, buffer solution with the capability to maintain their pH within a narrow range, avoiding the degradation of the sample. Let us first introduce the concept of pH. This

parameter is defined by the concentration of Hydrogen ions $\left[H^+\right]$ as:

$$\mathrm{pH} = -\log_{10}\left(\left[H^+\right]\right) \tag{6.5}$$

In pure water these ions originate from the dissociation of water molecules, a process that is defined by a dissociation constant K_w:

$$H_2O \overset{K_w}{\rightleftharpoons} H^+ + OH^- \quad \Rightarrow \quad K_w = \frac{[H^+]\,[OH^-]}{[H_2O]} \tag{6.6}$$

This expression can be rewritten in terms of the pH by rearranging terms:

$$\mathrm{pH} = pK_\mathrm{w} - \log_{10}\left(\frac{[H_2O]}{[OH^-]}\right) \Rightarrow pH = pK_\mathrm{w} - \log_{10}\left(\frac{[\mathrm{base}]}{[\mathrm{acid}]}\right) \tag{6.7}$$

where $pK_\mathrm{w} = -\log_{10}(K_\mathrm{w})$ and the expression in the right hand side correspondsto the Henderson-Hansselbalch equation. The same procedure as in pure water can be applied to model a buffer solution. The most common buffer solution is the Phosphate-Buffered Saline (PBS) solution, the composition of which is summarised in Table 6.1.

	1×PBS
NaCl	137 mM
KCl	2.7 mM
Na_2HPO_4	10 mM
KH_2PO_4	1.8 mM

Table 6.1: Typical PBS composition [83].

In the PBS solution, NaCl and KCl define the saline substrate while the $X_xH_{3-x}PO_4$ elements are those involved in the reactions regulating the pH:

$$\begin{aligned} H_3PO_4 &\overset{pK_{a_1}}{\rightleftharpoons} H_2PO_4^- + H^+ \\ H_2PO_4^- &\overset{pK_{a_2}}{\rightleftharpoons} HPO_4^{2-} + H^+ \\ HPO_4^{2-} &\overset{pK_{a_3}}{\rightleftharpoons} PO_4^{3-} + H^+ \end{aligned} \tag{6.8}$$

Using the Henderson-Hansselbalch equation we can define the concentration of the elements involved ($\left[H_2PO_4^-\right]$, $\left[HPO_4^{2-}\right]$ and $\left[PO_4^{3-}\right]$) as a function of the pH and the reaction constants:

$$\begin{aligned} \left[H_2PO_4^-\right] &= [H_3PO_4]\,10^{\mathrm{pH}-pK_{a_1}} \\ \left[HPO_4^{2-}\right] &= \left[H_2PO_4^-\right]10^{\mathrm{pH}-pK_{a_2}} \\ \left[PO_4^{3-}\right] &= \left[HPO_4^{2-}\right]10^{\mathrm{pH}-pK_{a_3}} \end{aligned} \tag{6.9}$$

The actual H_3PO_4 concentration can be obtained from the condition that the sum of all the elements must be equal to the concentration of $X_xH_{3-x}PO_4$ in the composition of the electrolyte, which is named as [PBS]:

$$[H_3PO_4] + \left[H_2PO_4^-\right] + \left[HPO_4^{2-}\right] + \left[PO_4^{3-}\right] = [\text{PBS}] \tag{6.10}$$

which, using the concentrations in (Eq 6.9) and rearranging terms, provides an expression for $[H_3PO_4]$:

$$[H_3PO_4] = \frac{[\text{PBS}]}{1 + 10^{\text{pH}-pK_{a_1}}\left(1 + 10^{\text{pH}-pK_{a_2}}\left(1 + 10^{\text{pH}-pK_{a_3}}\right)\right)} \tag{6.11}$$

Expressions (Eq 6.9) and (Eq 6.11) fully define the set of equations to evaluate the components of the reactions. The only unknown concentration is the one associated to the cations X^+, which can be obtained from the charge neutrality condition from the elements of the PBS [84]:

$$\left[X^+\right] = -z_{H_2PO_4^-}\left[H_2PO_4^-\right] - z_{HPO_4^{2-}}\left[HPO_4^{2-}\right] - z_{PO_4^{3-}}\left[PO_4^{3-}\right] \tag{6.12}$$

In the previous equations, the pK_{a_l} dependence on the temperature (T) and on the ionic strength (I) should be included [84]. The actual dependencies are given by:

$$pK_a(I,T) = pK_a(T) + (2z_a - 1)\left[\frac{A\sqrt{I}}{1+\sqrt{I}} - 0.1I\right] \tag{6.13}$$

where the temperature dependent component of pK_a is defined as:

$$pK_a(T) = pK_a + dpK_a/dT \cdot (T - 298.15K) \tag{6.14}$$

and I is defined as:

$$I = \sum_l^N (z^l)^2 c^l \tag{6.15}$$

Temperature is not a relevant parameter in this Thesis, as we will not address changes in the operation temperature of the devices. On the contrary, the ionic strength is a parameter that changes locally in the electrolyte, as it depends on the ion concentration. Even the ions associated to the PBS impact on I. Therefore, an iterative calculation controlled by the convergence on I must be performed to obtain the final values of $[H_3PO_4]$, $\left[H_2PO_4^-\right]$, $\left[HPO_4^{2-}\right]$, $\left[PO_4^{3-}\right]$ and $\left[X^+\right]$ associated to the pH regulation reactions. For the charged elements, these concentration values must be combined with

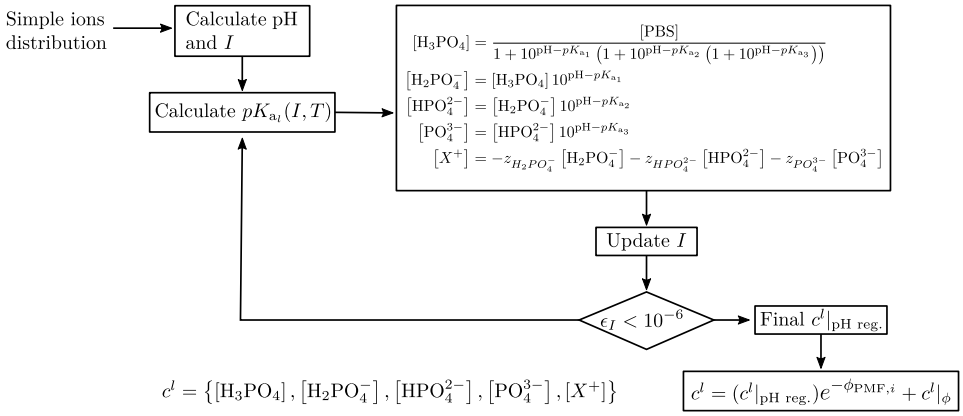

Figure 6.4: Scheme summarising the calculation of the charge related with the components of the PBS involved in the pH regulation. A first value of the reaction constants is evaluated from the simple ions local concentrations. Then, the concentrations of the PBS ions are evaluated and used to update the ionic strength I. The difference between this new value and the previous one is compared with a fixed threshold to determine if convergence is achieved. Finally, the concentrations obtained for each charged element are combined with a potential dependent term.

Parameter	Value
$pK_{a_1}(25°C)$	2.15
$pK_{a_2}(25°C)$	7.21
$pK_{a_3}(25°C)$	12.33

Parameter	Value
dpK_{a_1}/dT	0.0044 K^{-1}
dpK_{a_2}/dT	-0.0028 K^{-1}
dpK_{a_3}/dT	-0.026 K^{-1}

Parameter	Value
z_{a_1}	0
z_{a_2}	-1
z_{a_3}	-2
A $(25°C)$	0.5114

Table 6.2: Values for the constants used in the calculation of $pK_{a_i,T}$. Extracted from [84].

the distribution functions due to the change in the potential with respect to the reference electrode as in (Eq 6.2).

For the sake of completeness, Figure 6.4 shows an scheme summarizing the iterative procedure. As indicated in Figure 6.4, first, the value of each reaction constant, pK_a is evaluated using an initial ionic strength, I, using the local concentration of simple ions. Then, equations (Eq 6.9), (Eq 6.11) and (Eq 6.12) are used to obtain the concentration of the PBS ions and update I. The difference between this new I value and the previous one is compared with a fixed threshold in order to determine if convergence has been achieved. If so, the resulting concentrations for the charged composites are combined with the potential dependent term and considered within the self-consistent solution of Poisson equation. The values of all the reactions constants $pK_{a_l}(I,T)$ and related parameters required for the calculations of the PBS considered in this Thesis are extracted from [84] and summarised in Table 6.2.

6.3 Surface ion adsorption: Generic Site-Binding model

ISFET chemical sensors, such as pH sensors, are based on the adsorption of ions at the solid-state device surface. As depicted in Figure 6.5, the operation principle of these devices leverages the changes in the surface potential due to the capture of ions by the sensor surface, and its impact on the carrier distribution in the semiconductor beneath that sensing layer.

In order to properly simulate the sensor behaviour, a model for the charge adsorption at the electrolyte-solid interface is required. The most commonly used model is the Site-Binding (SB) model, that focuses on the reactions involving the adsorption of hydrogen ions at the surface, since pH sensors are the most commonly studied type of sensor. The SB model is indeed a particular case of a more generic description reported in [85] known as generic Site-Binding (gSB), which is the one implemented in our simulator.

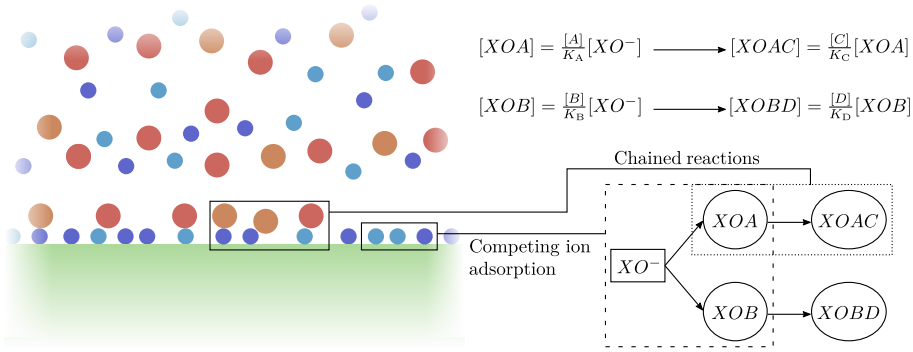

Figure 6.5: Reactions taking place at the electrolyte-solid surface that enable the operation of the chemical sensor. Ions can be directly adsorbed onto the surface or after the adsorption by another type of ions.

As shown in Figure 6.5, there are two type of reactions: competing ion adsorption and chained reactions. The first type considers the competitive occupation of the sites by different ions. The second deals with the reaction of ions with the sites already activated, so the amount of charge is conditioned by the amount of ions previously adsorbed. So that, any complex scenario can be modelled as a combination of these two simple ones.

Each reaction, either between the ions and the surface or between ions, is characterized by a reaction constant K and involves the active element concentration $[A]$, the adsorbed ion concentration $[B]$ and the product concentration $[AB]$:

$$A + B \overset{K}{\rightleftharpoons} AB \Rightarrow [AB] = \frac{[B]}{K}[A] \tag{6.16}$$

When analysing the adsorbed charge at the interface, all the reactions are translated as a set of equations, where the active element and the product concentrations are the variables to be solved. As introduced in [85], all these equations follow the form:

$$f_j = \frac{[B_i]}{K_{ij}} f_i \tag{6.17}$$

where the sub-index i refers to the active element, the sub-index j refers to the product and f_j stand for the normalized concentrations of these elements, which verifies the condition:

$$\sum_j f_j = 1 \tag{6.18}$$

Then, this generic formulation enables the definition of a system of equations whose unknowns are the normalised product concentrations f_j:

$$\left.\begin{array}{l} \frac{[B_i]}{K_{ij}} f_i - f_j = 0 \\ \sum_j f_j = 1; \end{array}\right\} \Rightarrow M\mathbf{f} = \mathbf{b} \left\{\begin{array}{ll} M_{ij} = \frac{[B_i]}{K_{ij}} & j \neq i \\ M_{jj} = -1 & \\ b_j = 0 & \\ M_{\mathrm{N}j} = b_{\mathrm{N}} = 1 & \end{array}\right. \tag{6.19}$$

where M_{ij} is the (i, j) element of the matrix M with size $N \times N$, which is related with the number of reactions $(N-1)$ and elements involved (N).

To exemplify the operation of this model, we focus on the basic SB model, that handles the capture of hydrogen ions at a solid surface. In this case there are only two reactions involved, the protonation of the active sites of the surface and its complexation with hydrogen ions nearby:

$$\left\{\begin{array}{l} X^- + H^+ \overset{K_A}{\rightleftharpoons} XH \\ XH + H^+ \overset{K_B}{\rightleftharpoons} XH^+ \end{array}\right. \Rightarrow \left\{\begin{array}{l} f_1 = [X^-] \\ f_2 = [XH] \\ f_3 = [XH^+] \end{array}\right. \tag{6.20}$$

where X^- stands for the active sites at the solid surface, and the matrix to solve the equations associated to each reaction is defined as:

$$M = \begin{bmatrix} [H^+]/K_A & -1 & 0 \\ 0 & [H^+]/K_B & -1 \\ 1 & 1 & 1 \end{bmatrix} \tag{6.21}$$

Figure 6.6 shows the evolution of the normalised concentrations f_j as a function of the solid surface potential and different pH values. These profiles corresponds to a SiO_2 surface ($pK_A = 6$ and $pK_B = -2$ [58]). In this case, the normalised concentrations corresponds to SiO^- (f_1), SiO (f_2) and $SiOH_2^+$ (f_3).

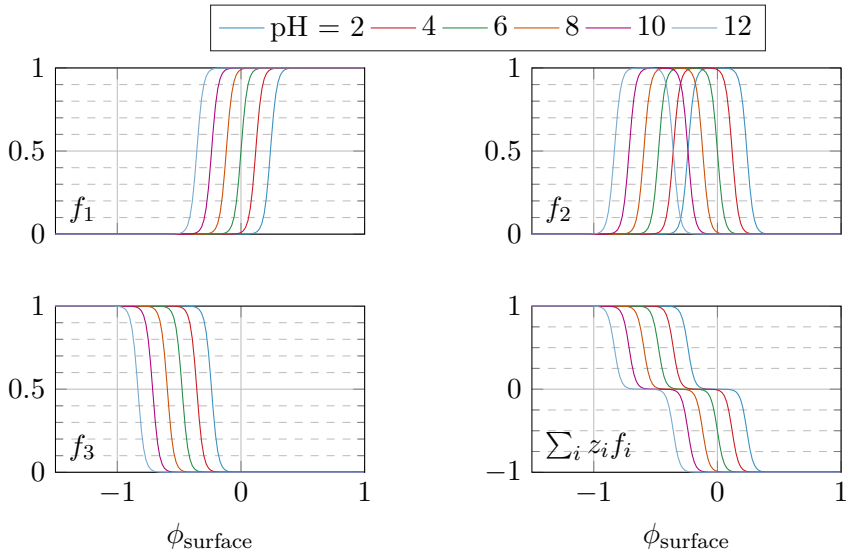

Figure 6.6: Normalised concentrations f_j for the SB applied to an SiO_2 surface ($pK_A = 6$ and $pK_B = -2$).

The profiles in Figure 6.6 show how the two elements involved in each reaction depict an opposite behaviour when ϕ_{surface} changes, e.g. f_2 increases as ϕ_{surface} becomes more negative while f_1 decreases. This can be explained as an increase of the local hydrogen ion concentration $[H^+]$ for more negative ϕ_{surface} values enables more active sites X^- to react with these H^+ ions. This is a simple scenario to illustrate the operation of this model, its application to more complex scenarios will be shown later in Chapter 8.

6.4 Biomolecule sensing layer

The modelling of the sensing layer for biomolecules involves more complexity than the adsorption of ions, as the size of the molecules could be of the order of magnitude of the device size. As noted in the introduction (Chapter 1), different modelling approaches can be found in the literature, although the most common ones are those based on rigid charged layers and charged blocks. This work is intended to extend that oversimplified description by defining three models to adapt to the large variety of features of the biomolecules: i) box-shaped model, ii) DNA specific model, and iii) fine charge distribution model. The details of each of them are presented hereunder.

6.4.1 Box-based model

This is the most basic model for molecules. As shown in Figure 6.7, in this case receptor (r) and target (t) molecules are described as charged boxes with two regions: a neutral (N) and a charged (Q) one. The size of these regions can be modified to adapt the characteristics of the molecule considered by setting their respective height h and width w. These blocks are immersed in the electrolyte region, so the ions distribution interacts with them. This later aspect is controlled by the block permeability to the ions, that is, whether ions are allowed to enter the spatial region occupied by the molecule blocks or not. The permeability is generally associated to the density of the molecule, i.e., a compact molecule would not allow ions to enter inside the volume occupied by the molecule. Three scenarios are then possible: i) fully permeable receptor-target complex, ii) permeable receptor, and iv) compact receptor-target complex. Figure 6.8 depicts an example for each of these scenarios showing how charge associated to free ions is distributed around the molecular charge.

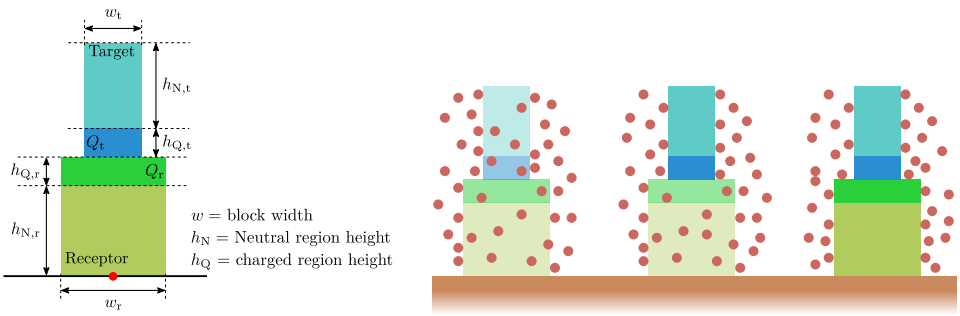

Figure 6.7: Description of molecules using the box-based model. Receptor and target molecules are modelled as boxes with a neutral and a charged region. Their sizes and charges adapt to the properties of the molecule to be considered. Right side of the figure shows a schematic of the three available models for the ion permeability of the receptor-target complex, i.e. from left to right: fully permeable receptor-target complex, permeable receptor and compact receptor-target complex.

The size and charge distribution of the molecule are included in a coarse-grained way. However, this model provides a fast and easy modelling of the molecules. Therefore, it adapts to those cases where there is a lack of information, and only net charge and approximated size, of the molecule is available, or quick coarse simulations are intended.

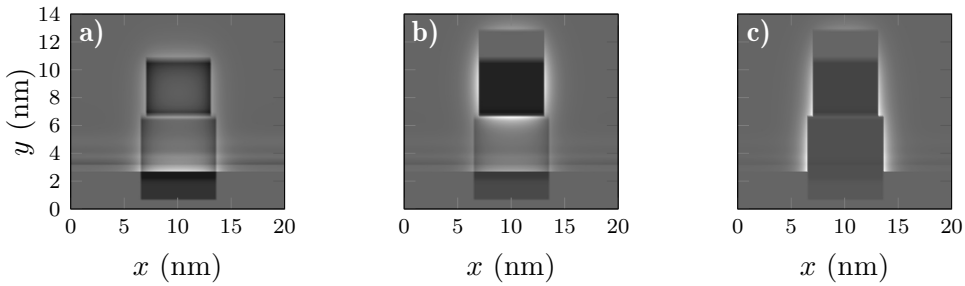

Figure 6.8: Examples of ion distribution for the box-shaped molecule model. From left to right surface plots show the three scenarios implemented:(a) fully permeable receptor-target complex, (b) permeable receptor, (c) compact receptor-target complex.

6.4.2 DNA model

This model is specifically designed for Deoxyribonucleic acid (DNA) based sensors, whose objective is to detect the presence of a certain DNA sequence in the sample. Thus, the receptor molecules are Single-Stranded DNA (ssDNA), with the complementary sequence the one to be detected. Once the ssDNA with the target sequence is attached to these receptors, a Double-Stranded DNA (dsDNA) molecule is formed. Figure 6.9 shows the model for the sensing layer of this type of sensors.

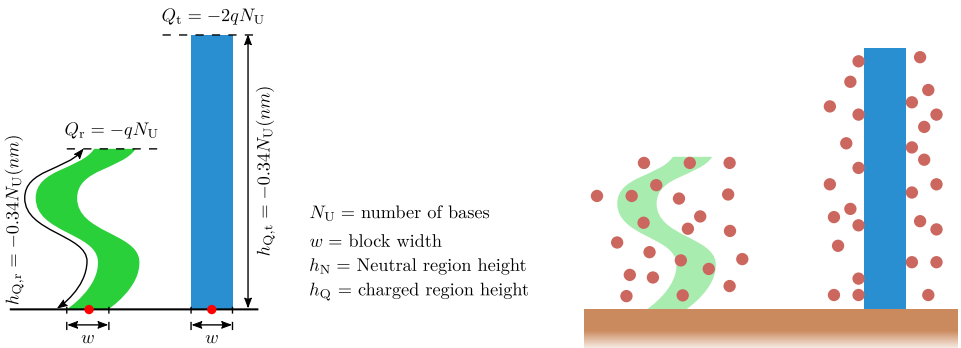

Figure 6.9: Description of the model for DNA molecules, including the most relevant geometric parameters and charges of the receptor (Q_r) and receptor-target (Q_t). In this case the receptor molecule corresponds to ssDNA while the receptor-target complex corresponds to dsDNA.

As depicted in Figure 6.9, ssDNA and dsDNA present different characteristics. ssDNA molecules are assumed to be flexible, so a box-based model is not appropriate. In contrast, we consider a sinusoid-shaped distribution representing the wrinkle shape due to its inherent flexibility [55]. This molecule is also slightly compact, so ions are allowed to enter the oc-

cupied region. On the contrary, the model for dsDNA, assumes that this molecule is more rigid and compact, so a box-shaped region where ions are not allowed to enter is implemented [55]. Figure 6.10 illustrates how ions are distributed in both scenarios in the surrounding of the region where the molecule is defined.

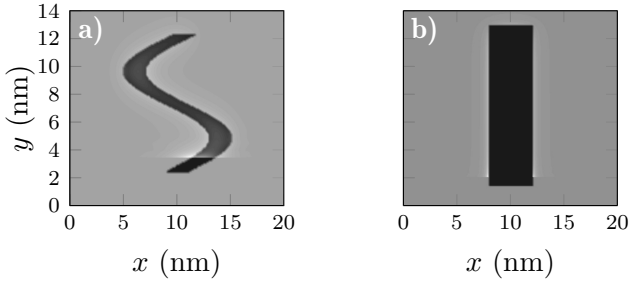

Figure 6.10: Examples of ion distribution for the DNA molecule model regarding the idle receptor (a) and receptor-target complex (b).

The charge and length of these molecules is related with the number of bases, or base pairs in the case of dsDNA, in their sequence. Each base is approximately 0.34 nm height and its charge corresponds to -1q [55]. For the dsDNA, the total length of the molecule is not modified but the charge is doubled. This model provides a more accurate description than the box-based model, but it is only focused on DNA molecules.

6.4.3 Fine charge distribution model

A more general and accurate model would be necessary to accurately treat any receptor-target pair. Thus, the model described in this section is the most accurate among the three here developed, and constitutes a noticeable step-forward in the state-of-the-art simulation of BioFETs. To do so, a 2D-profile of the molecule charge distribution is previously calculated, and then its precise shape can be considered. As depicted in Figure 6.11, this shape is encompassed inside a box whose size is defined by the dimensions of the molecule and where ions are not allowed to enter. A more illustrative example is depicted in Figure 6.12, where the ion distribution is depicted along with two different shapes for the idle receptor and the receptor-target complex scenarios.

The main objective of this model is to enable the integration of data obtained from atomic level descriptions, such as Molecular Dynamics (MD) simulations. This approach increases the accuracy of the description of the molecules at the cost of a higher computational time. The model has its origin in a fine-level profile that captures the detailed molecule charge distri-

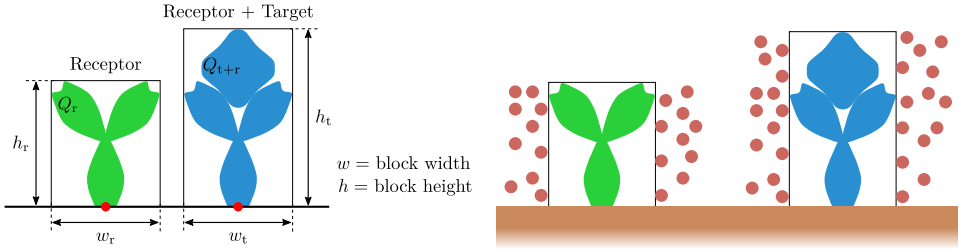

Figure 6.11: Description of the fine charge distribution model. The charge distribution imported from previous simulations of its specific atomic structure. Ions are not allowed to enter the molecule region, which is defined by a box shaped region that fits the considered distribution.

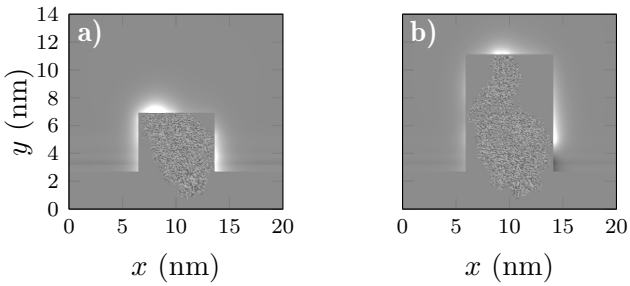

Figure 6.12: Examples of ion distribution for the fine charge distribution model for the two states of the receptor: idle (a) and activated (b).

bution (with fractions of Angstrom resolution) . This profile is framed into a square region, where ions are not allowed to enter to facilitate the convergence of the computation and implementation of the model. Therefore, the grid where the molecules are placed needs to be more dense compared with previous models to properly capture the arbitrary shape of the molecule under study. This fine mesh implies a higher computational burden and, in turn, a longer simulation time.

6.4.4 Spacial distribution of molecules

In addition to the charge distribution of molecules, the simulator implemented in this Thesis includes different options to determine their location in the sensing layer. Figure 6.13 illustrates the parameters used to achieve this purpose: the molecule width w_{M}, the distance between molecules d_k and the maximum number of molecule N_{max}. Receptor molecules are distributed following either a uniform or random distribution, making possible to evaluate the impact of this distribution on the sensor response.

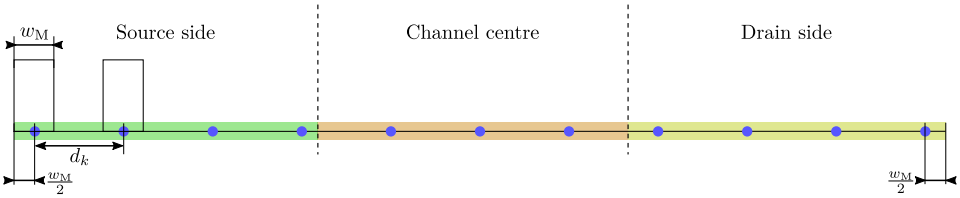

Figure 6.13: Parameters used to adress the location of molecules along the channel length. Boxes indicate the region where the molecule's charge with width w_M is distributed; d_k states for the distance between the centre of the bottom edge of these boxes. The sensing layer is split into three regions: source side (green), channel centre (orange) and drain side (yellow).

Uniform distribution

In this case, receptor molecules are distributed using a constant spacing, d_k, between them. To generate this distribution a maximum number of molecules to be placed, N_{max}, is set to define the value d_k to be used. However, if this value is lower than w_M, N_{max} is ignored and $d_k = w_M$. Hence, the total number of molecules to evaluate d_k is defined as:

$$N = \min\left(N_{Max}, \frac{L_{rec} - w_M}{w_M}\right) \tag{6.22}$$

where L_{rec} is the length of the receptor layer. Then, the position of the k-th receptor is calculated as:

$$\begin{cases} y_k &= p_0 + \left(w_M + \frac{\Delta_M}{2}\right) + k\,(w_M + \Delta_M) \quad k = 0, 1, \cdots, N-1 \\ \Delta_M &= \frac{L_{rec} - w_M}{N} - w_M \end{cases} \tag{6.23}$$

where p_0 is the first point of the receptor layer in the grid.

Random distribution

The second option to distribute the receptor molecules is to use a half-normal random distribution for the distance between one receptor and the next one. This distribution is determined by the mean value and a variance of normal distribution from which the half-normal stems. Figure 6.24 shows an example of the Probability Density Function (pdf) of the half-normal distribution with a minimum distance (mean value of the normal distribution) of $d_r = 20$ nm and $\sigma_d = 0.5 d_r$.

This half-normal pdf is used to generate an initial random value with $\mu = 0$ and $\sigma = 1$, $\mathcal{N}(0, 1)$ (where $\mathcal{N}$ stands for the normal distribution). Then, the position of each subsequent molecule is calculated based on the

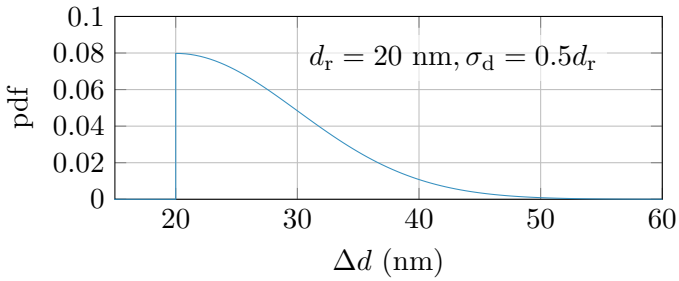

Figure 6.14: Probability density function of a half-normal distribution with a mean value of $d_r = 20$ nm and standard deviation of $\sigma_d = 0.5d_r$.

previous one using that half-normal random generator:

$$\begin{cases} d_k &= d_r + \Delta d = d_r + \sigma_d \left|\mathcal{N}(0,1)\right| \\ y_k &= y_{k-1} + d_k \end{cases} \tag{6.24}$$

The calculation of y_k from y_{k-1} requires a specific analysis for the $k = 0$ scenario that is addressed in Appendix C.

Random distribution: Position dependent standard deviation

A second random distribution has been implemented, which considers a position dependent σ value, making possible to define a high-density receptor region. A Gaussian profile is considered for $\sigma(y)$ so that a smooth transition from denser to spreader distribution regions is achieved:

$$\sigma(y) = \sigma_0 \left(1 - \beta(y)\right) = \sigma_0 \left(1 - exp\left(-\frac{1}{2}\left(\frac{y - \mu_y}{\alpha L_{rec}}\right)^2\right)\right) \tag{6.25}$$

here, the parameter μ_y controls the location of the high-receptor-density region and α tunes its size. μ_y is constrained to three predefined distributions: i) dense distribution near source, ii) dense distribution near drain and iii) dense distribution at the centre of the channel (see Figure 6.15). The position of each receptor is calculated using the same expression as in (Eq 6.24), but including the dependence on the position in σ:

$$\begin{cases} d_k = d_r + \sigma(y_{k-1}) \left|\mathcal{N}(0,1)\right| = d_r + \sigma_0 \left(1 - \beta(y_{k-1})\right) \left|\mathcal{N}(0,1)\right| \\ y_k = y_{k-1} + d_k \end{cases} \tag{6.26}$$

Like in the previous case, the calculation of y_k requires a specific analysis when $k = 0$ that is addressed in Appendix C. To test all the features of this

model, the three predefined distributions (μ_y) were evaluated. The results obtained after generating $50 \cdot 10^3$ samples are shown in Figure 6.15. Two different values of α are used (equation (Eq 6.25)): $\alpha = 0.125$ (top figures) and $\alpha = 0.375$ (bottom figures), showing that a lower value of α generate a smaller region with a high density of receptors and an abrupt transition to a more widespread distribution for these receptors.

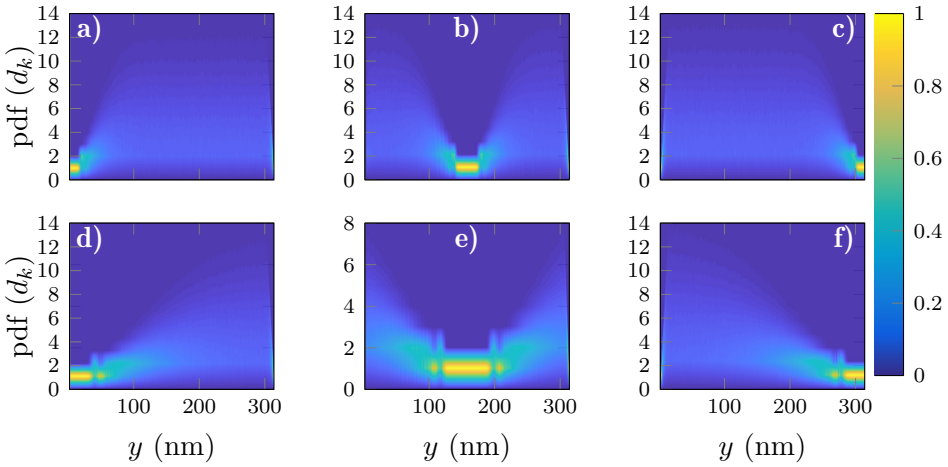

Figure 6.15: pdf of d_k along the receptor layer for two different values of α (Eq 6.25): $\alpha = 0.125$ (top figures) and $\alpha = 0.375$ (bottom figures). Columns corresponds to the three predefined locations for the dense receptor distribution: left (a, d), centre (b,e) and right (c, f).

Part IV

Results

CHAPTER 7

Simulation of 2D semiconductor based MOSFETs

7.1 Introduction

This first chapter of Part IV of the Thesis is focused on evaluating the self-consistent solver implemented to describe the electrostatics and transport in 2DMs semiconductor based MOSFETs. The following sections present the results of four different works performed with that purpose. Section 7.2 deals with the comparison between the charge-based and Fermi-level based schemes for the solution of the DD transport equation. The equivalence between both approaches is demonstrated along with the validation of the simulator with experimental data from the literature. Section 7.3, the Fermi-level based scheme is used to study Graphene Field-Effect Transistor (GFET)s, and more specifically the impact of access regions on the device performance. This scheme provides better numerical stability in comparison with the charge-based model for the simulation of these devices. In addition to that, this model enables the integration of an arbitrary DoS extracted from *ab-initio* as showed in the Section 7.4, where this feature is leveraged to analyse MOSFETs based on strained GaSe. Finally, Section 7.5 focuses on the results obtained from transient simulations. These results will be combined with experimental data to assess the impact of interface traps and their transient behaviour.

7.2 Simulation of monolayer MoS_2 double-gate MOSFETs

Concerning the transport in 2DMs based devices, as introduced in Chapter 5, two alternative formulations were considered for handling the DD description of the transport in the device, i.e., the current expressions (Eq 5.11) and (Eq 5.26). As indicated in Chapter 5, both approaches are equivalent under the Boltzmann approximation for non-degenerated semiconductors

(Section 2.6), but their numerical implementation differs considerably, as well as their capability to exchange information with lower levels of abstraction. The current expression based in (Eq 5.11) has been the most commonly used due to historical reasons related to its straightforward connection with the traditional description of the PN junction operation. Thus, it was initially adopted in the implemented solver, that was subsequently updated in order to include a description based in (Eq 5.26). This latter approach enables the connection with atomistic descriptions of the material electronic band-structure, by incorporating information extracted from *ab-initio* simulations.

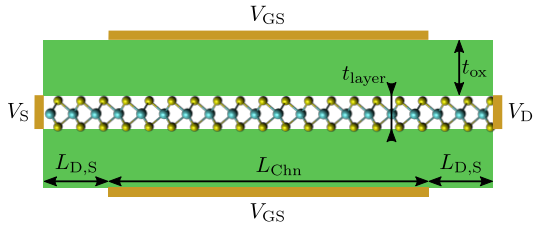

Figure 7.1: Structure of the double-gate device used to compare the two transport schemes for the monolayer MoS_2 based MOSFET device. L_{Chn} and $L_{D,S}$ stand for the channel and drain/source region lengths, while t_{layer} and t_{ox} are the channel and insulator thicknesses, respectively.

The results presented in this first section are intended to compare both approaches to the semiconductor transport and thus verify the correct behaviour of the simulator [1]. The device considered for the simulations is depicted in Figure 7.1, and it represents a monolayer MoS_2 dual gated MOSFET with a 500 nm-long channel (L_{Chn}) and two 200 nm-long highly conductive regions at source and drain sides ($L_{D,S}$). A 1 nm-thick SiO_2 insulating layer is considered for both, top and bottom gate. The source and drain are doped with donors, establishing the carrier injection into the channel to n-type.

	Valley degeneracy (g_v)	Effective mass (m^*)	$E - E_C$ (eV)
Λ (E_1)	6	0.6067	0.0881
Λ (E_2)	6	0.6067	3.4214
K	2	0.6175	0 (E_C minima)

Table 7.1: Values extracted from [87] to calculate the theoretical DoS profile.

As aforementioned, the Fermi-level based method (Eq 5.26) calculates

[1] The results obtained with the charge based simulation were published as a conference contribution in [86].

the carrier density profile using the DoS of the material. For the particular case here studied, the theoretical expression for the DoS of a 1D-confined electron gas under a parabolic dispersion relationship was combined with DFT results extracted from [87]. The data show that the K valley and the lower energy of the Λ valleys are those that contribute the most to the total charge in the semiconductor. Hence, the energies of Λ and K valleys are selected as they represent the minima of the conduction band. The parameters associated to each valley are summarised in Table 7.1, and the resulting DoS under the assumption of a parabolic dispersion relationship around the minima is depicted in Figure 7.2.

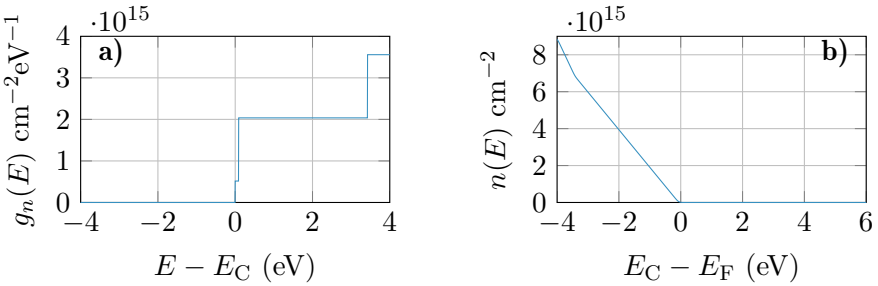

Figure 7.2: DoS (a) and corresponding carrier density profile (b) to be used in the simulations of the device depicted in Figure 7.1.

The electrical readout of the device encompasses the transfer ($I_{DS}-V_{GS}$) and output ($I_{DS}-V_{DS}$) characteristics for different bias conditions. The results obtained with the charge-based solution in (Eq 5.11) (labelled as Method 1) and the Fermi level-based method (labelled as Method 2) are depicted in Figure 7.3.

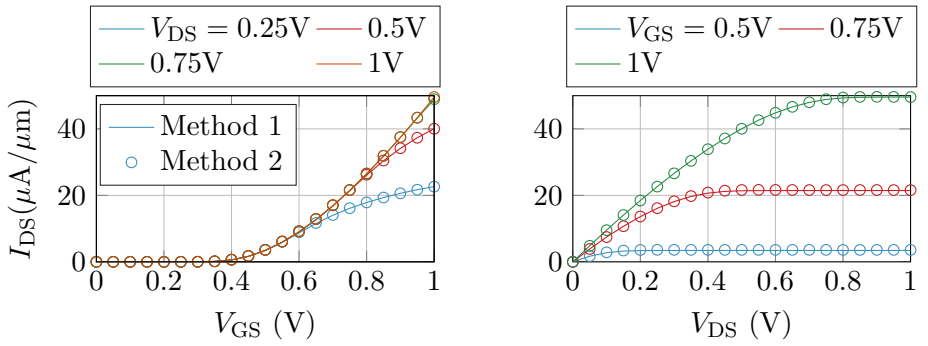

Figure 7.3: Comparison between the two transport schemes, the first one based on the charge solution (Method 1) and the second one based on the Fermi level solution (Method 2).

The good agreement observed in Figure 7.3 evidences the equivalence

of both methods for this particularly simplified DoS, based on a parabolic $E - \mathbf{k}$ relationship. Nevertheless, the differences between both models can be analysed in more detail by inspecting the 2D charge density and potential profiles, depicted in Figure 7.4 and Figure 7.5, respectively.

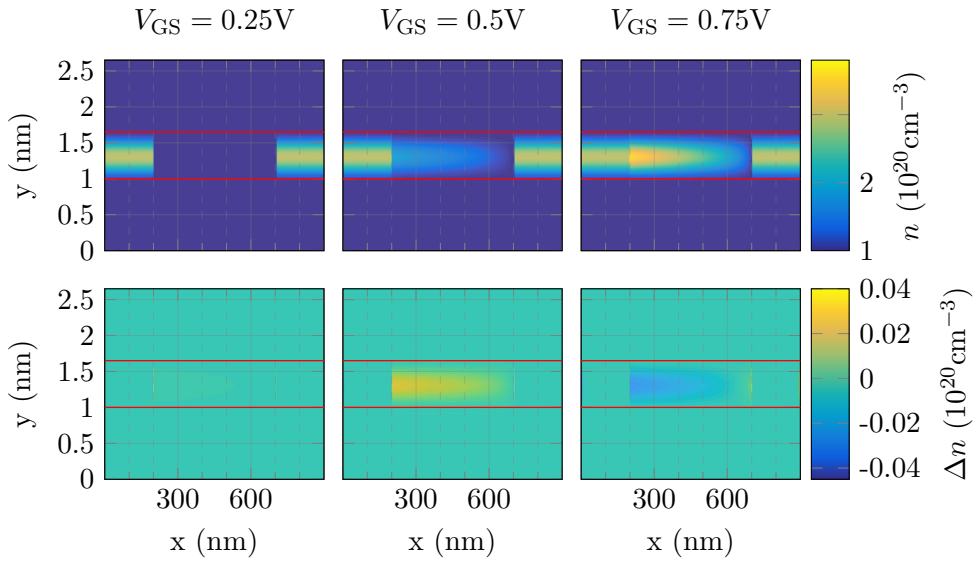

Figure 7.4: (top) 2D carrier density profile for three different gate biases: 0.25 V (left), 0.5 V (centre), and 0.75 V (right), obtained with the Fermi-level based solution. In all the cases V_{DS} is set to 0.5 V. This figure shows how the channel is generated as the gate bias increases and also the carrier depletion near the drain edge due to the reduced local electric field. Horizontal red lines indicate the edges of the semiconductor layer. (bottom) Difference in the carrier density obtained with both methods for each one of the situations depicted in the top figures.

Figure 7.4 shows three gate biases to illustrate the generation of the conductive channel between source and drain. Carriers accumulate close to the source region and their concentration progressively decreases towards the drain contact, illustrating the impact of the effective gate bias near this region, which is reduced by the applied drain voltage. Regarding the differences between both models, they are negligible for low gate biases ($V_{GS} = 0.25$ V) and tend to increase for higher gate biases. However, for those larger V_{GS} cases, the differences are still negligible when compared with the magnitude of n, as it corresponds to a small percentage. A feature to be highlighted is that, despite the high carrier density in the source and drain regions (10^{20} cm^{-3}), the magnitude of Δn in these regions is quite low and barely changes with the gate bias. For $V_{GS} = 0.5$ V, when the carrier density in the channel is lower that the charge in these regions, the

magnitude of Δn is higher in the centre of the channel. This behaviour can be explained by the high doping considered in these regions that stabilises the carrier density and potential independently of the biases considered in the simulations.

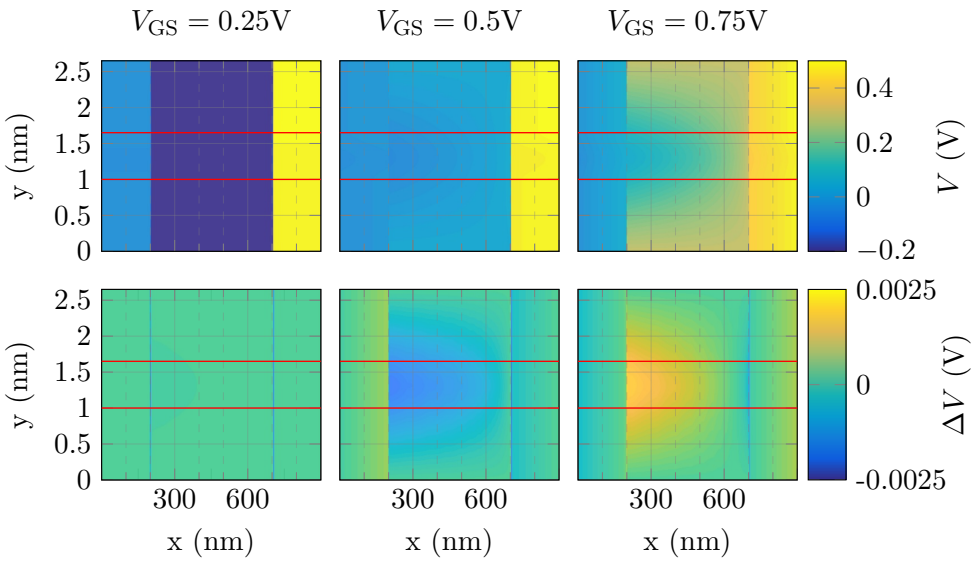

Figure 7.5: (top) 2D potential profile of the structure for three gate biases (0.25 V (left), 0.5 V (centre), and 0.75 V (right)) and $V_{DS} = 0.5$ V for the Fermi-level based solution. These profiles depicts how the potential changes in the middle of the channel due to the high accumulation of electrons. (bottom) differences in the potential profile obtained with the two methods for each of the profiles depicted in the top figures.

The 2D carrier density profiles depicted in Figure 7.4 are in agreement with the 2D potential distributions shown in Figure 7.5. Source and drain regions maintain a constant potential value in the three profiles, while it changes in a large extent in the channel region as the charge accumulates. Concerning ΔV, the difference between the electrostatic potential calculated with the two approaches, most of the comments on Figure 7.4 can be extended to the data represented in Figure 7.5 and it can be concluded that the differences between the values of V calculated with both models are minimal.

These 2D profiles are analysed along with $(E_C - E_F)$ (Figure 7.6) to check where the non-degenerated semiconductor condition $(E_C - E_F > 3k_BT)$ is verified. As depicted in Figure 7.6, the scenarios for which Δn and ΔV change to a larger extend match those where the Fermi-level surpasses the conduction band minima. In that case, the non-degenerated semiconductor condition is not verified, but Figure 7.5 and Figure 7.4 show that the

differences between the models are not remarkable.

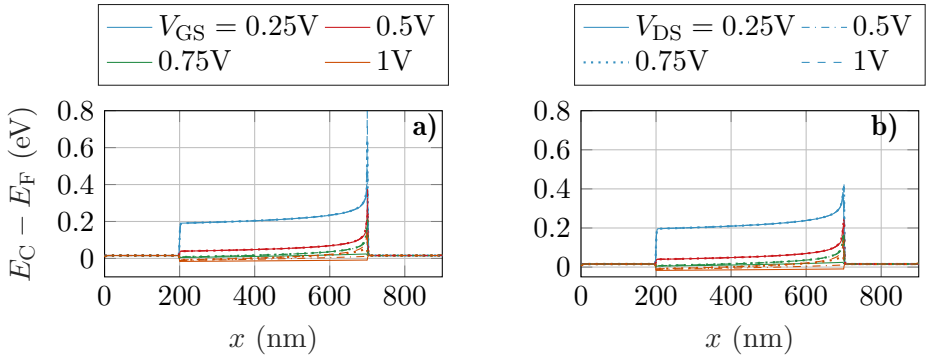

Figure 7.6: Distance between the conduction band and the Fermi level obtained with (a) the Fermi-level based method and (b) the charge based method. These profiles where obtained for different gate bias (line color) and different drain bias (line style).

7.2.1 Validation of the scheme for MOSFET simulation

The previous section evidenced the equivalence between both approaches for transport calculation (under the assumption of a simplified band-structure for the case of the Fermi-level based solution). However, a thorough assessment of the simulator requires its validation against real devices, i.e. the demonstration of the capability of the simulator to properly reproduce experimental results. To that end, here it is considered the work reported by D. Krasnozhon *et al.* [88], where a MOSFET based on monolayer MoS_2 with 30 nm-thick top gate oxide (HfO_2) and a 270 nm-thick substrate (SiO_2) is reported. The total length of the device is $L_{ch} = 340$ nm, with a 240 nm-long channel plus two access regions 50 nm-long each. The measured contact resistance and electron mobility are 2 k$\Omega\cdot\,\mu$m and 85 cm^2/Vs, respectively.

Aiming to emulate the effect of the contact resistances (R_c) in the numerical simulations, two doped regions were included at both edges of the semiconductor layer, and their doping was modified to fit $R_c = R_s = R_d$ to the reported experimental value of 2 k$\Omega\cdot\mu$m. Interface traps are a relevant magnitude in experimental MoS_2 devices, as it is discussed in [89, 90], and they were consequently introduced (as explained in Section 5.6) in these simulations. Two constant energetic profile at both insulator-MoS_2 interfaces provided the best agreement with the measurements [91]. In particular, we considered: *i*) at the top gate insulator interface, a constant profile of acceptor traps with $D_{it} = 10^{12}$ cm^{-2} eV^{-1} from mid-gap up to 0.57 eV towards the conduction band edge, and *ii*) at the substrate interface, a constant profile also of acceptor traps from midgap to the conduction band edge (i.e. 0.9 eV above midgap) with $D_{it} = 2.5\times10^{11}$ cm^{-2} eV^{-1}. The channel was undoped

with electron mobility $\mu = 85$ cm^2/Vs, saturation velocity $v_{\text{sat}} = 2.8 \cdot 10^6$ cm/s, electron effective mass $m^* = 0.61 m_0$ and bandgap width of $E_g = 1.8$ eV. The comparison between experimental data and simulation results is depicted in Figure 7.7, showing that the implemented device simulator is able to provide an excellent agreement along a large range of gate voltages.

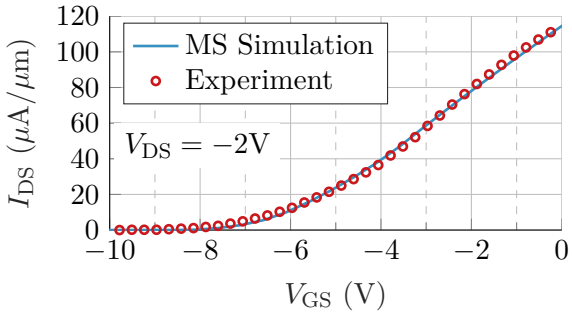

Figure 7.7: Experimental transfer characteristics of a MoS_2 FET reported in [88] (symbols) and results provided by our numerical solver (solid line).

Now we proceed to the validation of the developed simulator to study GFETs. In this case, as already indicated in Section 5.4.2, the charge transport in Graphene is handled according to the Fermi-level scheme but, for this unique material, using a common E_{F} for both, electrons and holes. The main reason for this choice is that the charge-based DD solution depicted significant numerical instabilities, hence this implementation was left aside. In particular, the GFET reported in [92] and [93] are fitted. Both publications address GFETs based on monolayer Graphene embedded between a SiO_2 layer, which acts as a substrate, and a Y_2O_3 layer, which acts as a front gate dielectric. In both cases, this Y_2O_3 layer is 5 nm thick while the substrate is 300 nm thick in [92], and 286 nm thick in [93]. For the device presented in [92], the distance between the source and drain contacts is 1.5 μm and the front gate length is 600 nm, whilst in [93] the device is 8.2μm long and its front gate is 7μm long. In other words, in both experimental devices the gate contact does not cover the whole region between source and drain contacts, thus creating two symmetrical under-lapped regions at both channel edges, the so-called device access regions. To reproduce the data reported in [92], the same mobility is assumed for both types of carriers ($\mu = \mu_{\text{n}} = \mu_{\text{p}}$) with a value of 90 cm^2/Vs, along with a puddle charge density of $N_{\text{p}} = 7 \cdot 10^{11}$cm^{-2} and an n-type intrinsic doping of 10^{12}cm^{-2}. In order to account for the Graphene-metal contact resistances, which are in series with the total resistance of the structure (R_{T}), we include two additional 100 nm-long regions with an intrinsic n-type doping ($5{\cdot}10^{10}$cm^{-2}) in both source and drain ends [94]. The back gate is grounded and V_{DS}

is set to 0.1 V. On the other hand, in order to fit the measurements reported in [93], the values used are μ =1091 cm^2/Vs (again, the same value is considered for electrons and holes), $N_\mathrm{p} = 8 \cdot 10^{11}\mathrm{cm}^{-2}$ and the Graphene layer intrinsic doping is set to $10^{11}\mathrm{cm}^{-2}$ (n-type). The back gate is also grounded and V_DS is set to 0.05 V. Making use of these parameters, both devices were simulated, the achieved transfer characteristics are shown together with the experimental ones in Figures 7.8a [92] and 7.8b [93]. The numerical $I - V$ characteristics accurately reproduce the laboratory measurements in the whole range of biases and are able to catch the transfer response of the electron and hole branches, specially in Figure 7.8b.

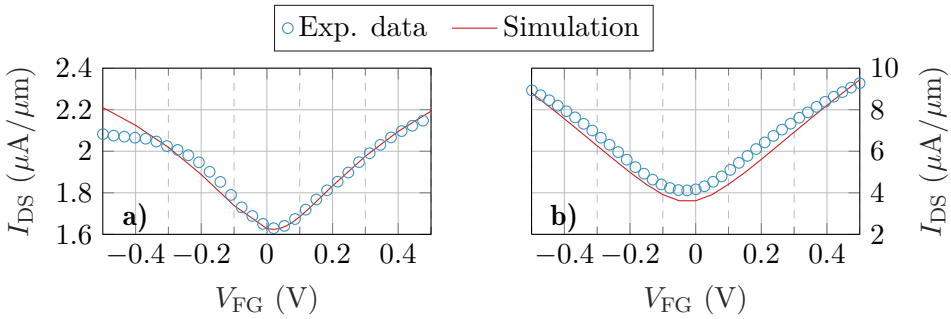

Figure 7.8: Comparison between the numerical simulation (solid line) and the experimental data (symbols) extracted from [92] (a) and [93] (b).

7.3 Role of access regions in the electrical characteristics of GFETs

The first investigation exploiting the implemented solver for GFETs is focused on the role of the access regions in the design and performance of GFETs [95]. In particular, we analyse in detail how the GFET transfer response is severely impacted by these regions, showing that they play a significant role in the asymmetric saturated behaviour commonly observed in these devices. We also investigate how the modulation of the access region conductivity (i.e. by the influence of a back gate) and the presence of imperfections in the Graphene layer (e.g., charge puddles) modify the transfer response.

Numerous experimental data depict the V-shaped transfer response expected for these devices according to the theory. However, they commonly show an asymmetry with respect to the Dirac voltage [96] that is usually explained considering different electron and hole mobility values, leaving out

of the spot the relevance of the gate underlapped areas [97, 98, 99]. The access regions (that might help to minimize the capacitance coupling between the gate and the source and drain contacts) impact strongly on the GFET electrical behaviour, as they constitute a noticeable resistance pathway for carrier transport. Partial attempts on the modelling of this issue have been discussed from an analytical resistance-based perspective in [98, 100], but a comprehensive study of their impact on the GFET performance is still lacking [101].

To achieve this goal, the basic structure shown in Figure 7.9 has been devised to carry out the required simulations. The Graphene flake is sandwiched in between a top insulator layer, with thickness t_{TOX} and dielectric permittivity $\varepsilon_{\mathrm{TOX}}$, and an insulating substrate, with thickness t_{BOX} and dielectric permittivity $\varepsilon_{\mathrm{BOX}}$. Both oxides are assumed thick enough to neglect any tunnelling current through them. A four-terminal device is considered, with a front gate extending over a length L_{Chn} (the device channel length), giving rise to two under-lapped regions of length L_{Acc} (the access region length) that connect the channel with the source and drain terminals. In those cases where back gate is considered, it extends all along the structure including the channel as well as the access regions. V_{FG}, V_{BG}, and V_{D} stand for the front gate, back gate, and drain terminal biases respectively, while the source terminal, V_{S}, is assumed to be grounded.

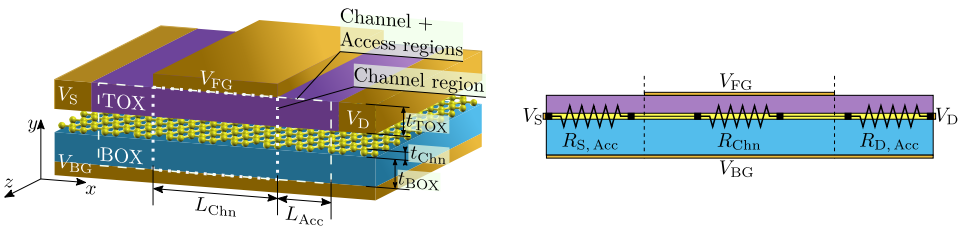

Figure 7.9: Schematic of the simulated GFET and the macroscopic characteristic resistances of the device. The dashed and dotted rectangles indicate the regions identified in the simulations: while the dotted rectangle only encompasses the channel region, the dashed one includes the access regions.

As indicated in Figure 7.9, the total resistance of the device (R_{T}) is controlled by the series combination of three resistances, corresponding to the source access region ($R_{\mathrm{S,Acc}}$), the channel region (R_{Chn}) and the drain access region ($R_{\mathrm{D,Acc}}$). First simulations are performed using the structure without access regions (i.e. the square defined by dotted lines in Figure 7.9) as a reference, and the structure with access regions (defined by dashed lines in Figure 7.9). The material stack comprises a monolayer Graphene sandwiched between a t_{TOX} =3 nm thick HfO_2 layer (front gate insulator) and a t_{BOX} =27 nm thick SiO_2 layer (back gate insulator). The front gate,

which determines L_{Chn}, is 100 nm long and both access regions are L_{Acc} =35 nm long. Electron and hole mobilities are assumed identical (μ = 1500 cm^2/Vs) and no chemical doping or puddle charge density is considered in the Graphene layer.

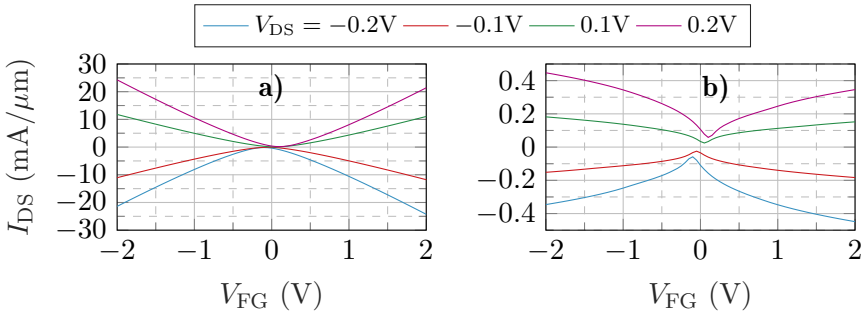

Figure 7.10: $I_{\text{DS}} - V_{\text{FG}}$ curves of the device without (a) and with (b) access regions.

The transfer characteristics of the device without access regions are depicted in Figure 7.10a for different values of V_{DS}. As can be observed, the device exhibits the ambipolar V-shaped $I - V$ response of an ideal GFET. The minimum of the $I - V$ curve defines the Dirac voltage (V_{Dirac}), which is slightly shifted to larger $V_{\text{FG}}(\approx V_{\text{DS}}/2)$ as V_{DS} increases. The behaviour is perfectly symmetric with respect to V_{Dirac}, reflecting the symmetry between electron and hole properties. When the access regions are included (Figure 7.10b), a marked variation of the GFET response is observed. First, there is a notable decrease in the values of I_{DS}, around a factor $\times 1/50$. Second, the transfer characteristic shows a saturation trend for high $|V_{\text{FG}}|$ which resembles much better the experimental response. Third, and more important, the $I - V$ characteristic is no longer symmetric with respect to V_{Dirac}, though the mobility is identical for both types of carriers.

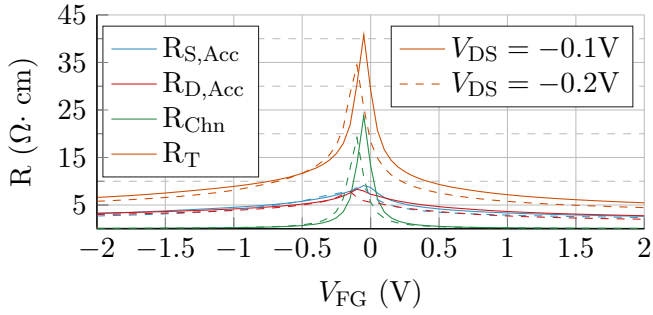

Figure 7.11: Resistance of the three device regions (channel, source and drain access regions) compared with the total resistance as a function of the front gate potential, for two V_{DS} values: -0.1 V (solid) and -0.2 V (dashed).

In order to provide insights into this behaviour, the resistances $R_{S,Acc}$, R_{Chn} and $R_{D,Acc}$ were individually calculated. Figure 7.11 shows their values for $V_{DS} = -0.1$ V (solid line) and $V_{DS} = -0.2$ V (dashed lines). The same behaviour is observed for positive V_{DS} values,which provide the same profiles mirrored with respect $V_{GS} = 0$ V. At the Dirac voltage, where the channel resistivity is the highest, R_{Chn} commands the series association, but still the access regions provide a non-negligible contribution. For $|V_{FG} - V_{Dirac}| > 0.2$ V the total resistance is mainly determined by $R_{S,Acc}$ and $R_{D,Acc}$. Consequently, the total resistance (R_T) is not controlled solely by the channel conductivity and, therefore, by the gate terminal. The weak dependence of $R_{S,Acc}$ and $R_{D,Acc}$ on V_{FG} is reflected in the I_{DS} trend to saturation highlighted in Figure 7.10b. As the values of $R_{S,Acc}$ and $R_{D,Acc}$ are higher than the channel resistance, a larger fraction of V_{DS} drops in the access regions reducing the effective potential at the channel edges with respect to the no-access-regions scenario, and consequently limiting the output current. In addition, the $R_{Acc} - V_{FG}$ dependence is not symmetric, so neither are the access region potential drops, resulting into a non-symmetric decrease of the output current, that is, an asymmetric $I_{DS} - V_{FG}$ curve as shown in Figure 7.10b. This lack of equivalence between the source and drain access regions is explored in detail hereunder.

In the previous simulations, we assumed that the gate is perfectly aligned in the middle of the channel leading to identical source and drain access regions ($L_S = L_D = L_{Acc}$) at both ends. A more realistic scenario should consider the impact of having non-equal L_S and L_D, enabling to test the non-equivalent role of $R_{S,Acc}$ and $R_{D,Acc}$ on the GFET response. To this purpose, structures where the top gate contact is not placed at the centre of the structure are analysed, resulting in access regions of different length. In particular, L_S (or L_D) is set equal to 35 nm, as in the previous simulations, whilst L_D (or L_S) is extended or shortened. Specifically, we considered four scenarios: (i) short source, (ii) short drain, (iii) long source and (iv) long drain. The length of the short and long access regions scenarios is 17.5 nm and 70 nm, respectively. The $I_{DS} - V_{FG}$ curves, along with the resistances $R_{S,Acc}$, $R_{D,Acc}$ and R_{Chn} obtained in each case, are depicted in Figure 7.12.

As expected, there are significant differences between devices. Shortening either the source or the drain access regions results in a higher output current (Figure 7.12a) and reduces both its saturation and its asymmetry with respect to the elongated scenario (Figure 7.10b). When comparing the shorter regions (Figure 7.12a) it is clearly observable that the L_S=17.5 nm device (solid lines) has a more symmetric response than the L_D=17.5 nm (dashed lines). This is more evident for V_{DS}=0.2 V and emphasizes the role of the source access region with respect to the drain access region. The higher impact of L_S is also observed in the data for the elongated devices

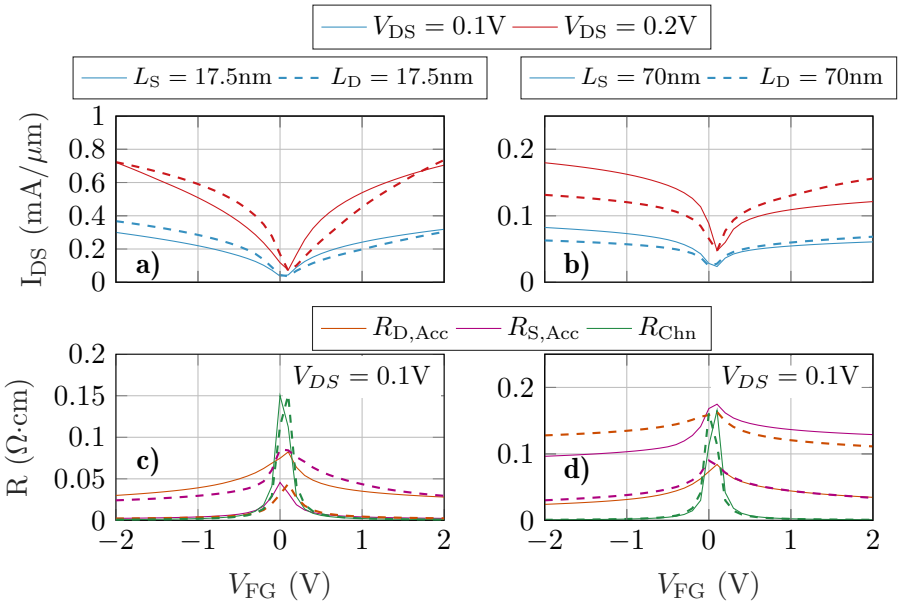

Figure 7.12: Transfer response (top) and structure resistances (bottom) as a function of the gate bias, i) reducing the length (left) of either the source (solid lines) or drain access region (dashed lines) down to 17.5 nm, and ii) increasing the length (right) of either the source (solid lines) or the drain access region (dashed lines) up to 70 nm.

(Figure 7.12b). The longer L_S results in an increased asymmetry between both branches. These results can be explained by analysing the resistances of the structure. Figure 7.12c and Figure 7.12d show $R_{S,Acc}$, $R_{D,Acc}$ and R_{Chn} as a function of V_{FG} for V_{DS}=0.1 V. When any access region is shortened (Figure 7.12c), its resistance is similar or lower to the channel resistance regardless V_{FG}. The resistance of the longer region controls the total current (except for V_{FG} close to zero). When one of the regions is elongated this effect is emphasized. The transfer responses in Figure 7.12b are clearly saturated due to the dominant role in the total conductivity of the longer access region.

The final part of this study analyses how the back gate and puddles modify the $I - V$ response of the GFET. The use of a back gate makes possible to modulate the access regions conductivity by means of an electrostatic doping, while the presence of puddles is a non-ideal effect typically present in Graphene. Figure 7.13a-c shows the transfer characteristic for three different values of V_{BG}: -1 V, 0 V and 1 V, assuming symmetric access regions with $L_S = L_D = 35$ nm . For $V_{BG} = 0$ V the results are quite similar to the scenario without a back gate. In the other two cases, depending on the polarity of V_{BG}, electrons or holes are accumulated in the Graphene layer. As a result, the p-type (n-type) branch is enhanced for

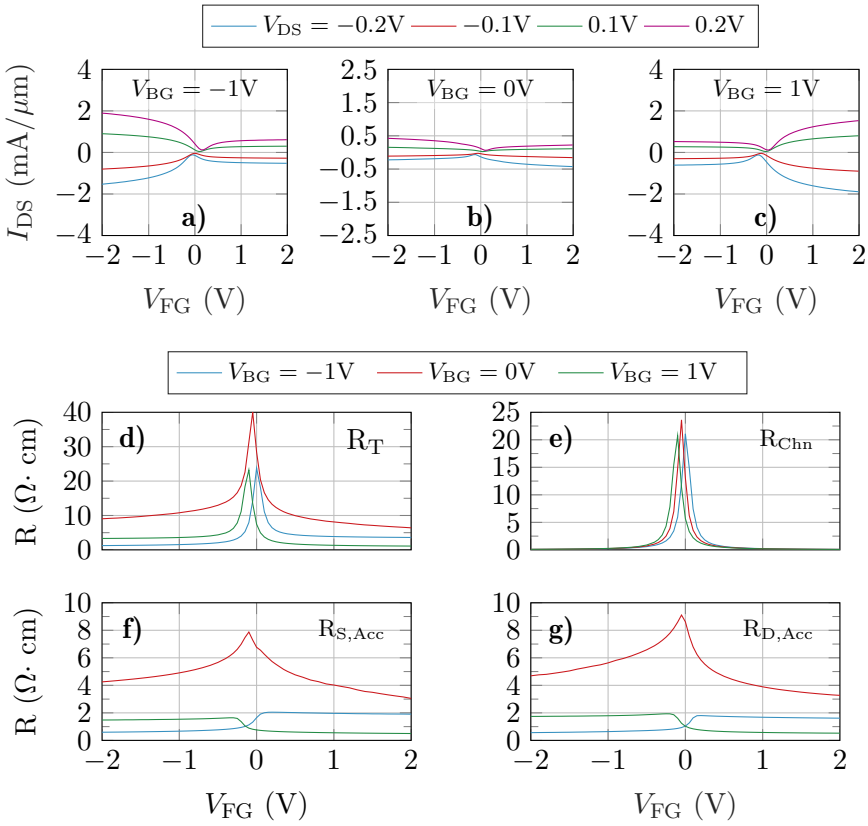

Figure 7.13: Top figures show the $I_{DS} - V_{FG}$ characteristics of the complete structure when three different back gate potentials are used (−1 V (a), 0 V (b) and 1 V (c)). Bottom figures show the total (d), channel (e), source (f) and drain (g) resistances for different back gate biases and $V_{DS} = -0.1$ V.

$V_{BG} = -1$ V ($V_{BG} = 1$ V), regardless the value of V_{DS}. As in the previous scenario, the origin of this behaviour can be traced back to the resistance associated to the access regions.

Figure 7.13d-g depicts the device resistances for different V_{BG} values and $V_{DS} = -0.1$ V. For $|V_{BG}| = 1$ V, the total resistance near the Dirac voltage is dominated by R_{Chn}. When V_{FG} is increased above V_{Dirac}, the symmetry of R_{Chn} is kept since it is mostly controlled by the front gate, while the asymmetry of $R_{S,Acc}$ and $R_{D,Acc}$ is exacerbated due to the electrostatic doping, giving rise to the large asymmetry observed in the transfer response in Figure 7.13a and Figure 7.13b. In particular, the asymmetric step-like dependence of the access resistances on V_{FG} for $V_{BG} \neq 0$ V is the result of the electrostatic competition between the front and back gates to control the access regions closer to the channel. When V_{FG} and V_{BG} have the same polarity, they add their electric forces to increase the carrier den-

sity in the aforementioned zones, increasing the conductivity and therefore lowering the whole access resistance. However, if V_{FG} is opposite to V_{BG}, both gates compete to accumulate different types of charges, resulting in a depleted region close to the channel edges that decreases the conductivity and increases the overall access region resistances. An equivalent conclusion was achieved in [102], where a strong modulation of the total resistance by two additional gates is observed, as in Figure 7.13.

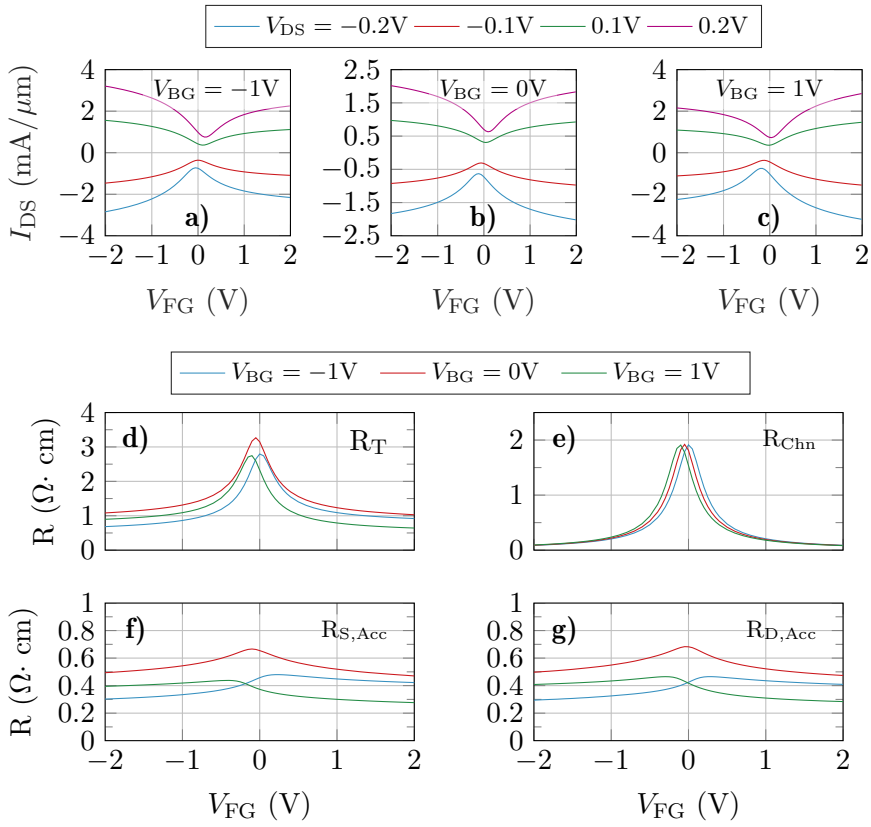

Figure 7.14: Top figures show the $I_{DS} - V_{FG}$ characteristics of the complete structure with puddles ($N_p = 10^{12}$ cm^{-2}) when three different back gate potentials are used (-1 V (a), 0 V (b) and 1 V (c)). Bottom figures show the total (d), channel (e), source (f) and drain (g) resistances for different back gate biases and $V_{DS} = -0.1$ V.

An additional aspect that cannot be overlooked is the effect of puddles in the Graphene layer [103, 104]. To shed light on this issue, Figure 7.14a-c include the $I_{DS} - V_{FG}$ response when a puddle charge density of $N_p = 10^{12}$ cm^{-2} is considered. Two major changes were observed after including the puddles: (i) the total current is increased compared with the structure without puddles, and (ii) the asymmetry is clearly reduced. These changes derive from the equal contribution of puddles to the conductivity of

both electrons and holes, and explain why the $I-V$ curves of some experimental devices are reasonably symmetric close to the Dirac voltage, where the conductivity of puddles is dominant. In this situation, the conductivity of the whole Graphene layer is increased for electrons and holes, in contrast with the electrostatic doping generated by the back gate. This non-selective improvement of the conductivity is translated into the resistances of the device: Figure 7.14d-g includes the $R-V_{\mathrm{FG}}$ relation for $N_{\mathrm{p}}=10^{12}$ cm^{-2}. The step-like behaviour of $R_{\mathrm{S,Acc}}$ and $R_{\mathrm{D,Acc}}$ is clearly softened when the puddles are included, resembling the $V_{\mathrm{BG}}=0$ V case. Therefore, according to the results for $V_{\mathrm{BG}}=0$ V, puddles are able to improve the overall conductivity of the channel, but reducing the capability of the back gate to modulate that conductivity. In Appendix D, the impact of access regions on the RF performance of GFETs, which was discussed in [95], is explained in detail.

7.4 Simulation of MOSFETs with arbitrary DoS

As discussed in (Section 7.2), the solution of the DD expressions using the Fermi-level based approach is equivalent to the most commonly used charge-based solution as far as an analytical simplified dispersion relationship is considered. The advantage of the Fermi-level solution, however, lays on its capability to integrate information about arbitrary material DoS profiles, such as the spatial dependencies of the electronic band-structure.

This unique capability is exemplified here simulating GaSe-based MOSFETs with strained channels combining semi-classical device-level simulations with material atomistic calculations [105]. This sort of multi-scale approach has been widely exploited from the quantum transport perspective, where DFT, maximally localized Wannier functions, and non-equilibrium Green functions are combined to study the limit of operation of 2D FETs as well as novel device concepts based on 2D materials [106, 107, 108, 109]. However, the combination of semi-classical transport with an atomic-level description of the material properties remains mostly unexplored [75].

In order to evidence the capabilities of this approach we have focused our attention on the evaluation of mechanical strain in 2DMs-based devices [110, 111]. Strain engineering has already been widely employed in conventional silicon technology to boost carrier transport properties with a remarkable industrial success [112]. In fact, due to the inherent mechanical flexibility of 2D materials, it is expected to become a key technology enabling on-demand modulation of the optical, mechanical or electrical properties. As an example, it has been demonstrated that the application of controlled strain originates both, a noticeable enhancement of the photoresponsivity of single-layer MoS_2 photodetectors [113], and the modulation of the Schottky barrier

height of metal-TMDs contacts modifying the device transport properties [114].

In this study Tight-Binding (TB) calculations characterizing the material band-structure are combined with the electrostatic-transport simulation scheme described in the previous chapters. More specifically, the electronic structure is described through a TB position-dependent DoS, which is later used for the evaluation of the free charge in the device-level simulations (Section 5.4.2). We focus on a particular subset of the 2DMs family: Metal Monochalcogenides (MM)s, and specifically on Gallium Selenide (GaSe) [115], where the possibility of synthesizing monolayer wrinkled structures has opened the path to inhomogeneous strain yielding to spatially varying band-structures at the nanoscale [116, 117, 118].

The TB model is able to capture particular features arising from the conformal changes in the crystal structure produced by localized strain in monolayer GaSe and the corresponding position dependent DoS. This implementation allows us to accurately include the effect of tensile or compressive strain with arbitrary patterns, such as those produced by substrate patterning or bubbling [116, 119], in the device level simulations so to achieve an accurate evaluation of the longitudinal carrier profiles in the framework of a DD transport description. This work was carried out in collaboration with the group of Prof. Juan José Palacios (UAM).

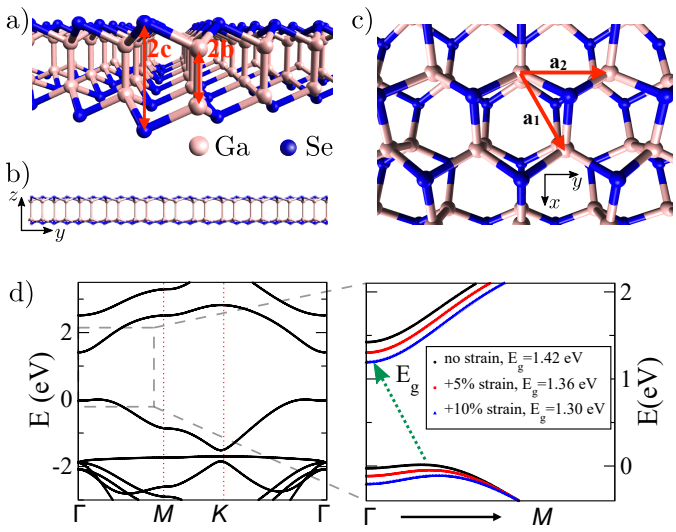

Figure 7.15: (a, b) Illustration of crystal structure and zoom of the unit cell vectors, (c) along with an example of a tensile strained structure. (d) Band-structure calculated for the relaxed GaSe monolayer using TB calculations and a detail of the change in E_g with several values of tensile strain in the ZZ direction.

In particular, for the TB calculations the unit cell of GaSe is composed

by two Se and two Ga atoms disposed in the outer and inner cell, respectively (as depicted in Figure 7.15). Their coordinates are Ga(0,0,$-b$), Ga(0,0,b), Se$\left(\frac{a}{2}, \frac{a\sqrt{3}}{2}, -c\right)$, and Se$\left(\frac{a}{2}, \frac{a\sqrt{3}}{2}, c\right)$, where $a = 2.25$ Å, $b = 1.27$ Å, and $c = 2.10$ Å. To form a layer, the unit cell is repeated following the cell vectors $\overrightarrow{a_1} = \frac{3a}{2}\left(1, \frac{1}{\sqrt{3}}, 0\right)$ and $\overrightarrow{a_2} = \left(0, a\sqrt{3}, 0\right)$.

To model this system we employ a nearest-neighbour TB Hamiltonian with four orbitals per atom (s, p_x, p_y and p_z). The Hamiltonian is given by

$$H = \sum_{i,j} t_{ij} c_i^\dagger c_j + c.c., \tag{7.1}$$

where t_{ij} is the nearest-neighbour hopping parameter and $c_i^\dagger$ (c_j) the destruction (creation) operator. We have used the Camara *et. al.* TB parametrization [120], that was implemented for a 3D GaSe system, fitting the bands for a monolayer (2D system) by correcting the unit cell reducing the distance between Se atoms. This approach accounts for the fact that outer atoms do not interact with others atoms of adjacent layers, and therefore their distance is decreased. We have considered tensile and compressive strain in the zigzag (ZZ) direction, i.e. along $\overrightarrow{a_2}$ Figure 7.15, having a 10% maximum strain with a soft cosine profile. To achieve a proper description of this situation supercells composed by 160 unit cells in the ZZ direction have been employed. This supercell is a box with four nearest-neighbour connection, with the following Hamiltonian:

$$H(k_{||}, k_\perp) = H_{00} + H_{01}^{||} e^{i\overrightarrow{k_{||}}\overrightarrow{a_{||}}} + H_{10}^{||} e^{-i\overrightarrow{k_{||}}\overrightarrow{a_{||}}} + H_{01}^{\perp} e^{i\overrightarrow{k_\perp}\overrightarrow{a_\perp}} + H_{10}^{\perp} e^{-i\overrightarrow{k_\perp}\overrightarrow{a_\perp}} \tag{7.2}$$

where H_{00} is the supercell Hamiltonian, and H_{01} and H_{10} are the nearest-neighbour forward and backward hopping Hamiltonian, respectively. The box directions are indicated by parallel $||$ and perpendicular $\perp$ symbols, and $\overrightarrow{k}$ and $\overrightarrow{a}$ represent the wavevector and real space vector for the box, respectively.

To calculate the DoS in systems with a big number of unit cells we have employed in one direction the Surface Green functions Matching Method [121, 122] where the local DoS g_l is calculated as:

$$g_l(E, k_\perp) = -\frac{1}{\pi} \mathrm{Im}\left[\mathrm{Tr}(G_l(E, k_\perp))\right] \tag{7.3}$$

where G_l is the Green function of the cell l, and E the energy. The system is considered homogeneous in the direction perpendicular to the strained ZZ; therefore, $k_\perp$ is a good quantum number. In that case, we can use the usual k-point summation technique to evaluate the total DoS per unit cell:

$$g_l(E) = \frac{1}{N_{k_\perp}} \sum_{k_\perp=1}^{N_{k_\perp}} w_{k_\perp} g_l(E, k_\perp) \tag{7.4}$$

where $w_\perp$ is the relative weight of each $k_\perp$. We have chosen $N_{k_\perp} = 130$ as the number of $k_\perp$, and a constant weight for each $k_\perp$, $w_\perp = 1$, in order to get a good approximation to the actual DoS. The final DoS profile depicts a spatial dependence in correspondence to the longitudinal position of the unit cells, y_l, and it is split into electron and hole DoS profiles as:

$$g_l(E) \begin{cases} g_l(E > E_g/2) = g_n(E, y_l) \\ g_l(E < E_g/2) = g_p(E, y_l) \end{cases} \tag{7.5}$$

that are linearly interpolated in the 2D (E, y) space so to define the profiles $g_n(E, y)$ and $g_p(E, y)$, in the device simulations.

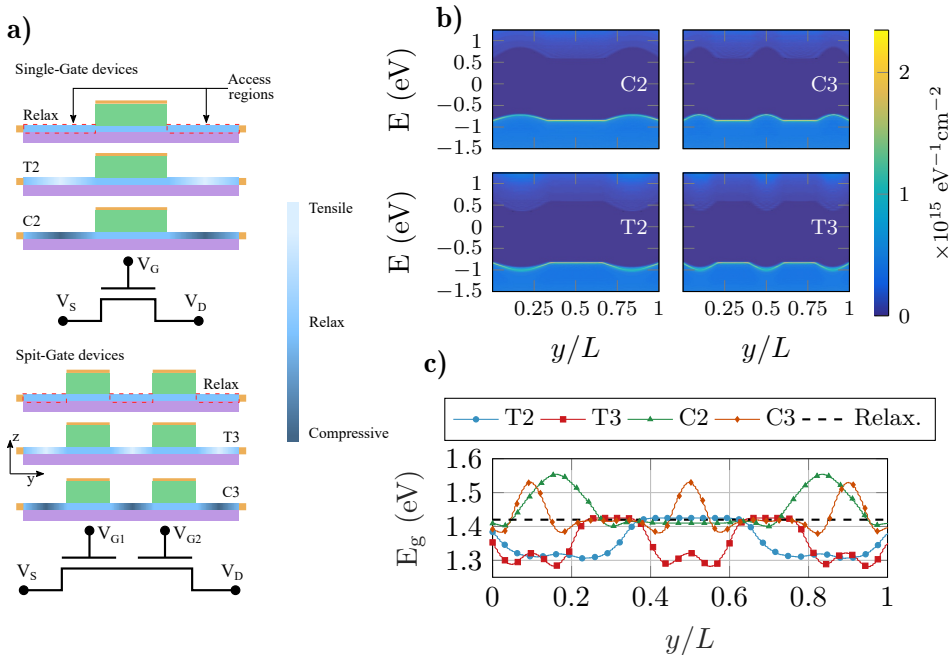

Figure 7.16: (a) Structures considered in the simulation of the SG (top) and SPG (bottom) scenarios. Strain, tensile (T) or compressive (C), is applied to the access regions, i.e. regions not covered by the gates. (b) DoS profiles of the structures considered and (c) their respective longitudinal E_g profiles.

To illustrate the capabilities of the this approach, we have considered the 2D-FET configurations shown in Figure 7.16a. In these devices the channel regions are relaxed (i.e. without strain), while the strain (tensile or compressive) is applied in those areas not covered by the gate, i.e. the access regions. In particular, four devices are evaluated, corresponding to two geometries, Single-Gate (SG) and Split-Gate (SPG) FETs, with both, n-type and p-type conductivity channels. Gate lengths are set to cover the relaxed semiconductor regions and so that, L_g =20.27 nm (52 unit cells) for the SG devices, and L_g =11.69 nm (30 unit cells) for the SPG devices. In addition, devices with completely relaxed channel are used as a reference. In this way, concurrently to the demonstration of the proposed platform, we assess the role of the strain to enhance the conductivity of the access regions, and thus as potential alternative to other approaches based on: locally gated devices [99, 123]; self-aligned gate contacts [124, 125]; locally charged insulators [126]; phase changes [127, 128]; or chemical doping [129, 130].

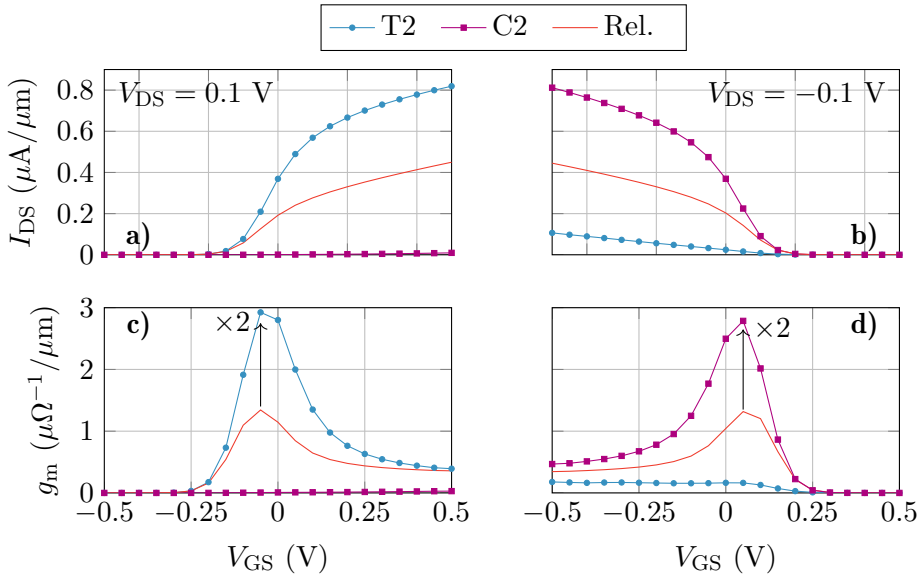

Figure 7.17: Transfer characteristics (top) and transconductance (bottom) of the SG structures. In all the cases we consider both n-type (a,c) and p-type (b,d) transistors to evaluate how strain impacts on the conduction of each type of carrier.

As previously stated, the GaSe monolayer is $160|\overrightarrow{a_2}|$-long corresponding to 62.3 nm in the relaxed devices. This length slightly changes according to the type of strain and the number of strained regions considered. In all cases the total length of channel and access regions is extended by two 5 nm-long regions with a high conductivity that emulate the source and drain contacts and determine the polarity of the device. Despite the importance

of contacts in the context of 2DMs-based FETs [90, 114, 131, 132, 133], here we try to focus exclusively on the impact of the applied strain on the device performance, avoiding other effects that could overshadow it. Finally, a 10 nm-thick HfO_2 layer covers the GaSe channels acting as gate insulator.

The DoS profiles corresponding to the different GaSe strained crystals are depicted in Figure 7.16b along with the local variations in the energy gap (E_g), Figure 7.16c. The relaxed material shows $E_g = 1.42$ eV. The compressive/tensile strain tends to increase/decrease this band gap, in good agreement with similar trends reported in the literature [116, 118, 134]. In particular, the strain-engineered control of the bandgap in GaSe nanosheets has been experimentally demonstrated in [119], with substantial decrease/increase in the energy gap (measured by exciton energy extraction) upon the application of uniaxial tensile/compressive strain.

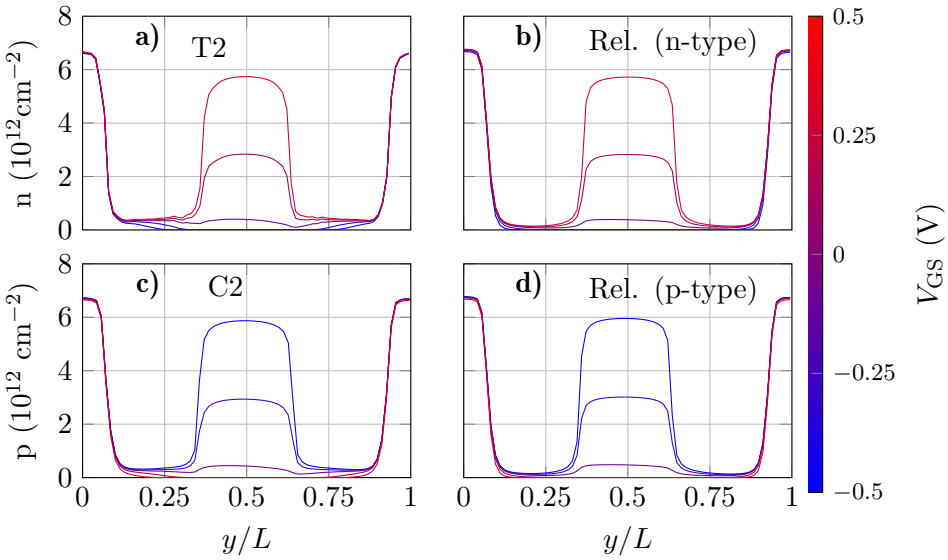

Figure 7.18: Longitudinal carrier density profiles of the n-type devices with tensile strain (a) and relaxed channels (b), and the p-type devices with compressive strain (c) and relaxed channels (d).

When these DoS profiles are introduced in the mesoscopic device self-consistent simulations, the transfer characteristics of the SG FETs depicted in Figure 7.17 for both n-type and p-type conduction are obtained for the SG device. A noticeable impact on the conduction of electrons and holes is observed: tensile strain (T2) enhances the electron conduction and degrades the hole current, while compressive strain (C2) results on the opposite behaviour. It is therefore evident that the application of strain on the access regions produces an effect similar to the chemical doping, promoting the

conduction of one specific type of carrier. This induced-doping strain relation has been evidenced for other 2DMs, such as black-phosphorus (BP) [135], where strain-modulated bandgap significantly alters the density of thermally activated carriers, impacting the conductance of BP-based FETs; or in single-layer MoS_2 [136], where experimental evidence of the direct relation between strain and doping has been shown by Raman mapping and electrical measurements.

When compared with the relaxed case, this local doping results in a relevant increase in the output current (Figure 7.17a and Figure 7.17b) and transconductance (Figure 7.17c and Figure 7.17d) by a twofold factor, when the appropriate strain is employed. These changes can be associated to an increase in the carrier density in the access regions due to the strain, which are depicted in Figure 7.18. These profiles show an almost equal main carrier density at the centre of the structure, independently of the strain applied. The most noticeable differences are observed in the access region: while the relaxed channel depicts a reduction of the carrier density in the access regions, this effect is less acute when strain is introduced in the structure.

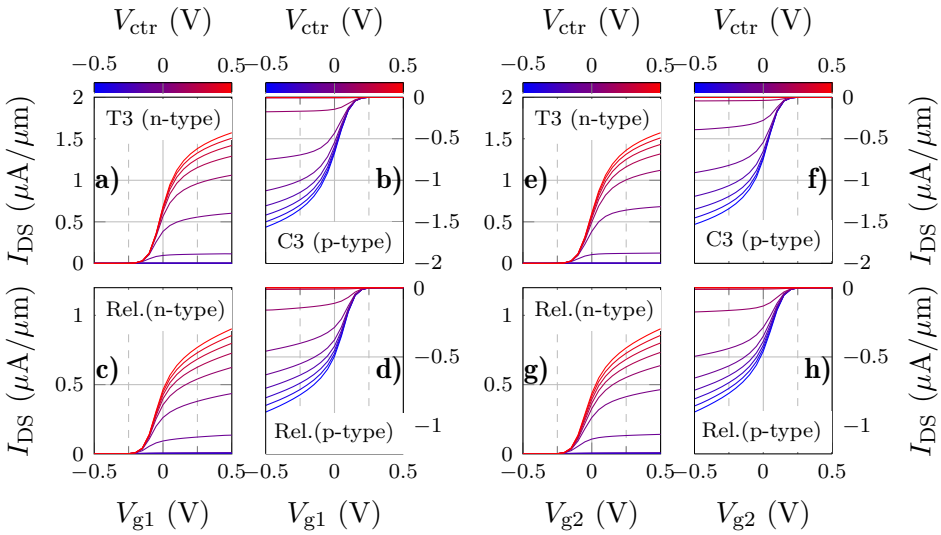

Figure 7.19: Left plots show the transfer response of the n-type devices (a,c) and p-type devices (b,d) for the SPG-1 configuration ($V_G = V_{g1}$, $V_{ctr} = V_{g2}$) and for the SPG-2 configuration ($V_G = V_{g2}$, $V_{ctr} = V_{g1}$), also for the n-type (e, g) and p-type (f,h) devices. $V_{DS} = 0.1$ V for all the scenarios. Strained devices correspond to the top panels and the relaxed ones to the bottom ones.

Next, we extend this analysis to the Split-Gate (SPG) devices shown in Figure 7.16a, taking advantage of the versatility of the proposed platform. This type of structures are appealing for non-linear applications, such as

mixers [137], or to implement different functionalities, such as logic gates, with a reduced number of transistors [138]. For the sake of relevance, we limit the investigation to tensile n-type and compressive p-type conduction. To analyse the SPG device operation, we set one gate performing a whole sweeping cycle V_G while the other acts as a control input V_{ctr}. Figure 7.19a-d shows the transfer responses for the SPG-1 configuration (i.e., ($V_G = V_{g1}$, $V_{ctr} = V_{g2}$)) while Figure 7.19e-h shows the data for the SPG-2 configuration (i.e., $V_G = V_{g2}$, $V_{ctr} = V_{g1}$). In all the cases, V_{DS} is set to 0.1 V.

A saturated $I - V$ trend is observed in all the situations. It should be highlighted, however, that this behaviour is originated not only by the strained access regions, but also by the channel under the control of the gate with a fixed conductivity. This is confirmed by the carrier density profiles depicted in Figure 7.20, where large fluctuations in the carrier density in that channel are observed when either V_{g1} or V_{g2} are swept and V_{ctr} is kept fixed. This aspect indeed enables the operation of the SPG device as a potential two-input logic gate, an study that deserves a future work.

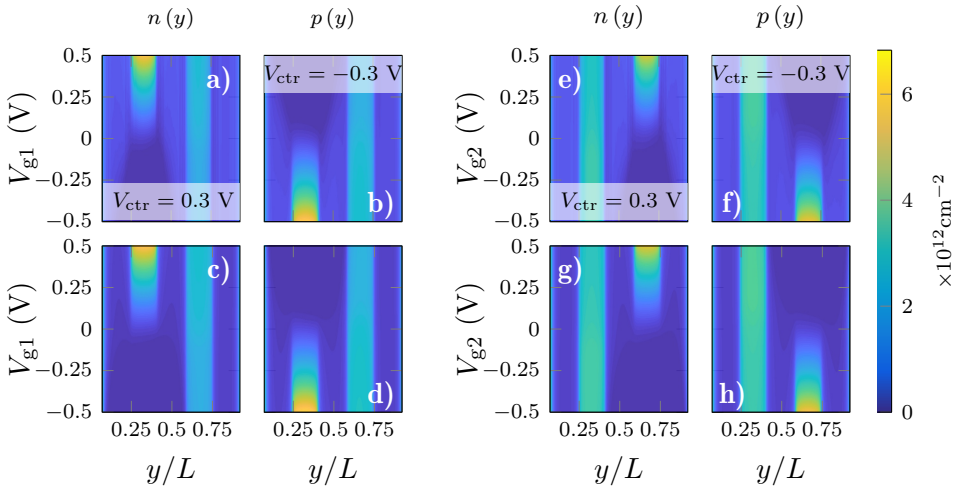

Figure 7.20: Longitudinal carrier density profiles as a function of the gate bias ($V_G = V_{g1}$ or V_{g2}) for the n-type (a,c,e,g) and p-type (b,d,f,h) devices. For the left panel $V_{ctr} = V_{g2} = \pm 0.3$ V and for the right panel $V_{ctr} = V_{g1} = \pm 0.3$ V. Strained devices correspond to the top row and the relaxed ones to the bottom one.

Figure 7.21 extends the SPG-FET analysis to the I_{on}/I_{off} ratio as a function of the control gate bias, V_{ctr}. A low-power specification has been considered for the definition of the OFF current, that is $I_{Off} = 10^{-4}$ μA/μm and $V_{On} = V_{Off} \pm 0.3$ V, according to [139]. Figure 7.21 evidenced that the ON-OFF ratio is clearly enhanced for the structures with strained access regions and it can be modulated by the control gate, the larger the conduc-

tivity of this region the better the resulting ON-OFF ratio in both p-type and n-type operation.

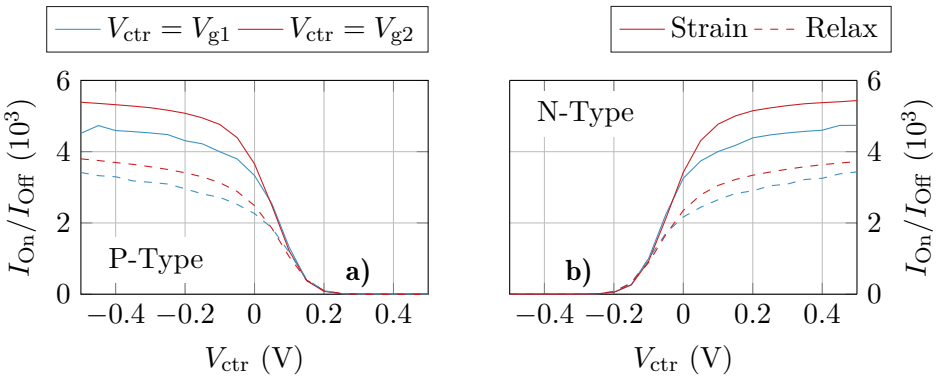

Figure 7.21: ON-OFF ratio of the SPG devices as a function of the control bias. The calculation of these values follows the Low-Power compliance: $I_{Off} = 10^{-4}$ μA/μm, $V_{On} = V_{Off} \pm 0.3$ V according to [139].

Notable differences in the ON-OFF ratio are observed when the control gate is interchanged (red *vs.* blue lines). Although the device structure is symmetric, the influence of each one of the two gates differ when a non-zero source-to-drain bias is applied. This is evidenced in Figure 7.22, where the hole longitudinal density profiles of the structure with compressive strain (p-type) are plotted for the SPG-1 (solid lines) and SPG-2 (dashed lines) configurations with $V_{ctr} = 0.4$ V and $V_G = -0.35$ V (i.e., one of the channels is OFF and the other is ON), in equilibrium (blue lines) and for $V_{DS} = -0.1$ V (red lines). In equilibrium (solid and dashed blue) both gates are symmetric, but when $V_{DS} = -0.1$ V is applied (solid and dashed red lines) the hole density under each gate differs to a relevant factor, depending on the device configuration. When the second channel is switched ON (SPG-2), its maximum charge density is lower compared with the charge accumulated at the first channel when it is ON (SPG-1). This difference is due to the effect of the drain bias, as it reduces the effective gate bias applied on the second channel. As a result, we observe the differences in the ON/OFF ratio shown in Figure 7.21.

These results show that this approach is suitable to capture the influence of the strain on the device electrical performance. In addition to this, it is observed that a properly engineered local strain could help to mitigate the negative impact of access regions and to control the polarity of the device, mimicking the effect of chemically doped 2D crystals coherently with the first experimental evidences demonstrating this strain-induced doping relation in 2DMs [119, 135, 136].

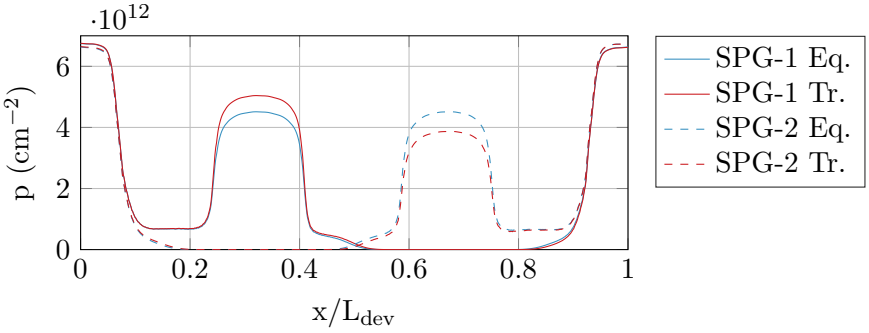

Figure 7.22: Longitudinal hole density profiles for the SPG-1 (solid) and SPG-2 (dashed) configurations with $V_{\mathrm{ctr}} = 0.4$ V and $V_{\mathrm{G}} = -0.35$ V. Blue lines correspond to the data obtained in the equilibrium scenario ($V_{\mathrm{DS}} = 0$ V) while red lines correspond to the $V_{\mathrm{DS}} = -0.1$ V scenario.

7.5 Hysteresis in MoS_2 MOSFET devices

This final section is dedicated to evaluate the time-dependent implementation of the DD equation previously discussed in Section 5.5. To this purpose we consider, as a case of study, the investigation of the hysteresis effect in the time-dependent response of MoS_2 FETs. This work has been the result of a collaboration with RWTH and AMO GmbH, during a three months research stay that took place in 2019, under the supervision of Prof. Max Lemme.

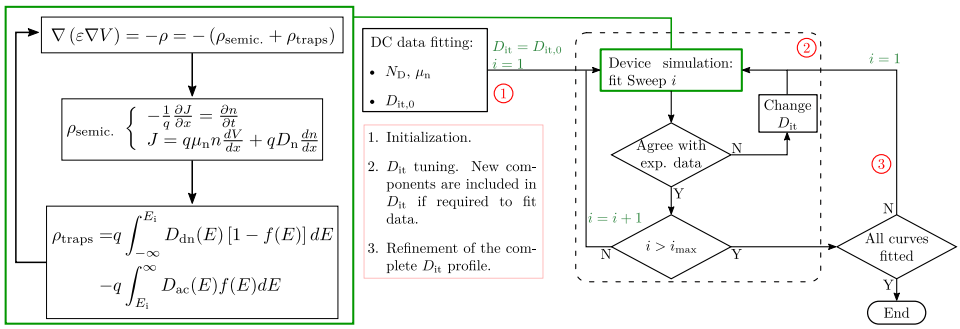

Figure 7.23: Flowchart used to extract the energetic D_{it} profile combining experimental data with numerical simulations. First, basic parameters like doping, carrier mobility and a first guess of D_{it} are estimated from DC curves. Then, the measurements with different sweep conditions are fitted by tuning D_{it}.

MoS_2 FETs are under an intense research spotlight, due to the potential that this material has exhibited for different applications. In spite of relentless experimental progress, device performance is still seriously impacted by the presence of defects and traps that results in hysteresis in their electrical

measurements. This feature is typically associated with charge trapping/detrapping processes, although their precise origin and understanding is still under debate [140]. Such behaviour cannot be reproduced by electrostatic simulations as it requires to take into account the history of the state of the device. In that concern, the simulations of MOSFET devices in a transient regime is the suitable tool to handle this type of studies. The time-dependent implementation of the simulator has been exploited to investigate the MoS_2 FETs hysteresis and its association with interface charge traps. To that end, simulations were combined with experimental data that depict the hysteresis aforementioned, aiming to extract the energetic profiles of the interface traps of the measured device from the device simulations [141].In this case, the experimental measurements correspond to a set of gate bias sweeps with the same minimum value and increasing the maximum applied bias. This is intended to progressively fill interface traps and extract the information from differences between the consecutive curves.

The flowchart of the method represented in Figure 7.23 starts with a fitting of the largest forward sweep with electrostatic simulations to extract basic parameters related with the material, that is, the intrinsic doping, carrier mobility and an initial energetic profile for charge traps, D_0. Next, transient simulations are used to fit the data and tune the initial energy profile for interface traps. First, the shortest sweep is fitted tuning the low energy components of the interface traps DoS, D_{it}. Then, the same procedure is followed with the data for subsequent sweeps applying higher voltages. The initial D_{it} for each sweep is the one previously obtained, which is then corrected by adding higher energy components. Once the data for all the sweeps are fitted, the process is repeated for a fine tuning of D_{it}. For all this process, D_{it} is assumed as a combination of Gaussian functions, as they provide smooth and easy to manage profiles.

For the experimental realization, 5 μm-long few-layer MoS_2 FETs with multiple channels, and a 35 nm thick Al_2O_3 bottom-gate dielectric were fabricated as described in [142]. An optical micrograph of the final device is shown in Figure 7.24. Raman measurements show the clear signature of MoS_2 in the channel (Figure 7.24).

Although the device is defined by multiple channels in a parallel configuration, for the simulation only one of these channels is considered. Thus, the results will be scaled later by the number of active channels when comparing simulations and the experimental data. The structure simulated is the one shown in Figure 7.25 and is defined by a 2.6 nm-thick ($\approx$4 layers) and 5 μm-long MoS_2 channel deposited above a 35 nm-thick Al_2O_3 substrate. The MoS_2 is left uncovered and consequently an insulating region with $\varepsilon_{\mathrm{r}} = 1$ is considered on top of it. Charge traps are located at the interface between the semiconductor and the substrate. As aforementioned, the MoS_2 FETs

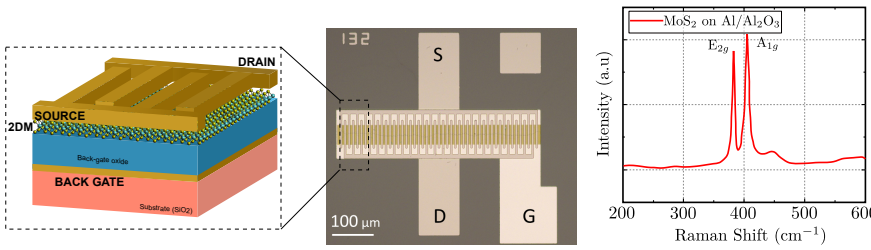

Figure 7.24: Optical micrograph of the device fabricated and Raman measurements of the MoS_2 layer [141].

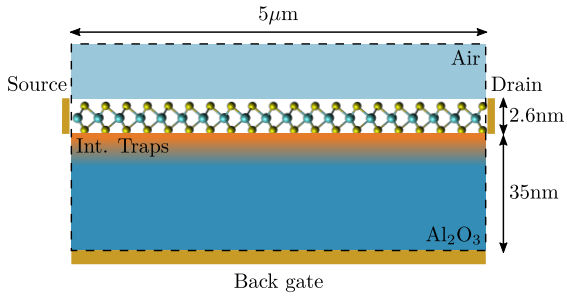

Figure 7.25: Structure considered for the simulations corresponding to a single channel of the multichannel structure depicted in Figure 7.24, with a 2.6 nm-thick MoS_2 ($\approx$4 layers) on top of the Al_2O_3 substrate. Simulations also include a region above the channel with $\varepsilon_r = 1$ and charge traps (orange) on the interface between the channel and the substrate.

were characterized through a set of forward-backward gate voltage sweeps. As shown in Figure 7.26, the minimum V_{GS} value was kept unaltered while the maximum value was progressively increased in each sweep. This procedure intends to set the same initial state of interface traps for every sweep, and progressively increase the amount of traps occupied as the bias for each new sweep is increased.

Figure 7.26 shows that as the range of the sweeps is increased a shift is observed for the backward branches of the curves, while the forward branch is quite similar for all of them. This fact indicates that the state of the device at the beginning of each backward sweep is modified. This change in the device state is also observed in g_m that depicts a more steep profile for the backward sweeps. Once the simulations and the tuning of the D_{it} profile is completed we obtain the experimental data fitting depicted in Figure 7.27. The extracted D_{it} profiles provides a good agreement between simulations and experimental data.

All the components defined for D_{it} are Gaussian functions whose parameters are summarised in Table 7.2. In this table, for each D_{it} contribution, μ corresponds to the mean energetic location, σ to the width (defined as en-

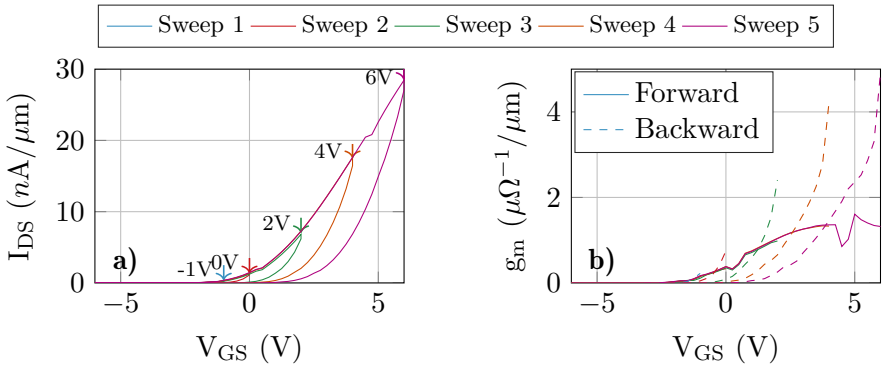

Figure 7.26: (a) $I_{DS} - V_{GS}$ and (b) $g_m - V_{GS}$ from the measurements for the MOSFET device.

ergetic variance of the pulse), D_{max} to the height, and τ the time constants for the charging τ_c and discharging τ_d events. Altogether, these components depict a profile similar to the one observed in [89, 91]. The only remarkable difference is the large component for very high energies, D_6 in Figure 7.27. That one, however, was extracted using only the data for the larger sweep and additional measurements would help to clarify if that component behaves as expected from simulations. However, this elaborated process does not seem straightforward as the results for the longer sweep ($V_{GS} = [-6, 6]$ V) shows a slight decrease in the transconductance (Figure 7.26b) for the forward sweep indicating a slight saturation of the $I_{DS} - V_{GS}$ curve. The origin of this saturation may be associated to the effect of parasitic resistances (e.g. contact resistances) that are able to mask the effect of charge traps in a extended gate bias sweep.

	μ (eV)	σ	D_{max} (cm^{-2} eV^{-1})	(τ_c, τ_d) (s)
D_1	0.5063	0.1415	$23.55 \cdot 10^{12}$	$(0.15, 0.1)$
D_2	0.475	0.0475	$1 \cdot 10^{12}$	$(0.08, 0.1)$
D_3	0.76	0.1501	$6.24 \cdot 10^{12}$	$(5, 8)$
D_4	0.7837	0.095	$1.3 \cdot 10^{12}$	$(0.15, 1 \cdot 10^{-3})$
D_5	0.8835	0.1093	$0.6 \cdot 10^{12}$	$(0.2, 1 \cdot 10^{-3})$
D_6	0.9357	0.0114	$23 \cdot 10^{12}$	$(5.5, 1 \cdot 10^{-3})$

Table 7.2: Parameters used to define each component of the energetic profile of charge traps D_{it}. All of them are described by a gaussian profile, so μ corresponds to their energetic location, σ to their width and D_{max} to their height. (τ_c, τ_d) stand for the time constants that determine their temporal behaviour.

The D_{it} profiles depicted in Figure 7.27 show that there are three components with a noticeable magnitude. At first sight, these components can

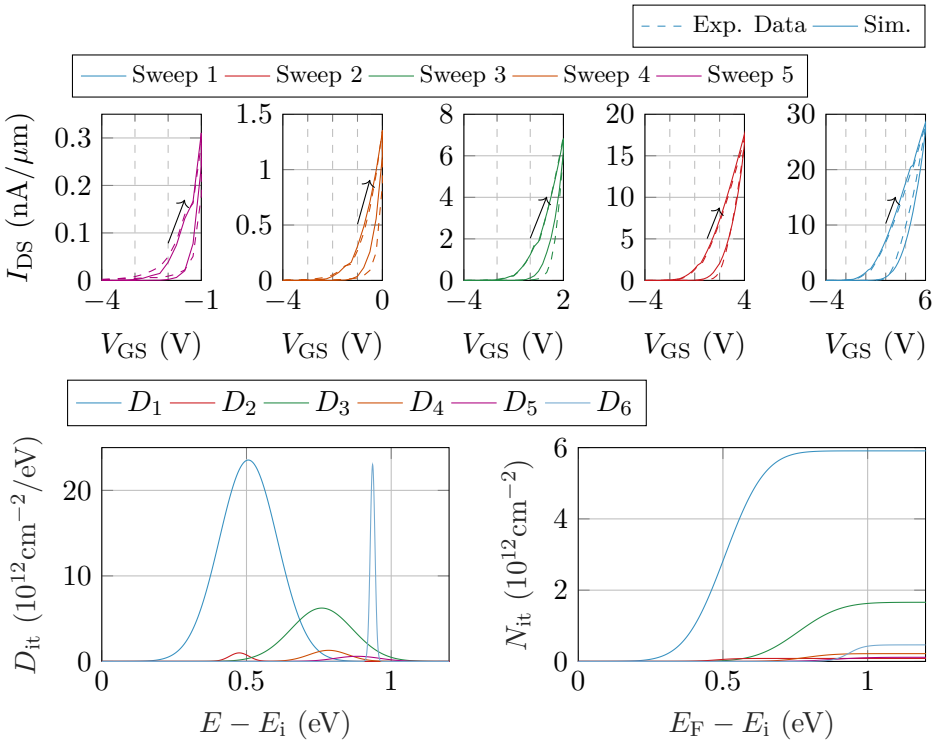

Figure 7.27: (top) Data fitting for each of the sweeps performed using the final D_{it} profile. (bottom) D_{it} components extracted for the DoS of the interface traps through the fitting process and their respective $N_{it} - E_F$ profiles.

be understood as those with the higher impact on the transfer response of the device, while others only provide fine adjustments to the experimental data. To evaluate this analysis, Figure 7.28, shows the $I - V$ characteristics of the MoS_2 FET with the complete D_{it} and with a simplified D_{it} (i.e. considering only the three components with a higher magnitude).

The curves plotted in Figure 7.28 reveal that although hysteresis is also observed in the simplified case, I_{DS} is much higher when using the simplified D_{it}. Thus, the impact of the components with a lower magnitude cannot be neglected to achieve a proper fit. This conclusion is also supported by the $N_{it} - V_{GS}$ and $E_{F,n} - V_{GS}$ profiles extracted from the fitting process and depicted in Figure 7.29.

The curves in Figure 7.29 show that $E_{F,n}$ depicts a clear hysteresis cycle even for low gate biases. This behaviour, however, cannot be extended to N_{it} as the hysteresis in this magnitude is observed only for medium/large V_{GS} values. This result reveals the high impact of interface traps, as an almost negligible difference between the forward and backward data in N_{it} comes along with a noticeable change in $E_{F,n}$.

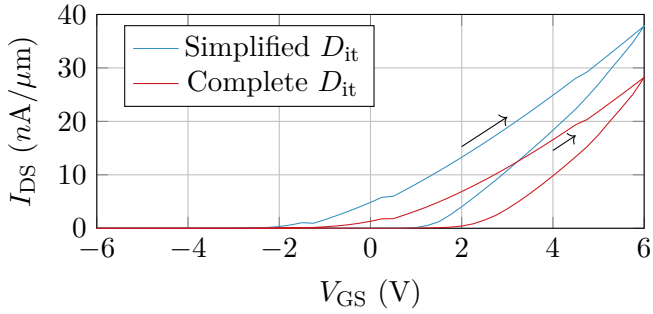

Figure 7.28: Comparison between the characteristics obtained with the complete D_{it} and the simplified D_{it}.

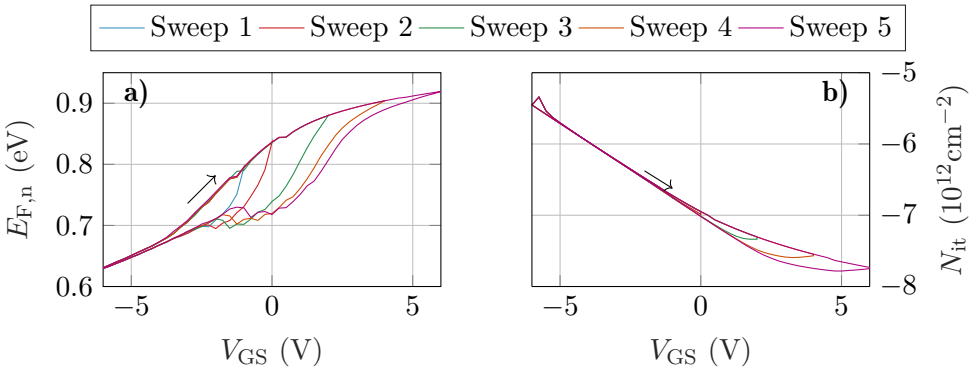

Figure 7.29: (a) Profile of the Fermi level in the centre of the structure and (b) charge density associated to interface traps as a function of the gate bias.

This difference can also be traced back to the time constants (τ_c, τ_d) associated to each D_{it} component. Despite the higher magnitude of D_3 and D_6, their time constants are also larger, so their impact is lowered. To illustrate the impact in the device behaviour of these time constants, the values obtained from the fitting process have been modified. In order to simplify this analysis, we consider the same time constants for all the components of the charge traps. Under this assumption, three scenarios were considered: i) ideal traps that react instantaneously to changes in the bias conditions of the device, $(\tau_c, \tau_d) = (10^{-6}, 10^{-6})$ s; ii) large charging time constant, $(\tau_c, \tau_d) = (2.5, 10^{-6})$ s; and iii) large discharging time constant, $(\tau_c, \tau_d) = (10^{-6}, 2.5)$ s. Figure 7.30 shows the transfer responses obtained for these three scenarios, along with the data previously obtained to fit the experimental measurements.

The ideal traps scenario (case i) does not show any hysteresis, as charge traps behave in the same way independently of the direction of the sweep. This changes when an asymmetry is introduced in the time constants. The

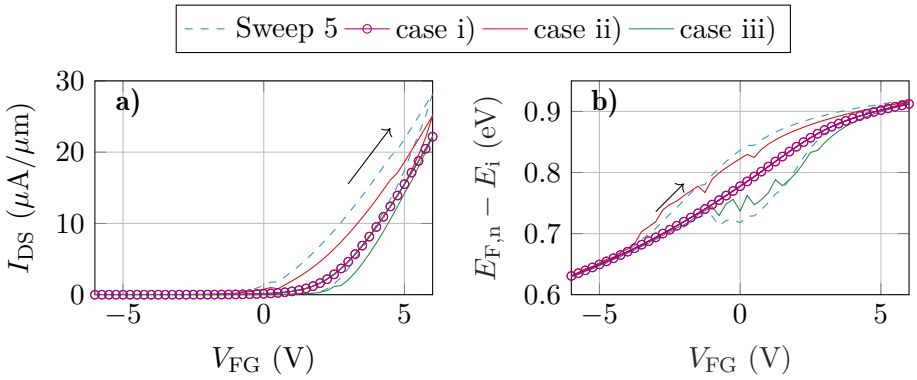

Figure 7.30: a) $I_{DS} - V_{GS}$ and b) $E_F - V_{GS}$ for the three scenarios considered for time constants along with the data previously obtained after the fitting process.

data for the high τ_c (ideal charging, case ii) scenario, depict a higher output current for the forward branch, which indicates that the impact of charge traps is reduced due to their delayed response. For the high τ_d (ideal discharging, case iii) scenario, the delayed response of traps is translated into a larger threshold voltage for the backward branch and a larger change in I_{DS}, as charge associated to traps behaves as a constant charge. When this data is compared with the one achieved fitting Sweep 5 (see Figure 7.27), we observe that the curve with larger τ_c provides a similar behaviour in the forward branch. This can be extended to the curve for the large τ_d scenario, that also mimics the data for the backward branch of Sweep 5, taking into account the horizontal shift due to the different initial conditions of the backward sweep in each case. All these comments can be extended to the $E_{F,n}$ profiles depicted in Figure 7.30b. There, if the profiles for the large τ_c and large τ_d scenarios are combined, the resulting profiles resemble in a large extend the data for Sweep 5. As a conclusion, a common charging constant could be considered for all the D_{it} components as a first approximation to reproduce the behaviour of the device, although a fine analysis such as the one performed in this work is able to provide much more information on the nature of these components.

CHAPTER 8

Simulation of 2D based BioFET devices

8.1 Introduction

In this second chapter of Part IV of the Thesis, we will focus on the structures that contain the electrolyte, i.e., the complete BioFET. First, the model for the electrolyte is validated in two different situations, isolated and integrated with the semiconductor models. Then, several results obtained using the models of the sensing interface, those for the receptor-target complex and surface ion adsorption, are presented. First, the box-based model is used to illustrate the impact of the model election in the results achieved from BioFET simulations. The results show noticeable differences when using the different models, providing some insights on the importance of the proper modelling of the biomolecules in these numerical simulations. Second, the model for the fine molecule charge distribution is used along with the simulation scheme for graphene based devices using a real molecule. That study presents the great potential of this model and some interesting results about the impact of the amorphous shape of the molecule in the response of the sensor. Next, the randomization in the receptor location and activation is used to study its impact on MoS_2 BioFETs for DNA detection. The results obtained from that study supply some insights on the impact of device-to-device variability in the sensor response and regarding their optimization. Finally, the integration of information from PMF profiles in the SB model for surface ion adsorption is analysed through an equivalent reaction constant. To that end, several surface chemical reactions schemes are evaluated and compared with the results provided with PMF profiles.

8.2 Validation of the BioFET simulator

The transport model of the semiconductor devices is now combined with the electrolyte description to build up a comprehensive simulation scheme

for BioFETs. The developed simulator has been subject of a two-step validation process. First, the model for complex electrolytes has been validated by comparing with the well-established Debye-Hückel analytical approximation. Next, the semiconductor device is included along with the electrolyte in the simulations to validate the complete scheme by comparing with experimental results of a MoS_2 BioFET. All data regarding this validation were published in [143].

8.2.1 Complex electrolyte simulation

The validation of the model for the complex electrolyte is performed using a planar-capacitor-like structure with an electrolyte and an oxide layer between two plates as depicted in Figure 8.1.

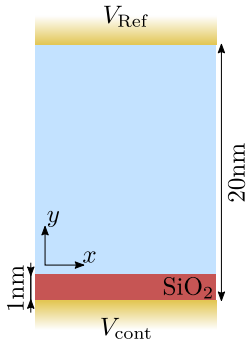

Figure 8.1: (a) Simulated structure to be compared with the Debye-Hückel approximation: a 1 nm thick oxide (red) is in contact with an electrolyte (cyan) between two contacts (gold).

A PBS solution, previously described in Section 6.2, is employed as the electrolyte of these simulations and a 1 nm-thick SiO_2 layer is the insulator over the bottom plate. The top contact acts as a reference electrode (V_{Ref}), while the bottom electrode bias is modified to analyse the profiles of the potential near the oxide surface (V_{cont}). Those profiles will be later compared with the Debye-Hückel approximation that follows an exponential dependence:

$$\phi(x) = \phi_0 \mathrm{e}^{-x/\lambda_{\mathrm{D}}} \tag{8.1}$$

with λ_{D} the Debye length defined as [84]:

$$\lambda_{\mathrm{D}} = \sqrt{\frac{\varepsilon k_{\mathrm{B}} T}{2 N_{\mathrm{Avg}} q^2 I}} \tag{8.2}$$

where ε is the electrolyte permittivity and the rest of the parameters have already been defined. Three different electrolytes have been considered:

0.01×PBS, 0.1×PBS and 1×PBS. The concentrations of the ions for the 1×PBS electrolyte are indicated in Table 8.1, while for the other two cases their concentrations only need to be scaled by 0.01 (0.01×PBS) and 0.1 (0.1×PBS), respectively.

Element	Concentration
Na^+	137 mM
Cl^-_{NaCl}	137 mM
K^+	3 mM
Cl_{KCl}	3 mM

Element	Concentration
NaH_3PO_4	10mM
H^+	10^{-pH}
OH^-	10^{-14+pH}

Table 8.1: Electrolyte concentration with 1×PBS as a function of the pH.

Figure 8.2 shows the potential profiles obtained for different (V_{cont}) values (ranging from 2 mV up to 10 mV) and the three aforementioned electrolyte concentrations. Each of these profiles is compared with the Debye-Hückel equation (Eq 8.1), where ϕ_0 is set by the oxide-electrolyte interface potential from numerical simulations and λ_D is analytically evaluated using (Eq 8.2) for each electrolyte composition. The simulated potential profiles match to an excellent agreement the exponential approximation up to the position of the SiO_2 layer at $y = 1$ nm for all cases, validating the complex electrolyte modelling.

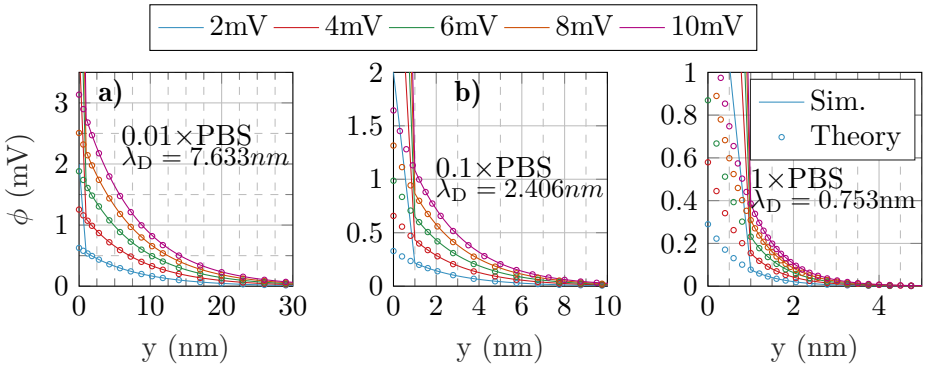

Figure 8.2: Potential profile near the oxide surface (solid lines) using different V_{cont} values and the Debye-Hückel approximation for each case (circles). From left to right, the PBS concentrations used are: (a) 0.01×PBS, (b) 0.1×PBS and (c) 1×PBS.

The potential profile self-consistently determines the ion concentration in the electrolyte. In order to illustrate its distribution, Figure 8.3 shows the concentration profiles as a function of the position for a 0.1×PBS and $V_{\text{cont}} = 10$ mV. The ion concentration derived from NaH_3PO_4, that depends on the pH as described in Section 6.2, reveals a strong modulation of the concentration (Figure 8.3 bottom right) demonstrating that a proper electrostatic modelling of the electrolyte cannot neglect these complex reactions.

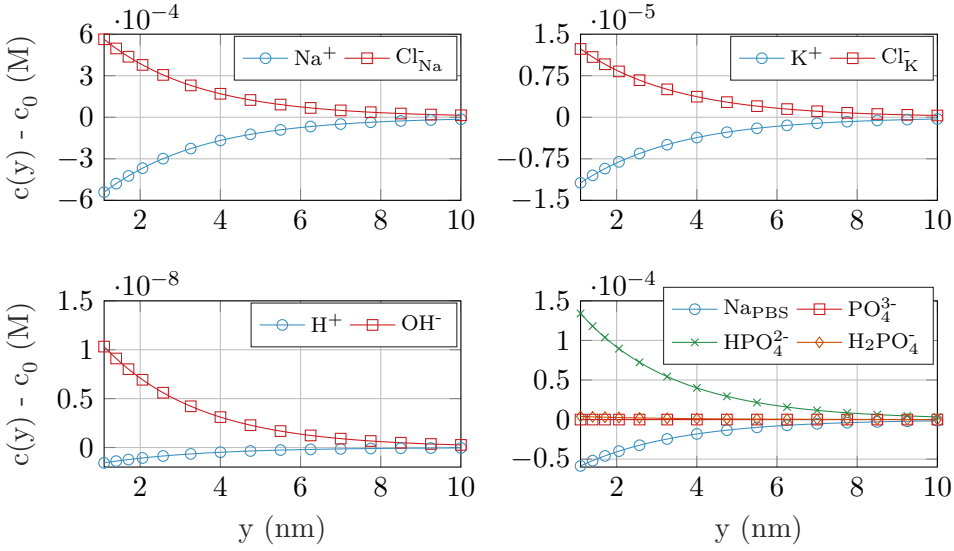

Figure 8.3: Concentration of the ions present in the electrolyte as a function of the position. The electrolyte composition is 0.1×PBS and $V_{\text{cont}} = 10$ mV.

8.2.2 FET device gated by an electrolyte

Once the isolated complex electrolyte has been tested, the semiconductor region is included in the simulation in order to validate the complete BioFET simulation scheme. The experimental data for this validation were obtained from the work of Sarkar et al. [16], that provides the transfer characteristic of an electrolyte-gated device in the absence of target molecules. The device is based on a 5 nm thick layer of MoS_2 sandwiched between a 270 nm thick SiO_2 layer (substrate) and a 30 nm thick HfO_2 layer. The semiconductor channel is 5 μm long and it is only controlled by the electrolyte gate. The electrolyte composition is 0.01×PBS.

The channel is 5 nm thick (around 7-8 MoS_2 layers), quite thick compared with its monolayer version but enough to provide a strong quantization of the energy levels (Section 5.2.1), so the hybrid implementation of

the Schrödinger equation (Section 5.2.2) is considered for this simulation. The model for charge traps described in Section 5.6 is also included in the simulations. Two scenarios for the oxide-semiconductor interface are considered in order to illustrate their impact in the device response: pristine interface (no traps) and non-ideal interface. Regarding the DoS of these charge traps, acceptor traps with a constant energetic profile is considered for both SiO_2-MoS_2 ($5 \cdot 10^{10}$ eV^{-1} cm^{-2}) and MoS_2-HfO_2 ($5 \cdot 10^{12}$ eV^{-1} cm^{-2}) interfaces. These scenarios are also combined with an electrolyte voided of ions to achieve a deeper insight of the impact of the electrolyte modelling in the simulations. Figure 8.4 shows the experimental transfer characteristics extracted from [16] and the simulation results.

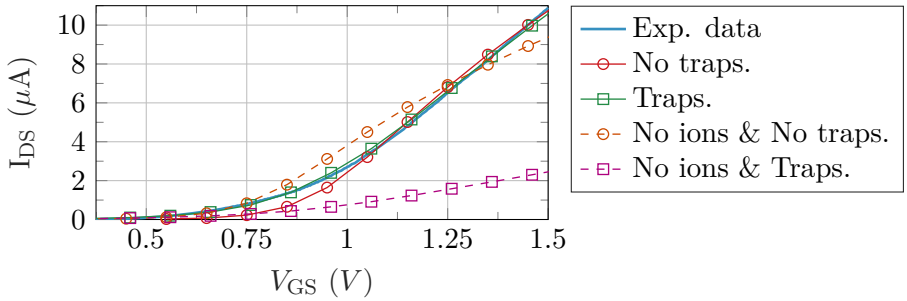

Figure 8.4: Comparison of the transfer characteristics measured by Sarkar el al. [16] (solid blue) and the results of the BioFET simulations, with ions (solid) and w/o ions (dashed). Markers indicate if interface traps are considered in the simulations (squares) or not (circles).

The data depicted in Figure 8.4 show that the trend of these curves when the electrolyte does not contain ions are far from the experimental results. However, when the ions are included in the simulations the agreement with the experiment is considerably improved and the match is, indeed, excellent when the effect of interface traps is incorporated. The very good fitting with the experimental data evidences that the electrolyte-semiconductor system, including the coupling between the two regions of the device and the non-idealities at the interfaces, is correctly modelled. Once the electrolyte model is validated for both scenarios, isolated and combined with the semiconductor, the next step is to include the model of the molecules within the simulator. Next sections expose the results obtained with the different models described in Section 6.4.1. In order to avoid an excessive segmentation in the presentation of the results obtained with each approach, we introduce the model in each case and their corresponding electrical results when it is inserted in the whole structure incorporating the semiconductor.

8.3 Simulation of monolayer MoS_2 BioFET with box-based molecule models

As previously described in Section 6.4.1, the box-based molecule model considers different alternatives regarding the interaction between the ions in the electrolyte and the molecule box. In this particular case three scenarios are considered: fully permeable box (Model 1), permeable neutral receptor and solid target (Model 2), solid receptor-target complex (Model 3). These models are first analysed only with the model of the electrolyte using the structure depicted in Figure 8.5, which also indicates the characteristics of the box-shaped molecule. The size of the neutral receptor ($h_n = 2$ nm) is chosen to be close to the Debye length of the 0.1×PBS electrolyte ($\lambda_D = 2.406$ nm), and thus, three screening cases will be studied: i) weak screening (0.01×PBS), ii) strong screening (1×PBS) and iii) quasi-complete compensation (0.1×PBS).

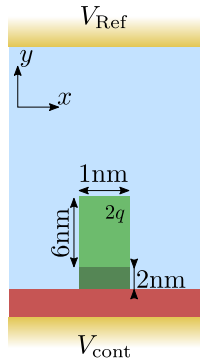

Figure 8.5: Characteristics of the box-shaped molecule considered in the simulations. Neutral receptor is 2 nm-height, a value close the Debye length of the 0.1×PBS electrolyte. The charged target is 6 nm-height and contains a charge of 2 q.

Figure 8.6 shows the total ion charge density distribution when the three interaction models are used for the 0.1×PBS concentration. The influence of each molecule model on the ion distribution is clearly observable. The impact of the different PBS concentrations is shown in Figure 8.7, where the longitudinal charge density profiles at $y = 6$ nm are depicted for the different PBS concentrations.

Figure 8.7 shows that far away from the molecular charge, the ionic charge density (N_{elec}) is roughly the same independently of the interaction model used. Near the molecular charge, nevertheless, large differences in N_{elec} arise. Model 1 presents the maximum of the ion concentration at the molecule centre while in Models 2 and 3 the ions are prevented from entering into the molecular region.

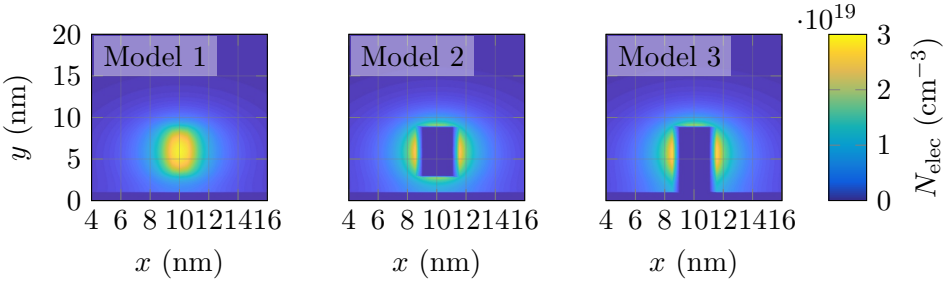

Figure 8.6: 2D colormap of the total ion charge density near the oxide layer when the three different molecular models are used. The electrolyte composition is 0.1×PBS and $V_{cont} = 5$ mV.

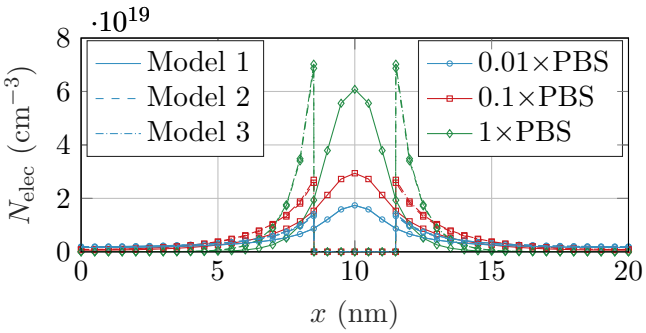

Figure 8.7: Longitudinal charge density profiles at $y = 6$ nm. The cases depicted correspond to the three interaction models when the PBS concentration is modified: 0.01×PBS, 0.1×PBS and 1×PBS.

The sensing mechanism of the BioFET device is based on its capability to reproduce the molecule charges in the channel. That depends, of course, on the PBS ion concentration in the surrounding medium, and to what extent the molecule charge is screened by the electrolyte. In order to understand the differences between the molecular models in this regard, Figure 8.8 shows the contact charge (Q_{cont}), that emulates the channel in a BioFET device, and the electrolyte charge (Q_{elec}) normalized to the molecular charge (Q_M) in the structure. Since the molecular charge is positive, the changes of Q_{cont} from negative to positive indicate that Q_M is completely screened and the charge evaluated in the contact is modulated by Q_{elec}.

The relation Q/Q_M vs. V_{cont} always follows a linear trend, and the values obtained using the different models become closer as the PBS concentration is increased. For a given PBS concentration, Models 1 and 3 define the extreme values of Q/Q_M and Model 2 provides intermediate results that approach those of Model 1 or Model 3 depending on the PBS. Thus, for low

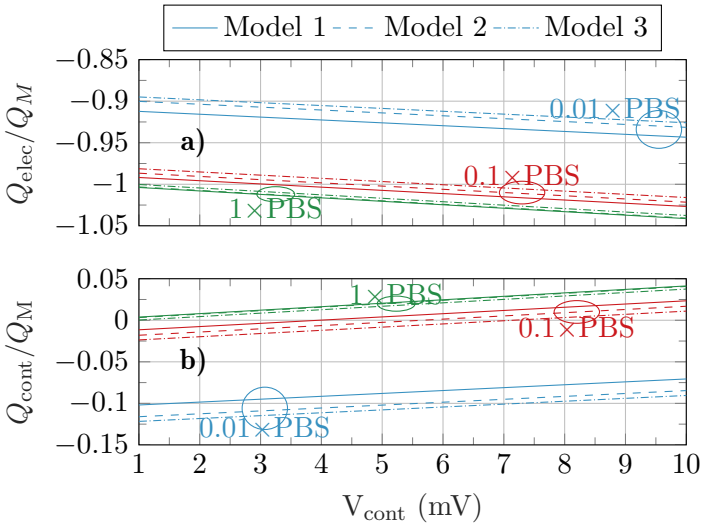

Figure 8.8: Charge density associated to the electrolyte (a) and oxide contact (b) relative to the molecule charges as a function of V_{cont}. The change in the sign of Q_{cont} indicates that the molecule charge is completely screened.

PBS concentrations, the screening is expected to be weak and the values of Model 2 are closer to those of Model 3, while for high PBS concentrations, where a high screening takes place, Model 2 approaches to the results of Model 1. This adaptability of Model 2 can be explained according to the relative role of the neutral and charged regions of the molecule under different screening conditions. In a high screening situation, the contact charge is mainly determined by the charge of the ions located between the oxide interface and the molecule charged region. The neutral receptor region is modelled in the same way in Models 1 and 2 and therefore the results obtained with both models are similar. In the weak screening case the charged region of the molecule gains relevance and Model 2 is similar to Model 3.

Now, the box-based model of the molecules is included in the device level simulation. The complete device structure shown in Figure 8.9 is simulated. The device follows the design of the experimental data provided in [16] (Section 8.2.1), but using a monolayer MoS_2 as semiconductor channel, to explore the performance limit in a 2D BioFET. The electrolyte composition (0.01×PBS) and interface traps (constant profile and a value of $5 \cdot 10^{10}$ $eV^{-1}cm^{-2}$ for the SiO_2-MoS_2 interface and $5 \cdot 10^{12}$ $eV^{-1}cm^{-2}$ for the MoS_2-HfO_2 interface) are the same too. Fifteen molecules are distributed uniformly over the HfO_2 layer. The same values as those indicated in Figure 8.5 are used for these generic molecules, except some changes in the charge and size of the neutral region. In particular, Q_M is increased up to 200 q to obtain a more noticeable impact on the device response and the value

-200 q is also considered. Regarding the size of the neutral region, two cases were also analysed based on the Debye screening length ($\lambda_D = 7.633$ nm) to emulate two different screening scenarios:

- First case: low screening. $h_N = 4$ nm so that the distance from the device surface to the molecular charge is lower than the Debye screening length.
- Second case: large screening. $h_N = 20$ nm so that the distance from the device surface to the charged region of the molecule is higher than the Debye screening length.

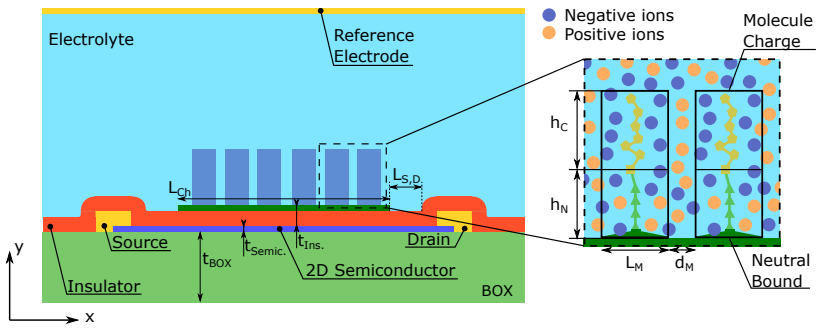

Figure 8.9: Structure of the 2D-material based BioFETs. Its design resembles the one employed to fit the data extracted from [16] but using a monolayer MoS_2 channel sandwiched between a 270 nm thick SiO_2 layer (substrate) and a 30 nm thick HfO_2 layer. Molecules are considered on top of this latter and are included in the simulations using the box-based model described in Section 6.4.1. A sketch summarising the parameters that rule this model is depicted in the right side of the figure.

In both cases the $I_{DS} - V_{GS}$ response of the device is compared to the situation when no molecules are attached to the insulator surface, I_{DS_0}. The change in the transference response is calculated as $S = (I_{DS_0} - I_{DS})/I_{DS_0}$ and the results of the simulations using $h_N = 4$ nm and $h_N = 20$ nm are depicted in Figure 8.10 for the Model 1 (solid), Model 2 (dash-dotted) and Model 3 (dashed with squares).

The $S - V_{GS}$ profiles in Figure 8.10 show that Models 1 and 2 depict the same behaviour, the change in the sign of Q_M makes the output current higher ($Q_M > 0$) or lower ($Q_M < 0$) than I_{DS_0}. This makes sense as a negatively charged molecule acts as a negative gate voltage reducing the electron density in the channel and, as a consequence, lowering the output current. The same argument can be applied to a positive Q_M, which acts as a positive gate voltage. As a result, symmetric $S - V_{GS}$ profiles are observed with a scaling down factor as h_N increases, which is expected as $h_N = 20$ nm $> \lambda_D$ [55]. Then, differences between the two models are

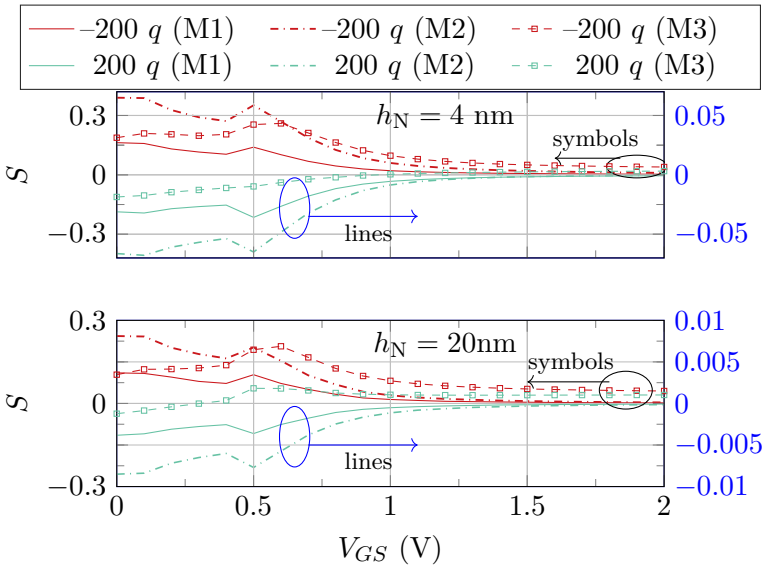

Figure 8.10: Change in the transfer response of the device when molecules are included in the simulations. The molecular charge is set to –200 q (red) and 200 q (green) using the three interaction models.

reduced only to a scale factor, being Model 2 the one that provides a higher S. This latter can be explained through the differences in the modelling of the molecular charge. In Model 1 ions are allowed to enter the region where the charge is defined, so it is notably screened even for the $h_{\mathrm{N}} = 4$ nm case. On the contrary, Model 2 allows ions to enter only in the neutral region, so the screening of Q_{M} is lower and it depends on the size of the neutral region: a shorter neutral region limits the amount of ions that can be accumulated and thus screen the molecular charge. This discussion cannot be applied to the data obtained with Model 3. In that case, the same symmetry depicted by the other two models is not observed, and for most of the cases the I_{DS} response tends to be lower than the reference I_{DS_0}. In addition to that, S does not show such a noticeable reduction when h_{N} is increased from 4 nm to 20 nm. Actually, S increases when h_{N} also grows and $Q_{\mathrm{M}} > 0$. In this model ions are not allowed to enter inside the molecule, neither the charged region nor the neutral one, so the screening of the molecule charge is significantly lower than in the other two cases. This also explains the independence, or low dependence, on h_{N} as the neutral region is always free of charge. This later results evidences the relevance of a proper modelling of the molecular charge distribution and its interaction with the electrolyte. Further refinement of the model in this regard are treated in the next section.

8.4 Graphene BioFET for the detection of SARS-CoV-2

In contrast to the previous section, focused on the box-based molecule model, this section takes advantage of the fine molecule model (Section 6.4.3) and the transport model for graphene based devices (Section 5.4.2) presented in the previous chapters, to study a Graphene based Field-Effect Transistor-based Biosensor (GBioFET) for the early detection of Severe Acute Respiratory Syndrome Corona Virus 2 (SARS-CoV-2). This is intended to provide a broad overview of the potential of the models developed in this Thesis.

In the specific case of the detection of the SARS-CoV-2 using the GBioFET technology, prior to the extraction of the molecule shape and charge distribution in the idle (ρ_{idle}) and activated (ρ_{act}) states, it is worth to recall the infection mechanism of this virus so to define the receptor-target pair of the biosensor that are later finely mapped. The structure of this virus is determined by a lipid membrane encasing its genetic load. The most remarkable element in this membrane is a set of spike proteins that surround the whole structure, and give rise to the characteristic appearance of the virus, a circular body enclosed by a halo that looks like a corona. These spike proteins, as indicated in Figure 8.11, are composed of two subunits, named S1 and S2 respectively. The former is meant to bind the virus to the cell surface, while the latter enables the virus core envelope to join the cell membrane releasing its genetic load [144].

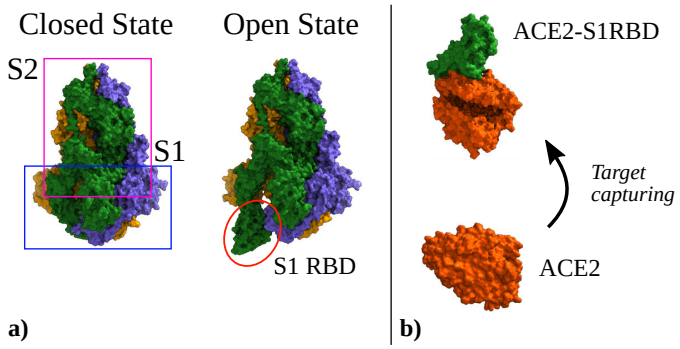

Figure 8.11: (a) Three-dimensional structure of the Spike glycoprotein head in its closed state (PDBe ID:6vxx[145]) and open state (PDBe ID:6vyb[145]). It is composed by two subunits named S1 and S2. In the open state the S1RBD is exposed so that the virus can be attached to the cell surface. (b) Structure of the human ACE2 (PDBe ID:1o86[146]) used as attachment point by SARS-CoV-2; and its complex with the S1RBD (PDBe ID:6m0j[147]).

The main entry point to the cell used by SARS-CoV-2 is the Angiotensin Converting Enzyme 2 (ACE2) [148, 149, 150] (see Figure 8.11). The ACE2 molecule interacts with the S1 Receptor Binding Domain (S1RBD) so that

the virus gets attached to the cell surface. After this capturing process, the S1 unit is cleaved from the main body of the spike protein leaving the S2 unit exposed, making possible the fusion of the cell and virus membranes [144]. According to the aforementioned infection mechanism, here we focus on the ACE2-S1RBD complex, where the ACE2 acts as receptor molecule.

To achieve an accurate description of the electrostatic properties of the ACE2 and ACE2-S1RBD complex, they are modelled in atomic detail. This part of the work was done in collaboration with Prof Rebecca Wade and Dr. Daria Kokh from Heidelberg Institute of Theoretical Studies [151]. For such accurate description of the molecules, they employed structures with PDBe ID: 1o86 [146] and PDBe ID: 6m0j [147] for the ACE2 and ACE2-S1RBD complex respectively. Glycans (NAG) are removed from the structures and missing loops are built using MODBASE web site [152]. One Zn^{2+} and one or two (complex and ACE2, respectively) Cl^{-} ions are retained in calculations. Proteins are protonated at pH 7.4 and partial charges at each atom are generated using PDB2PQR server [153] (ions are omitted at this step). The total charge of the ACE2 protein and the complex is -12 q and -22 q, respectively. Zn^{2+} and Cl^{-} are added back to the structure.

The resulting charge distribution of the unbound (idle state) ACE2 receptor (ρ_{idle}) and the bound (activated state) ACE2-S1RBD complex (ρ_{act}) are included in the 2D biosensor simulation as depicted in Figure 8.12. There, a projection plane is defined according to the orientation of the molecule on top of the sensor. Next, it is discretized to generated a grid where the 3D charge distribution of the molecule is mapped. Once the 2D profile is obtained, it is replicated in the grid defined for the simulation of the device according to the location of the molecules along the sensing surface.

In this particular case, molecules are mapped into a spatial grid of 8 nm×6 nm in the case of the ACE2 molecule, and 8 nm×10 nm in the case of the ACE2-S1RBD complex. In both cases the size of the grid in the region occupied by the molecules is 0.5 nm×0.5 nm. The resulting projections are depicted in Figure 8.13 along with their respective 3D profiles.

Once the target receptor-pair is defined and its charge distribution has been obtained, we exploit the previously described approach to study the sensitivity of GBioFETs as sensors for the detection of the SARS-CoV-2 with an unprecedented precision, capturing the finest details in the interaction between the molecules at the sensing interface and the graphene channel. To this purpose, we consider a 500 nm-long graphene layer on top of a SiO_2 substrate. Source and drain regions span 50 nm from the edges of the structure and each of them is covered by a 20 nm thick HfO_2 layer. In the 400 nm-long remaining region, a 3 nm thick lipid layer that hosts the receptor molecules is considered. Simulations are carried out with 10 recep-

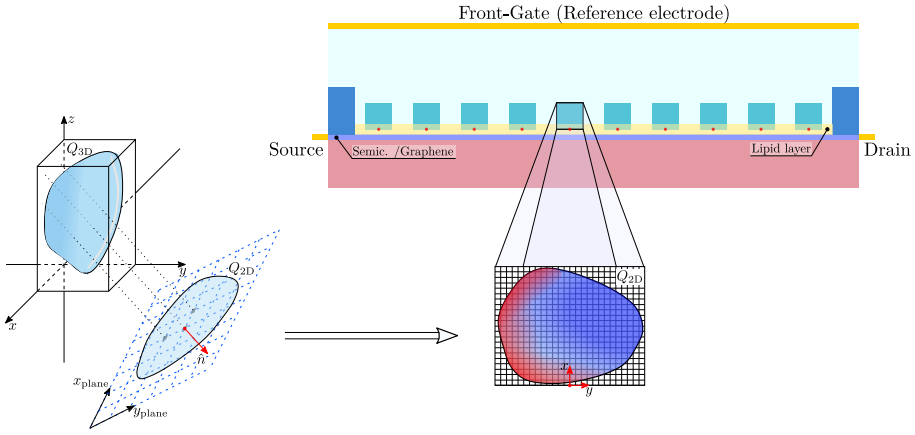

Figure 8.12: Projection of the 3D molecule charge distribution to obtain the 2D profiles used in the device simulation. Vector $\hat{n}$ sets the desired orientation for the projection plane that is later discretized to define the 2D charge profiles of the molecules. The extracted profiles are used in the device simulations by replicating them along the longitudinal axis according to the defined positions.

tors uniformly distributed along the structure. A liquid electrolyte covering the top surface of the sensor is defined by a 1×PBS solution. Finally, a reference electrode is immersed on the liquid electrolyte to set a reference voltage. Figure 8.14 depicts a schematic of the considered GBioFET.

Thus, we tested the sensitivity of the GBioFET to the presence of ACE2-S1RBD complexes by determining through self-consistent simulations the transfer response of the device ($I_{DS} - V_{FG}$) assuming different percentages of activated receptors, α. The results are collected in Figure 8.15a. The device response can be qualitatively split into three regions: (i) the gate bias around the point of minimum conductivity, i.e. the Dirac voltage V_{Dirac}, (ii) the p-type branch, corresponding to negative gate biases, i.e. to the left of V_{Dirac}, and (iii) the n-type branch, corresponding to positive gate biases, i.e. to the right of V_{Dirac}. As can be observed, at V_{Dirac} the channel exhibits its lowest conductivity and the GBioFET does not show noticeable changes when the S1RBD molecules are attached to the ACE2 receptors, evidencing this bias region as poorly responsive to detect the presence of the virus. Concerning the p-type branch, a slight modification in the output current is observed as α varies. The transfer response spreads out as the gate bias gets more negative, but within a limited range. In this case, actually, the curves are almost parallel, so the change observed in I_{DS} can be mainly related with the change in V_{Dirac} and $I_{DS}(V_{Dirac})$. On the contrary, the n-type branch reveals itself as the most sensitive operation region: the magnitude of the output current is lower than the p-type branch, but it reveals a higher sensitivity to changes in α.

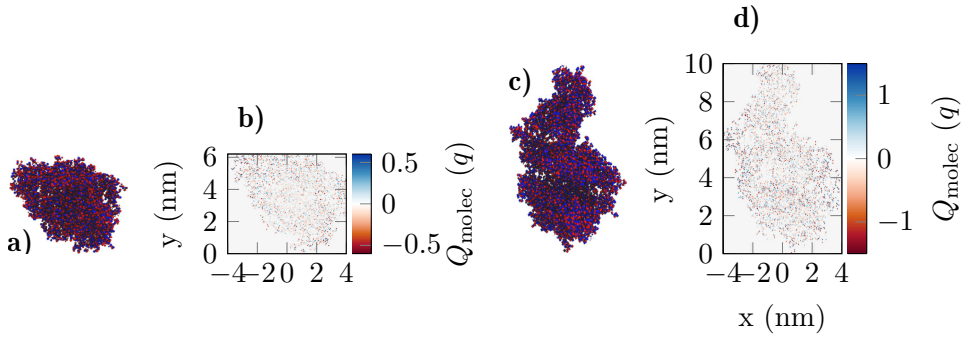

Figure 8.13: Charge distribution of the ACE2 (a) and the ACE2-S1RBD (c) complex viewed from the projection plane. Blue dots indicate positively charged elements while red dots indicate negatively charged elements in the molecular structure. Figures (b) and (d) shows the final result of the projection of the 3D charge distributions (Figure 8.12) prior to their integration in the simulation of the GBioFET device.

More importantly, the transfer characteristic manifests a counter-intuitive behaviour with the activation percentage. Both the ACE2 receptor and the S1RBD are negatively charged. Thus, when the receptors are activated (i.e. ACE2-S1RBD complex is formed), they contribute with a higher amount of negative charge to the electrolyte than in the idle state (ACE2 receptor only). As a consequence, as α augments one would expect an increase in the output current in the p-branch due to a higher hole concentration induced by the activated receptors and, conversely, a reduction of the output current in the n-branch due to a diminished electron concentration. On the contrary, we observe that I_{DS} decreases (increases) for higher α values in the p-branch (n-branch). A similar behaviour has been also reported in a very recent experimental realization in [14] where the capture of the negatively charged spike protein does not result in a direct increase (decrease) of the p-branch (n-branch) sensor current. In that case the receptor, a spike-protein antigen, is positively charged, but the capturing of the negative spike protein should, in principle, reduce the net positive charge at the sensing interface and have the same intuitive consequences above explained.

We can further analyse this behaviour leading our attention to the actual electron and hole densities in the graphene layer for different occupation percentages as a function of V_{FG} (see Figure 8.15b). As expected, below V_{Dirac} holes are the majority carriers in the channel but their concentration barely changes with α. The inset exhibits a zoom of this $p - V_{\text{FG}}$ profiles evidencing a slight reduction of the hole concentration as the number of activated receptors increases. On the other hand, above V_{Dirac} electrons are dominant, but a non-negligible amount of holes is still present in the

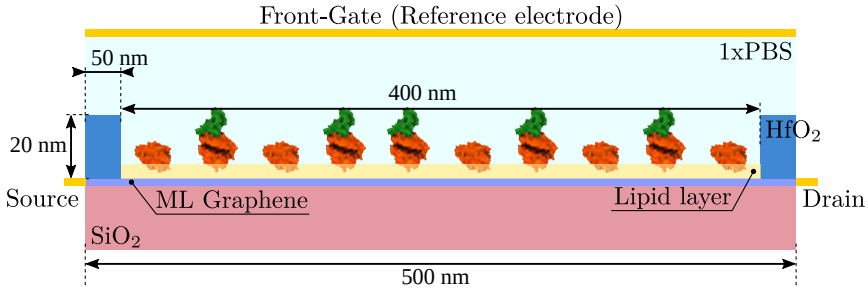

Figure 8.14: Schematic depiction of the GBioFET with a 500 nm-long graphene layer deposited above a SiO_2 substrate. 50 nm source and drain regions are covered by a 20 nm-thick HfO_2 layer, while the 400 nm-long channel is covered by a 3 nm-thick lipid membrane that hosts the receptor molecules. To model the substrate of the sample we considered an electrolyte defined by a 1×PBS solution. A reference electrode in direct contact with the solution is also indicated.

n-branch. In addition to this, the amount of electrons in the graphene layer is modulated in a larger extent by α when compared with the holes in the p-branch, so that we can associate both facts with the larger change in I_{DS} observed for the n-type branch. Electron and hole concentrations, although coherent with the I_{DS} results, still show trends with α that are not intuitive: i.e. the hole (electron) density decreases (increases) as more receptors become activated and therefore more negative charge is present in the electrolyte.

In order to shed light on this issue, we have analysed the longitudinal charge profiles under each receptor with $\alpha = 0.6$ at two gate biases, one in the p-branch ($V_{FG} = -0.5$ V) and another in the n-branch ($V_{FG} = 0.5$ V) (Figure 8.16a and Figure 8.16b, respectively). The charge varies along the channel mimicking locally the changes due to the molecule activation. To analyse in detail these variations, we select the region under the sensing layer and split it into 10 sub-regions, in correspondence to the 10 receptors, and plot the resulting localized charged profiles, evaluating the impact that a change in the receptor state has on the main carrier distribution (Figure 8.16c and Figure 8.16f for holes and electrons, respectively). In these plots, dashed (solid) lines correspond to the main carrier distribution under activated (idle) receptors. The profiles for each state overlap with small differences associated to the subtleties of the channel local changes. The hole density (Figure 8.16c) shows a noticeable increase when the S1RBD (negatively charged) is captured by the ACE2 receptor. Although the peak in the hole concentration under the activated pair is higher, its profile is narrowed and the resulting overall hole concentration (i.e. the integral of the charge profiles) decreases. For the electron density in the channel (Figure 8.16f) the situation is reversed: under the negatively charged receptors the

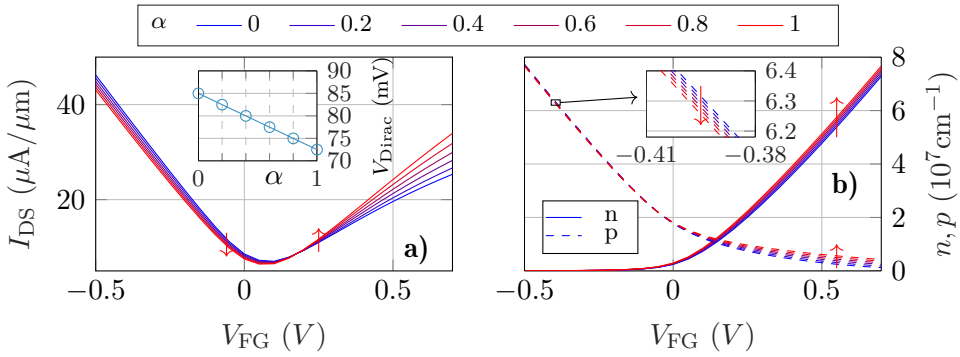

Figure 8.15: (a) Transfer response of the GBioFET device for different receptor occupation percentages (α). Inset shows the change of the Dirac voltage when that activation percentage is modified. All the data were obtained for a constant $V_{DS} = 0.1$ V. (b) Electron (solid) and hole (dashed) concentrations in the graphene layer as a function of the reference electrode bias (V_{FG}) and occupation percentage α. The inset shows a zoom of the hole concentration to highlight the trend of this parameter as α is modified.

concentration drops significantly (solid lines), but after the complexation of the receptors (dashed lines) the extension of the depleted region becomes narrower, giving rise to a net increase in the electron concentration. The density profiles of minority carriers (Figure 8.16d for electrons and Figure 8.16e for holes) depicts a quite similar behavior.

The previous analysis is also supported by the electric field distribution under the molecules as depicted by Figure 8.17 for both molecule states (idle at Figure 8.17a-b and activated at Figure 8.17c-d) and both V_{FG} values in the p- and n-branch (i.e., $V_{FG} = -0.5$ V for Figure 8.17a, c, and $V_{FG} = 0.5$ V in Figure 8.17b, d, respectively). The edges of the graphene layer are indicated by arrow heads aside each plot. The regions where the electric field is normal to the graphene layer correspond to those locations where the carrier concentration changes to a larger extent. When switching from idle (Figure 8.17e-f) to activated (Figure 8.17g-h) those regions with higher electric field shift from right to left, which is consistent with the charge profiles depicted in Figure 8.17c and Figure 8.17d. The present analysis evidences the necessity of a fine-grained treatment of the molecular shape and its charge distribution so to capture the subtleties of the electrostatic interaction between the receptor and the graphene channel.

Finally, we analyse the sensor response using two definitions for this parameter, the absolute (S_a) and relative (S_r) change in the output current:

$$\begin{aligned} S_a &= I_{DS} - I_{DS,0} \\ S_r &= \frac{I_{DS}}{I_{DS,0}} - 1 \end{aligned} \tag{8.3}$$

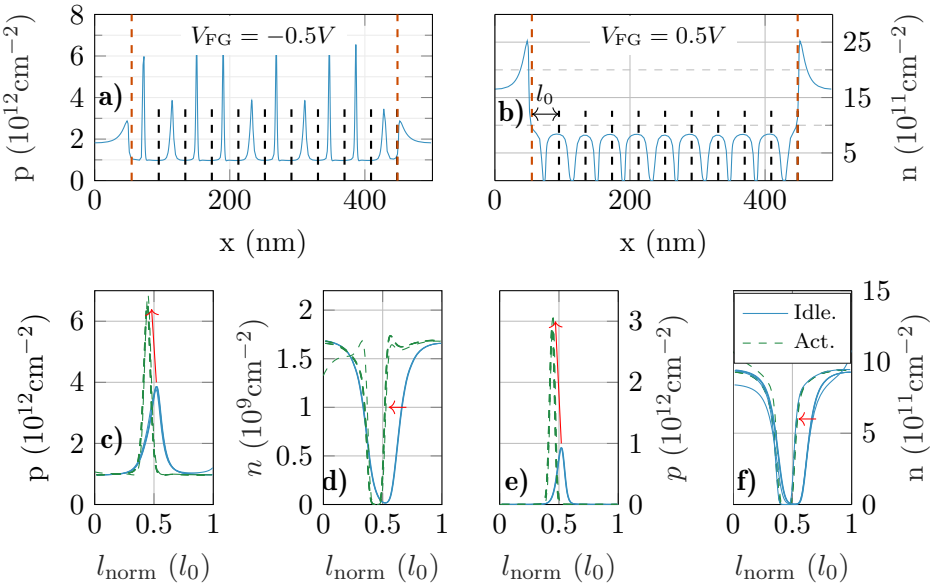

Figure 8.16: Longitudinal majority carrier density profiles (a,b) and superimposed carrier concentrations (c-f) under each receptor. To obtain these latter we consider a region of length l_0 under each receptor and $\alpha = 0.6$ (6 receptors are activated) to observe the changes in the carrier concentrations when the receptor is activated. These regions are indicated in subplots (a) and (b) by black dashed lines, red lines indicate the limits of the lipids layer.

where $I_{DS,0}$ corresponds to the output current for $\alpha = 0$. Both S_a and S_r changes with V_{FG} and α as depicted in Figure 8.18a and Figure 8.18b, respectively. The sensor presents a noticeable sensitivity and capability to detect the S1RBD when it is bound to the corresponding ACE2 receptor what assures its specificity. The sensitivity is higher in the n-branch than in the p-branch, reaching relatives changes in the output current of 30% in the former case when all the molecules are activated. Its dependence on the gate bias also varies in both cases: while in the p-branch it reaches a maximum (around $V_{FG} = 0$ V), then decreases and eventually saturates; in the n-branch the sensitivity increases monotonically with V_{FG} indicating that higher positive biases favour the sensing capabilities of the GBioFET. Indeed, the maximum sensitivity within the range of biases here simulated occurs for $V_{FG} = 0.7$ V. The inset shows the sensor response at this particular bias as a function of the occupation percentage. Interestingly, the sensitivity increases linearly with α guaranteeing also the linearity of the sensor response at this bias point.

All the data exposed above demonstrate the GBioFET potential to achieve a reliable detection of SARS-CoV-2, particularly when it operates

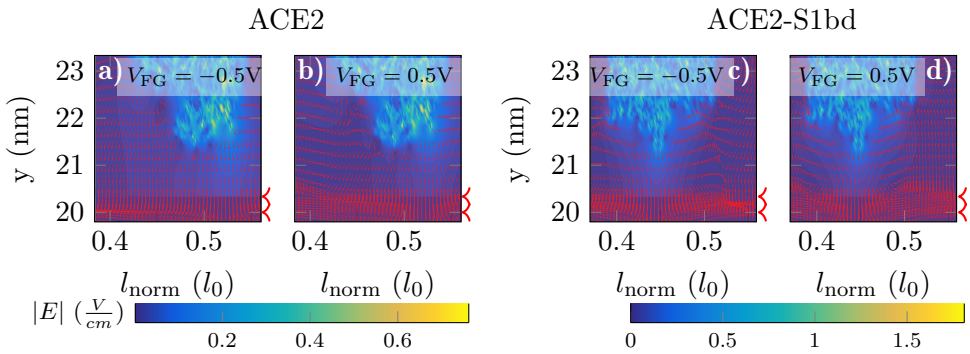

Figure 8.17: The electric field distribution under two receptor molecules in idle state (a,b) and activated state (c,d) for two different gate biases: −0.5 V (a,c) and 0.5 V (b,d). They show how the charge of the molecule is redistributed giving rise to a change in the electric field in the graphene layer, the limits of which are indicated by arrow heads. The regions where the vertical component of the electric field is stronger correspond to those where the carrier concentration is modified in a larger extent in Figure 8.16. When moving from one state to other, the modification of the region with a high vertical electric field gives rise to the changes in the profiles depicted in Figure 8.16c-f.

in the n-branch. A detailed study of the electron and hole density variations due to the electric field generated by the ACE2 and the ACE2-S1RBD pair charge distributions, namely, when the receptors are idle or activated, enable us to explain what is, in principle, a counter-intuitive behaviour of the sensor response, that would be obscured by more simplistic computational treatments, rationalizing the observed behaviour in experimentally fabricated sensors. Then, the fine-grained level of description proposed here, which is possible due to a multiscale approach to the electrolyte device physics, results in an exceptional level of detail to capture the sensor response.

8.5 Device variability in DNA-BioFETs

In this section, the model for the randomization of the spatial distribution and activation of the receptors discussed in Section 6.4 is evaluated in the context of MoS_2 BioFETs aiming for the detection of DNA molecules. In particular, the randomization of the positions of the receptor molecules in the sensing interface is used to emulate device-to-device variations, while the randomization in the receptor activation pattern emulates the changes in the response of a single device. Different receptor distributions and activation configurations are considered in order to assess the technology robustness against variability. The reference structure is depicted in Figure 8.19 and it is defined by a 400 nm-long monolayer MoS_2 (0.65 nm-thick)

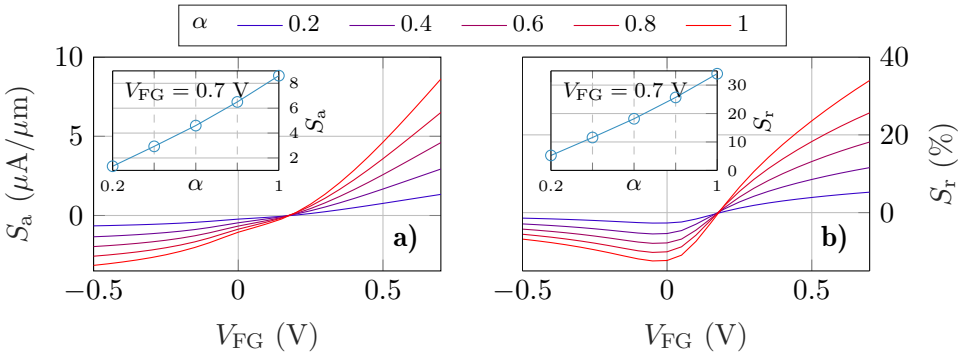

Figure 8.18: Absolute (a) and relative (b) change of the output current with respect to the 0% occupation scenario. The insets show the response in each case at the bias where the device output shows the largest changes.

sandwiched between a 20 nm-thick SiO_2 layer, acting as substrate, and a 10 nm-thick SiO_2 layer. The MoS_2 layer is assumed to have a residual intrinsic n-type doping ($N_D = 6.5 \cdot 10^{10}$ cm^{-2}) and a carrier mobility of 50 cm^2/Vs. The sensing interface is 300 nm-long and it is located at the centre of the structure, above the 10 nm-thick SiO_2 layer, in direct contact with the liquid electrolyte. There, $N = 12$ receptors are placed using the distributions previously described in Section 6.4. Regarding the modelling of these molecules, the specific model for DNA molecules outlined in Section 6.4.2 is used assuming that each molecule has 120 base pairs. Finally, the electrolyte is based on a PBS solution, with 1×PBS and 0.1×PBS the cases considered.

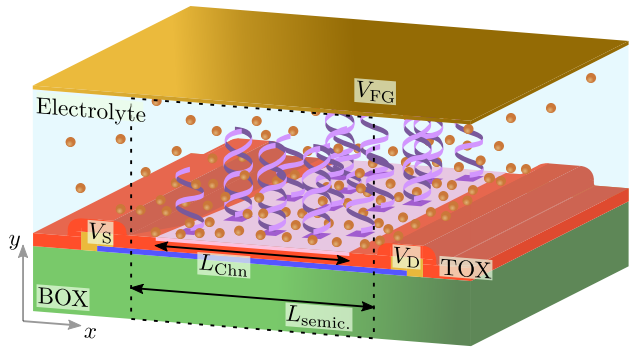

Figure 8.19: Structure of the MoS_2-based DNA BioFET. The structure is based on a MoS_2 monolayer sandwiched between two SiO_2 layers: 20 nm-thick Buried Oxide (BOX) and 10 nm-thick Top Oxide (TOX). The receptor layer is placed above the TOX and defines the size of the channel L_{Ch} (300 nm), while the total length of the device corresponds to this length plus the source and drain regions (50 nm).

The objective is to evaluate the impact of the randomization in the location of the receptor molecules and their activation in the response of the BioFET device. To that end, the three random distributions implemented in the simulator and described in Section 6.4.4 are considered along with an uniform receptor distribution scenario, which serves as a reference to evaluate the impact of the randomization in the sensing interface. For the randomized distribution of receptors governed by (Eq 6.25), the values $\sigma_0 = 0.5$ nm and $\alpha = 1/8$ are considered. V_{DS} is set to 0.1 V while front gate bias (V_{FG}), defined by the reference electrode immersed in the electrolyte, is modified to obtain the $I_{DS} - V_{FG}$ curves for different sensing interface states, i.e., different receptor occupation percentages P, and eventually the device response S, which in this case is defined as:

$$S(P) = \Delta I_{DS} = I_0 - I_{DS} \tag{8.4}$$

where I_0 stands for the output current for the $P = 0\%$ scenario. The $I_{DS} - V_{FG}$ and $S(P) - V_{FG}$ responses are depicted in Figure 8.20 for the uniformly distributed receptors scenario and for two PBS concentrations: 1×PBS (solid lines) electrolyte and 0.1×PBS (dashed lines).

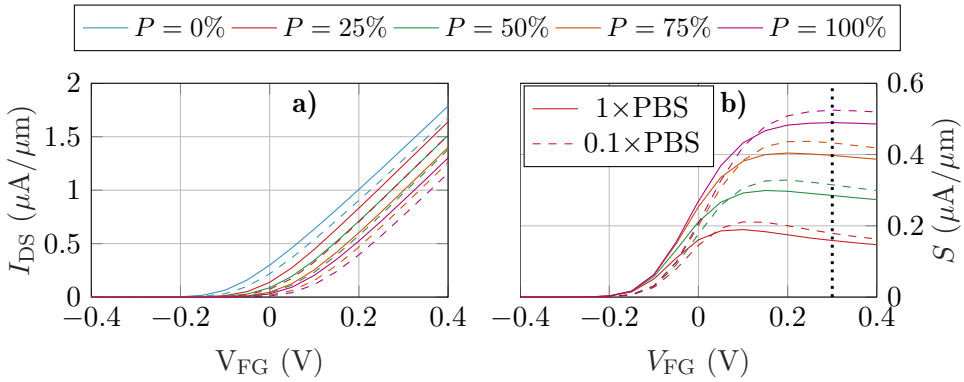

Figure 8.20: a) $I_{DS} - V_{FG}$ and b) $S - V_{FG}$ for five values of P with an uniform distribution of receptors. Solid and dashed lines correspond to the 1×PBS electrolyte and 0.1×PBS electrolyte scenarios, respectively.

Figure 8.20 shows, as expected, that a higher amount of activated receptors gives rise to a shift of the curves towards positive gate biases. This fact can be explained by the increase in the negative charge of the dsDNA molecules which leads to higher threshold voltages. When the ionic strength of the electrolyte is reduced, that is, we move from the 1×PBS electrolyte to the 0.1×PBS electrolyte, this shift is larger. The capability of the electrolyte to screen the charge of the molecules is reduced and the impact of

their negative charge in the carrier concentration contained in the semiconductor channel is higher. This is also confirmed by Figure 8.21 where the net charge in the electrolyte region (ions and molecules) for different values of P and $V_{FG} = 0.3$ V is shown. Considering a 0.1×PBS provides a more significant variation of the charge as P increases.

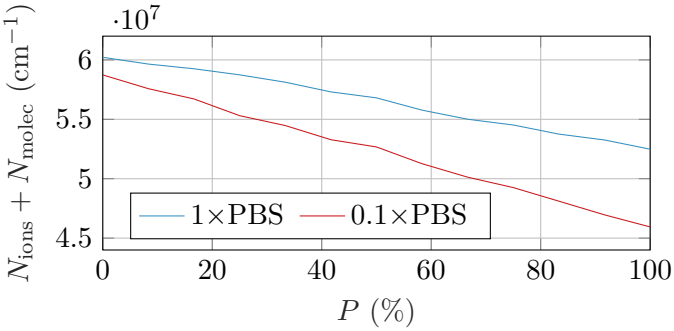

Figure 8.21: Integrated net charge in the electrolyte region (ions and molecules) as a function of the receptor occupation percentage P at $V_{FG} = 0.3$ V.

An example of the $I_{DS} - V_{FG}$ curves for different randomized distribution of receptors in the three scenarios available: i) channel centred, ii) source centred and iii) drain centred, are depicted in Figure 8.22. The results are quite similar to those for the uniformly distributed receptors, the increase of P generates a horizontal shift towards positive V_{FG} values that is larger for the 0.1×PBS solution.

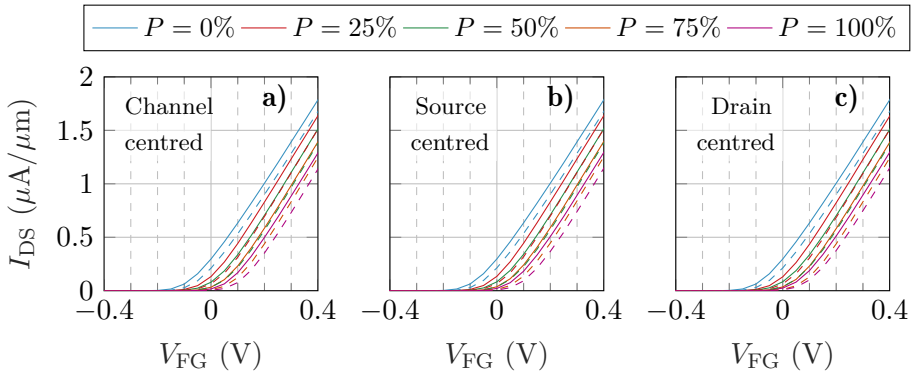

Figure 8.22: $I_{DS} - V_{FG}$ curves for the channel centred (a), source centred (b) and drain centred (c) molecule distributions.

The results in Figure 8.22 corresponds to a single receptor distribution, but in order to obtain statistically significant variabilities for the different spatial distributions, it is necessary to evaluate different distributions for

each scenario and study the changes in the response, i.e. in S. There are two sources of randomization for the sensing interface that are analysed separately. First, the receptor distribution that accounts for different receptor locations in a fixed activation configuration. Second, the activated receptors distribution that considers different activation configurations of the receptors for a fixed P value and receptor location. Figure 8.23 illustrates these two cases with examples: Figure 8.23a shows different distributions of receptors with a fixed configuration of activated receptors, while Figure 8.23b shows a fixed random distribution of receptors with different configuration of activated receptors.

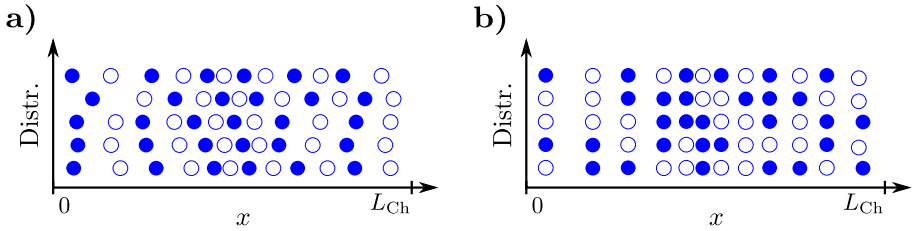

Figure 8.23: Example of five channel centred distributions with $P = 50\%$, where filled and empty circles represent activated and idle receptors, respectively. (a) Distribution variability: several receptor distributions are studied for a fixed activated receptor configuration. (b) Activation variability: several activated receptor configurations are studied for a fixed receptor distribution.

In the following, for the sake of clarity we will characterise the device response by S, at a fixed V_{FG} value. In this way it will be possible to collect and discuss the large amount of distributions and scenarios in a tractable and comprehensible way. The point $V_{FG} = 0.3$ V is chosen as the one at which the response of the device at full occupation, i.e. $S(P = 100\%)$, is maximum for the uniform receptor distribution (Figure 8.20). Next subsections are devoted to analyse the two scenarios for the randomization of the sensing interface from the analysis of $S(V_{FG} = 0.3$ V).

8.5.1 Randomized distribution variability

First, the randomized location of the receptors is considered using ten different random distributions for each of the three distribution scenarios aforementioned. A set of $S(P)$ responses is obtained for each scenario and the data is used to extract the standard deviation σ_S and mean value S_μ to characterise each distribution. These results are depicted in Figure 8.24 for the three scenarios where the standard deviation is indicated with the shadowed regions around the solid line indicating the mean $S(P)$ response. All these data are obtained using a 1×PBS electrolyte (blue lines) and a 0.1×PBS electrolyte (red lines). For the sake of comparison, the results for

uniformly distributed receptors are also depicted (black).

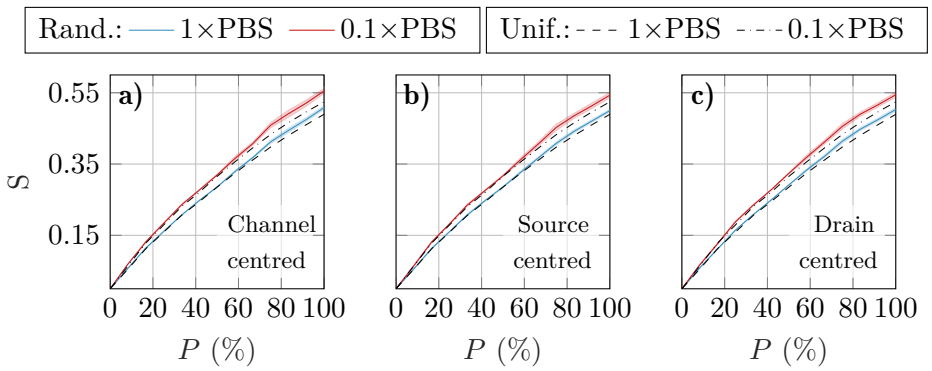

Figure 8.24: Sensor response as a function of the activation percentage for the (a) channel centred, (b) source centred and (c) drain centred receptor distribution scenarios. The values of S_μ and their respective σ_S are extracted from the data obtained by evaluating ten random distributions for each scenario. Black lines corresponds to the results obtained for the uniform distribution. Both 1×PBS (blue) and 0.1×PBS (red) electrolytes were used with all the distributions.

At first sight, Figure 8.24 shows that the simulations with a 0.1×PBS electrolyte provide higher sensitivity. This behaviour can be easily explained by the screening capability of the electrolyte. An electrolyte with a reduced ion concentration (0.1×PBS) enables a lower screening of the molecules that is translated into a higher coupling between them and the semiconductor channel. The standard deviation increases for higher P values and its is also modulated by the change in the bulk ion concentration. More specifically, a lower σ_S is observed for the 1×PBS electrolyte. When compared with the data from the uniformly distributed receptors (black lines) the simulations for the randomized receptor distribution provide a slightly higher S independently on the region where receptors are concentrated. This is due to a larger density of receptors in a particular region of the structure when the randomized scenarios are considered. The number of receptors is not changed, but when receptors are closer to each other, ions have less capability to accumulate and screen the molecule charge. This is verified with the 2D and 1D profiles of the charge associated to ions depicted in Figure 8.25 for the uniformly distributed receptors (Figure 8.25a) and one of the channel centred distributions (Figure 8.25b). These profiles show how ions accumulate around molecules, generating a diffusion layer around them. The 1D profiles for 1×PBS (blue lines) for the uniform distribution show how the diffusion layers around two consecutive molecules are separated, but get merged when a 0.1×PBS electrolyte (red lines) is considered. This effect is more acute for the channel centred distribution, where this merging of the diffusion layers is observed even for the 1×PBS electrolyte.

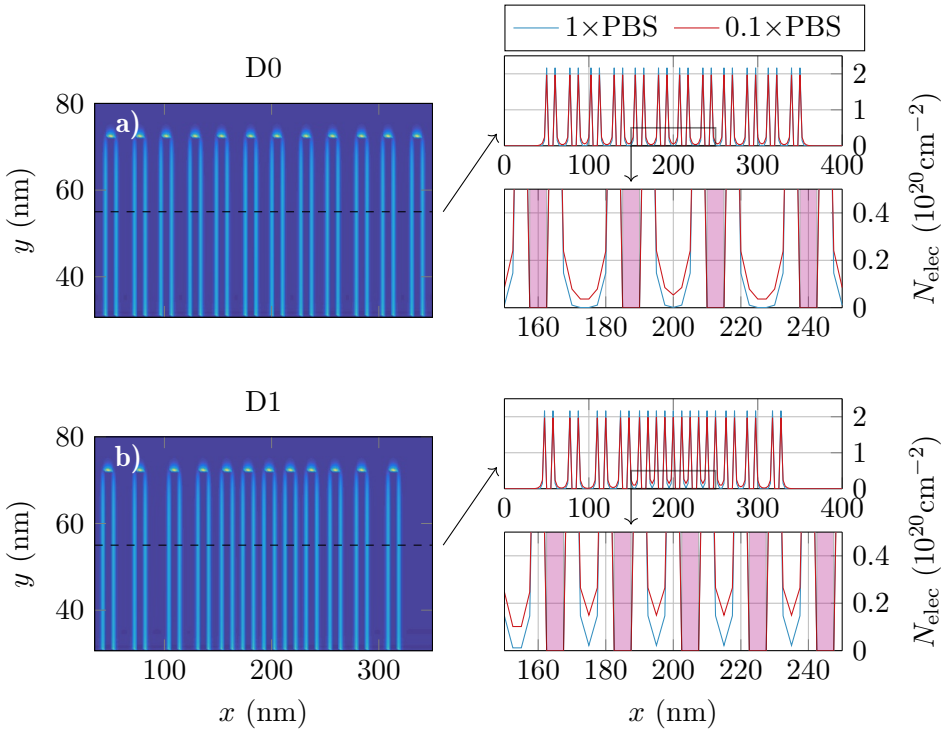

Figure 8.25: 2D distribution of the ions around the molecules for the uniform distribution (a) and one of the channel centred distributions (b). Figures on the right side shows a longitudinal cut (along X axis) of the 2D profiles at $y = 55$ nm and their detail at the centre of the channel (x coordinate between 150 nm and 250 nm). Molecule positions are indicated by red coloured regions.

When analysing the variability in the sensor response, one of the elements to be considered is the minimum change in the activation of the receptors that can be detected taking into account σ_S. If $S_\mu(P_i)$ and $S_\mu(P_{i-1})$ (i.e., the sensitivity mean values for a set of distributions with consecutive P values) happened to be closer than the addition of their standard deviations, $\sigma_S(P_i)$ and $\sigma_S(P_{i-1})$, the values P_i and P_{i-1} cannot be reliably measured. This limit can be defined as the resolution of the sensor, and we propose the ratio ζ to evaluate how it is impacted by the device variability:

$$\zeta(P_i) = \frac{S_\mu(P_i) - S_\mu(P_{i-1})}{\sigma_S(P_i) + \sigma_S(P_{i-1})} \tag{8.5}$$

A ζ value greater than 1 assures an unique relation between sensitivity and activation percentage. We evaluated this ratio for consecutive P values for non-uniform scenarios (Figure 8.26), finding that in all cases $\zeta > 1$. However, it should be noted that the larger dispersion of the data simulated

for 0.1×PBS solutions in Figure 8.24 is translated into lower ζ values in Figure 8.26 making them closer to the $\zeta = 1$ limit.

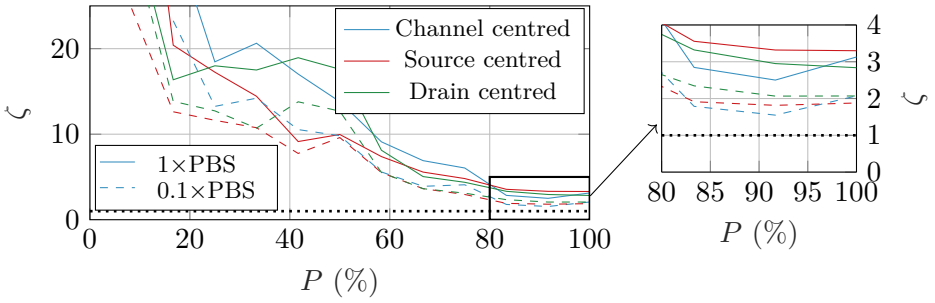

Figure 8.26: ζ ratio for the different distributions considered. Three colours and two line styles depict distinct scenarios and PBS concentrations, respectively. Dotted black line indicates the $\zeta = 1$ limit.

8.5.2 Randomized activation variability

The second aspect to be investigated is the influence of the variations in the receptor activation. For a single fabricated device with a certain distribution of N receptors, among which $N_{act} = \lfloor PN \rfloor$ of them are activated, there are $\frac{N!}{N_{act}!(N-N_{act})!}$ possible combinations of activated and idle receptor molecules. There are two cases where, obviously, only one configuration is possible, $P = 0\%$ and $P = 100\%$, while the number of combinations increases for intermediate values of P. Among them, we selected 12 random activated receptor configurations for each value of P. This is applied to the four distribution scenarios considered: uniform distribution (reference scenario), channel centred, source shifted and drain shifted. As before, 1×PBS and 0.1×PBS electrolytes are evaluated.

Figure 8.27 shows the $S_\mu - P$ profiles and their respective σ_S for the channel centred, source centred and drain centred, along with the data for the uniform receptor distributions (black lines). The channel centred scenario depicts higher S_μ and σ_S values when compared with the reference scenario. Concerning the results for the source centred and drain centred cases, the standard deviation is much lower in comparison with the channel centred scenario, although S are lower too, approaching the uniform receptor distribution scenario. This is more significant in the drain centred scenario, where differences with respect to the uniform distribution scenario are small. The data in Figure 8.27 evidences that a 1×PBS electrolyte provides lower S_μ and σ_S values, similarly to the receptor-location randomization scenario.

Finally, the profile of ζ has lower values compared with the previous

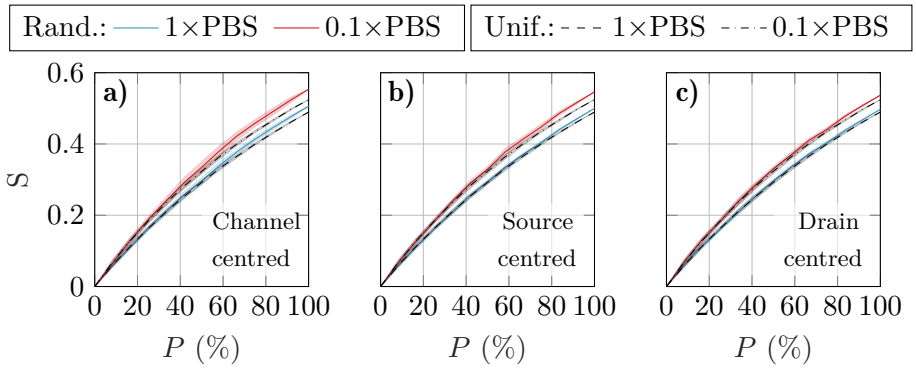

Figure 8.27: Device sensitivity as a function of P for the three receptor distribution scenarios considered ((a) channel centred, (b) source centred and (c) drain centred) when the activation of these receptors is randomized. The set of data to extract S_μ and σ_S is obtained from 12 different random activation distributions of receptors and two electrolytes: 1×PBS and 0.1×PBS. The data for the uniform receptor distribution is also included in each figure for the sake of comparison as black lines.

values depicted in Figure 8.28, particularly for intermediate values of P. This makes sense as the amount of combinations for that range of P values is quite large (the number of combinations reaches its maximum within the interval $50\% \leq P \leq 60\%$). This result indicates that the resolution of the sensor is more compromised by the randomization of the receptor activation than with their location, in other words, the random activation of the receptors is the commanding factor in order to hamper the quantization of the activated receptors in the sensor.

8.6 MoS_2 pH sensors: Site-Binding vs PMF

In Chapter 6 two key elements were introduced in order to properly model the physics of the insulator-electrolyte interface, the Potentials of Mean Force (PMF) profiles and the Site-Binding (SB) model. They are integrated in the simulations in distinct ways and reproduce specific physical aspects of the electrolyte which are, however, connected in subtle ways.

The SB is employed to model ion adsorption, and it has been frequently employed for hydrogen ions. The adsorbed ions generate a surface charge that depends on the electrolyte pH and the electrostatic potential in that region. The PMF profiles, on the contrary, are calculated for cations and anions aiming to include detailed atomistic information about the unique features of the interaction of each ion with the surface as well as among the different ions.

Both models can be integrated by exploiting the PMF profiles to deter-

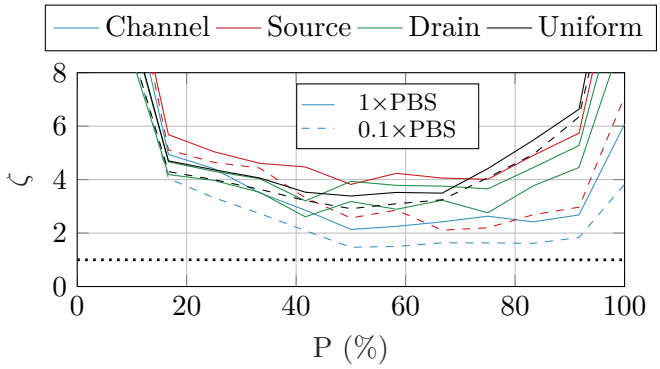

Figure 8.28: ζ ratio obtained from the randomization of the receptor activation. Different colours and line styles depict varying scenarios and PBS concentrations, respectively. Black line corresponds to $\zeta = 1$.

mine a reaction constant able to be included in the SB model [154, 155, 156]:

$$K_d = \left[N_{\text{Avg}} \cdot 10^3 \int_0^d 2\pi r^2 e^{\phi_{PMF}} dr \right]^{-1} \tag{8.6}$$

where d is chosen as the distance from the interface at which the PMF profiles have a negligible impact. The reaction constant is not the unique parameter relevant for the SB model. It is necessary to know the particular flow of reactions that take place at the interface between the ions and the active sites that are driven by K_d. In that concern, three schemes are evaluated and compared with the results obtained using the PMF profiles and the basic SB model, where the side reactions are not included.

For this study, the electrolyte considered in the simulations is a NaCl based solution, so the PMFs will include the effect of both ions, Na^+ and Cl^-, on the surface reactions. As indicated in Figure 8.29, three SB modified schemes are considered.

The first one is based on [9] where Na^+ ions interacts with the available sites at the insulator surface, while Cl^- ions interacts with the sites already activated with H^+:

$$\begin{aligned} &XO^- \overset{K_A}{\rightleftharpoons} XOH \overset{K_B}{\rightleftharpoons} XOH_2^+ \overset{K_C}{\rightleftharpoons} XOH_2Cl \\ &XO^- \overset{K_D}{\rightleftharpoons} XONa \end{aligned} \tag{8.7}$$

Two additional novel schemes are proposed. Both of them includes the additional reactions at the end of the sequence of reactions of the basic SB model, so ions are considered to interact with the final product of the SB reactions, either releasing a H^+ ion,

$$\begin{aligned} XO^- &\overset{K_A}{\rightleftharpoons} XOH \overset{K_B}{\rightleftharpoons} XOH_2^+ \overset{K_C}{\rightleftharpoons} XOHCl + H^+ \\ XOH_2^+ &\overset{K_D}{\rightleftharpoons} XOHNa^+ + H^+ \end{aligned} \tag{8.8}$$

or by not releasing it:

$$\begin{aligned} XO^- &\overset{K_A}{\rightleftharpoons} XOH \overset{K_B}{\rightleftharpoons} XOH_2^+ \overset{K_C}{\rightleftharpoons} XOH_2^+ - Cl^- \\ XO^- &\overset{K_D}{\rightleftharpoons} XOH_2^+ - Na^+ \end{aligned} \tag{8.9}$$

basic SB	$XO^- \overset{K_A}{\rightleftharpoons} XOH \overset{K_B}{\rightleftharpoons} XOH_2^+$
modified SB 1	$XO^- \overset{K_A}{\rightleftharpoons} XOH \overset{K_B}{\rightleftharpoons} XOH_2^+ \overset{K_C}{\rightleftharpoons} XOH_2Cl$ $XO^- \overset{K_D}{\rightleftharpoons} XONa$
modified SB 2	$XO^- \overset{K_A}{\rightleftharpoons} XOH \overset{K_B}{\rightleftharpoons} XOH_2^+ \overset{K_C}{\rightleftharpoons} XOHCl + H^+$ $XOH_2^+ \overset{K_D}{\rightleftharpoons} XOHNa^+ + H^+$
modified SB 3	$XO^- \overset{K_A}{\rightleftharpoons} XOH \overset{K_B}{\rightleftharpoons} XOH_2^+ \overset{K_C}{\rightleftharpoons} XOH_2^+ - Cl^+$ $XO^- \overset{K_D}{\rightleftharpoons} XOH_2^+ - Na^+$

Table 8.2: Reactions considered in the four schemes used in the simulations of the pH sensor.

	Value	basic SB	modified SB 1	modified SB 2	modified SB 3
K_A	6	$\frac{[XO^-][H^+]}{[XOH]}$	$\frac{[XO^-][H^+]}{[XOH]}$	$\frac{[XO^-][H^+]}{[XOH]}$	$\frac{[XO^-][H^+]}{[XOH]}$
K_B	-2	$\frac{[XOH][H^+]}{[XOH_2^+]}$	$\frac{[XOH][H^+]}{[XOH_2^+]}$	$\frac{[XOH][H^+]}{[XOH_2^+]}$	$\frac{[XOH][H^+]}{[XOH_2^+]}$
K_C	$97.7{\cdot}10^{-3}$		$\frac{[XOH_2^+][Cl^-]}{[XOH_2Cl]}$	$\frac{[XOH_2^+][Cl^-]}{[XOHCl^-][H^+]}$	$\frac{[XOH_2^+][Cl^-]}{[XOH_2^+ - Cl^-]}$
K_D	$97.1{\cdot}10^{-3}$		$\frac{[XO^-][Na^+]}{[XONa]}$	$\frac{[XOH_2^+][Na^+]}{[XOHNa^+][H^+]}$	$\frac{[XOH_2^+][Na^+]}{[XOH_2^+ - Na^+]}$

Table 8.3: Dissociation constants for each of the schemes in Table 8.2

These schemes are intended to emulate the results for the simulations combining the SB model and the PMF profiles. As aforementioned, the reaction constants K_C and K_D are obtained from the PMF profiles associated to the ions involved in their respective reactions (according to expression (Eq 8.6)). The four schemes for surface ion adsorption and their dissociation constants are summarised in Table 8.2 and Table 8.3, respectively, and their $N_{\text{it}} - \phi_{\text{interf}}$ profiles are depicted in Figure 8.29.

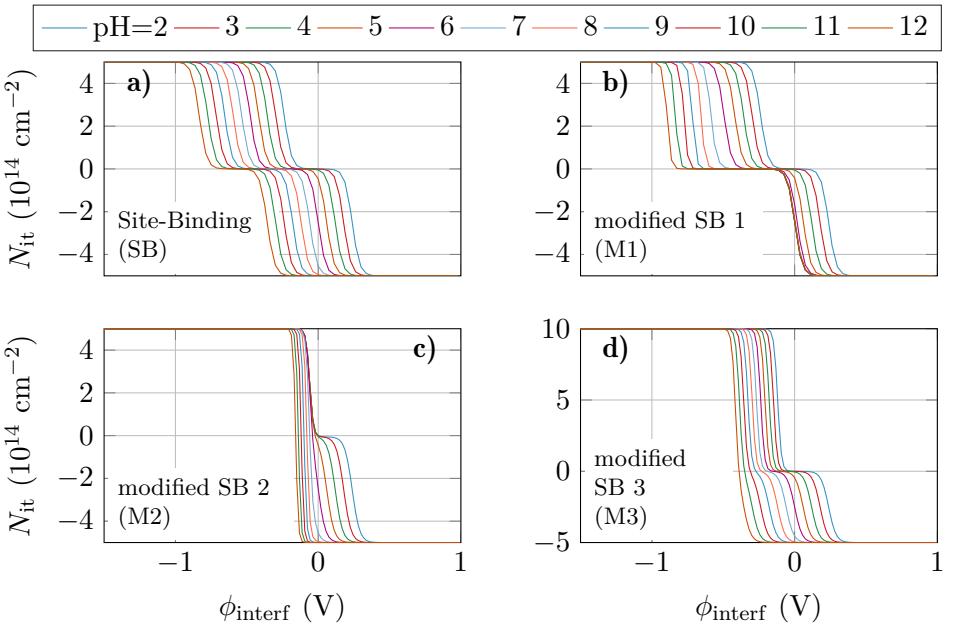

Figure 8.29: $N_{it} - \phi_{interf}$ profiles for the different surface ion adsorption models considered for the pH sensor.

Remarkable differences in the $N_{it} - \phi_{interf}$ profiles can be observed among the four schemes shown in Figure 8.29. SB and M1 schemes follow a similar trend, although the $N_{it} = 0$ plateau for M1 increases as the pH does too. Schemes M2 and M3 depict this plateau only for low pH values, and it disappears as higher values of the pH are considered. This behaviour is originated by the reaction involving Na^+ ions.

The comparison between these SB models is now evaluated in the sensing surface of a MoS_2 based pH ISFET, as depicted in Figure 8.30. That structure is defined by a 100 nm-long monolayer MoS_2 semiconductor on top of a SiO_2 substrate. The MoS_2 layer is covered by a 5 nm-thick SiO_2 layer that is in contact with the electrolyte, acting as a sensing layer. Regarding the electrolyte, it is defined by a NaCl based solution with $[Na^+] = [Cl^-] = 100$ mM. The PMF profiles for these ions (shown in Figure 8.31) are extracted from [157], where MD simulations involving these two ions and a SiO_2 surface were carried out.

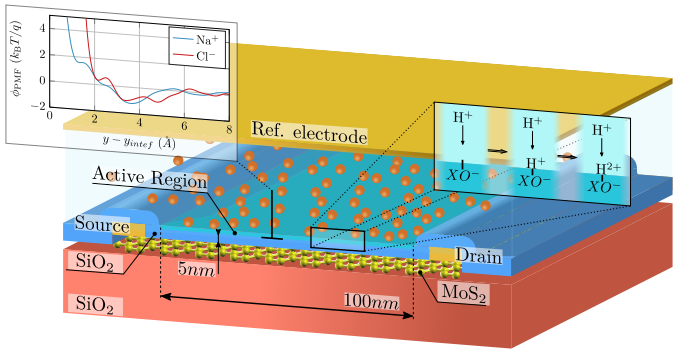

Figure 8.30: Structure of the pH ISFET considered in the simulations. The hydrogen ion adsorption is handled with the SB model and the surface interaction with other ions is included with PMF profiles.

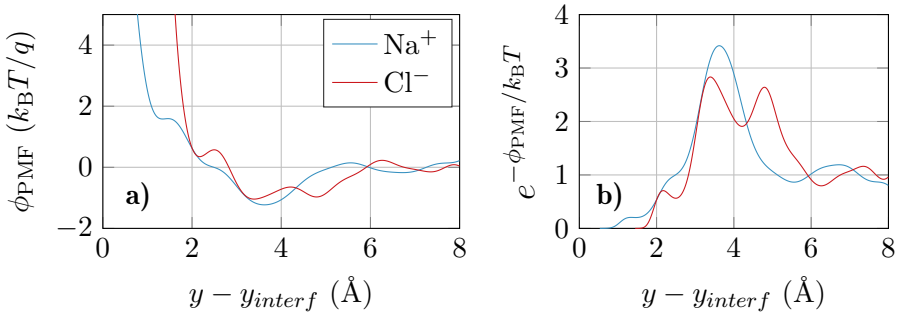

Figure 8.31: a) PMF profiles extracted from [157] and b) their spatial-dependent contribution to the concentration of Na^+ and Cl^- ions.

Next, the transfer response of the device ($I_{DS} - V_{GS}$) is determined for different pH values of the solution. The results are used to describe the behaviour of the sensor and compare the outcome of the different schemes: i) basic SB model (*only* SB), ii) basic SB model combined with the PMF profiles for the ion distribution (PMF+SB), iii) scheme M1, iv) scheme M2 and v) scheme M3. Three electrical readouts are considered to analyse the sensor response when using each of these schemes: a) changes in I_{DS} generated by changes in pH [158], b) changes in the threshold voltage [16], and c) varying gate bias to keep a constant I_{DS} as pH changes [9]. In all the cases $V_{DS} = 0.1$ V.

8.6.1 pH dependent I_{DS}

The simplest definition of the sensor response is based on changes in the output current with respect to a reference state. In this case, the latter is assumed to correspond to pH=7 and $V_{FG} = 0.2$ V, as it is the bias that provides a symmetric $I_{DS}-$pH response for the *only SB* scenario. The results obtained for the five surface interaction schemes considered are depicted in Figure 8.32.

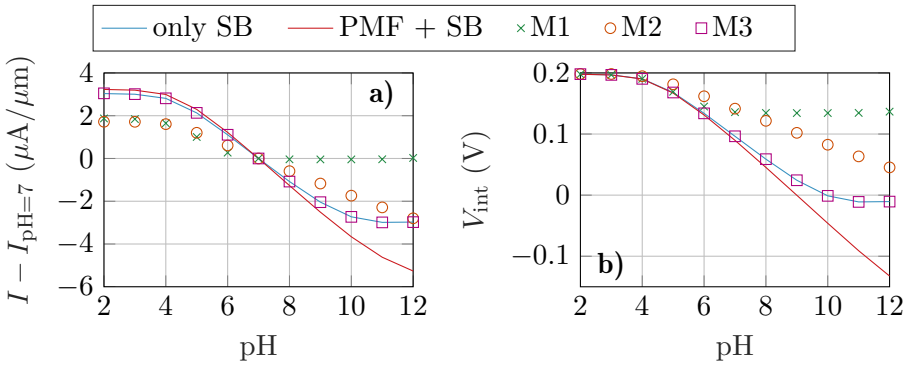

Figure 8.32: a) Change in the output current and b) interface potential evolution with the pH values simulated for each of the five schemes considered regarding solid-electrolyte surface interactions.

Figure 8.32 shows the change in the output current with respect to the pH= 7 scenario along with the respective interface potential V_{int} profile. These results show clear differences between the schemes here employed. First, results considering only the regular SB model depicts a saturated trend for low (pH$\leq$4) and high (pH$\geq$10) pH values. When PMF profiles are included in the simulations, this saturation is observed for low pH values, but it is reduced for high pH values. This trend is also observed for the M2 scheme but with a scale factor. With regards to the M1 and M3 schemes, the former depicts a strong saturation for pH values above 7, while the latter accurately reproduces the behaviour of the SB model.

The $V_{int}-$pH profiles of Figure 8.32b lead to similar comments when comparing the different models. When the SB model is considered along with PMF profiles, the saturation of the $V_{int}-$pH curves disappear for large pH values, showing a linear trend. M2 is the only scheme able to reproduce this linear variation but with a reduced slope. M3 mimics the behaviour of the *only* SB scenario, while M1 depicts a strong saturation for pH values above 6.

The results regarding the output current I_{DS} and potential interface V_{int} are complemented with the profiles of the charge associated to ions in the electrolyte and charge associated to the SB model. Their respective 2D

profiles can be integrated along the device cross-section so to obtain the results depicted in Figure 8.33:

$$\begin{aligned} N_{\text{elec}} &= \int_0^L \int_{y_{\text{interf}}}^{y_{\text{interf}}+1nm} N_{\text{elec}}(x,y)dydx \\ N_{\text{int}} &= \int_0^L N_{\text{int}}(x, y_{\text{interf}})/t_{\text{SB}}dx \end{aligned} \tag{8.10}$$

where y_{interf} is the position of the solid-electrolyte interface and t_{SB} the size of the region associated to the SB charge, which corresponds to the grid size at the solid-electrolyte interface (this charge is assumed to extend one point of the grid in the direction perpendicular to the interface).

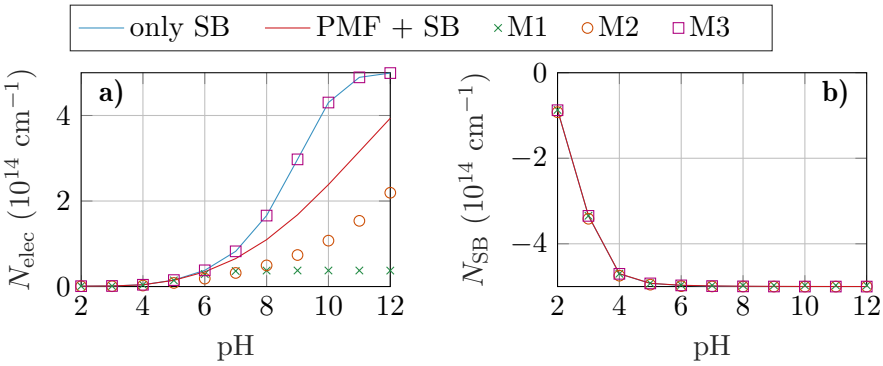

Figure 8.33: a) electrolyte ions and b) SB associated charge profiles as a function of the pH for $V_{\text{GS}} = 0.2V$.

Surprisingly, there are not differences between the $N_{\text{SB}}-$pH profiles in Figure 8.33b, which indicates that the response of the device is mainly generated by the distribution of ions in the electrolyte. The *only SB* and PMF+SB schemes uses the same $N_{\text{it}} - \phi_{\text{interf}}$ ($\phi_{\text{interf}} = V_{\text{int}} - V_{\text{GS}}$) profile, so the differences between them in the $N_{\text{elec}}-$pH profiles corresponds directly to the impact of the PMF. As depicted in Figure 8.33a, these profiles give rise to a slower evolution of N_{elec} that can be associated to the limited ion concentration near the interface.

8.6.2 pH dependent threshold voltage

A more elaborated definition of the sensor response is based on changes of the threshold voltage V_{th}. In this case, this parameter is extracted from the transfer responses as the gate bias at which the derivative of the transconductance is maximum. Figure 8.34 shows the $V_{\text{th}}-$pH profiles extracted from simulation for the different models.

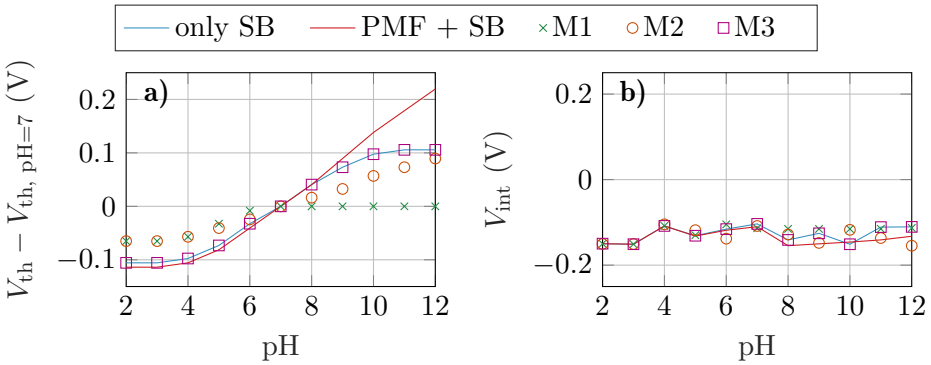

Figure 8.34: a) differences in the threshold voltage (V_{th}) with respect to the pH= 7 scenario, and b) evolution of the potential at the interface V_{int}.

The response of the sensor based on V_{th} has a saturated trend in both extremes of the pH range considered, with M1 depicting the strongest saturation. The exception is the PMF+SB and M2 scenarios, which does not show a saturation at the edges of the pH range. With regards to V_{int} at the threshold voltage, it is independent of the pH values (V_{int} ≈-0.13±0.02V). As indicated in Section 3.4, in a regular MOSFET, the bias $V_{GS} = V_{th}$ generates the channel to enter the strong inversion regime and the band bending to reach this situation only depends on the characteristics of the semiconductor (Eq 3.5). In the case of the ISFET, this definition is translated as the reference electrode bias that generates the same potential at the solid-electrolyte interface. Therefore, it makes sense to obtain a constant V_{int} when V_{GS} follows the profiles depicted in Figure 8.34 as the pH is modified.

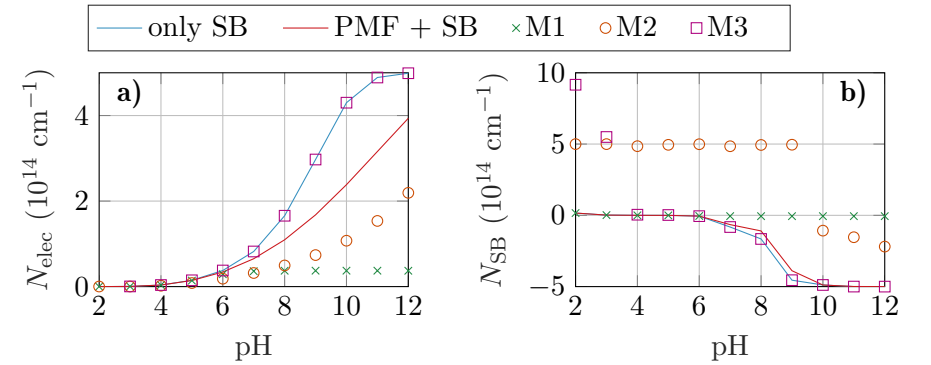

Figure 8.35: a) Electrolyte and b) interface associated charge as a function of the pH of the solution for $V_{GS} = V_{th}$.

The $N_{elec}-$pH and $N_{SB}-$pH curves in this case are depicted in Fig-

ure 8.35. The differences in N_{elec} with respect to the data in Figure 8.33 are negligible, demonstrating that the electrolyte changes are not varying significantly in this range of bias. However, the differences between the $N_{SB} - \phi_{interf}$ profiles for the different schemes are more remarkable. As ϕ_{interf} is constant, the changes observed are generated by the horizontal shift observed in the $N_{it} - \phi_{interf}$ profiles plotted in Figure 8.35 as the pH is modified.

8.6.3 pH dependent control gate bias

Finally, we consider as electrical readout the MOSFET gate bias (controlled by a closed loop) necessary to keep the same value of I_{DS} while the pH value is modified, as in [9]. This scenario cannot be simulated as it is, so it is emulated by obtaining an $I_{DS}(V_{FG}, \text{pH})$ map. It is then used to extract the V_{FG} values that provides $I_{DS}(V_{FG} = 0.2\text{V}, \text{pH}=7) = 6\mu\text{A}/\mu\text{m}$ for the different pH values considered. The resulting $V_{ctr}-$pH profile for each scheme is depicted in Figure 8.36.

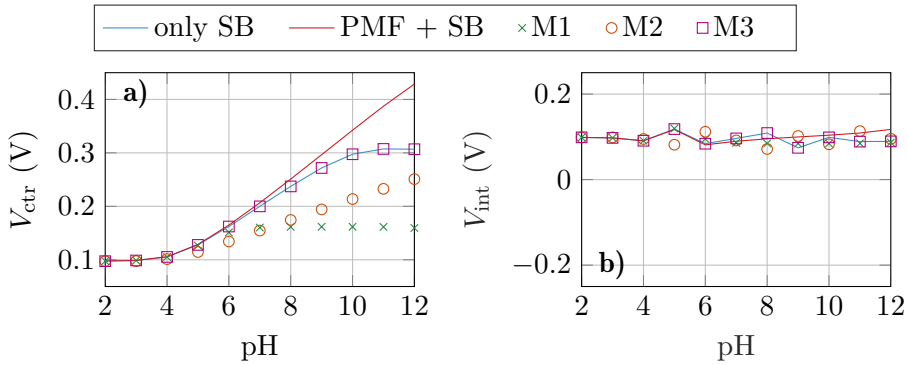

Figure 8.36: a) $V_{ctr}-$pH profiles obtained with the five schemes considered and b) their respective $V_{int}-$pH profiles.

This scenario is quite similar to the previous one regarding the $V_{th}-$pH relation, as a constant I_{DS} requires a constant V_{int}, which in this case it corresponds to V_{int} ≈96.15±0.1mV. The results for the different schemes do not differ below pH= 5, while above this value they depict different trends. M2 and the PMF+SB scenario follow a linear trend, although the evolution of V_{ctr} is much softer for the M2 scheme. M1 provides a $V_{ctr}-$pH profile with a strong saturation, for pH values above 9 the change in V_{ctr} is negligible. Finally, the M3 scheme mimics the behaviour of the *only* SB scenario, similar to previous sections.

The constant V_{ctr} obtained in this case is translated into the charge profiles depicted in Figure 8.37. The N_{SB} profiles in this case are equal,

following a similar trend to Figure 8.33, as all the schemes show the same behaviour for positive values of ϕ_{interf}, and the charge in the electrolyte does not change significantly with respect to the previous scenarios.

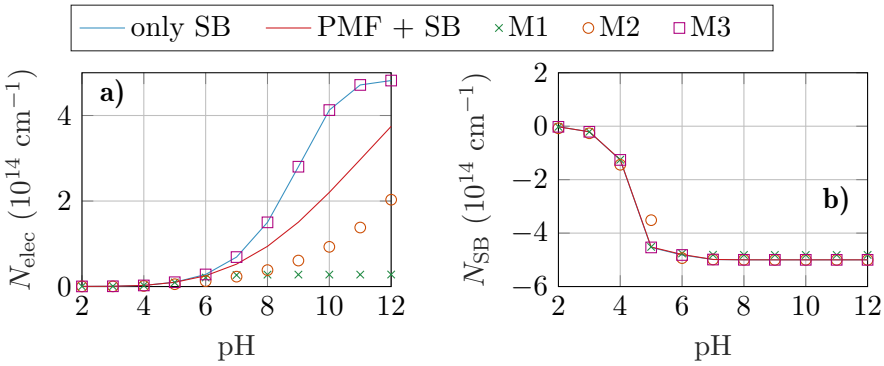

Figure 8.37: a) Electrolyte and b) interface associated charge as a function of the pH of the solution for $V_{\text{GS}} = V_{\text{ctr}}$.

Part V

Conclusions

CHAPTER 9

Conclusions and future work

9.1 Conclusions

The main objective of this Thesis was the development of a comprehensive set of numerical tools specifically designed to analyse 2DMs-based FET biosensors, able to provide a deeper understanding of their operation principles and to shed light in the fundamental physical and electrical parameters involved in their optimization. In that concern, the main contributions of this work to the state-of-the-art are the following:

- A semi-classical transport model that integrates the DoS of the materials enabling the integration of information from *ab-initio* calculations. The most common fashion combining information in a multi-scale approach in computational nanoelectronics is based in quantum transport approaches that handle the charge transport in the device by means of non-equilibrium Green functions exploiting TB or Wannier-like Hamiltonians. These approaches are computationally very expensive and are mostly focused on ultra short channel devices, aiming to propose new device concepts or predict the ultimate performance of the devices. Current realizations of 2DM-based MOSFETs, however, are closer to the semi-classical transport paradigm. Therefore, the multiscale semi-classical approach presented in this work is a relevant contribution to the state-of-the-art, and its capabilities has been demonstrated by analysing GaSe MOSFETs with strained channels.

- A flexible model for charge traps enabling generic energetic profiles and location in the structure. A complex modelling of interface traps is introduced and exploited to explain experimental data of MoS_2 FETs. Non-idealities in real devices and their associated complexities are the ultimate frontier between idealized simulation and realistic experimental realizations. The implementation and validation of the

trap model presented in this Thesis showed up as a powerful tool in that concern, reproducing in a very good manner the behaviour of real devices, even in the transient regime, and paving the way for a better understanding of the role of traps in MoS_2 FETs.

- A model of complex electrolytes that encompasses steric effects, contribution of pH regulation reactions of PBS and surface interactions for simple ions. The combination of these models provides a complete description of the electrolyte, being the most novel the integration of PMF profiles. This feature enables the possibility to integrate information from MD simulations, and other similar *ab-initio* approaches from liquid solutions, to handle ions-solid interactions in a quite precise manner.

- A model for the sensing interface involving the charge distribution of molecules and the location of receptors. The large variety of biomolecules requires a flexible model to adapt their properties to the device scale. In that regard, the developed numerical simulator provided a flexible generic one (the box based model) for a rapid modelling of these elements together with two more sophisticated ones: a precise modelling of the molecule shape and charge distribution (fine molecule model) obtained from MD simulations, and a specific one for DNA molecules, developed due to the simplicity of their modelling. They might be subject of future improvements, but in the form that they have been presented provide an important contribution in the avant-garde of state-of-the-art. These models come along with the possibility to randomize the location of receptor molecules in order to study device-to-device variations and perform statistical assessments of the sensor on the sensor response, enabling technology-centred studies focusing on features related with the fabrication of commercial applications.

- The simulation scheme has been used to evaluate the impact of access regions in the transfer response of GFET devices. The results show how these regions are able to emulate the behaviour of asymmetric $I-V$ responses while, keeping symmetric carrier mobility, refuting the commonly associated asymmetry in mobility to experimental transfer responses with the same feature. In this regard, the access region associated to the source contact showed up as the one with a higher impact on the transfer response asymmetry. Simulations also include the effect of a back gate as a method to improve the conductivity of these regions. This additional gate reduces the resistivity of these regions, as expected, but at the cost of a highly asymmetric response.

- The *ab-initio* - DD integration capabilities of the Fermi-level based

DD have been used to study GaSe MOSFETs with strained channels. Single and split gate devices are analysed showing a relation between the type of strain considered and the type of main carrier observed. This work provides some insights about mechanical strain technology as a doping method for 2DMs, that is still a mayor obstacle for the industrial adoption of 2DM-based devices, thus illustrating the usefulness of this approach.

- The transport model for GFETs and the fine receptor-target charge distribution model are combined to evaluate the capability of this type of devices for the detection to SARS-CoV-2. Results depict a higher response in the n-branch of the device response, which, at first sight, appears counter-intuitive as the considered receptor-target complex is negatively charged. This, however, was explained with a detailed analysis of the carrier density and potential profiles in the structure revealing the significant role of the charge distribution of the receptor and receptor-target complex in the behaviour of the device.

- Device-to-device variability is analysed in MoS_2 BioFETs for DNA detection, combining the specific receptor-target model for DNA molecules and the randomization of the receptor location. Different receptors distribution and activation configurations are analysed. The simulations show that a higher concentration of receptors at the centre of the channel provides some improvement of the sensor response, even compared with the ideal uniform receptor distribution, and that the randomization in the receptor activation pattern has a higher impact on the variability of the sensor response rather than the receptor location.

9.2 Future work

The numerical platform developed in this Thesis exhibits a great potential not only due to the complexity of the models implemented but also due to the possibility to connect simulations with lower abstraction level calculations. There are many options for further studies taking advantage of these features with the following ones being planed as continuation works of this Thesis:

- Time dependent simulations of electrolytes: time dependency is included in the models for FET devices (semiconductor charge transport and charge traps), but its extension to the models related with the electrolyte and the sensing interface is pending.

- Self-consistent buffer-solution pH regulation reactions: the current implementation of the complex electrolyte assumes a constant pH when evaluating the local changes in the concentrations of the components related with the buffer. The next step in the implementation of this model entails the self-consistent calculation of these concentrations along with the pH.

- The inclusion of the self-consistent calculation of molecule charge with local pH by introducing the isoelectric point of molecules to address the changes of their charge with the local pH, is a future continuation of the fine-molecule modelling.

- Extending the list of buffer solutions supported is also an aspect to be evaluated: this Thesis addresses the reactions related with PBS solution, but there are other existing buffer solutions that involves different components.

- Simulation of heterostructures: One the most attractive features of 2DMs is the possibility of fabricating heterostructures (vertical or lateral) with enhanced characteristics. In this regard, the models for the semiconductor device would need to be extended to analyse the use of these structures for BioFET devices.

- Contact resistances: experimental data fitting was done by adding regions with limited conductivity (doping), so to reproduce the impact of contact resistances. More sophisticated models of the contact resistances are of interest to more realistically treatment of this aspect in 2DMs-based devices.

Part VI

Appendices

Appendix A **Density of states**

This appendix is intended to define the expressions used to calculate the charge density for different confinement cases. Apart from the confinement scenario considered, the carrier density can be obtained as the sum of the occupied states of each conduction band energy:

$$n = \int_{E_c}^{\infty} g\left(E\right) f_n\left(E\right) dE \tag{A.1}$$

where $g(E)$ is the Density of States (DoS) and $f_n(E)$ is the Fermi-Dirac function.

A.1 No confinement

In this case, electrons can move in all directions without any restriction. Then, the density of states is evaluated as:

$$g_{3D}\left(E\right) = \frac{1}{2\pi^2}\left(\frac{2m^*}{\hbar^2}\right)^{3/2} E^{1/2} \tag{A.2}$$

Then the electron density is calculated by making use of (Eq A.1) as:

$$\begin{aligned} n &= \int_{E_C}^{\infty} \frac{1}{2\pi^2}\left(\frac{2m^*}{\hbar^2}\right)^{3/2} \frac{\left(E-E_C\right)^{1/2}}{1+e^{\frac{E-E_F}{K_{\mathrm{B}}T}}} dE \\ &= \frac{1}{2\pi^2}\left(\frac{2m^* k_{\mathbf{B}} T}{\hbar^2}\right)^{3/2} \int_0^{\infty} \frac{\left(\frac{E-E_C}{k_{\mathbf{B}}T}\right)^{1/2}}{1+e^{\frac{(E-E_C)-(E_F-E_C)}{K_{\mathrm{B}}T}}} d\frac{E-E_C}{k_{\mathbf{B}}T} \\ &= N_{C_{3D}} \mathcal{F}_{\frac{1}{2}}\left(\frac{E_F-E_C}{k_{\mathbf{B}}T}\right) \end{aligned} \tag{A.3}$$

where $\mathcal{F}_{\nu}\left(x\right)$ is the Fermi integral function, defined as:

$$\mathcal{F}_{\nu}\left(x\right) = \int_0^{\infty} \frac{\tau^{\nu}}{e^{\tau-x}+1} d\tau \tag{A.4}$$

and $N_{\mathrm{C_{3D}}}$ is calculated as:

$$N_{\mathrm{C_{3D}}} = \frac{1}{2\pi^2}\left(\frac{2m^* k_{\mathbf{B}} T}{\hbar^2}\right)^{3/2} \tag{A.5}$$

A.2 1D confinement

When the movement of electrons is limited in one of the directions, it is said that there is unidimensional confinement. In this case, the density of states is calculated as:

$$g_{2D} = \frac{m^*}{\pi\hbar^2} \tag{A.6}$$

The electron density is obtained as in the previous section, but using g_{2D} instead of g_{3D}:

$$\begin{aligned} n &= \frac{m^* k_{\mathbf{B}} T}{\pi\hbar^2}\int_0^\infty \frac{1}{1+e^{\frac{(E-E_C)-(E_F-E_C)}{K_{\mathrm{B}}T}}} d\frac{E-E_C}{k_{\mathbf{B}}T} \\ &= N_{C_{2D}}\mathcal{F}_0\left(\frac{E_F-E_C}{k_{\mathbf{B}}T}\right) \end{aligned} \tag{A.7}$$

where $N_{\mathrm{C_{2D}}}$ is calculated as:

$$N_{\mathrm{C_{2D}}} = \frac{m^* k_{\mathbf{B}} T}{\pi\hbar^2} \tag{A.8}$$

A.3 2D confinement

Now, the movement of electrons is limited in two directions. The density of states in this case is defined as:

$$g_{1D} = \frac{1}{\pi}\left(\frac{m^*}{\hbar^2}\right)^{1/2} E^{-1/2} \tag{A.9}$$

If this density of states is used to calculate the electron density, the following expression is achieved:

$$\begin{aligned} n &= \frac{1}{\pi}\left(\frac{m^* k_{\mathbf{B}} T}{\hbar^2}\right)^{1/2}\int_0^\infty \frac{\left(\frac{E-E_C}{k_{\mathbf{B}}T}\right)^{-1/2}}{1+e^{\frac{(E-E_C)-(E_F-E_C)}{K_{\mathrm{B}}T}}} d\frac{E-E_C}{k_{\mathbf{B}}T} \\ &= N_{C_{1D}}\mathcal{F}_{-\frac{1}{2}}\left(\frac{E_F-E_C}{k_{\mathbf{B}}T}\right) \end{aligned} \tag{A.10}$$

where $N_{\mathrm{C_{1D}}}$ is calculated as:

$$N_{\mathrm{C_{1D}}} = \frac{1}{\pi}\left(\frac{m^* k_{\mathbf{B}} T}{\hbar^2}\right)^{1/2} \tag{A.11}$$

Appendix B **Finite Differences method**

In this Thesis, the numerical resolution of the differential equations that model the devices is based on the Finite Difference (FD) approach. In this appendix, this method is introduced. Numerical methods target the solution of equations that cannot be solved analytically, that is, through symbolic manipulation. To that end, several approximation are considered to translate the equations to the discrete world. The most remarkable advantage of this translation is the use computational calculus to solve these equations. As just mentioned, this work makes use of the FD method, based on the Taylor series expansion. Given a function $f(x)$, defined into the interval (a, b) along with all its k-derivatives, it can be evaluated around a point x_i by its k-order Taylor series expansion as:

$$f(x) = f(x_i) + \frac{x - x_i}{1!} \left.\frac{df}{dx}\right|_{x_i} + \frac{(x - x_i)^2}{2!} \left.\frac{d^2 f}{dx^2}\right|_{x_i} + \cdots + \frac{(x - x_i)^k}{k!} \left.\frac{d^n f}{dx^k}\right|_{x_i} \tag{B.1}$$

where the latest term defines the error, named as truncation error, committed when using k terms.

The FD methods splits the interval (a, b) into subintervals of size Δ, and the function $f(x)$ is evaluated in each of the x_i points defined by these subintervals:

$$f(x_i) = f(a + i\Delta), \quad i = 0, 1, \cdots, \left\lfloor \frac{b - a}{\Delta} \right\rfloor \tag{B.2}$$

The discretization of the interval (a, b) can be done with a varying Δ, so that some regions inside (a, b) are explored in more detail. In this case:

$$\begin{cases} f(x_i) = f(x_{i-1} + \Delta_{i-1}), \quad i = 1, \cdots, \left\lfloor \frac{b-a}{\Delta} \right\rfloor \\ x_0 = a; \end{cases} \tag{B.3}$$

In this work, a non-uniform grid is considered for the resolution of the equations, that is, Δ depends on the index i ($\Delta_i = x_i - x_{i-1}$). Setting this

as the starting point, it is possible to define the approximated expressions of the derivatives of the functions. In this case we are only interested in the first and second order derivatives. Beginning with the first order derivatives, there are three ways to evaluated them: backward, centred and forward approximations. First, the backward approximation uses the previous point x_{i-1} to state the derivative:

$$\frac{df(x)}{dx} \equiv \frac{f(x_i) - f(x_{i-1})}{\Delta_{i-1}} \tag{B.4}$$

Forward approximation follows the same motive, but using the following point x_{i+1}:

$$\frac{df(x)}{dx} \equiv \frac{f(x_{i+1}) - f(x_i)}{\Delta_i} \tag{B.5}$$

Finally, the centred approximation is a combination of the previous ones, which makes use of both previous and next points:

$$\frac{df(x)}{dx} \equiv \frac{f(x_{i+1}) - f(x_{i-1})}{\Delta_{i-1} + \Delta_i} \tag{B.6}$$

Moving to the second derivative, its definition based on df/dx:

$$\begin{aligned}\frac{d^2f(x)}{dx^2} =& \frac{d}{dx}\left(\frac{df}{dx}\right) \equiv \frac{d}{dx}\left(\frac{1}{\Delta_{i-1}/2 + \Delta_i/2}\left(\frac{df(x_{i+1/2})}{dx} - \frac{df(x_{i-1/2})}{dx}\right)\right) \\ =& \frac{1}{\Delta_{i-1}/2 + \Delta_i/2}\left(\frac{f(x_{i+1}) - f(x_i)}{\Delta_i} - \frac{f(x_i) - f(x_{i-1})}{\Delta_{i-1}}\right)\end{aligned} \tag{B.7}$$

where the index $i \pm 1/2$ states of for the mid points.

All these expressions are valid for a 1D space, however, the same procedure can be used to obtain the expressions for two or more dimensions.

Appendix C Randomized molecule distribution

The random distributions of molecules introduced in Section 6.4.4 for the simulation of BioFETs have shown an implementation issue related with the definition of y_{k-1}, needed to locate the first molecule. Two options were analysed to define this parameter: i) a fixed initial point based on the location of the receptor layer, and ii) a randomized initial point near the initial point of the receptor layer. In the case of the fixed initial point, this is set to:

$$y_{-1} = p_0 + \frac{l_M}{2} \tag{C.1}$$

where p_0 is the initial point of the receptor layer. For the randomized initial point, a list of random points is generated starting from p_L to p_0. Then, the closest point to $p_0 + l_M/2$ is chosen as y_{k-1} to set the position of the first receptor molecule.

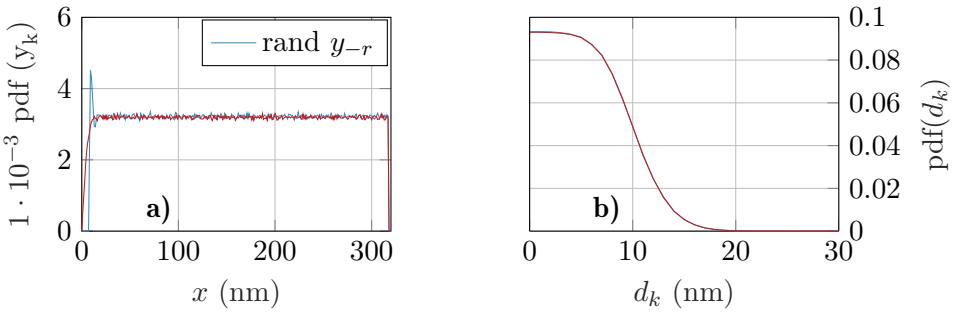

Figure C.1: (a) pdf of the position of the molecules y_k along receptor layer using a fixed initial point y_{-1} (blue) or randomizing it (red), and (b) pdf of the post-processed distance between molecules d_k in each case.

Figure C.2 shows that both methods provide the same pdf profile for d_k but a slightly different pdf profile for y_k. Far from the initial point there is

no differences between the methods, but near $y = 0$ the randomized initial point method depicts a softer profile akin to the ideal uniform distribution. This analysis is extended with changes in d_r, obtaining the profiles depicted in Figure C.2. That figure depicts the Probability Density Function of the hypothetical position of the molecules, y_k, along a 300 nm-long receptor layer, using two different values of d_r and the two methods aforementioned to set y_{-1}. These profiles were extracted by generating $50 \cdot 10^3$ distributions of molecules.

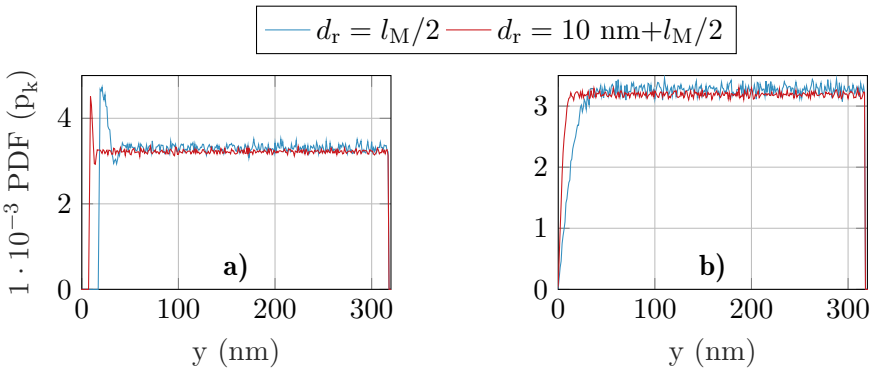

Figure C.2: pdf of the position of the molecules y_k along receptor layer using a fixed initial point y_{-1} (a) or randomizing it (b). Two values of d_r are considered for each case: $l_\mathrm{M}/2$ and 10 nm$+l_\mathrm{M}/2$.

Figure C.2 shows that the pdf profile for the fixed y_{-1} is more impacted by changes in d_r. A shorter space between molecules enlarges the width of the peak with higher probability and the width of the region where no molecules are placed. For the randomized y_{-1} scenario, a shorter d_r only generates a softer transition to the region with constant pdf profile.

The previous analysis is repeated with the random distribution with a position dependent σ. The same two options, fixed and randomized y_{-1}, were tested obtaining the profiles depicted in Figure C.3.

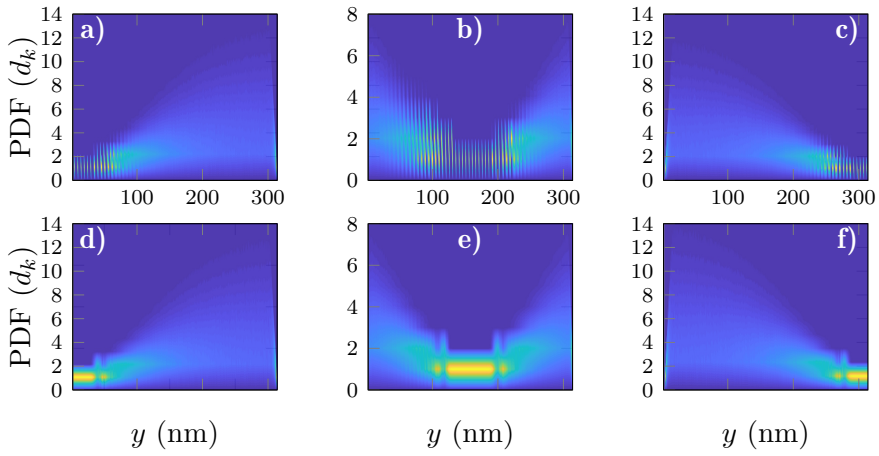

Figure C.3: pdf of d_k along the receptor layer for the three scenarios considered: dense distribution near $y = 0$ (a, d), dense distribution at the centre of the sensing layer (b,e), and dense distribution near $y = L$ (c,f). Plots at the top show the distribution when a fixed initial point is considered, while the plots at the bottom show the distribution when this initial point is randomized.

Figure C.3 shows that a fixed staring point for the molecule distribution removes the randomness of the molecule distribution in the high-receptor-density region. This is not desired, so the randomized y_{-1} is the method that provides the desired behaviour.

Appendix D Impact of access regions in GFETs RF performance

The analysis described in Section 7.3 was extended to determine the impact of the access regions in the Radio-Frequency (RF) performance. This analysis was performed through the cut-off frequency, f_T, as a RF Figures of Merit (FoM). The value of f_T is calculated as in [128, 159]:

$$f_T = \frac{1}{2\pi} \frac{g_m}{C_{fg}} \tag{D.1}$$

where g_m is the transconductance and C_{fg} the front gate capacitance.

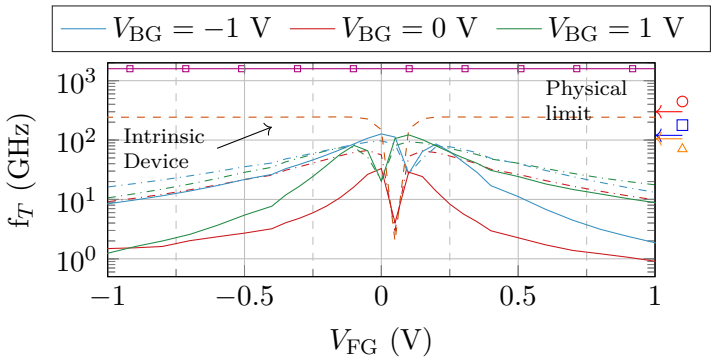

Figure D.1: f_T of the back-gated device with access regions under two scenarios: no puddles (solid lines) and $N_p = 10^{12}$ cm^{-2} (dash-dotted lines). The values obtained for the intrinsic device are depicted by the purple dashed line. The arrows labelled by marks on the right side axis indicate the values of f_T extracted from [160] (circles) and [161] (squares and triangles). The yellow line indicates the physical limit for graphene $v_F/2\pi L$, determined by the transit time L/v_F, with the Fermi velocity $v_F \approx 10^8 cm/s$ and L =100 nm (squares).

Figure D.1 shows f_T as a function of V_{FG} under two scenarios: no puddles (solid lines) and $N_p = 10^{12}$ cm^{-2} (dash-dotted lines). To assess the

impact of the access regions, the performance of the intrinsic device (structure indicated by the dotted rectangle in Figure 7.9) is depicted too (dashed lines). In addition, to evaluate the magnitude of the calculated values, the experimental measurements of f_T reported in [160] and [161] are indicated by the arrows on the right side axis of Figure D.1. Despite the device structure and the bias conditions are different, the channel lengths of these experimental devices are similar to the ones simulated here (144 nm [160] and 140 nm [161]), and therefore constitute a good reference. Importantly, a de-embedding procedure was carried out for the RF measurements of these experimental devices by using specific "short" and "open" structures with identical layouts in order to remove the effects of the parasitics associated with the pads and connections, but not the contact and access region resistances.

Including the access regions results in a quite different response compared with the intrinsic device, as the associated parasitic resistances provoke a bias dependent decay of f_T. Considering the scenario without puddles, when the back gate is properly biased, f_T is considerably improved. If we analyse Figure D.1 jointly with Figure 7.13 and Figure 7.14, those combinations of V_{FG}, V_{BG} for which the $R_S - V_{FG}$ ($R_D - V_{FG}$) curve shows its minimum values, are those for which f_T shows a greater improvement. When R_S (R_D) is higher, f_T is spoiled with respect to the $V_{BG} = 0$ V case. This relation between the access region conductivity and the improvement of the RF performance was experimentally observed in [99], where a higher f_T was demonstrated when a GFET with two additional electrodes was properly biased to control such conductivity. When puddles are included, the channel conductivity increases, reducing the control of the back-gate bias, and simultaneously results in a more symmetric $f_T - V_{FG}$ dependence.

Appendix E **List of publications**

E.1 Directly related with the Thesis

Papers

- Toral-Lopez, A.; Marin, E. G.; Gonzalez-Medina, J. M.; Romero, F. J.; Ruiz, F. G.; Morales, D. P.; Rodriguez, N. & Godoy, A., *Assessment of three electrolyte–molecule electrostatic interaction models for 2D material based BioFETs*, ***Nanoscale Advances*, Royal Society of Chemistry (RSC)**, 2019, 1, 1077-1085.

- Toral-Lopez, A.; Marin, E. G.; Medina, A.; Ruiz, F. G.; Rodriguez, N. & Godoy, A., *GFET Asymmetric Transfer Response Analysis through Access Region Resistances*, ***Nanomaterials*, MDPI AG**, 2019, 9, 1027.

- Toral-Lopez, A.; Santos, H.; Marin, E. G.; Ruiz, F. G.; Palacios, J. J. & Godoy, A., *Multi-scale modeling of 2D GaSe FETs with strained channels*, **Nanotechnology, *IOP Publishing***, 2021.

Conference contributions

- Toral-Lopez, A.; Gonzalez-Medina, J. M.; Marin, E. G.; Marin-Sanchez, A.; Medina, A.; Ruiz, F. G. & Godoy, A., *Simulation of 2D semiconductor based MOSFETs*, **spanish Conference on Electron Devices (CDE)**, 2018.

- Toral-Lopez, A.; Marin, E. G.; Medina, A.; Ruiz, F. G.; Rodriguez, N. & Godoy, A., *Simulation of 2D-material based BioFETs targeting single-molecule detection applications*, **Single-Molecule Sensors and nanosystems International Conference (SI3C)**, 2019.

- Toral-Lopez, A.; Marin, E.; Cuesta, J.; Ruiz, F.; Pasadas, F.; Medina-Rull, A. & Godoy, A., *Numerical study of surface chemical reactions*

in 2D-FET based pH sensors, **2020 International Conference on Simulation of Semiconductor Processes and Devices (SISPAD), IEEE**, 2020.

- Toral-Lopez, A.; Schneider, D. S.; Reato, E.; Marin, E. G.; Pasadas, F.; Wang, Z.; Lemme, M. C. & Godoy, A., *Hysteresis analysis of MoS_2 Field Effect Transistors*, **2021 Silicon Nanoelectronics Workshop (SNW)**, 2021.

E.2 Other thematics

Papers

- Pasadas, F.; Marin, E. G.; Toral-Lopez, A.; Ruiz, F. G.; Godoy, A.; Park, S.; Akinwande, D. & Jiménez, D., *Large-signal model of 2DFETs: compact modeling of terminal charges and intrinsic capacitances*, ***npj 2D Materials and Applications*, Springer Science and Business Media LLC**, 2019, 3.

- Toral-Lopez, A.; Pasadas, F.; Marin, E. G.; Medina-Rull, A.; Gonzalez-Medina, J. M.; Ruiz, F. J. G.; Jiménez, D. & Godoy, A., *Multi-scale analysis of radio-frequency performance of 2D-material based field-effect transistors*, **Nanoscale Advances, *Royal Society of Chemistry (RSC)***, 2021, 3, 2377-2382.

- Nandan, K.; Yadav, C.; Rastogi, P.; Toral-Lopez, A.; Marin-Sanchez, A.; Marin, E. G.; Ruiz, F. G.; Bhowmick, S. & Chauhan, Y. S., *Compact Modeling of Multi-layered MoS_2 FETs including Negative Capacitance Effect*, **IEEE Journal of the Electron Devices Society, *Institute of Electrical and Electronics Engineers (IEEE)***, 2020, 1-1.

Conference contributions

- Toral-Lopez, A.; Pasadas, F.; Marin, E. G.; Medina-Rull, A.; Ruiz, F. J. G.; Jimenez, D. & Godoy, A., *Device-to-circuit modeling approach to Metal – Insulator – 2D material FETs targeting the design of linear RF applications*, **2019 International Conference on Simulation of Semiconductor Processes and Devices (SISPAD), IEEE**, 2019.

- Nandan, K.; Yadav, C.; Rastogi, P.; Toral-Lopez, A.; Marin-Sanchez, A.; Marin, E. G.; Ruiz, F. G.; Bhowmick, S. & Chauhan, Y. S., *Compact Modeling of Surface Potential and Drain Current in Multi-layered MoS_2 FETs*, **2020 4th IEEE Electron Devices Technology & Manufacturing Conference (EDTM), IEEE**, 2020

BIBLIOGRAPHY

[1] S. William. Circuit element utilizing semiconductive material, September 25 1951. US Patent 2,569,347.

[2] K. Dawon. Electric field controlled semiconductor device, August 27 1963. US Patent 3,102,230.

[3] Gordon E Moore et al. Progress in digital integrated electronics. In *Electron Devices Meeting*, volume 21, pages 11–13, 1975.

[4] International technology roadmap for semiconductors (ITRS) 2009. Online, 2009.

[5] Shun Mao, Jingbo Chang, Haihui Pu, Ganhua Lu, Qiyuan He, Hua Zhang, and Junhong Chen. Two-dimensional nanomaterial-based field-effect transistors for chemical and biological sensing. *Chemical Society Reviews*, 46(22):6872–6904, 2017.

[6] P. Bergveld. Development of an ion-sensitive solid-state device for neurophysiological measurements. *IEEE Transactions on Biomedical Engineering*, BME-17(1):70–71, jan 1970.

[7] Stanley D. Moss, Jiri. Janata, and Curtis C. Johnson. Potassium ion-sensitive field effect transistor. *Analytical Chemistry*, 47(13):2238–2243, nov 1975.

[8] R.G. Kelly. Microelectronic approaches to solid state ion selective electrodes. *Electrochimica Acta*, 22(1):1–8, jan 1977.

[9] C.D. Fung, P.W. Cheung, and W.H. Ko. A generalized theory of an electrolyte-insulator-semiconductor field-effect transistor. *IEEE Transactions on Electron Devices*, 33(1):8–18, jan 1986.

[10] D.L. Harame, L.J. Bousse, J.D. Shott, and J.D. Meindl. Ion-sensing devices with silicon nitride and borosilicate glass insulators. *IEEE Transactions on Electron Devices*, 34(8):1700–1707, aug 1987.

[11] H. Abe, M. Esashi, and T. Matsuo. ISFET's using inorganic gate thin films. *IEEE Transactions on Electron Devices*, 26(12):1939–1944, dec 1979.

[12] Abdelhamid Errachid, Nadia Zine, Josep Samitier, and Joan Bausells. FET-based chemical sensor systems fabricated with standard technologies. *Electroanalysis*, 16(22):1843–1851, nov 2004.

[13] Stanley D. Moss, Curtis C. Johnson, and Jiri Janata. Hydrogen, calcium, and potassium ion-sensitive FET transducers: A preliminary report. *IEEE Transactions on Biomedical Engineering*, BME-25(1):49–54, jan 1978.

[14] Giwan Seo, Geonhee Lee, Mi Jeong Kim, Seung-Hwa Baek, Minsuk Choi, Keun Bon Ku, Chang-Seop Lee, Sangmi Jun, Daeui Park, Hong Gi Kim, Seong-Jun Kim, Jeong-O Lee, Bum Tae Kim, Edmond Changkyun Park, and Seung Il Kim. Rapid detection of COVID-19 causative virus (SARS-CoV-2) in human nasopharyngeal swab specimens using field-effect transistor-based biosensor. *ACS Nano*, 14(4):5135–5142, apr 2020.

[15] Simon Q. Lud, Michael G. Nikolaides, Ilka Haase, Markus Fischer, and Andreas R. Bausch. Field effect of screened charges: Electrical detection of peptides and proteins by a thin-film resistor. *ChemPhysChem*, 7(2):379–384, jan 2006.

[16] Deblina Sarkar, Wei Liu, Xuejun Xie, Aaron C. Anselmo, Samir Mitragotri, and Kaustav Banerjee. MoS_2 field-effect transistor for next-generation label-free biosensors. *ACS Nano*, 8(4):3992–4003, apr 2014.

[17] Gengfeng Zheng, Fernando Patolsky, Yi Cui, Wayne U Wang, and Charles M Lieber. Multiplexed electrical detection of cancer markers with nanowire sensor arrays. *Nature Biotechnology*, 23(10):1294–1301, sep 2005.

[18] Xiaojie Duan, Tian-Ming Fu, Jia Liu, and Charles M. Lieber. Nanoelectronics-biology frontier: From nanoscopic probes for action potential recording in live cells to three-dimensional cyborg tissues. *Nano Today*, 8(4):351–373, aug 2013.

[19] Tzahi Cohen-Karni, Quan Qing, Qiang Li, Ying Fang, and Charles M. Lieber. Graphene and nanowire transistors for cellular interfaces and electrical recording. *Nano Letters*, 10(3):1098–1102, mar 2010.

[20] Lucas H. Hess, Alina Lyuleeva, Benno M. Blaschke, Matthias Sachsenhauser, Max Seifert, Jose A. Garrido, and Frank Deubel. Graphene

transistors with multifunctional polymer brushes for biosensing applications. *ACS Applied Materials & Interfaces*, 6(12):9705–9710, jun 2014.

[21] Eric Stern, Robin Wagner, Fred J. Sigworth, Ronald Breaker, Tarek M. Fahmy, and Mark A. Reed. Importance of the debye screening length on nanowire field effect transistor sensors. *Nano Letters*, 7(11):3405–3409, nov 2007.

[22] V. Pachauri and S. Ingebrandt. Biologically sensitive field-effect transistors: from ISFETs to NanoFETs. *Essays In Biochemistry*, 60(1):81–90, jun 2016.

[23] Lucas H. Hess, Christoph Becker-Freyseng, Michael S. Wismer, Benno M. Blaschke, Martin Lottner, Felix Rolf, Max Seifert, and Jose A. Garrido. Electrical coupling between cells and graphene transistors. *Small*, 11(14):1703–1710, nov 2014.

[24] Hongsuk Nam, Bo-Ram Oh, Mikai Chen, Sungjin Wi, Da Li, Katsuo Kurabayashi, and Xiaogan Liang. Fabrication and comparison of MoS_2 and WSe_2 field-effect transistor biosensors. *Journal of Vacuum Science & Technology B, Nanotechnology and Microelectronics: Materials, Processing, Measurement, and Phenomena*, 33(6):06FG01, nov 2015.

[25] Joonhyung Lee, Piyush Dak, Yeonsung Lee, Heekyeong Park, Woong Choi, Muhammad A. Alam, and Sunkook Kim. Two-dimensional layered MoS_2 biosensors enable highly sensitive detection of biomolecules. *Scientific Reports*, 4(1):7352, dec 2014.

[26] K. S. Novoselov. Electric field effect in atomically thin carbon films. *Science*, 306(5696):666–669, oct 2004.

[27] Jose María González Medina. Transistores de efecto de campo basados en materiales bidimensionales. Master's thesis, Universidad de Granada, 2014.

[28] Shengli Zhang, Meiqiu Xie, Fengyu Li, Zhong Yan, Yafei Li, Erjun Kan, Wei Liu, Zhongfang Chen, and Haibo Zeng. Semiconducting group 15 monolayers: A broad range of band gaps and high carrier mobilities. *Angewandte Chemie International Edition*, 55(5):1666–1669, dec 2015.

[29] Boubekeur Lalmi, Hamid Oughaddou, Hanna Enriquez, Abdelkader Kara, Sébastien Vizzini, Bénidicte Ealet, and Bernard Aufray. Epitax-

ial growth of a silicene sheet. *Applied Physics Letters*, 97(22):223109, nov 2010.

[30] M E Dávila, L Xian, S Cahangirov, A Rubio, and G Le Lay. Germanene: a novel two-dimensional germanium allotrope akin to graphene and silicene. *New Journal of Physics*, 16(9):095002, sep 2014.

[31] Jianping Ji, Xiufeng Song, Jizi Liu, Zhong Yan, Chengxue Huo, Shengli Zhang, Meng Su, Lei Liao, Wenhui Wang, Zhenhua Ni, Yufeng Hao, and Haibo Zeng. Two-dimensional antimonene single crystals grown by van der waals epitaxy. *Nature Communications*, 7:13352, nov 2016.

[32] Xufan Li, Ming-Wei Lin, Alexander A. Puretzky, Juan C. Idrobo, Cheng Ma, Miaofang Chi, Mina Yoon, Christopher M. Rouleau, Ivan I. Kravchenko, David B. Geohegan, and Kai Xiao. Controlled vapor phase growth of single crystalline, two-dimensional GaSe crystals with high photoresponse. *Scientific Reports*, 4(1), jun 2014.

[33] A. Kuc, N. Zibouche, and T. Heine. Influence of quantum confinement on the electronic structure of the transition metal sulfide TS_2. *Physical Review B*, 83(24), jun 2011.

[34] Vy Tran, Ryan Soklaski, Yufeng Liang, and Li Yang. Layer-controlled band gap and anisotropic excitons in few-layer black phosphorus. *Physical Review B*, 89(23), jun 2014.

[35] A. K. Geim and I. V. Grigorieva. Van der waals heterostructures. *Nature*, 499(7459):419–425, jul 2013.

[36] Li Xie, Mengzhou Liao, Shuopei Wang, Hua Yu, Luojun Du, Jian Tang, Jing Zhao, Jing Zhang, Peng Chen, Xiaobo Lu, Guole Wang, Guibai Xie, Rong Yang, Dongxia Shi, and Guangyu Zhang. Graphene-contacted ultrashort channel monolayer MoS_2 transistors. *Advanced Materials*, 29(37):1702522, jul 2017.

[37] C. Casiraghi, M. Macucci, K. Parvez, R. Worsley, Y. Shin, F. Bronte, C. Borri, M. Paggi, and G. Fiori. Inkjet printed 2d-crystal based strain gauges on paper. *Carbon*, 129:462–467, apr 2018.

[38] Silvia Conti, Lorenzo Pimpolari, Gabriele Calabrese, Robyn Worsley, Subimal Majee, Dmitry K. Polyushkin, Matthias Paur, Simona Pace, Dong Hoon Keum, Filippo Fabbri, Giuseppe Iannaccone, Massimo

Macucci, Camilla Coletti, Thomas Mueller, Cinzia Casiraghi, and Gianluca Fiori. Low-voltage 2d materials-based printed field-effect transistors for integrated digital and analog electronics on paper. *Nature Communications*, 11(1), jul 2020.

[39] Duck-Jin Kim, Il Yung Sohn, Jin-Heak Jung, Ok Ja Yoon, N.-E. Lee, and Joon-Shik Park. Reduced graphene oxide field-effect transistor for label-free femtomolar protein detection. *Biosensors and Bioelectronics*, 41:621–626, mar 2013.

[40] Byunghoon Ryu, Hongsuk Nam, Bo-Ram Oh, Yujing Song, Pengyu Chen, Younggeun Park, Wenjie Wan, Katsuo Kurabayashi, and Xiaogan Liang. Cyclewise operation of printed MoS_2 transistor biosensors for rapid biomolecule quantification at femtomolar levels. *ACS Sensors*, 2(2):274–281, feb 2017.

[41] Byunghoon Ryu, Erika Yang, Younggeun Park, Katsuo Kurabayashi, and Xiaogan Liang. Fabrication of prebent MoS_2 biosensors on flexible substrates. *Journal of Vacuum Science & Technology B, Nanotechnology and Microelectronics: Materials, Processing, Measurement, and Phenomena*, 35(6):06G805, nov 2017.

[42] Michael Taeyoung Hwang, Mohammad Heiranian, Yerim Kim, Seungyong You, Juyoung Leem, Amir Taqieddin, Vahid Faramarzi, Yuhang Jing, Insu Park, Arend M. van der Zande, Sungwoo Nam, Narayana R. Aluru, and Rashid Bashir. Ultrasensitive detection of nucleic acids using deformed graphene channel field effect biosensors. *Nature Communications*, 11(1), mar 2020.

[43] Lu Wang, Ye Wang, Jen It Wong, Tomás Palacios, Jing Kong, and Hui Ying Yang. Functionalized MoS_2 nanosheet-based field-effect biosensor for label-free sensitive detection of cancer marker proteins in solution. *Small*, 10(6):1101–1105, jan 2014.

[44] Hongsuk Nam, Bo-Ram Oh, Pengyu Chen, Mikai Chen, Sungjin Wi, Wenjie Wan, Katsuo Kurabayashi, and Xiaogan Liang. Multiple MoS_2 transistors for sensing molecule interaction kinetics. *Scientific Reports*, 5(1):10546, may 2015.

[45] In-Young Chung, Hyeri Jang, Jieun Lee, Hyunggeun Moon, Sung Min Seo, and Dae Hwan Kim. Simulation study on discrete charge effects of SiNW biosensors according to bound target position using a 3D TCAD simulator. *Nanotechnology*, 23(6):065202, jan 2012.

[46] Daniele Passeri, Arianna Morozzi, Keida Kanxheri, and Andrea Scorzoni. Numerical simulation of ISFET structures for biosensing devices with TCAD tools. *BioMedical Engineering OnLine*, 14(Suppl 2):S3, 2015.

[47] F. Pittino, P. Palestri, P. Scarbolo, D. Esseni, and L. Selmi. Models for the use of commercial TCAD in the analysis of silicon-based integrated biosensors. *Solid-State Electronics*, 98:63–69, aug 2014.

[48] Andrea Bandiziol, Pierpaolo Palestri, Federico Pittino, David Esseni, and Luca Selmi. A TCAD-based methodology to model the site-binding charge at ISFET/electrolyte interfaces. *IEEE Transactions on Electron Devices*, 62(10):3379–3386, oct 2015.

[49] Thomas Windbacher, Viktor Sverdlov, Siegfried Selberherr, Clemens Heitzinger, Norbert Mauser, and Christian Ringhofer. Simulation of field-effect biosensors (BioFETs). In *2008 International Conference on Simulation of Semiconductor Processes and Devices*. IEEE, sep 2008.

[50] Xuan Yang and D. K. Schroder. Some semiconductor device physics considerations and clarifications. *IEEE Transactions on Electron Devices*, 59(7):1993–1996, jul 2012.

[51] C Heitzinger, R Kennell, G Klimeck, N Mauser, M McLennan, and C Ringhofer. Modeling and simulation of field-effect biosensors (BioFETs) and their deployment on the nanoHUB. *Journal of Physics: Conference Series*, 107:012004, mar 2008.

[52] Hongsuk Nam, Bo-Ram Oh, Pengyu Chen, Jeong Seop Yoon, Sungjin Wi, Mikai Chen, Katsuo Kurabayashi, and Xiaogan Liang. Two different device physics principles for operating MoS_2 transistor biosensors with femtomolar-level detection limits. *Applied Physics Letters*, 107(1):012105, jul 2015.

[53] Aniket Kakatkar, T S Abhilash, R De Alba, J M Parpia, and H G Craighead. Detection of DNA and poly-l-lysine using CVD graphene-channel FET biosensors. *Nanotechnology*, 26(12):125502, mar 2015.

[54] Rakhi Narang, Manoj Saxena, and Mridula Gupta. Analytical model of pH sensing characteristics of junctionless silicon on insulator ISFET. *IEEE Transactions on Electron Devices*, 64(4):1742–1750, apr 2017.

[55] A. Poghossian, A. Cherstvy, S. Ingebrandt, A. Offenhäusser, and M.J. Schöning. Possibilities and limitations of label-free detection of DNA

hybridization with field-effect-based devices. *Sensors and Actuators B: Chemical*, 111-112:470–480, nov 2005.

[56] Abir Shadman, Ehsanur Rahman, and Quazi D.M. Khosru. Monolayer MoS_2 and WSe_2 double gate field effect transistor as super nernst pH sensor and nanobiosensor. *Sensing and Bio-Sensing Research*, 11:45–51, dec 2016.

[57] Kanak Datta, Abir Shadman, Ehsanur Rahman, and Quazi D. M. Khosru. Trilayer TMDC heterostructures for MOSFETs and nanobiosensors. *Journal of Electronic Materials*, 46(2):1248–1260, nov 2016.

[58] David E. Yates, Samuel Levine, and Thomas W. Healy. Site-binding model of the electrical double layer at the oxide/water interface. *Journal of the Chemical Society, Faraday Transactions 1: Physical Chemistry in Condensed Phases*, 70(0):1807, 1974.

[59] Itamar Borukhov, David Andelman, and Henri Orland. Steric effects in electrolytes: A modified Poisson-Boltzmann equation. *Physical Review Letters*, 79(3):435–438, jul 1997.

[60] Xinrong Yang, W. R. Frensley, Dian Zhou, and Wenchuang Hu. Performance analysis of Si nanowire biosensor by numerical modeling for charge sensing. *IEEE Transactions on Nanotechnology*, 11(3):501–512, may 2012.

[61] S.M. Sze and Kwok K. Ng. *Physics of Semiconductor Devices*. John Wiley & Sons, Inc., apr 2006.

[62] Ben G. Streetman and Sanjay Kumar Banerjee. *Solid state electronic devices, 6th ed.* Prentice-Hal, 2006.

[63] Supriyo Datta. *Quantum Transport: Atom to Transistor*. Cambridge University Press, 2005.

[64] D. R. Hartree. The wave mechanics of an atom with a non-coulomb central field. part i. theory and methods. *Mathematical Proceedings of the Cambridge Philosophical Society*, 24(1):89–110, jan 1928.

[65] V. Fock. Näherungsmethode zur lösung des quantenmechanischen mehrkörperproblems. *Zeitschrift für Physik*, 61(1-2):126–148, jan 1930.

[66] J. C. Slater. A simplification of the hartree-fock method. *Physical Review Journals Archive*, 81(3):385–390, feb 1951.

[67] P. Hohenberg and W. Kohn. Inhomogeneous electron gas. *Physical Review Journals Archive*, 136(3B):B864–B871, nov 1964.

[68] W. Kohn and L. J. Sham. Self-consistent equations including exchange and correlation effects. *Physical Review*, 140(4A):A1133–A1138, nov 1965.

[69] D. M. Ceperley and B. J. Alder. Ground state of the electron gas by a stochastic method. *Physical Review Letters*, 45(7):566–569, aug 1980.

[70] J. P. Perdew and Alex Zunger. Self-interaction correction to density-functional approximations for many-electron systems. *Physcial Review B*, 23(10):5048–5079, may 1981.

[71] Dragica Vasileska, Stephen Goodnick, and Gerhard Klimeck. *Computational Electronics*. CRC Press, jun 2010.

[72] Juan Bisquert, Peter Cendula, Luca Bertoluzzi, and Sixto Gimenez. Energy diagram of semiconductor/electrolyte junctions. *The Journal of Physical Chemistry Letters*, 5(1):205–207, dec 2013.

[73] Peter W. Cheung Clifford D. Fung and Wen H. Ko. A generalized theory of an Electrolyte-Insulator-Semiconductor Field-Effect Transistor. *IEEE Transactions On Electron Devices*, 33(1):8–18, January 1986.

[74] Bingjie Cai, Shuting Wang, Le Huang, Yong Ning, Zhiyong Zhang, and Guo-Jun Zhang. Ultrasensitive label-free detection of PNA–DNA hybridization by reduced graphene oxide field-effect transistor biosensor. *ACS Nano*, 8(3):2632–2638, feb 2014.

[75] M. Perucchini, D. Marian, E. G. Marin, T. Cusati, G. Iannaccone, and G. Fiori. Electronic transport in 2D-based printed FETs from a multiscale perspective. *Advanced Electronic Materials*, 2021.

[76] Siegfried Selberherr. *Analysis and Simulation of Semiconductor Devices*. Springer Vienna, 1984.

[77] Xufeng Wang. *Nanomos 4.0: a tool to explore ultimate si transistors and beyond*. PhD thesis, Purdue University, West Lafayette, Indiana, 2010.

[78] James G. Champlain. A first principles theoretical examination of graphene-based field effect transistors. *Journal of Applied Physics*, 109(8):084515, apr 2011.

[79] Enrique González Marín. *Modeling and simulation of semiconductor nanowires for future technology nodes.* PhD thesis, University of Granada, 2014.

[80] Nadine Schwierz, Dominik Horinek, and Roland R. Netz. Reversed anionic hofmeister series: The interplay of surface charge and surface polarity. *Langmuir*, 26(10):7370–7379, may 2010.

[81] Matthew A. Brown, Guilherme Volpe Bossa, and Sylvio May. Emergence of a stern layer from the incorporation of hydration interactions into the gouy–chapman model of the electrical double layer. *Langmuir*, 31(42):11477–11483, oct 2015.

[82] Nadine Schwierz, Dominik Horinek, and Roland R. Netz. Anionic and cationic hofmeister effects on hydrophobic and hydrophilic surfaces. *Langmuir*, 29(8):2602–2614, feb 2013.

[83] Sigma-Aldrich. PBS recipe. online. last visited: 04/10/2021.

[84] Stefan Birner. *Modeling of semiconductor nanostructures and semiconductor–electrolyte interfaces.* PhD thesis, Technische Universität München, 2011.

[85] L. J. Mele, P. Palestri, and L. Selmi. General approach to model the surface charge induced by multiple surface chemical reactions in potentiometric FET sensors. *IEEE Transactions on Electron Devices*, 67(3):1149–1156, mar 2020.

[86] A. Toral-Lopez, J. M. Gonzalez-Medina, E. G. Marin, A. Marin-Sanchez, A. Medina, F. G. Ruiz, and A. Godoy. Simulation of 2D semiconductor based MOSFETs. In *CDE*, 2018.

[87] F. G. Ruiz, B. Biel, J. M. Medina, A. Toral, E. G. Marin, I. M. Tienda-Luna, and A. Godoy. Calculation of the ballistic current of few-layer MoS_2 Field-Effect Transistors. In *19th International Conference on Electron Dynamics in Semiconductors, Optoelectronics and Nanostructures.*, page 162. Universidad de Salamanca, 2015.

[88] Daria Krasnozhon, Dominik Lembke, Clemens Nyffeler, Yusuf Leblebici, and Andras Kis. MoS_2 transistors operating at gigahertz frequencies. *Nano Letters*, 14(10):5905–5911, sep 2014.

[89] Ronen Dagan, Yonatan Vaknin, and Yossi Rosenwaks. Gap state distribution and fermi level pinning in monolayer to multilayer MoS_2 field effect transistors. *Nanoscale*, 12(16):8883–8889, 2020.

[90] Changsik Kim, Inyong Moon, Daeyeong Lee, Min Sup Choi, Faisal Ahmed, Seunggeol Nam, Yeonchoo Cho, Hyeon-Jin Shin, Seongjun Park, and Won Jong Yoo. Fermi level pinning at electrical metal contacts of monolayer molybdenum dichalcogenides. *ACS Nano*, 11(2):1588–1596, jan 2017.

[91] M. Takenaka, Y. Ozawa, J. Han, and S. Takagi. Quantitative evaluation of energy distribution of interface trap density at MoS_2 MOS interfaces by the terman method. In *2016 IEEE International Electron Devices Meeting (IEDM)*, pages 139–142. IEEE, dec 2016.

[92] Zhenxing Wang, Huilong Xu, Zhiyong Zhang, Sheng Wang, Li Ding, Qingsheng Zeng, Leijing Yang, Tian Pei, Xuelei Liang, Min Gao, and Lian-Mao Peng. Growth and performance of yttrium oxide as an ideal *high-k* gate dielectric for carbon-based electronics. *Nano Letters*, 10(6):2024–2030, jun 2010.

[93] Zhiyong Zhang, Huilong Xu, Hua Zhong, and Lian-Mao Peng. Direct extraction of carrier mobility in graphene field-effect transistor using current-voltage and capacitance-voltage measurements. *Applied Physics Letters*, 101(21):213103, nov 2012.

[94] Stefano Venica, Massimiliano Zanato, Francesco Driussi, Pierpaolo Palestri, and Luca Selmi. Modeling electrostatic doping and series resistance in graphene-FETs. In *2016 International Conference on Simulation of Semiconductor Processes and Devices (SISPAD)*. IEEE, sep 2016.

[95] A. Toral-Lopez, E. G. Marin, A. Medina, F. G. Ruiz, N. Rodriguez, and A. Godoy. GFET asymmetric transfer response analysis through access region resistances. *Nanomaterials*, 9(7):1027, jul 2019.

[96] Antonio Di Bartolomeo, Filippo Giubileo, Francesco Romeo, Paolo Sabatino, Giovanni Carapella, Laura Iemmo, Thomas Schroeder, and Grzegorz Lupina. Graphene Field-Effect transistors with niobium contacts and asymmetric transfer characteristics. *Nanotechnology*, 26(47):475202, nov 2015.

[97] Alexander S. Mayorov, Roman V. Gorbachev, Sergey V. Morozov, Liam Britnell, Rashid Jalil, Leonid A. Ponomarenko, Peter Blake, Kostya S. Novoselov, Kenji Watanabe, Takashi Taniguchi, and A. K. Geim. Micrometer-scale ballistic transport in encapsulated graphene at room temperature. *Nano Letters*, 11(6):2396–2399, jun 2011.

[98] Soumya Jain and Aloke K. Dutta. Resistance-based approach for drain current modeling in graphene FETs. *IEEE Transactions on Electron Devices*, 62(12):4313–4321, dec 2015.

[99] C. Al-Amin, M. Karabiyik, and N. Pala. Fabrication of graphene field-effect transistor with field controlling electrodes to improve f_T. *Microelectronic Engineering*, 164:71–74, oct 2016.

[100] Han Wang, A Hsu, Jing Kong, D A Antoniadis, and T Palacios. Compact virtual-source current–voltage model for top- and back-gated graphene field-effect transistors. *IEEE Transactions on Electron Devices*, 58(5):1523–1533, may 2011.

[101] Gianluca Fiori and Giuseppe Iannaccone. Multiscale modeling for graphene-based nanoscale transistors. *Proceedings of the IEEE*, 101(7):1653–1669, jul 2013.

[102] Q. Wilmart, A. Inhofer, M. Boukhicha, W. Yang, M. Rosticher, P. Morfin, N. Garroum, G. Fève, J.-M. Berroir, and B. Plaçais. Contact gating at GHz frequency in graphene. *Scientific Reports*, 6(1), feb 2016.

[103] J. Martin, N. Akerman, G. Ulbricht, T. Lohmann, J. H. Smet, K. von Klitzing, and A. Yacoby. Observation of electron–hole puddles in graphene using a scanning single-electron transistor. *Nature Physics*, 4(2):144–148, nov 2007.

[104] Yuanbo Zhang, Victor W. Brar, Caglar Girit, Alex Zettl, and Michael F. Crommie. Origin of spatial charge inhomogeneity in graphene. *Nature Physics*, 5(10):722–726, aug 2009.

[105] Alejandro Toral-Lopez, Hernan Santos, Enrique G Marin, Fran G Ruiz, Juan Jose Palacios, and Andrés Godoy. Multi-scale modeling of 2D GaSe FETs with strained channels. *Nanotechnology*, 33(10):105201, dec 2021.

[106] E. G. Marin, M. Perucchini, D. Marian, G. Iannaccone, and G. Fiori. Modeling of electron devices based on 2-D materials. *IEEE Transactions on Electron Devices*, 65(10):4167–4179, oct 2018.

[107] Damiano Marian, Enrique G. Marin, Giuseppe Iannaccone, and Gianluca Fiori. Sub-maxwellian source injection and negative differential transconductance in decorated graphene nanoribbons. *Physical Review Applied*, 14(6):064019, dec 2020.

[108] Enrique G. Marin, Damiano Marian, Marta Perucchini, Gianluca Fiori, and Giuseppe Iannaccone. Lateral heterostructure field-effect transistors based on two-dimensional material stacks with varying thickness and energy filtering source. *ACS Nano*, 14(2):1982–1989, jan 2020.

[109] E. G. Marin, D. Marian, G. Iannaccone, and G. Fiori. Tunnel-field-effect spin filter from two-dimensional antiferromagnetic stanene. *Physical Review Applied*, 10(4):044063, oct 2018.

[110] Shikai Deng, Anirudha V. Sumant, and Vikas Berry. Strain engineering in two-dimensional nanomaterials beyond graphene. *Nano Today*, 22:14–35, oct 2018.

[111] Zhiwei Li, Yawei Lv, Liwang Ren, Jia Li, Lingan Kong, Yujia Zeng, Quanyang Tao, Ruixia Wu, Huifang Ma, Bei Zhao, Di Wang, Weiqi Dang, Keqiu Chen, Lei Liao, Xidong Duan, Xiangfeng Duan, and Yuan Liu. Efficient strain modulation of 2D materials via polymer encapsulation. *Nature Communications*, 11(1), mar 2020.

[112] Yongke Sun, Scott E. Thompson, and Toshikazu Nishida. *Strain Effect in Semiconductors*. Springer US, 2010.

[113] Patricia Gant, Peng Huang, David Pérez de Lara, Dan Guo, Riccardo Frisenda, and Andres Castellanos-Gomez. A strain tunable single-layer MoS_2 photodetector. *Materials Today*, 27:8–13, jul 2019.

[114] Sian-Hong Tseng, Hung-Yi Chen, Wei-Ting Hsu, Hsiang-Chen Wang, Yuan-Yao Li, Wen-Hao Chang, Ming-Pei Lu, and Ming-Yen Lu. Influences of contact metals on the performances of MoS_2 devices under strains. *The Journal of Physical Chemistry C*, 123(50):30696–30703, nov 2019.

[115] G. Fischer and J.L. Brebner. Electrical resistivity and hall effect of single crystals of GaTe and GaSe. *Journal of Physics and Chemistry of Solids*, 23(10):1363–1370, oct 1962.

[116] David Maeso, Sahar Pakdel, Hernán Santos, Nicolás Agraït, Juan José Palacios, Elsa Prada, and Gabino Rubio-Bollinger. Strong modulation of optical properties in rippled 2D GaSe via strain engineering. *Nanotechnology*, 30(24):24LT01, mar 2019.

[117] Zhiwei Peng, Xiaolin Chen, Yulong Fan, David J. Srolovitz, and Dangyuan Lei. Strain engineering of 2D semiconductors and graphene: from strain fields to band-structure tuning and photonic applications. *Light: Science & Applications*, 9(1), nov 2020.

[118] Cheng-Wei Liu, Jin-Ji Dai, Ssu-Kuan Wu, Nhu-Quynh Diep, Sa-Hoang Huynh, Thi-Thu Mai, Hua-Chiang Wen, Chi-Tsu Yuan, Wu-Ching Chou, Ji-Lin Shen, and Huy-Hoang Luc. Substrate-induced strain in 2D layered GaSe materials grown by molecular beam epitaxy. *Scientific Reports*, 10(1), jul 2020.

[119] Yecun Wu, Huei-Ru Fuh, Duan Zhang, Cormac Ó Coileáin, Hongjun Xu, Jiung Cho, Miri Choi, Byong Sun Chun, Xuju Jiang, Mourad Abid, Mohamed Abid, Huajun Liu, Jing Jing Wang, Igor V. Shvets, Ching-Ray Chang, and Han-Chun Wu. Simultaneous large continuous band gap tunability and photoluminescence enhancement in GaSe nanosheets via elastic strain engineering. *Nano Energy*, 32:157–164, feb 2017.

[120] M. O. D. Camara, A. Mauger, and I. Devos. Electronic structure of the layer compounds GaSe and InSe in a tight-binding approach. *Physical Review B*, 65(12), mar 2002.

[121] Leonor Chico, Lorin X. Benedict, Steven G. Louie, and Marvin L. Cohen. Quantum conductance of carbon nanotubes with defects. *Physical Review B*, 54(4):2600–2606, jul 1996.

[122] Marco Buongiorno Nardelli. Electronic transport in extended systems: Application to carbon nanotubes. *Physical Review B*, 60(11):7828–7833, sep 1999.

[123] Chowdhury Al-Amin, Mustafa Karabiyik, Raju Sinha, and Nezih Pala. Lowering contact resistance of graphene FETs with capacitive extension of ohmic contacts for enhanced RF performance. In Thomas George, Achyut K. Dutta, and M. Saif Islam, editors, *Micro- and Nanotechnology Sensors, Systems, and Applications VII*. SPIE, may 2015.

[124] Rongzhou Zeng, Ping Li, Junhong Li, Yongbo Liao, Qingwei Zhang, and Gang Wang. Self-aligned graphene transistor. *Electronics Letters*, 53(24):1592–1594, nov 2017.

[125] Myung-Ho Jung, Goon-Ho Park, Tomohiro Yoshida, Hirokazu Fukidome, Tetsuya Suemitsu, Taiichi Otsuji, and Maki Suemitsu. High-performance graphene field-effect transistors with extremely small access length using self-aligned source and drain technique. *Proceedings of the IEEE*, 101(7):1603–1608, jul 2013.

[126] Devin Verreck, Goutham Arutchelvan, Cesar J. Lockhart De La Rosa, Alessandra Leonhardt, Daniele Chiappe, Anh Khoa Augustin Lu, Geoffrey Pourtois, Philippe Matagne, Marc M. Heyns, Stefan De Gendt,

Anda Mocuta, and Iuliana P. Radu. The role of nonidealities in the scaling of MoS_2 FETs. *IEEE Transactions on Electron Devices*, 65(10):4635–4640, oct 2018.

[127] Michel Houssa, Konstantina Iordanidou, Ashish Dabral, Augustin Lu, Geoffrey Pourtois, Valeri Afanasiev, and André Stesmans. Contact resistance at MoS_2-based 2D metal/semiconductor lateral heterojunctions. *ACS Applied Nano Materials*, 2(2):760–766, jan 2019.

[128] Damiano Marian, Elias Dib, Teresa Cusati, Enrique G. Marin, Alessandro Fortunelli, Giuseppe Iannaccone, and Gianluca Fiori. Transistor concepts based on lateral heterostructures of metallic and semiconducting phases of MoS_2. *Physical Review Applied*, 8(5), nov 2017.

[129] Lingming Yang, Kausik Majumdar, Han Liu, Yuchen Du, Heng Wu, Michael Hatzistergos, P. Y. Hung, Robert Tieckelmann, Wilman Tsai, Chris Hobbs, and Peide D. Ye. Chloride molecular doping technique on 2D materials: WS_2 and MoS_2. *Nano Letters*, 14(11):6275–6280, oct 2014.

[130] Ajjiporn Dathbun, Youngchan Kim, Yongsuk Choi, Jia Sun, Seongchan Kim, Byunggil Kang, Moon Sung Kang, Do Kyung Hwang, Sungjoo Lee, Changgu Lee, and Jeong Ho Cho. Selectively metallized 2D materials for simple logic devices. *ACS Applied Materials & Interfaces*, 11(20):18571–18579, apr 2019.

[131] Kshitij Bhargava and Vipul Singh. Electrical characterization and parameter extraction of organic thin film transistors using two dimensional numerical simulations. *Journal of Computational Electronics*, 13(3):585–592, apr 2014.

[132] Sekhar Babu Mitta, Min Sup Choi, Ankur Nipane, Fida Ali, Changsik Kim, James T Teherani, James Hone, and Won Jong Yoo. Electrical characterization of 2D materials-based field-effect transistors. *2D Materials*, 8(1):012002, nov 2020.

[133] Adrien Allain, Jiahao Kang, Kaustav Banerjee, and Andras Kis. Electrical contacts to two-dimensional semiconductors. *Nature Materials*, 14(12):1195–1205, nov 2015.

[134] Ching-An Chuang, Min-Han Lin, Bo-Xian Yeh, and Ching-Hwa Ho. Curvature-dependent flexible light emission from layered gallium selenide crystals. *RSC Advances*, 8(5):2733–2739, 2018.

[135] Zuocheng Zhang, Likai Li, Jason Horng, Nai Zhou Wang, Fangyuan Yang, Yijun Yu, Yu Zhang, Guorui Chen, Kenji Watanabe, Takashi Taniguchi, Xian Hui Chen, Feng Wang, and Yuanbo Zhang. Strain-modulated bandgap and piezo-resistive effect in black phosphorus field-effect transistors. *Nano Letters*, 17(10):6097–6103, sep 2017.

[136] Salvatore Ethan Panasci, Emanuela Schilirò, Giuseppe Greco, Marco Cannas, Franco M. Gelardi, Simonpietro Agnello, Fabrizio Roccaforte, and Filippo Giannazzo. Strain, doping, and electronic transport of large area monolayer MoS_2 exfoliated on gold and transferred to an insulating substrate. *ACS Applied Materials & Interfaces*, 13(26):31248–31259, jun 2021.

[137] A. M. Bughio, S. Donati Guerrieri, F. Bonani, and G. Ghione. Multi-gate FinFET mixer variability assessment through physics-based simulation. *IEEE Electron Device Letters*, 38(8):1004–1007, aug 2017.

[138] Roman Sordan, Floriano Traversi, and Valeria Russo. Logic gates with a single graphene transistor. *Applied Physics Letters*, 94(7):073305, feb 2009.

[139] International roadmap for devices and systems (IRDS) 2020. Online, 2020.

[140] Antonio Di Bartolomeo, Luca Genovese, Filippo Giubileo, Laura Iemmo, Giuseppe Luongo, Tobias Foller, and Marika Schleberger. Hysteresis in the transfer characteristics of MoS_2 transistors. *2D Materials*, 5(1):015014, oct 2017.

[141] Alejandro Toral-Lopez, Daniel S. Schneider, Eros Reato, Enrique G. Marin, Francisco Pasadas, Zhenxing Wang, Max C. Lemme, and Andres Godoy. Hysteresis analysis of MoS_2 field effect transistors. In *2021 Silicon Nanoelectronics Workshop (SNW)*, 2021.

[142] Daniel S. Schneider, Annika Grundmann, Andreas Bablich, Vikram Passi, Satender Kataria, Holger Kalisch, Michael Heuken, Andrei Vescan, Daniel Neumaier, and Max C. Lemme. Highly responsive flexible photodetectors based on MOVPE grown uniform few-layer MoS_2. *ACS Photonics*, 7(6):1388–1395, may 2020.

[143] A. Toral-Lopez, E. G. Marin, J. M. Gonzalez-Medina, F. J. Romero, F. G. Ruiz, D. P. Morales, N. Rodriguez, and A. Godoy. Assessment of three electrolyte–molecule electrostatic interaction models for 2D material based BioFETs. *Nanoscale Advances*, 1(3):1077–1085, 2019.

[144] Alexandra C. Walls, M. Alejandra Tortorici, Joost Snijder, Xiaoli Xiong, Berend-Jan Bosch, Felix A. Rey, and David Veesler. Tectonic conformational changes of a coronavirus spike glycoprotein promote membrane fusion. *Proceedings of the National Academy of Sciences*, 114(42):11157–11162, oct 2017.

[145] Alexandra C. Walls, Young-Jun Park, M. Alejandra Tortorici, Abigail Wall, Andrew T. McGuire, and David Veesler. Structure, function, and antigenicity of the SARS-CoV-2 spike glycoprotein. *Cell*, 181(2):281–292.e6, apr 2020.

[146] Ramanathan Natesh, Sylva L. U. Schwager, Edward D. Sturrock, and K. Ravi Acharya. Crystal structure of the human angiotensin-converting enzyme–lisinopril complex. *Nature*, 421(6922):551–554, jan 2003.

[147] Jun Lan, Jiwan Ge, Jinfang Yu, Sisi Shan, Huan Zhou, Shilong Fan, Qi Zhang, Xuanling Shi, Qisheng Wang, Linqi Zhang, and Xinquan Wang. Structure of the SARS-CoV-2 spike receptor-binding domain bound to the ACE2 receptor. *Nature*, 581(7807):215–220, mar 2020.

[148] Jun Lan, Jiwan Ge, Jinfang Yu, Sisi Shan, Huan Zhou, Shilong Fan, Qi Zhang, Xuanling Shi, Qisheng Wang, Linqi Zhang, and Xinquan Wang. Structure of the SARS-CoV-2 spike receptor-binding domain bound to the ACE2 receptor. *Nature*, 581(7807):215–220, mar 2020.

[149] Daniel Wrapp, Nianshuang Wang, Kizzmekia S. Corbett, Jory A. Goldsmith, Ching-Lin Hsieh, Olubukola Abiona, Barney S. Graham, and Jason S. McLellan. Cryo-EM structure of the 2019-nCoV spike in the prefusion conformation. *Science*, 367(6483):1260–1263, feb 2020.

[150] Mushtaq Hussain, Nusrat Jabeen, Fozia Raza, Sanya Shabbir, Ayesha A. Baig, Anusha Amanullah, and Basma Aziz. Structural variations in human ACE2 may influence its binding with SARS-CoV-2 spike protein. *Journal of Medical Virology*, apr 2020.

[151] Hits mcm webpage. online.

[152] U. Pieper. MODBASE, a database of annotated comparative protein structure models, and associated resources. *Nucleic Acids Research*, 32(90001):217D–222, jan 2004.

[153] T. J. Dolinsky, J. E. Nielsen, J. A. McCammon, and N. A. Baker. PDB2pqr: an automated pipeline for the setup of poisson-boltzmann electrostatics calculations. *Nucleic Acids Research*, 32(Web Server):W665–W667, jul 2004.

[154] M.K. Gilson, J.A. Given, B.L. Bush, and J.A. McCammon. The statistical-thermodynamic basis for computation of binding affinities: a critical review. *Biophysical Journal*, 72(3):1047–1069, mar 1997.

[155] Yuqing Deng and Benoît Roux. Computations of standard binding free energies with molecular dynamics simulations. *The Journal of Physical Chemistry B*, 113(8):2234–2246, jan 2009.

[156] R. Sivakumarasamy, R. Hartkamp, B. Siboulet, J.-F. Dufrêche, K. Nishiguchi, A. Fujiwara, and N. Clément. Selective layer-free blood serum ionogram based on ion-specific interactions with a nanotransistor. *Nature Materials*, 17(5):464–470, feb 2018.

[157] Remco Hartkamp, Bertrand Siboulet, Jean-François Dufrêche, and Benoit Coasne. Ion-specific adsorption and electroosmosis in charged amorphous porous silica. *Physical Chemistry Chemical Physics*, 17(38):24683–24695, 2015.

[158] Honglei Wang, Peng Zhao, Xuan Zeng, Chadwin D Young, and Walter Hu. High-stability pH sensing with a few-layer MoS_2 field-effect transistor. *Nanotechnology*, 30(37):375203, jul 2019.

[159] Frank Schwierz. Graphene transistors: Status, prospects, and problems. *Proceedings of the IEEE*, 101(7):1567–1584, jul 2013.

[160] Lei Liao, Yung-Chen Lin, Mingqiang Bao, Rui Cheng, Jingwei Bai, Yuan Liu, Yongquan Qu, Kang L. Wang, Yu Huang, and Xiangfeng Duan. High-speed graphene transistors with a self-aligned nanowire gate. *Nature*, 467(7313):305–308, sep 2010.

[161] Yanqing Wu, Keith A. Jenkins, Alberto Valdes-Garcia, Damon B. Farmer, Yu Zhu, Ageeth A. Bol, Christos Dimitrakopoulos, Wenjuan Zhu, Fengnian Xia, Phaedon Avouris, and Yu-Ming Lin. State-of-the-art graphene high-frequency electronics. *Nano Letters*, 12(6):3062–3067, may 2012.

ACRONYMS

2DMs 2D materials. x, xvi, xviii, xix, 6–8, 11, 54–57, 61, 64, 65, 94, 108, 109, 113, 114, 116, 164, 166, 167

ACE2 Angiotensin Converting Enzyme 2. 136–140, 142, 143

BC Boundary Conditions. 51, 52

BioFET Field-Effect Transistor-based Biosensor. x, xii, xiii, xvi, xviii, xix, 6–9, 11–13, 32, 39, 40, 44, 45, 74, 75, 77, 86, 126, 127, 129, 130, 132–134, 143–145, 166, 167, 180

BJT Bipolar Junction Transistor. 4

DD Drift-Diffusion. x, xii, xviii, 61, 62, 64, 66, 94, 100, 108, 109, 117, 165, 166

DFT Density Functional Theory. 20–23, 96, 108

DNA Deoxyribonucleic acid. xi, 85, 86, 126, 143, 144, 165, 166

DoS Density of States. xi, xii, xvii, xviii, 22, 23, 25, 26, 49, 59, 60, 64, 65, 67–69, 71, 94–97, 108–111, 113, 118, 121, 130, 164, 172

dsDNA Double-Stranded DNA. 85, 86, 145

EIS Electrolyte-Insulator-Semiconductor. 8, 38, 39

EISFET Electrolyte-Insulator-Semiconductor Field-Effect Transistor. 39

EMA Effective Mass Approximation. 24, 55

ES Electrolyte-Semiconductor. 8, 9

FD Finite Difference. 44, 47, 62, 66, 70, 176

FET Field-Effect Transistor. x–xii, xvi–xix, 4–6, 11, 13, 37, 108, 112–115, 117, 118, 121, 164–166

FoM Figures of Merit. 184

GBioFET Graphene based Field-Effect Transistor-based Biosensor. 136–142

GFET Graphene Field-Effect Transistor. xii, 94, 100–105, 108, 165, 166, 185

gSB generic Site-Binding. 81

HF Hartree-Fock. 21

IoT Internet of Things. 5, 6

ISFET Ion-Sensitive Field-Effect Transistor. 6, 12, 13, 32, 40, 75, 81, 154, 155, 158

LDA Local Density Approximation. 22

mB modified Boltzmann. 75, 76

MD Molecular Dynamics. xi, xvii, 76, 86, 154, 165

MM Metal Monochalcogenides. 7, 109

MOS Metal-Oxide-Semiconductor. 32, 35–38, 57

MOSFET Metal-Oxide-Semiconductor Field-Effect Transistor. xii, xviii, 4–6, 8, 11, 13, 32–37, 54, 61, 66, 74, 94, 95, 99, 108, 118, 120, 158, 159, 164, 166

MS Metal-Semiconductor. 32, 33

PBS Phosphate-Buffered Saline. 78–80, 127–129, 131–133, 138, 140, 144–148, 150–152, 165, 167

pdf Probability Density Function. 88, 90, 180–182

PMF Potentials of Mean Force. xi, xiii, xvii, xix, 76, 77, 126, 151–159, 165

RF Radio-Frequency. 4, 108, 184, 185

S1RBD S1 Receptor Binding Domain. 136–140, 142, 143

SARS-CoV-2 Severe Acute Respiratory Syndrome Corona Virus 2. 136, 137, 142, 166

SB Site-Binding. xi, xiii, xvii, xix, 81–83, 126, 151–159

SG Single-Gate. 111–113

SoC System on Chip. 5

SPG Split-Gate. 111, 112, 114–117

ssDNA Single-Stranded DNA. 85

TB Tight-Binding. 109, 110, 164

TCAD Technology Computer Aided Design. xii, xviii, 9–11

TMD Transition Metal Dichalcogenides. 7, 8, 109

ZZ zigzag. 109, 110